

*GEOPOLYMER-BASED MOISTURE AND  
CHLORIDE SENSORS FOR NUCLEAR  
CONCRETE STRUCTURES*

Lorena Biondi

Civil and Environmental Engineering

University of Strathclyde

Glasgow, United Kingdom

A dissertation submitted for the degree of Doctor of Philosophy

July 2020



## DECLARATION

This thesis is the result of the author's original research. It has been composed by the author and has not been previously submitted for examination which has led to the award of a degree.

The copyright of this thesis belongs to the author under the terms of the United Kingdom Copyright Acts as qualified by University of Strathclyde Regulation 3.50. Due acknowledgement must always be made of the use of any material contained in, or derived from, this thesis.

Signed: Lorena Biondi

Date: 01/06/2020

To myself, for the courage of going beyond my limits,

To my family, for trusting, loving and supporting me always,

To Carmelo, the safe harbour and lighthouse of my life,

To God, my Strength.

*Dedication.*

*“Life without enquiry is not worth living for a man.”*

*Plato, Apology, 38a (399 b.C.)*

## ABSTRACT

The reinforced concrete structures that support transport, energy and urban networks in developed countries are over half a century old, and are facing widespread deterioration. The main cause of degradation — reinforcement corrosion, accelerated by moisture and chloride exposure — costs the global economy a staggering \$2.3 trillion per year (3.4% GDP, 2013). The nuclear industry faces a particular challenge, as concrete assets are usually coastal and can underpin safety-critical structures and radiation barriers. Passively-cooled waste stores, for example, are often ventilated with unfiltered sea air.

To deliver structural health monitoring and maintenance strategies, industry requires both moisture/chloride sensors and concrete repair materials. To date, monitoring and maintenance have been viewed as separate challenges. The work in this thesis demonstrates that geopolymer binders — a class of adhesive concrete repair materials — can be electrically interrogated and used to monitor moisture and chloride concentrations on concrete surfaces, or as stand-alone sensors. This can be achieved without sacrificing the ability of the geopolymer to form an effective repair.

This thesis outlines first-time demonstrations of moisture and chloride sensors based on fly ash geopolymers, and the fabrication of additive-free, ambient-cured, non-structural geopolymer repairs. In achieving these aims, the work demonstrates that affordable, combined monitoring and maintenance technologies for concrete can be delivered. Reducing the number of steps in deploying repairs and sensors will allow more of our ageing concrete infrastructure to be updated and repaired, so that it can meet modern expectations of safety, and remain resilient in the face of climate change.

## ACKNOWLEDGEMENTS

I would like to express my sincere gratitude to all the people who helped, guided and accompanied me in the PhD journey, and in this work of thesis. First of all, special thanks go to my academic supervisors, Dr Marcus Perry and Dr Andrea Hamilton, and to the supervisors from NNL and Sellafield.ltd, Dr Gary Bolton, Dr Christopher Gallagher, and Dr Robert Bernard. I am very grateful to all of them for giving me the opportunity to undertake this PhD experience and for entrusting me with this interesting and challenging research project. I also thank them for the availability and support they gave me during these three years.

A special thank goes in particular to my first academic supervisor, Dr Marcus Perry. I will bring with me all the precious lessons I have learnt from him, in both the professional and the human field. I am very grateful to Marcus for his continuous support to my research, with lot of patience, motivation, enthusiasm, and knowledge. His guidance helped me throughout the research and the writing-up of this thesis and has been one of the most precious gifts of this experience. It has been a process of trial and error, during which I had the opportunity to learn a lot and where he always encouraged me to find solutions and alternatives by trusting in my own capabilities. He was always present to give the proper advice, which sometimes was just to take a break and enjoy the rare Scottish sunny days.

Another special thank goes to my second supervisor, Dr Andrea Hamilton, for all the support, the patience and the time she dedicated to me: the multidisciplinary of my research project was an opportunity to learn and grow for me, but also a big challenge, that I was able to face also with the help of her knowledge and guidance in materials analysis.

A particular thank also to Dr Jack McAlorum for his help and support during my last year of PhD, for his feedbacks on my work and for his help with electronic and programming matters.

I would like to particularly thank my colleague, Christos Vlachakis, for his support and friendship during this journey, for the useful brainstorming meetings in the lab after full working days and the precious advices and help we provided each to the other.

I am grateful to all the staff of the Civil and Environmental Engineering laboratories of the University of Strathclyde: to Dr Mara Knapp, for her help and availability in any kind of

lab/health and safety matter; to Dr Tatyana Peshkur, for her technical support during analysis of ion leaching; to the technicians, Derek McNee, James Francis and Gavin Gibson, for their precious help in technical lab issues.

Thanks to Professor Alessandro Tarantino for experimental design support, and to Dr John Douglas for assistance in defining non-linear surface fits.

I gratefully acknowledge the funding sources that made my PhD work possible. I was funded by the National Nuclear Laboratory (NNL), the Engineering and Physical Sciences Research Council (EPSRC), the Royal Society and the Scottish Funding Council's Oil & Gas Innovation Centre.

Finally, thanks to all the friends I met in Scotland, who greatly enriched my PhD experience.

A huge thank goes to my family, my mum Cettina, and my sisters, Giulia, Alice and Chiara, for their continuous support, encouragement and love, and for trusting always me and supporting my decisions and my projects, even if they brought me abroad and far from them.

Lastly but not the least, a great thank goes to God, for the multiple Gifts he gives me every day, and in particular for the Gifts He gave me during this experience.

I preciously would like to thank Carmelo, my fiancée, the biggest precious gift of my Scottish experience and of my life, for his Love, Patience and Faith, fundamental rocks of my life. Thanks for all the tireless support and help he gave me during my PhD journey, and to have helped me facing all the difficult moments of it. Thanks to him for encouraging always me to trust my capabilities and my work, and for the precious help he gave me from his experience, for his technical and moral support.

Thanks to my father, for being always with me, watching over my life and my journey.

*Lorena Biondi*

*July 2020*

## INITIALISMS AND ACRONYMS

AAM	Alkali-Activated Materials
AASHTO	American Association of State Highway Transportation Officials
AC	Alternating Current
ACM	Alternative Cementitious Materials
AGC	Associated General Contractors (of America)
ARTBA	American Road & Transportation Builders Association
ASR	Alkali-Silica Reaction
ASTM	American Society for Testing and Materials
BNG	British Nuclear Group
BS	British Standard
CFD	Computational Fluid Dynamic
CFs	Carbon Fibers
CNFs	Carbon Nanofibers
CNTs	Carbon Nanotubes
CPE	Constant Phase Elements
DC	Direct Current
DSLR	Digital Single-Lens Reflex
EIS	Electrochemical Impedance Spectroscopy
EN	European regulatory standard

ER	Electrical Resistivity
ERT	Electrical Resistivity Tomography
ESR	External Sulphate Reactions
FBG	Fiber Bragg Grating
FE	Finite Element
FTIR	Fourier-Transform Infrared
GBFS	Granulate Blast Furnace Slag
GDF	Geological Disposal Facility
GDP	Gross Domestic Product
HEPA	High-Efficiency Particulate Air
HLW	High Level Waste
IAEA	International Atomic Energy Agency
IC	Ion Chromatography
ICPOES	Inductively Coupled Plasma Optical Emission Spectrometry
ILW	Intermediate Level Waste
ISE	Ion Selective Electrodes
ISR	Internal Sulphate Reactions
LLW	Low Level Waste
LOCA	Loss Of Cooling Accident
LOI	Loss On Ignition
LPG	long-Period fiber Grating

LVDT	Linear Variable Displacement Transducer
MAGNOX	MAGnesium Non-OXidising
MEMS	Micro-Electro-Mechanical Systems
MK	Metakaolin
NDA	Nuclear Decommissioning Authority
NDT	Non-Destructive Techniques
NEMS	Nano-Electro-Mechanical Systems
NMR	Nuclear Magnetic Resonance
NNL	National Nuclear Laboratories
OFS	Optical fiber sensors
ONR	Office for Nuclear Regulations
OPC	Ordinary Portland Cement
PP	Polypropylene
RD	Relative (bulk) Density
RH	Relative Humidity
RMS	Root Mean Square
SEM	Scanning Electron Microscopes
SH	Sodium Hydroxide
SHM	Structural Health Monitoring
SPRS	Sellafield Product and Residue Store
SS	Sodium Silicate

THORP	Thermal Oxide Reprocessing Plant
UK	United Kingdom
US	United States
XRD	X-Ray Diffraction

# CONTENTS

<b>1. Introduction</b>	<b>1</b>
<b>1.1. Context of research</b>	<b>1</b>
<b>1.2. Contributions to knowledge</b>	<b>3</b>
<b>1.3. Thesis structure</b>	<b>4</b>
<b>1.4. Publications arising from this thesis</b>	<b>5</b>
1.4.1. Journal papers	5
1.4.2. Conference papers	6
<b>1.5. Funding</b>	<b>6</b>
<b>References</b>	<b>7</b>
<b>2. Research Context and Motivation</b>	<b>8</b>
<b>2.1. Introduction</b>	<b>8</b>
<b>2.2. Concrete degradation: role of water and chloride</b>	<b>9</b>
2.2.1. Introduction to concrete degradation	9
2.2.1.1. Other concrete degradation causes	10
2.2.2. Corrosion of steel rebars	12
2.2.2.1. Carbonation	13
2.2.2.2. Chloride contamination of concrete	15
<b>2.3. Structural health of nuclear store buildings</b>	<b>16</b>
2.3.1. Store buildings longevity	16
2.3.2. Store buildings environmental control	19

2.3.3.	Nuclear radioactive products: waste and assets	21
2.3.3.1.	Radioactive waste	22
2.3.3.2.	Plutonium inventory: asset	23
2.3.4.	Sellafield Product and Residue Store (SPRS)	23
2.3.4.1.	SPRS packages	24
2.3.4.2.	SPRS internal configuration and working principle	24
2.3.4.3.	SPRS passive cooling system: risk for structural health	27
<b>2.4.</b>	<b>Maintenance and monitoring in nuclear stores: a novel solution</b>	<b>27</b>
2.4.1.	Chloride and moisture control in UK nuclear stores	28
2.4.2.	Novel solution: combined multifunctional technology	29
<b>2.5.</b>	<b>Summary</b>	<b>31</b>
	<b>References</b>	<b>33</b>
<b>3.</b>	<b><i>Geopolymer materials and applications</i></b>	<b>36</b>
<b>3.1.</b>	<b>Introduction</b>	<b>36</b>
<b>3.2.</b>	<b>Geopolymer materials</b>	<b>37</b>
3.2.1.	Geopolymerisation	37
3.2.1.1.	First stage: Destruction-Coagulation	39
3.2.1.2.	Second stage: Coagulation-Condensation	40
3.2.1.3.	Third stage: Condensation-Crystallization	40
3.2.2.	Alkaline solution	41
3.2.3.	Fly ash geopolymers	42
3.2.3.1.	Fly Ash: chemical composition and classification	43

3.2.3.2.	Fly ash geopolymers structural analysis	45
<b>3.3.</b>	<b>Geopolymer applications: state of the art</b>	<b>47</b>
3.3.1.	Geopolymers for concrete maintenance, repair and protection	48
<b>3.4.</b>	<b>Summary</b>	<b>50</b>
	<b>References</b>	<b>52</b>
<b>4.</b>	<b><i>Ambient Cured Fly Ash Geopolymers as coatings and repairs for concrete</i></b>	<b>57</b>
<b>4.1.</b>	<b>Introduction</b>	<b>57</b>
<b>4.2.</b>	<b>Theory and state of the art</b>	<b>59</b>
4.2.1.	Factors affecting geopolymer coatings on concrete substrates	59
4.2.1.1.	Shrinkage and curing	60
4.2.1.2.	Adhesion, workability and setting time	61
4.2.1.3.	The concrete substrate	62
4.2.1.4.	Efflorescence	63
4.2.2.	Repair materials, requirements and classification	63
<b>4.3.</b>	<b>Materials and methods</b>	<b>67</b>
4.3.1.	Materials	67
4.3.2.	Geopolymer synthesis	70
4.3.3.	Application to substrate	71
4.3.4.	Concrete substrate roughness	71
4.3.5.	Curing conditions for geopolymers	73
4.3.6.	Analysis methods	74
4.3.6.1.	Vicat needle test	74

4.3.6.2.	Isothermal calorimetry	74
4.3.6.3.	X-Ray diffraction analysis	74
4.3.6.4.	Compressive strength	75
4.3.6.5.	Visual inspection and quantification of cracks	75
4.3.6.6.	Bond strength test	78
4.3.6.7.	Thermal expansion measurement	80
<b>4.4.</b>	<b>Results and discussion</b>	<b>81</b>
4.4.1.	Coating Integrity	82
4.4.1.1.	Coating thickness	82
4.4.1.2.	Setting and mixing time	84
4.4.1.3.	Concrete age	88
4.4.1.4.	Efflorescence	88
4.4.2.	Preliminary repair performance evaluation	91
4.4.2.1.	Compressive strength	91
4.4.2.2.	Bond strength	94
4.4.2.3.	Thermal expansion	95
<b>4.5.</b>	<b>Further discussion</b>	<b>96</b>
<b>4.6.</b>	<b>Summary and future work</b>	<b>97</b>
	<b>References</b>	<b>100</b>
<b>5.</b>	<b><i>Geopolymer-based moisture sensors</i></b>	<b>106</b>
5.1.	<b>Introduction</b>	<b>106</b>
5.2.	<b>State of the art</b>	<b>109</b>

5.2.1.	Previous geopolymer-based sensor applications	109
5.2.2.	Moisture monitoring methods for structural health: a review	111
5.2.2.1.	Capacitive sensors	112
5.2.2.2.	NEMS/MEMS (nano-/micro- electro-mechanical systems) sensors	113
5.2.2.3.	Fiber-optic sensors	114
5.2.2.4.	Concrete electrical resistance/conductivity/impedance measurements	116
<b>5.3.</b>	<b>Theory: impedance-based geopolymer sensors</b>	<b>118</b>
5.3.1.	Geopolymer's conductivity	118
5.3.2.	Electrochemical impedance spectroscopy (EIS)	118
5.3.2.1.	The electrical impedance of geopolymers	121
5.3.3.	Temperature and moisture sensing principle of geopolymer system	124
<b>5.4.</b>	<b>Materials and Methods</b>	<b>127</b>
5.4.1.	Sensor fabrication	127
5.4.2.	Interrogation system	128
5.4.3.	Calibration methods	128
5.4.4.	Post-mortem examination of ion leaching	131
<b>5.5.</b>	<b>Results and discussion</b>	<b>132</b>
5.5.1.	Geopolymer cell impedance response	132
5.5.2.	Temperature dependence of impedance	133
5.5.3.	Moisture dependence of impedance	135
5.5.4.	Sensor response	138
5.5.5.	Sensor precision	141
5.5.6.	Sensor repeatability	141

5.5.7.	Critical comparison with other sensors	143
5.5.8.	Ion leaching	143
5.5.9.	Sensor drift	144
<b>5.6.</b>	<b>Summary and future work</b>	<b>144</b>
	<b>References</b>	<b>147</b>
<b>6.</b>	<b><i>Geopolymer-based chloride sensors</i></b>	<b>152</b>
<b>6.1.</b>	<b>Introduction</b>	<b>152</b>
<b>6.2.</b>	<b>Theory and state of the art</b>	<b>154</b>
6.2.1.	State of the art: chloride monitoring methods for SHM	154
6.2.1.1.	Ion selective electrodes (ISE) device	155
6.2.1.2.	Fiber optic sensors	157
6.2.1.3.	Electrical Resistivity (ER)	158
6.2.2.	Development of a new geopolymer chloride sensor for nuclear stores	160
6.2.3.	Theory: geopolymer chloride sensor	163
6.2.3.1.	Sensing principle	164
<b>6.3.</b>	<b>Materials and methods</b>	<b>166</b>
6.3.1.	Sensor fabrication	166
6.3.2.	Interrogation system	167
6.3.3.	Sodium Chloride solutions	167
6.3.4.	Calibration method	168
<b>6.4.</b>	<b>Results and discussion</b>	<b>172</b>
6.4.1.	Impedance response of the sensor cell plus NaCl solution	173

6.4.2.	Chloride and frequency dependence of impedance	174
6.4.3.	Sensor response	180
6.4.4.	Sensor precision	185
<b>6.5.</b>	<b>Summary and future work</b>	<b>187</b>
	<b>References</b>	<b>189</b>
<b>7.</b>	<b><i>Preliminary investigation of geopolymer coating sensors</i></b>	<b>192</b>
<b>7.1.</b>	<b>Introduction</b>	<b>192</b>
<b>7.2.</b>	<b>Theory: sensing principle of the geopolymer coating system</b>	<b>193</b>
<b>7.3.</b>	<b>Materials and methods</b>	<b>196</b>
7.3.1.	Sensor fabrication	196
7.3.1.	Interrogation system	198
7.3.2.	Calibration methods	198
7.3.2.1.	Moisture and temperature calibration	198
7.3.2.2.	NaCl calibration	199
<b>7.4.</b>	<b>Results and discussion</b>	<b>200</b>
7.4.1.	Coating-concrete cell impedance response	200
7.4.2.	Moisture, temperature, NaCl and frequency dependence	203
7.4.3.	Moisture and temperature preliminary characterisation	206
7.4.3.1.	Sensor response	206
7.4.3.2.	Precision	208
7.4.4.	NaCl preliminary characterization	209
7.4.4.1.	Sensor response	209

7.4.4.2. Precision	210
<b>7.5. Summary and future work</b>	<b>210</b>
<b>References</b>	<b>213</b>
<b>8. Conclusions and Future work</b>	<b>214</b>
<b>8.1. Industrial and scientific relevance</b>	<b>215</b>
8.1.1. Industry relevance of the work	215
8.1.2. Main scientific findings	217
8.1.2.1. Geopolymer coating integrity	218
8.1.2.2. Geopolymer coatings as non-structural repairs for concrete	219
8.1.2.3. Geopolymers as stand-alone moisture and temperature sensors	220
8.1.2.4. Geopolymers as stand-alone NaCl concentration sensors	221
8.1.2.5. Self-sensing coatings for moisture, NaCl	222
<b>8.2. Future work</b>	<b>223</b>
<b>8.3. Closing remarks on future direction of the technology</b>	<b>226</b>
8.3.1. Deployment methods	226
8.3.2. Interrogation and data transfer systems	227
<b>References</b>	<b>228</b>
<b>APPENDICES</b>	<b>229</b>
<b>Appendix 1 – Mathematical formulation of sensor precision</b>	<b>230</b>
<b>Appendix 2 – Mathematical formulation of Pooled Repeatability</b>	<b>235</b>
<b>Appendix 3 – Chloride geopolymer sensor characterization: Data Tables</b>	<b>236</b>
<b>Appendix 4 - Circuit model parameters and fits for geopolymer cells with NaCl</b>	<b>238</b>

<b>Appendix 5 -Moisture calibration fit parameters for geopolymer cells with NaCl</b>	<b>242</b>
<b>Appendix 6 - Tables of circuit model parameters for coating cells</b>	<b>243</b>
<b>Appendices references</b>	<b>244</b>

# 1. INTRODUCTION

## 1.1. Context of research

Reinforced concrete is globally the most used material in construction today, prized for its high strength and relative affordability [1]. Most concrete structures are durable enough to withstand 50-100 years of service life, but they are often life-extended, or exposed to external factors that accelerate degradation. Concrete infrastructure maintenance in the United Kingdom is a multi-billion pound problem, that brings with it additional unquantified social costs [2]. For this reason, ongoing inspection, monitoring and maintenance are major requirements for ensuring structural health, and managing risk [3].

Degradation in reinforced concrete is mostly due to corrosion of the reinforcing steel bars, which in coastal environments is triggered by the combined action of chloride ions and water content [4-7]. For this reason, an increased interest in water and chloride content monitoring technologies in concrete has been shown over the years, and the need for novel competing and multifunctional technologies is particularly urgent in the case of safety critical structures, such as nuclear structures.

Nuclear structures are coastal, often made from reinforced concrete, and in most cases play some role in the containment of radioactive material (e.g. nuclear containments and stores). These structures are intended to last for more than 100 years, despite the presence of radioactive packages (sources of heat and high ionising radiation levels), close proximity to the sea, and the absence of air filtering in some cases. Providing non-invasive monitoring

and maintenance technologies for concretes facing these environments is, unsurprisingly, not a solved problem.

Most of the existing water and chloride sensing methods for concrete in academic and commercial literature are somewhat invasive (requiring forethought and/or drilling of holes for probes), and they are not radiation resistant [8]. For this reason, the current monitoring systems in UK nuclear store buildings are Relative Humidity (RH) sensors and environmental chloride sensors: no sensing systems are applied directly to concrete for water and chloride content monitoring [9]. The need for an affordable, distributed, non-invasive technology for water and chloride sensing in nuclear concretes is the basis of the research work outlined in this thesis.

Geopolymers, often frequently referred to as alkali-activated materials, are a promising technology for solving this challenge. Geopolymers are often viewed as a low-carbon ordinary Portland cement replacement, with most research groups developing geopolymer concretes [10]. These materials can, however, form concrete repairs, may have a high radiation resistance, and also exhibit an underutilised high electrolytic conductivity that can be used for sensing [11-13]. The hypothesis underpinning this PhD project was that interrogation of changes in the electrical impedance of geopolymer repair skins, or stand-alone cured moulds, could be linked to changes in moisture or chloride content. One challenge is that geopolymers are often cured at elevated temperatures (at or above 40 °C) and at intermediate relative humidity, quite different to the cool and humid ambient environments found in most parts of UK nuclear facilities. Bringing heat sources or more complex additives into nuclear facilities represents a risk that would hinder the technology's deployment.

The main goal of this project is therefore to produce a first time demonstration and characterization of a moisture and chloride sensor based on ambient-cured geopolymer materials. In particular, the technology has been developed according to the requirements, environmental conditions and limitations of the Sellafield Product and Residue Store (SPRS), which is one of the largest civil nuclear storage facilities in the world. It is intended to safely and securely store all of the UK's civil stock of separated plutonium until 2120 [14].

The envisaged application of this work, beyond the scope of this thesis, will be the development of geopolymer repairs that form distributed skin sensors for mapping moisture and chloride levels over large concrete surfaces. The work outlined in this thesis

constitutes the first important step: development and characterization of the technology for point location sensing. The contributions to knowledge which this thesis provides are outlined in the following section.

## 1.2. Contributions to knowledge

This thesis provides a number of important knowledge contributions in the following three fields of research:

1. structural health monitoring in a nuclear context;
2. ambient-curable geopolymer coatings for concrete;
3. moisture and chloride geopolymer sensors.

The unique industry-challenge- and scientific-knowledge- contributions of this thesis are:

- A detailed literature review of the research context (reinforced concrete degradation causes, existing monitoring systems in nuclear stores, nuclear store requirements, and current technology limitations) reveals the unmet need for structural health monitoring technologies in a nuclear context. It highlights the need for non-invasive, affordable, radiation resistant, and easy-to-use methods for monitoring moisture and chloride content.
- A review of existing moisture and chloride sensing technologies and methods highlights the limitations of each technology for nuclear applications.
- A review of geopolymer materials as sensors for concrete outlines environmental parameters already investigated for geopolymer sensing (temperature and strain), highlighting the lack of investigation of chemical sensing (such as moisture and chloride). This review also highlights the added advantage of simultaneously using geopolymer sensors as repairs and protective materials for concrete.
- An experimental investigation to develop ambient-curable geopolymer coatings for concrete, explicitly showing that coating integrity and mechanical properties make them suitable for use as non-structural repairs for concrete (as defined in

harmonised British-European standards). The coatings are produced by altering only the composition of the material, the coating thickness, and the mixing time. This is a novel result, since it demonstrates that heating and additives are not required to deploy this material in cool and humid environments.

- A first-time demonstration of geopolymer-based moisture and chloride sensors. Sensor performance was analysed in detail for the moisture, chloride and temperature ranges of interest for a nuclear context. This contribution constitutes both an important scientific result and an optimistic result for the industrial application.
- An experimental investigation demonstrates, for the first time, the feasibility of moisture and chloride geopolymer skin sensors for concrete. This constitutes an important contribution for the future development of a distributed skin sensors.
- Finally, the application of Electrochemical Impedance Spectroscopy (EIS) to geopolymer binders and coatings provides an important and novel contribution to the knowledge of the electrical conduction mechanism of geopolymers, outlining a proper circuit model to describe the system, validated by experimental evidence.

### 1.3. Thesis structure

The remainder of this thesis is structured as follows.

Chapter 2 introduces the research background and highlights the motivations behind the work described in this thesis. Concrete degradation causes and mechanisms are described, together with nuclear store building requirements. The need for a novel multifunctional monitoring technologies in a nuclear context is demonstrated.

Chapter 3 provides an introduction and description of geopolymer materials and applications, highlighting why they are a suitable choice for this application, and describing the properties they have which are of interest for this work.

Chapter 4 focuses on the experimental investigation of ambient cured geopolymer coatings, describing the issues encountered and demonstrating that high-integrity repairs can be achieved with an affordable, minimal-steps procedure.

Chapters 5 and 6 present, respectively, detailed experimental investigations of stand-alone (i.e. non-coating) geopolymer moisture sensors and chloride sensors. These chapters also provide a literature review of existing geopolymer sensors (originally limited to strain and temperature sensing), and the state of the art of competing moisture and chloride sensing methods. These two chapters demonstrate the feasibility of using ambient cured geopolymers as moisture and chloride sensors.

Chapter 7 outlines a preliminary experimental investigation of geopolymer coatings as moisture and chloride sensors, and provides an assessment of sensor performance.

Chapter 8 provides an overall summary, conclusions, suggestions for future work, and an overview on future applications of the technology.

A series of appendices offer additional details regarding additional data, and the implementation and description of approaches and algorithms described in the thesis.

## 1.4. Publications arising from this thesis

### 1.4.1. Journal papers

L. Biondi, M. Perry, C. Vlachakis, Z. Wu, A. Hamilton, and J. McAlorum, "Ambient Cured Fly Ash Geopolymer Coatings for Concrete," *Materials*, vol. 12, p. 923, 2019.

<https://doi.org/10.3390/ma12060923>.

L. Biondi, M. Perry, J. McAlorum, C. Vlachakis, and A. Hamilton, "Geopolymer-based moisture sensors for reinforced concrete health monitoring," *Sensors and Actuators B: Chemical*, vol. 309, p. 127775, 2020.

<https://doi.org/10.1016/j.snb.2020.127775>

C. Vlachakis, M. Perry, L. Biondi, and J. McAlorum, "3D printed temperature-sensing repairs for concrete structures," *Additive Manufacturing*, p. 101238, 2020.

<https://doi.org/10.1016/j.addma.2020.101238>

L. Biondi, M. Perry, J. McAlorum, C. Vlachakis, and A. Hamilton, "Geopolymer-based NaCl sensors for reinforced concrete health monitoring", **writing in progress**.

### 1.4.2. Conference papers

L. Biondi, M. Perry, C. Vlachakis, and A. Hamilton, "Smart cements: repairs and sensors for concrete assets," in Sensors and Smart Structures Technologies for Civil, Mechanical, and Aerospace Systems 2018, 2018, p. 105982U.

C. Vlachakis, L. Biondi, and M. Perry, "3D printed smart repairs for civil infrastructure," in 9th European Workshop on Structural Health Monitoring Series (EWSHM), 2018, pp. 1-12.

J. McAlorum, M. Perry, C. Vlachakis, and L. Biondi, "Autonomous Application of Smart Cement Sensor-repairs," Structural Health Monitoring 2019, 2019.

C. Vlachakis, L. Biondi, J. McAlorum, and M. Perry, "Self-Sensing 3D Printed Repair for Concrete Substrates," Structural Health Monitoring 2019, 2019.

## 1.5. Funding

This work was funded in part by the National Nuclear Laboratory ICASE award (NNL/UA/022), EPSRC (EP/L014041/1), the Royal Society (RG160748) and the Scottish Funding Council's Oil & Gas Innovation Centre.

## References

- [1] Z. Guo, *Principles of reinforced concrete*: Butterworth-Heinemann, 2014.
- [2] A. Beeby and E. Etman, "Repair of reinforced concrete beams with corroded reinforcement using CFRP plates," in *INTERNATIONAL CONFERENCE ON STRUCTURAL FAULTS AND REPAIR*, 1999.
- [3] N. Buenfeld, R. Davies, A. Karimi, and A. Gilbertson, "Intelligent monitoring of concrete structures," 2008.
- [4] L. Bertolini, B. Elsener, P. Pedeferra, E. Redaelli, and R. Polder, *Corrosion of steel in concrete* vol. 392: Wiley Online Library, 2013.
- [5] J. P. Broomfield, "Corrosion of steel in concrete: Understanding," *Investigation and Repair, E&FN, London*, pp. 1-15, 1997.
- [6] H. Böhni, *Corrosion in reinforced concrete structures*: Elsevier, 2005.
- [7] A. de Kagenack and C. Pinel, "The Joint Convention on the Safety of Spent Fuel Management and on the Safety of Radioactive Waste Management," *International & Comparative Law Quarterly*, vol. 47, pp. 409-425, 1998.
- [8] M. Torres-Luque, E. Bastidas-Arteaga, F. Schoefs, M. Sánchez-Silva, and J. F. Osmá, "Non-destructive methods for measuring chloride ingress into concrete: State-of-the-art and future challenges," *Construction and building materials*, vol. 68, pp. 68-81, 2014.
- [9] I. O. f. Standardization, *Corrosion of Metals and Alloys: Corrosivity of Atmospheres: Measurement of Environmental Parameters Affecting Corrosivity Atmospheres*: ISO, 2012.
- [10] T. Sathanandam, P. O. Awoyera, V. Vijayan, and K. Sathishkumar, "Low carbon building: Experimental insight on the use of fly ash and glass fibre for making geopolymer concrete," *Sustainable Environment Research*, vol. 27, pp. 146-153, 2017.
- [11] S. Hanjitsuwan, P. Chindapasirt, and K. Pimraksa, "Electrical conductivity and dielectric property of fly ash geopolymer pastes," *International Journal of Minerals, Metallurgy, and Materials*, vol. 18, pp. 94-99, 2011.
- [12] X.-M. Cui, G.-J. Zheng, Y.-C. Han, F. Su, and J. Zhou, "A study on electrical conductivity of chemosynthetic Al<sub>2</sub>O<sub>3</sub>-2SiO<sub>2</sub> geopolymer materials," *Journal of Power Sources*, vol. 184, pp. 652-656, 2008.
- [13] M. Saafi, A. Gullane, B. Huang, H. Sadeghi, J. Ye, and F. Sadeghi, "Inherently multifunctional geopolymeric cementitious composite as electrical energy storage and self-sensing structural material," *Composite Structures*, vol. 201, pp. 766-778, 2018.
- [14] C. P. Gallagher, P. M. Cook, R. Hanratty, and M. Moorcroft, "Maintaining Safe Storage of UK Plutonium," presented at the The Nuclear Institute Congress, Manchester (UK), 2013.

## 2. RESEARCH CONTEXT AND MOTIVATION

### 2.1. Introduction

The main task outlined in this thesis is to address the problem of monitoring and maintenance in reinforced concrete structures, and in particular in a nuclear context, where environmental conditions and containments systems may lead to critical configurations for corrosion of steel rebars and the consequent concrete degradation.

A key role for triggering corrosion of steel rebars in reinforced concrete is played by the combined action of water and chloride. This is particularly important in the case of structures in proximity to a seawater environment, and with limited or no air filtering systems, as in the case of some nuclear buildings. In this context, preventive actions are needed, such as monitoring of the ingress of both chloride and moisture and, at a later stage, maintenance.

This chapter gives a detailed overview on the context and motivation for this research work: it provides a technical description on the role played by water and chloride in reinforced concrete degradation (section 2.2), details the reasons for water and chloride monitoring and maintenance in nuclear store structures made by reinforced concrete (section 2.3), and highlights the key needs which the technology developed and characterised in this work aims to solve, its novelty and efficacy (section 2.4).

This chapter essentially highlights the research need: it explains why there is a lack of systems which can provide effective moisture and chloride monitoring role in a nuclear context, and outlines a need for multifunctional systems which can also protect and repair concrete while monitoring.

## 2.2. Concrete degradation: role of water and chloride

Water content and chloride in reinforced concrete are two highly interconnected factors, and their combined action on reinforced concrete leads to structural integrity issues which have a high cost and impact [1-4]. This introductory section describes the concrete degradation issue from a technical point of view, giving an overview of its causes, and the process of corrosion of the steel reinforcement, which constitutes the primary cause of concrete degradation in reinforced concrete structures.

### 2.2.1. Introduction to concrete degradation

Concrete is a composite material consisting in a dense coherent mass, obtained by binding fine and coarse aggregates (sand and gravel, or crushed rock such as limestone or granite) with Portland cement [5, 6]. Concrete has some advantages, such as: easy manufacturing, utilizing local materials, low investment, and it is a mouldable substance (can be made into any structure of complicated shape and different sizes) [7].

Concrete also has weaknesses: it has a low tensile strength, and a low cracking resistance. For this reason, the combination of concrete with a proper quality and quantity of steel reinforcement, together with other technical measures (selection of raw materials, mix and cure technique, construction management, pre-stressing, and improvement of calculation method), will give to the final structure the improved strength and ductility to satisfy safety and service conditions [7]. The mutual compensation of the behaviour of both materials, concrete and reinforcing steel, leads to a structural material with high strength, good integrity, corrosion and fire resistances and flexible use [7].

For some time it was actually believed that reinforced concrete structures could last “forever”, but they do deteriorate over time [6]. The complex chemistry of cement, the use of steel reinforcement and the exposition of concrete to a variety of environments result in

several different processes of deterioration [8]. A number of durability-related problems for concrete have emerged and stimulated research investigation: alkali-silica reactions, sulphate attack and reinforcement corrosion.

Among degradation causes, the primary cause of deterioration in reinforced concrete structures is considered to be the corrosion of steel reinforcement, primarily due to two independent reasons: (i) the carbonation of the cover concrete and (ii) the presence of chloride ions at the steel surface [6]. In particular, water content (or moisture) of concrete has a key role in degradation mechanisms of reinforced concrete structures, and chloride concentration in concrete is of critical importance for corrosion of the steel reinforcement in reinforced concrete. Section 2.2.2 presents a detailed description of the role of water content and chloride for the corrosion mechanisms since they are the most important cause of concrete degradation for reinforced concrete structures, both in general, and for the specific application of this work, which will be described in detail in section 2.3.

Indeed, the corrosion induced by chloride is a problem which has reached alarming proportions since the 1970s, leading to very high repair costs, which sometimes overcome the initial construction cost, and in extreme situations it has led to the collapse of structures [9]. However, water content (or moisture) has a key role in all the chemical mechanisms which lead to concrete deterioration mentioned above, not just the corrosion mechanisms of reinforced concrete. For this reason, the next section will give an overview on the role of moisture in the minor causes of concrete degradation.

#### 2.2.1.1. Other concrete degradation causes

The other (less frequent or minor in this context) concrete degradation causes where water plays a key role are: Alkali-Silica Reaction (ASR) and Sulphate attack. These mechanisms may affect concrete independently from the presence of steel reinforcement, and they are less important than corrosion. For completeness, this paragraph gives an overview on them by looking at the role of moisture.

The alkali-silica reaction (ASR) is a time-dependent phenomenon (it typically takes between 5 and 12 years to develop) which occurs during the service life of a structure, giving visible external warnings of internal damage, and it may affect strength, stiffness, serviceability, safety, and stability. ASR is a particular variety of chemical reactions within concrete, involving alkali hydroxides (usually derived from the alkalis present in the cement

used) and reactive forms of silica (present within aggregate particles), and **requires water** for it to produce the alkali-silica gel reaction product which swells with the **absorption of moisture** [10].

The phenomenon of ASR is complex and, although there are many interacting and interdependent parameters that influence its occurrence, it has been recognized the simultaneously conjunction of three conditions necessary for the initiation of the alkali-silica reaction, such as: a) presence of **high levels of water** (relative humidity greater than 80-85%); b) amount of alkali in concrete; and c) reactive silica (reactive aggregates) [11]. Although all the three conditions must be verified to start the reaction, it must be noted that the susceptible silica and the alkali concentration may depend on the **capillary water availability**, which is required to transport the reactive ions and to let the gel swell. Moreover, variations of local concentrations of reactive silica and concrete alkalinity arise from material **porosity** and **permeability**, and are determined by conditions such as concrete placement, variable compaction, **moisture/thermal movements** and, above all, by **microclimatic conditions of heat and moisture** [10]. Therefore, among these conditions, moisture plays the fundamental role, on which also the other conditions depend.

The other minor cause of concrete degradation is sulphate attack. Sulphate attacks can be external or internal depending on the source of the sulphate ions [12], and it is possible to distinguish between internal sulphate reactions (ISR) and external sulphate reactions (ESR) [11]: ISR can occur only in **damp environments**, in massive cast-in-place concrete parts in summer or on heat-treated concrete parts, and it produces calcium trisulfoaluminate **hydrated** mineral species containing sulphates, known as ettringite, and resulting from the reaction between calcium aluminates and gypsum; ESR is a chemical breakdown mechanism where components of the cement paste of concrete are attacked by sulphate ions coming from an external source, such as soils, **groundwater**, **seepage water**, or sulphuric acid **rain** due to atmospheric industrial pollution. A loss of concrete strength, severe micro-cracking and overall expansion of a structural element, with surface spalling, delamination and exfoliation, are caused by the expansion of the products of reaction, such as the secondary ettringite<sup>1</sup>.

---

<sup>1</sup> The ettringite formed during sulphate attack on hardened concrete is called secondary ettringite to be distinguished from the primary ettringite that forms during hydration of cement.

Sulphate attack does not lead to the abrupt structural collapse of structures in most cases. The detrimental action of sulphates on field concrete is affected by factors such as: strength of the sulphate solution, **permeability**, composition and quality of concrete, ambient temperature and **humidity** [12]. Therefore, **the role of water** in the case of sulphate attack is important, not only because water is the mean through which sulphates can enter concrete, but also for the following reasons [12]: sulphate ions migrate through the **capillary pores** of concrete for diffusion, driven by the concentration gradient and thus they trigger complex chemical reactions with active components of the hardened cement paste, and **the reactions proceed in the aqueous medium filling the pores**.

### 2.2.2. Corrosion of steel rebars

In the normal highly alkaline environment of reinforced concrete,  $\text{pH} > 11.5$  (usually in the range 12.5–13.5), and the surface of steel rebars is covered with a thin passive oxide film, which protects the steel from corrosion. Under certain conditions, the passive film becomes unstable leading to corrosion [1]. The ‘de-passivation’ mechanism happens for two main reasons: carbonation and chloride contamination.

Corrosion of the reinforcement can be a widespread general corrosion (common in carbonation), or a very local attack (common in chloride pitting corrosion). General corrosion results in cracking and spalling of concrete, since the products of corrosion swell creating internal stress, and some reduction of the cross-section of the bars is also commonly seen, while for the localised pitted corrosion, even deep pits randomly distributed in the bars may appear before any external evidence of concrete deterioration is seen [3], thus making it more dangerous. Corrosion takes place if all the following four processes are possible:

a) anodic reaction ( $2\text{Fe} \rightarrow 2\text{Fe}^{2+} + 4e^{-}$ );

b) cathodic reaction ( $\text{O}_2 + 2\text{H}_2\text{O} + 4e^{-} \rightarrow 4\text{OH}^{-}$ );

c) flux of ions between the site of the anodic reaction and the site of the cathodic reaction;

d) flux of electrons.

Each process is triggered by specific conditions: the anodic reaction, which is the dissolution of the metal, takes place only when the passive layer breaks down for carbonation or for a

critical level of chloride in concrete; the cathodic reaction takes place only if a reasonable amount of oxygen is available at the interface reinforcement-concrete; the flux of ions between the two reaction sites is possible only if the medium between the two sites is a well conducting electrolyte; the flux of electrons is possible only if there is a metallic connection between the sites of the two reactions [3].

In normal alkaline conditions of good quality concrete, in the absence of chloride, the anodic and cathodic reactions happen and they are balanced each by the other, and the products of both reactions combine together and in a last stage they are responsible of the production of the stable film that passivates the reinforcing steel. The stability of this film depends essentially on the oxygen availability that controls reaction b) above and on the pH of the interstitial solution in the interface steel/concrete [9].

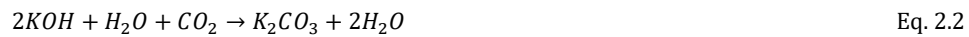
Once the corrosion is initiated, its propagation rate depends on four factors: (i) **moisture content** and concrete resistivity; (ii) temperature; (iii) oxygen availability; and (iv) pH of concrete pore water [3]. It must be noted that oxygen availability and concrete resistivity depends on concrete **permeability** and **moisture** content: at high moisture content, the diffusion coefficient of oxygen is very low. The transport of gases ( $O_2$ ,  $CO_2$ ), water and ions ( $Cl^-$ ) in concrete depends on: **water suction and penetration**; diffusion and permeability coefficient; and ion mobility. In particular, water suction and diffusion play a key role for corrosion triggering due to carbonation and chloride ions uptake [3]. For concrete structures exposed to the atmospheric zone in marine environments, both carbonation and chloride ingress may occur either simultaneously or in succession [13]. The two following sections describe in detail the two processes.

#### 2.2.2.1. Carbonation

Carbonation is a chemical phenomenon due to chemical reactions between the carbon dioxide,  $CO_2$ , which comes from the atmosphere and dissolves in the pore solution of concrete, and the alkaline components of cement paste, such as NaOH, KOH,  $Ca(OH)_2$  and calcium-silicate hydrates (bases which give the water in the pores of concrete a high pH, around 13) [3]. These reactions cause a reduction of the pH in the concrete pore solution by neutralizing alkaline components.

In detail, carbonation in concrete can be divided into three main stages [11]: a)  $CO_2$  diffuses in concrete; b)  $CO_2$  dissolves in pore water; c) chemical reactions between dissolved carbon

dioxide and alkaline components, which result in carbonate production, thus lowering the pH of the interstitial solution from about 13 to about 6-9. The full carbonation reactions are described by the following equations [3]:



Among the carbonation products, only  $CaCO_3$  is deposited, since it has a much lower solubility compared with  $Na_2CO_3$  and  $K_2CO_3$ , which remains dissolved in the pore water. These products occupy a greater volume than does the original non-corroded metal: this leads to a pressure build up around the steel rebars, which is the cause of cracks and finally of the spalling of the concrete above the steel rebars.

If there is enough  $CO_2$  and water, the carbonates react further, thus leading to a further reduction of the pH of concrete [3]. Therefore, **water plays a key role** in triggering the carbonation reactions, and also the speed of carbonation depends on the **moisture content** of the concrete: transport of  $CO_2$  in concrete is very slow in pores filled with water, but **the carbonation process can't take place without water**, because water is necessary for the dissolution of  $CO_2$ . For this reason, **the most dangerous range of moisture** for carbonation is between 50% and 80% [1], and there is a maximum rate of carbonation at a medium range of relative humidity [3]. Carbon dioxide is unavoidable as it is everywhere in the air and the content of carbon dioxide in the air is rising.

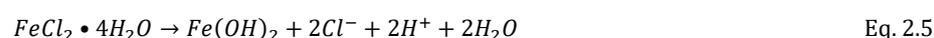
Furthermore, it is important to note that the carbonation process can also have an impact on **chloride** transport, ingress and distribution in concrete [13]: carbonation of chloride contaminated concretes results in a decrease of the chloride binding capacity, that causes the release of the bound Cl in concretes and pushes chlorides inwards; carbonated concretes exposed to chlorides results in an increased penetration of chlorides much deeper into the concrete due to possible presence of carbonation induced micro-cracking in the near-surface region.

### 2.2.2.2. Chloride contamination of concrete

In concrete, **chloride** may come from internal sources, for instance the mix ingredients, or from external sources, such as **sea water**, water with dissolved de-icing salts, or floors containing chloride. The fastest ingress of chloride into concrete is caused by **capillary suction of water** which contains chloride, and the chloride ingress is accelerated by wetting and drying cycles of concrete [3].

In many countries the most important degradation mechanism for reinforced concrete infrastructures is the penetration of chloride ions from seawater or de-icing salts into concrete and the associated risk for reinforcement corrosion. For this reason, many studies have been conducted on the corrosion mechanism induced by chloride, and in particular on the chloride concentration threshold value for triggering corrosion in steel rebars [1, 14, 15]. This threshold value corresponds to a sufficient concentration of chloride ions measured at the rebar depth that can cause the breaking down of the passive protective layer and the pitting corrosion to occur [16].

The chloride ions act as catalysts to corrosion: they are not consumed in the process but rather help to break down the passive film on the steel and allow the corrosion process to proceed quickly. The reactions which describe the process are:



After corrosion starts, acids are present, pits form and the rust generates over the pits, concentrating the acid. In this circumstance, the anodes and cathodes are often well separated with large cathodic areas supporting small, concentrated anodic areas. This is known as the macro cell phenomenon [16].

The chloride concentration threshold value is affected by numerous interrelated parameters [1]: properties of the steel/concrete interface, pore solution chemistry, electrochemical potential of the steel (related to the pH of the pore solution), and the amount of oxygen at the surface of the steel. Therefore, the chloride threshold value shows a complexity and a variety which make its determination in different circumstances a complicated problem [16]: concrete pH varies with the type of cement and the concrete

mixture; chlorides can be chemically and physically bound in concrete; in very dry concrete or surface-treated concrete, corrosion may not occur even at very high chloride ion concentrations because not enough moisture or oxygen is present in concrete to activate the corrosion reaction; and corrosion can be suppressed if there is total water saturation due to oxygen starvation. Therefore, corrosion can be initiated by relatively low levels of chlorides (threshold level of about 0.2% chloride by weight of cement), if **water** and oxygen are available, instead a higher concentration of chloride (up to 1.0% or more) is required if water and oxygen are excluded [2, 16].

## 2.3. Structural health of nuclear store buildings

As seen in the previous section, chloride and water content are two fundamental interconnected parameters which play a key role in reinforced concrete degradation, and their ingress into reinforced concrete structures requires limit and control. For this reason, structural health monitoring solutions for concrete should monitor water and chloride. This is particularly important in nuclear context, where concrete assets are usually coastal, and often play the crucial role of containment of radioactive packaged materials. This is the case of radioactive products and waste store structures.

The term *storage* in nuclear context describes the holding of radioactive materials or waste in facilities, called *stores*, that provide this containment, with the intention of retrieval [4]. The primary function of a store in nuclear context is to store packaged radioactive material in a manner that protects workers, the public and the environment from hazards associated with the interim storage of radioactive materials or waste packages until they are exported [17]. For this reason, the store buildings are subjected to specific requirements, such as ventilation systems, quality of concrete and environmental control. In such structures, structural integrity, together with avoiding, preventing and limiting concrete degradation, is one of the primary importance requirements to extent store longevity.

### 2.3.1. Store buildings longevity

The UK Nuclear Decommissioning Authority (NDA) Industry Guidance document on interim storage [17] (effective from January 2017) outlines the necessary steps which determine store longevity. The starting point is the target design life, which should typically be at least 100 years for both new and existing stores. For new stores, any requirement for

an earlier store replacement should be avoided, while for existing stores, where the design life does not meet the design target, store refurbishment or the transfer of packages into a modern store should be considered.

In order to meet the target design life, a store should be subjected to appropriate quality standards and control. Among them it is worth to mention: a) the use of *appropriate concrete grades*, where levels of chlorides and other components within the mix during construction and level of penetration post construction are key components to meeting the design life; b) provision of additional concrete cover over any rebar; c) use of *high performance concrete*; d) designing and constructing the structure according to the relevant codes with consideration given to reducing design crack width limits; e) the use of *stainless steel reinforcement*.

All these requirements reduce the risk associated with the features and components which can limit the life-time of a store. An important step to assess the longevity of existing stores and establish the design criteria for future stores is to identify these features and components. They can be classified depending on three aspect of the store and its equipment: *design, management* and *continued operation*. The features for each aspect of the store and the factors affecting each feature are presented in Table 2.1 [17]. Among them, particular attention should be given to the continued operation features, where **structural integrity** plays an important role: it can be a life limited feature, and the main factors affecting it (as already seen in detail in section 2.2) are considered to be **concrete degradation** and **corrosion of steel reinforcement**.

Aspect	Features	Factors affecting features
1 Design	Design life; Siting requirements; Regulatory and stakeholder views.	External factors, such as floods, earthquakes, tsunami, etc...  Storage capacity; Local demographics; Hydrogeological properties.  Planning and permitting issues; Environmental and safety considerations; Socio-economic factors and cost issues; Changes in regulatory requirements.
2 Management	Knowledge of management of issues and security.	Staff with appropriate skills, knowledge and experience; Organisational learning; Records management for waste packages, environment, store equipment and store maintenance.
3 Continued operation	Structural integrity of the facility;  Operation of plant and equipment	Subsidence and settlement; Concrete degradation, strength, hardness and carbonation; Corrosion of concrete reinforcing bars; Structural elements to bear loads; Elements to exclude water and control inadvertent surface water deposited on the floor; Integrity of external cladding. Passive or active ventilation and/or heating systems, and auxiliary systems, including water supply, drainage, gas and compressed air.

Table 2.1 – Features limiting the life of a store building and factors affecting the features, for each aspect of the store and its components.

Finally, at the design stage the plan is to **replace or refurbish** various components of the store periodically. For some the components replacement and refurbishment is considered relatively straightforward (e.g. building envelope fabrics, external ventilation systems and power supplies), while for others, like the reinforced concrete structures, it is potentially considerably more complex. Among the last ones it is worth to mention major reinforced concrete or structural steelwork building structures.

After having described all the steps and factors which play a role on the store longevity, it is clear that this is determined by the life-limiting feature with the shortest lifetime and which cannot practicably be replaced or refurbished. In this context, environmental control plays a fundamental role in extending the life-time of nuclear store buildings.

### 2.3.2. Store buildings environmental control

Environmental control in a store environment allows for the avoidance of extremes conditions which are harmful for the building health, such as condensation, or levels of RH at the deliquescence point of any contaminant salts. It is important to note that the store may have some constraints, such as particular weather conditions over the 100 years of operation, and the location of the store: the stores are usually located close to the reactors so that spent fuel does not have to be transported long distances, and reactors themselves are usually coastal for access to emergency cooling water [18].

As we can expect from the detailed description of the reinforced concrete degradation causes and mechanisms in section 2.2, among the main **key parameters** which need to be controlled in the store environment in order to limit concrete structural integrity issues according to [17], we can mention:

- 1) temperature and RH;
- 2) moisture;
- 3) **contaminants** (mainly **chloride** for coastal locations).

Table 2.2 shows the key aspects to consider for each parameter and the necessary required control methods, according to [17].

Key parameter	Key aspects to consider	Controls
1	Temperature and RH	<p>Connected to the risk of cycles of condensation and to the contaminants potentially deposited on store life-limiting features and waste packages.</p> <ul style="list-style-type: none"> <li>• Passive controls;</li> <li>• Actively managed Heating, Ventilating, and Air Conditioning (HVAC);</li> <li>• Contingency plan.</li> </ul>
2	Moisture	<p>Internal sources:</p> <ul style="list-style-type: none"> <li>• store materials (concrete);</li> <li>• waste packages conditioned with hydraulic cements or encapsulating 'wet wastes';</li> <li>• concrete overpacks.</li> </ul> <p>External sources:</p> <ul style="list-style-type: none"> <li>• migration from surrounding soil into the foundation, or transfer tunnels;</li> <li>• unconditioned damp air condensing on 'cold' surfaces;</li> <li>• inadequate performance of guttering, roofs, or cladding or other advantageous openings leading to infiltration;</li> <li>• infiltration of rainwater during import and export operations.</li> </ul> <ul style="list-style-type: none"> <li>• Designing out the risk of moisture ingress;</li> <li>• Providing detectors;</li> <li>• Proscribing practices that may foster water ingress;</li> <li>• Maintenance of store components;</li> <li>• Dehumidification on inlets to the store.</li> </ul>
3	Contaminants (corrosive materials: chloride is prevalent for coastal locations)	<p>Internal sources:</p> <ul style="list-style-type: none"> <li>• Salts arising from concrete;</li> </ul> <p>External sources:</p> <ul style="list-style-type: none"> <li>• Sea salts aerosols;</li> <li>• De-icing salts.</li> </ul> <ul style="list-style-type: none"> <li>• Limiting practices that may result in deposition of salts onto containers or concretes;</li> <li>• Filtration of inlet air to prevent ingress of saline;</li> <li>• Cladding or coating the internal/external store walls;</li> <li>• Monitoring.</li> </ul>

Table 2.2 – Key parameters to control in the store environment, key aspects and control methods proposed by the guidance [17].

As we can see from the control measures in Table 2.2, two other important parameters to be controlled in the store environment, which have great impact on moisture and contaminants ingress and deposition on concrete surfaces, are: ventilation/cooling systems

and filtration of air inlets. These two arrangements are highly interconnected, because the presence of filtration mechanism for air inlets depends on the ventilation/cooling method used in the store. Ventilation is the process of exchanging or replacing air in any space to provide high indoor air quality, introduces outside air, keeps interior building air circulating, and prevents stagnation of the interior air. The ventilation/cooling methods can be of two types [19]:

- 1) *Active system*, which is a forced ventilation system, since it is provided mechanically, for example by fan motors, actuators for vents and valves, and runs on electricity;
- 2) *Passive system*, which is a natural ventilation system that makes use of natural forces, such as wind and thermal buoyancy, to circulate air to and from an indoor space.

A more detailed discussion on the comparison of the benefits and risks of these methods is presented in paragraph 2.3.4.3, where the case of a specific nuclear store is discussed. The need of a ventilation or cooling system, and the choice of a particular type of arrangement is closely connected to the radioactive material contained in the stored packages. The radioactive material which is stored can be of different types (spent fuel, radioactive waste generated from nuclear reactor activities, or separated plutonium), which are introduced and described in the next paragraph.

### 2.3.3. Nuclear radioactive products: waste and assets

Radioactivity is the tendency of unstable nuclei to transform themselves into other more stable elements, through the *radioactive decay process*, by emitting high energy charged particles ( $\alpha$ ,  $\beta$ ) or ionising radiations ( $\gamma$ ). Every radioactive species decays with a specific *activity*, which is defined as the number of nuclei which decay in the time unit, following the exponential law of Eq. 2.6:

$$N(t) = N_0 e^{-\lambda t} \quad \text{Eq. 2.6}$$

where  $N(t)$  is the radioisotope population at the time  $t$ ,  $N_0$  is the radioisotope population at a chosen initial time, and  $\lambda$  is the decay constant characteristic of each nuclear species, on which other two important parameters depend (the average life and the half-life, which is the period of time needed to reduce the initial population of nuclei to 50%) [20].

The production of energy in nuclear reactors is the human activity where the biggest amounts of radioactivity are produced [21]. In nuclear reactors, the fission reaction of  $^{235}\text{U}$  and  $^{239}\text{Pu}$  is induced by neutrons, and huge amounts of heat are produced, which is converted in electric energy. The fission products are the radioactive isotopes  $^{137}\text{Cs}$  and  $^{90}\text{Sr}$ , which are responsible of heat and penetrating radiation production, and which show half-lives of 30 years. The fission products are disposed as High Level Waste (described in paragraph 2.3.3.1) [22]. The main products of nuclear activities are radioactive waste and plutonium 'asset'.

#### 2.3.3.1. Radioactive waste

According to IAEA (International Atomic Energy Agency) [23], radioactive waste coming from nuclear facilities can be classified, according to their half-life and their activities, into three main classes: LLW (Low Level Waste), ILW (Intermediate Level Waste) and HLW (High Level Waste). LLW has limited amounts of long lived radionuclides, requires robust isolation and containment for periods of up to a few hundred years and it is suitable for disposal in engineered near surface facilities.

ILW contains more long lived radionuclides, and it needs no provision, or limited provision, for heat dissipation during its storage and disposal. ILW requires disposal at greater depths, of the order of tens of metres to a few hundred metres. HLW shows levels of activity concentration high enough to generate significant quantities of heat by the radioactive decay process, or waste with large amounts of long lived radionuclides that need disposal in deep, stable geological formations usually several hundred metres or more below the surface (Geological Disposal Facility, GDF). However, the GDF concept may include a significant period of storage / care and maintenance of packaged wastes before the backfilling of the repository is completed. Wastes are therefore expected to be kept in "interim storage" for many years [17].

Another source of waste which need disposal and/or temporary storage is the decommissioning activity of many nuclear power plants and nuclear facilities which recently reached the end of their lifetime. The term *decommissioning* describes all the management and technical actions associated with cessation of operation and withdrawal from service of a nuclear facility, and it involves activities associated with dismantling of plant and equipment, decontamination of structures and components, demolition of

buildings, remediation of contaminated ground and disposal or temporary storage of the resulting waste [24].

### 2.3.3.2. Plutonium inventory: asset

Another important product of nuclear reactor and reprocessing activities is Plutonium: during the fission reactions in the reactor, uranium atoms capture neutrons produced during fission, thus forming heavier elements such as  $^{239}\text{Pu}$  (transuranic elements), which show a half-life of about 24000 years. Reprocessing activities, which are carried out in appropriate reprocessing nuclear facilities, separate residual uranium and plutonium from fission products and irradiated fuel, thus allowing their re-use as fuel [22]. Globally around 54 percent of all separated plutonium is currently held in peaceful nuclear programs, and around 46 percent is held in military programs [25].

The UK currently has a significant inventory of separated plutonium which has been generated from reprocessing activities on the Sellafield site<sup>2</sup> (mostly reprocessing of Magnox<sup>3</sup> and Oxide<sup>4</sup> fuel). The UK government has designated this material as an *asset* and it must be stored in a form which does not exclude future re-use until a final decision is made, and for planning purposes this is taken to be a period up to 100 years. This material needs to be stored in purpose-built engineered storage facilities which meet relevant safety and security requirements. To ensure its safe and secure storage, all plutonium products and residues which have been generated during operations on the site, until the end of the operations at Sellafield, are/ will be stored at a new purpose-built facility, described in Paragraph 2.3.4: the Sellafield Product and Residue Store (SPRS) [27].

### 2.3.4. Sellafield Product and Residue Store (SPRS)

Sellafield Product and Residue Store (SPRS) has been designed and constructed to ensure the safe and secure storage of Plutonium ( $\text{PuO}_2$ ) and plutonium residues produced at the

---

<sup>2</sup> Sellafield is a large multi-function nuclear site in Cumbria (England), former nuclear power generating site. The Sellafield current key activities include nuclear fuel reprocessing, nuclear waste storage and nuclear decommissioning [26].

<sup>3</sup> Magnox (Magnesium non-oxidising) is an alloy of magnesium with small amounts of aluminium and other metals, which is used in cladding unenriched uranium fuel with a non-oxidising covering.

<sup>4</sup> The fuel of fission reactors is usually based on metal oxide, since the oxide melting point is much higher than that of metals and because it cannot burn.

Sellafield nuclear site since reprocessing activities began in the mid 1960s. This material will be stored there until the government makes a decision on the final disposal of the UK stockpile of separated plutonium. The store has been built with an intended operational life of at least 100 years. Therefore, the structural health of such building is of critical importance, also because it is the first naturally-cooled plutonium store on the Sellafield nuclear site, demonstrating a new approach to the storage of separated plutonium. The following paragraphs describe the features and the working principle of this store, aiming to identify the potential risks for its structural health, and their provenience. The main reference for the following section is a paper dedicated to the safe storage of UK Plutonium, and to SPRS in particular, from the Nuclear Institute Congress 2013 [27].

#### 2.3.4.1. SPRS packages

The plutonium stored at SPRS comes from two streams of plutonium production on the Sellafield nuclear site:

1. Plutonium powder from the reprocessing of Magnox reactor fuel has a moderate decay heat, and it is stored in **Magnox packages** which comprise of a nested can design (an aluminium screw-top inner can, a polythene bag and a weld-sealed stainless steel outer can);
2. Plutonium powder from the reprocessing of oxide fuel from the Thermal Oxide Reprocessing Plant (THORP) has a typical decay heat higher than the Magnox one, and it is stored in a **THORP package** which share a similar nested can design (a stainless steel screw-top inner package, a stainless steel breathing intermediate and a welded, sealed, stainless steel outer).

Since the packages stored in SPRS release decay heat, a cooling system is provided, together with particular precautions for heat dissipation.

#### 2.3.4.2. SPRS internal configuration and working principle

The product packages in SPRS are placed in extruded aluminium storage tubes which allow the packages to rest on conductive rails, allowing heat to be transferred to the aluminium extrusion. The extrusions themselves act as a heat sink, allowing the transfer of heat from the radioactive plutonium powder to the extrusion via the metallic outer can. On the other hand, they also act as a secondary containment layer for the materials as the airflow or the

cooling system cools the extrusions and never comes into direct contact with the packages themselves. Figure 2.1 below shows a schematic representation of an extrusion section with three THORP or Magnox product packages.

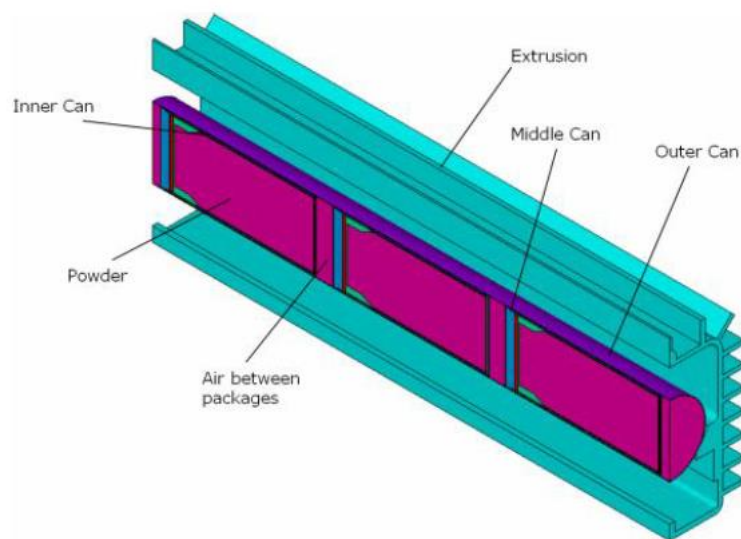


Figure 2.1 – Schematic representation of an extrusion section with three THORP or Magnox product packages [27].

Unlike the other plutonium stores on the Sellafield site, which operate with a mechanically driven airflow cooling system (active), SPRS is the only plutonium store in Sellafield which uses a natural cooling system (passive): the decay heat from packages generates buoyancy force which drives airflow through the store, without the need of a forced mechanically driven airflow. The cooling airflow acts as an efficient heat transfer medium, since it removes heat from the aluminium extrusions, which have a high thermal conductivity (209.4 W/mK [28]).

SPRS is made by several storage cells, each divided into 8 rows of 5 extrusions, where the lower 4 rows store the Magnox packages, while the upper 4 rows store the THORP packages, so that their higher decay heat can drive the flow through the cell, thus encouraging a positive air flow across the cooler Magnox packages. Figure 2.2 (a) shows the schematic configuration of a storage cell in SPRS, where the cooling airflow enters through ducting at the base of the cell, as the buoyancy force draws air up through the cell. The airflow removes heat from the extrusions, rising its temperature, to be then removed from the store through outlet stacks on the top of the building, with a difference  $\Delta T$  between the temperature at the cell outlet and the temperature at the cell inlet. A measure of how effectively the store works was monitored throughout active commissioning, by calculating the heat carried by the cooling airflow. To demonstrate that the store could be safely operated, it was necessary to

generate computer models of both the store and the packages and to predict their behaviour during normal and fault conditions, since SPRS represents the first time that a naturally-cooled plutonium store had been considered, in the Sellafield nuclear site. Two pairs of CFD (Computational Fluid Dynamic) and FE (Finite Element) models were generated during the design and commissioning of SPRS, with the purpose of demonstrating that temperatures within the store would have not reached levels where pressurisation of the packages within could threaten pressure limits. Figure 2.2 (b) shows the CFD thermal model of a full loaded storage cell at SPRS.

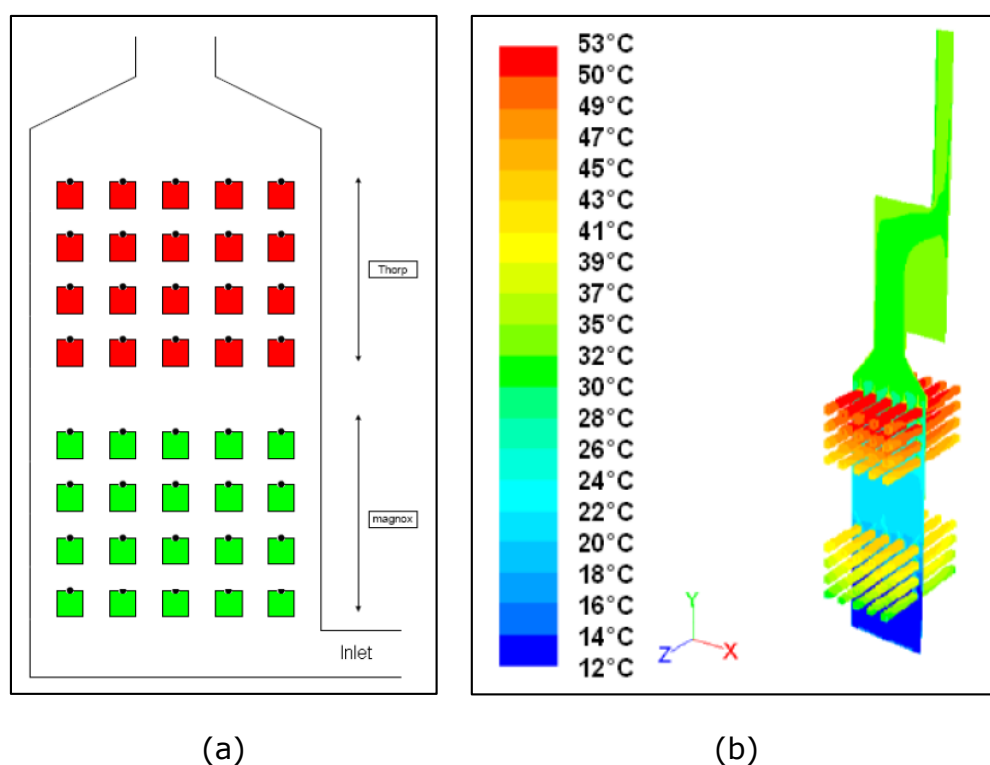


Figure 2.2 – a) Schematic representation of a storage cell in SPRS [27], b) CFD thermal model of a full loaded storage cell at SPRS [27].

With the help of modelling, the safe operation of the store was successfully demonstrated and data gathered during the active commissioning programme proved that packages were stored in conditions beneficial to long-term storage. Consent to operate was issued by the Office for Nuclear Regulations (ONR) in October 2012 and the store has continued operationally since then.

#### 2.3.4.3. SPRS passive cooling system: risk for structural health

The use of a passive cooling arrangement in SPRS has significant benefits, since it does not require any manual intervention to operate (it-self regulates): this effectively eliminates a Loss Of Cooling Accident (LOCA) scenario, because, as it operates passively, it does not have any credible scenarios which would prevent airflow moving through the store. However, it is worth noting that passive cooling system operates at very low flow velocities, compared to active (mechanically forced) cooling systems, and this has three main consequences [29]:

1. If the airflow is slow enough, the air has enough time to cool to the dew point temperature before it moves away from cold surfaces;
2. Any sort of filtration of inlet air methods cannot be used, due to the increase pressure differential this would place on the airflow.
3. Indeed, the introduction of HEPA (High-Efficiency Particulate Air), coalescence or bag filters, to remove salt, moisture and particulate from the air (as it happens in case of active ventilation systems), would act as a barrier for the air flow, thus compromising the effectiveness and safety of the store.
4. For the absence of such filtering systems in stores such as the SPRS, particular attention needs to be put at the ingress of moisture, chloride and other contaminants which can lead to corrosion of packages and steel reinforcement of concrete. This is even more important, since the average value of RH measured annually in the store air corridors is around 70-80%, according to internal Sellafield reports.
5. In this case, monitoring and maintenance are the most effective and applicable control measures among those listed in Table 2.2. For this reason, nuclear industry shows an increased interest to technologies which can limit and monitor the ingress of chloride and moisture directly onto concrete structures, and which can play a maintenance role when the concrete shows degradation signals.

## 2.4. Maintenance and monitoring in nuclear stores: a novel solution

The process of determining and tracking structural integrity and assessing the nature of damage in a structure is known as *Structural Health Monitoring* (SHM) [30]. The nuclear industry is actively looking for new methods of structural health monitoring to assure that

the nuclear store buildings life time will meet the intended target life time of 100 years. Among these methods, monitoring of chloride and moisture ingress into concrete would constitute a powerful instrument of prevention for reinforcement corrosion. This is particularly important for store buildings such as SPRS, which operates a passive cooling system, thus increasing the risk of condensation and the levels of chloride and moisture in concrete, as seen in section 2.3.4.3.

The research project of this work of thesis was conceived together with Nuclear Industry (National Nuclear Laboratories (NNL) and Sellafield) to find a solution to the lack of effective means to monitor moisture and chloride ingress. It is useful at this point to give an overview on the existing moisture and chloride control systems in nuclear stores, the lacks that they present, and the environmental requirements. This overview is given in section 2.4.1. Section 2.4.2 introduces the technology proposed in this work, and briefly highlights its novelty and advantage in comparison with the existing methods.

### 2.4.1. Chloride and moisture control in UK nuclear stores

In UK nuclear store buildings, the environmental control, intended as *monitoring*, is mainly a control of Relative Humidity (RH) and temperature: humidity monitoring is not as extensive as temperature monitoring. Relatively few operators monitor chloride levels and very few have implemented monitoring measures such as corrosion coupons [31]. So far, chloride monitoring of the storage facilities have been carried out using techniques which give representative surface salt deposition measurements, such as: (i) vertical and horizontal plates of 304L Stainless steel coupled with a salt contamination meter, and (ii) chloride candles, which is a wet chemistry method measuring atmospheric salt content [32]. Therefore, the monitoring of chloride levels is applied to the deposition of chloride onto the steel surface of radioactive packages, and on atmospheric salt content, not on chloride content in concrete.

The strategies adopted for moisture control are either minimising moisture entry or removing moisture from the building envelope [31], more than moisture monitoring in concrete, and the guidances of the nuclear regulator institutes are referred to the RH. The British Nuclear Group (BNG) extant guidance [33] suggests a target of 80% maximum relative humidity for care and maintenance of packages in stores, based on considerations of the critical relative humidity for corrosion of mild steel (packages and reinforced concrete) [31]. The draft Magnox guidance [34] (which is an update of Reference [33])

indicates a range for relative humidity between 30% and 75%, with recommended upper limits of 50% for a combination of high chloride and low humidity, and 75% for low chloride and high humidity (which are set in combination with recommended values for waste package temperature) [31].

We can conclude that in nuclear store buildings RH and temperature monitoring are applied, and chloride levels are measured in the atmosphere and as deposition on the steel surfaces of radioactive packages, while no monitoring is directly applied to concrete to measure the levels of water and chloride ingress. The same thing applies to the inlets/ducts (air corridors) of the stores, which are in direct contact with the outside air, and thus cooler and more humid. Therefore, the structural health monitoring of concrete in such store buildings shows a clear need for chloride and moisture content sensing technologies. Also - given the propensity for cracking, there may also be a need for repairs.

#### 2.4.2. Novel solution: combined multifunctional technology

The ideal forefront technologies which industry is looking for, in order to solve the monitoring and maintenance need for structural health, should meet some advantageous requirements of different nature:

- Affordable costs;
- Much flexible to apply to any surface and shape;
- Forefront performances in terms of resolution, repeatability and precision;
- Multifunctional.

Among the techniques for monitoring chloride and moisture in concretes, currently there is a growing interest for non-destructive methods [35]: they preserve the features and the usefulness of the material, consist of external or embedded equipment, and can be taken at several points of the structure and times [36, 37]. A detailed review on the existing methods to sense moisture and chloride in concrete will be presented respectively in chapter 5 and 6. Here the main methods are mentioned, in order to briefly highlight the novelty and improvement represented by the technology proposed in this work.

According to [35], non-destructive methods to monitor chloride ingress into concrete are mainly Ion Selective Electrodes (ISE), Electrical Resistivity (ER) and Optical fiber sensors (OFS). Methods for continuous moisture monitoring in concrete include OFS, dielectric permittivity and capacitive sensors, and concrete electrical impedance measurements, among the others. These methods will be reviewed in detail in chapters 5 and 6.

The sensing methods based on electrical resistivity and impedance measurements, mentioned above, have been directly applied onto concrete so far. These methods would be more effective if applied onto an electrolytic material more conductive than concrete, which can be applied onto concrete as a layer or used as a separate sensor deployed nearby the concrete structure in different critical locations. This is what the new technology proposed in this work does, consisting of alkali-activated materials (called here geopolymers) coupled with stainless steel electrodes and an electrical impedance interrogation system for Electrochemical Impedance Spectroscopy (EIS).

This system is novel because it represents the first time demonstration of the feasibility of moisture and chloride geopolymer sensors. This technology takes advantage of existing techniques and materials to make a novel use of them. More specifically, this work combined the demonstrated performances as repair and protection for concretes of geopolymer materials (that it will be shown in detail in chapter 4) with their most advantageous properties, such as electrical conductivity among the others, to design and develop a combined technology which can play at the same time a maintenance and a sensing role. Therefore, this new system combines the chloride and moisture measurements through changes in the electrical impedance of geopolymer binders, playing also the role of repair and protection to concrete.

As the reader can already assume, this leads to the development of a multifunctional technology easily applicable to any surface and shape. The geopolymer used for this system is obtained by cheap components, and with a simplified manufacture process which doesn't require additional steps or materials, as we will see in detail in chapter 4. This makes the technology also highly affordable (\$USD 5/kg), satisfying the requirements the most convenient technology should have. All of them will be discussed and demonstrated in the following chapters, with a work that, at this stage, can be configured as the experimental laboratory demonstration of the feasibility and characterisation of the proposed technology under its different aspects.

This technology is not only important for the application in a nuclear context, but for a wide range of structures where maintenance, and chloride/moisture monitoring can support structural health. Moreover, this technology doesn't constitute only an important research achievement from the application point of view (e. g. for structural health monitoring), but it also represents a further step in scientific knowledge, since this is the first time demonstration in literature of geopolymer materials as moisture and chloride sensors, and it also investigates and extends the knowledge of the electrical conduction mechanism of geopolymers, by outlining a proper model to describe the system, validated by experimental evidence.

## 2.5. Summary

This chapter has outlined the importance of a monitoring and maintenance technology which can prevent the critical levels of moisture and chloride into nuclear concrete containments, and thus avoid the corrosion of steel rebars and the consequent concrete degradation.

The background of the main causes of concrete degradation and of the issues and needs in nuclear concrete containments has been investigated in detail, especially for the specific nuclear context in which the research project has been conceived. As already mentioned in the previous paragraph, the technology proposed and characterised in this work of thesis consists of geopolymer materials coupled with an electrical interrogation system. Despite the technology can be applied to any concrete structure, the design and development of this technology has taken into account the specific needs and limitations of the nuclear context. This chapter has shown some of the limitations of nuclear store buildings, and in particular the specific limitations of the SPRS store in Sellafield, such as the absence of air filtering systems (due to the presence of a passive system to cool down the heat generated by the nuclear Plutonium packages stored inside the building). Other limitations in such environment, as well as in a nuclear context in general, are:

- (i) the proximity to the sea, due to the coastal location of nuclear stores, which is the cause of high humidities inside the store, and in particular in the inlets and ducts of the building;

- (ii) the presence of radioactive packages inside the store, which is the cause of heat and high ionising radiation levels; for this reason, further heat sources and materials which radiation and/or heat could damage should be avoided;
- (iii) materials which produce  $\gamma$ -products under interactions with radiation are prohibited;
- (iv) radiation resistant materials are preferred;
- (v) in the UK in particular, ambient-cold temperatures are more likely to be prevalent;
- (vi) internal data reports of temperature and RH in the air corridors and ducts of the SPRS store show low temperatures and high RH levels.

For all these reasons, adding additives / heat treatments to geopolymers has been avoided in this work, not just because of cost, but because of the nuclear context. Geopolymers indeed can cure at room temperature [38]. Moreover, previous work in literature has demonstrated the radiation resistance of geopolymer materials (especially for fly ash geopolymers, where changes in pore structure due to  $\gamma$ -rays irradiation were found to be minimal) and their suitability for the encapsulation of radioactive waste [39, 40]. This is a further reason for the choice of geopolymer materials for this particular technology, and it indicates that it might be possible the future application of the technology in proximity of radioactive environments.

The main application of the technology has been conceived mainly for an application into the air inlets and ducts of the store building, which are cooler and with high RH levels, and for this reason chapter 4 demonstrates the ambient temperature and high RH curing of geopolymer materials, with no additives, and it highlights the main issues encountered in the process, and the repair potentiality of the material. For the same reason, in chapter 5 and 6, intermediate-high moisture levels are considered and temperatures  $5^{\circ}\text{C} \leq T \leq 30^{\circ}\text{C}$ .

In order to fully understand the geopolymer system proposed in this thesis, the next chapter provides an overview on geopolymer materials and their main applications, with a particular focus on fly ash geopolymers, and repair/protection applications for concrete. A more detailed review on geopolymer sensing applications will be presented in chapter 5.

## References

- [1] L. Bertolini, B. Elsener, P. Pedferri, E. Redaelli, and R. Polder, *Corrosion of steel in concrete* vol. 392: Wiley Online Library, 2013.
- [2] J. P. Broomfield, "Corrosion of steel in concrete: Understanding," *Investigation and Repair, E&FN, London*, pp. 1-15, 1997.
- [3] H. Böhni, *Corrosion in reinforced concrete structures*: Elsevier, 2005.
- [4] A. de Kageneck and C. Pinel, "The Joint Convention on the Safety of Spent Fuel Management and on the Safety of Radioactive Waste Management," *International & Comparative Law Quarterly*, vol. 47, pp. 409-425, 1998.
- [5] G. C. Bye, *Portland cement: composition, production and properties*: Thomas Telford, 1999.
- [6] Y. Zhao, J. Dong, Y. Wu, and W. Jin, "Corrosion-induced concrete cracking model considering corrosion product-filled paste at the concrete/steel interface," *Construction and Building Materials*, vol. 116, pp. 273-280, 2016.
- [7] Z. Guo, *Principles of reinforced concrete*: Butterworth-Heinemann, 2014.
- [8] N. Buenfeld, R. Davies, A. Karimi, and A. Gilbertson, "Intelligent monitoring of concrete structures," 2008.
- [9] M. Montemor, A. Simoes, and M. Ferreira, "Chloride-induced corrosion on reinforcing steel: from the fundamentals to the monitoring techniques," *Cement and Concrete Composites*, vol. 25, pp. 491-502, 2003.
- [10] R. N. Swamy, *The alkali-silica reaction in concrete*: CRC Press, 2002.
- [11] M. Jedidi and O. Benjeddou, "Chemical causes of concrete degradation," *MOJ Civil Engineering*, vol. 4, pp. 219-223, 2018.
- [12] M. Basista and W. Weglewski, "Chemically assisted damage of concrete: a model of expansion under external sulfate attack," *International journal of damage mechanics*, vol. 18, pp. 155-175, 2009.
- [13] Y. Wang, S. Nanukuttan, Y. Bai, and P. Basheer, "Influence of combined carbonation and chloride ingress regimes on rate of ingress and redistribution of chlorides in concretes," *Construction and Building Materials*, vol. 140, pp. 173-183, 2017.
- [14] G. Glass and N. Buenfeld, "43 CHLORIDE THRESHOLD LEVELS FOR CORROSION INDUCED DETERIORATION OF STEEL IN CONCRETE," in *PRO 2: International RILEM Workshop on Chloride Penetration into Concrete*, 1997, p. 429.
- [15] U. Angst, B. Elsener, C. K. Larsen, and Ø. Vennesland, "Critical chloride content in reinforced concrete—a review," *Cement and concrete research*, vol. 39, pp. 1122-1138, 2009.
- [16] A. Poursaee, "Corrosion of steel in concrete structures," in *Corrosion of Steel in Concrete Structures*, ed: Elsevier, 2016, pp. 19-33.
- [17] N. D. Authority, "Industry Guidance—Interim Storage of Higher Activity Waste Packages (Integrated Approach)," 2011.
- [18] R. A. Pielke Sr, *Climate vulnerability* vol. 1: Newnes, 2013.

- [19] A. Handbook, "HVAC systems and equipment," *American Society of Heating, Refrigerating, and Air Conditioning Engineers, Atlanta, GA*, pp. 1-10, 1996.
- [20] K. S. Krane and D. Halliday, *Introductory nuclear physics*, 1987.
- [21] E. Dossier, "La Radioprotezione in Italia: La Salvaguardia della Popolazione e dell'Ambiente," *Rapporto ISBN*, pp. 88-8286, 1999.
- [22] U. N. R. Commission, "Backgrounder on Radioactive Waste," ed, 2007.
- [23] I. S. S. N. GSG-1, "Classification of radioactive waste. General safety guide," ed: International Atomic Energy Agency Vienna, 2009.
- [24] O. f. E. Co-operation and Development, *Decommissioning Nuclear Power Plants: Policies, Strategies and Costs*: OECD Publishing, 2003.
- [25] Z. Mian and A. Glaser, "Global Fissile Material Report 2015: Nuclear Weapon and Fissile Material Stockpiles and Production," in *presentation at NPT Review Conference, May, 2015*.
- [26] "Annual Review of Performance," 2017-2018.
- [27] C. P. Gallagher, P. M. Cook, R. Hanratty, and M. Moorcroft, "Maintaining Safe Storage of UK Plutonium," presented at the The Nuclear Institute Congress, Manchester (UK), 2013.
- [28] K. Gieck and R. Gieck, *A collection of technical formulae*: Gieck, 2007.
- [29] *WASTE PACKAGE SPECIFICATION AND GUIDANCE DOCUMENTATION: WPS/630: Guidance on Environmental Conditions during Storage of Waste Packages*, 2008.
- [30] P. C. Chang, A. Flatau, and S. Liu, "Health monitoring of civil infrastructure," *Structural health monitoring*, vol. 2, pp. 257-267, 2003.
- [31] N. T. p. I. Centre, "Store Environmental Controls – Best Practice and Guidance," vol. NT/722500385/R554/Issue 1, ed, March 2009.
- [32] I. O. f. Standardization, *Corrosion of Metals and Alloys: Corrosivity of Atmospheres: Measurement of Environmental Parameters Affecting Corrosivity Atmospheres*: ISO, 2012.
- [33] B. N. Group, "Guidance for Care and Management of ILW Packages," vol. ET/ACOP/001, Issue 2, ed, October 2004.
- [34] M. N. a. M. South, "Guidance for Care and Maintenance of ILW Packages," vol. R&D 03-2008/09N, Issue 1, ed, January 2009.
- [35] M. Torres-Luque, E. Bastidas-Arteaga, F. Schoefs, M. Sánchez-Silva, and J. F. Osma, "Non-destructive methods for measuring chloride ingress into concrete: State-of-the-art and future challenges," *Construction and building materials*, vol. 68, pp. 68-81, 2014.
- [36] R. Prakash, "Non-destructive testing of composites," *Composites*, vol. 11, pp. 217-224, 1980.
- [37] B. Elsener, L. Zimmermann, and H. Böhni, "Non destructive determination of the free chloride content in cement based materials," *Materials and Corrosion*, vol. 54, pp. 440-446, 2003.
- [38] J. Davidovits, "Geopolymers: inorganic polymeric new materials," *Journal of Thermal Analysis and calorimetry*, vol. 37, pp. 1633-1656, 1991.
- [39] L. Leay, A. Potts, and T. Donoclift, "Geopolymers from fly ash and their gamma irradiation," *Materials Letters*, vol. 227, pp. 240-242, 2018.

- [40] C. Shi and A. Fernández-Jiménez, "Stabilization/solidification of hazardous and radioactive wastes with alkali-activated cements," *Journal of hazardous materials*, vol. 137, pp. 1656-1663, 2006.

# 3. GEOPOLYMER MATERIALS AND APPLICATIONS

## 3.1. Introduction

Alkali-activated materials (AAMs) are a class of cementitious binders which can demonstrate similar properties to ordinary cement, ceramic materials and zeolites, and are potentially an important and cost-effective component of the future toolkit of sustainable construction materials [1]. Their properties, such as high thermal and chemical stability, compressive strength, adhesive behaviour, and high electrical conductivity, have brought AAMs to be intensively studied as a viable economical alternative to organic polymers and inorganic cements in several different applications [2]: military [3]; aircrafts [4-7]; thermal insulating and thermal shock resistant materials [8-11]; fire-proof building materials [12, 13]; hybrid inorganic-organic composites [14, 15]; encapsulation of radioactive waste [16, 17]; protective coatings [18-22]; infrastructure rehabilitation and reinforced concrete repair [23-28]; self-sensing materials for structural health monitoring [2, 29-34]. Some of them are reviewed in section 3.3, while the ‘smart sensing’ applications are reviewed in chapter 5.

For completeness it must be said that there are controversial opinions on the nomenclature to describe alkali-activated materials: they are commonly referred to as ‘geopolymers’, ‘low-temperature aluminosilicate glass’, ‘alkali-activated cement’, ‘geocement’, ‘alkali-bonded ceramic’, ‘inorganic polymer concrete’ and ‘hydroceramic’ [35]. In this work, they are referred as geopolymers.

This chapter has two main sections, section 3.2 and section 3.3, which aim respectively to:

1. give an overview of geopolymer materials (the geopolymerization process, geopolymer properties, and in particular fly ash geopolymers which are used in this work), thus giving the necessary theoretical background for the scope of this thesis (for a more detailed description of geopolymer systems, in general readers are directed to [36, 37]);
2. provide a detailed literature review on the state of the art of geopolymer applications.

Finally a chapter summary is presented in section 3.4.

## 3.2. Geopolymer materials

Geopolymers form as the result of several reactions between an alkaline activator and inorganic materials which are rich in silicon (Si), aluminium (Al) and oxygen (O). Geopolymers may be synthesized at ambient or elevated temperature by alkaline activation of aluminosilicates obtained from industrial wastes, calcined clays, melt-quenched aluminosilicates, natural minerals, or mixtures of two or more of these materials [38]. Typical inorganic precursors for geopolymer synthesis include blast furnace slag, metakaolin and fly ash [36, 39-41]. Solutions used as chemical activators in the synthesis of geopolymers are *alkali metal hydroxides (MOH)* and/or *silicates*, typically a combination of Sodium Hydroxide (SH or NaOH) and Sodium Silicate (SS or  $Na_2SiO_3$ ) [42, 43]. Filler materials, including conventional concrete aggregates (such as basalt), sand or fibers, may be used to enhance desirable properties including strength and density [38].

The ground work on alkali-activation was completed in the 1950s by Prof Glukhovsky and co-workers, and then, Joseph Davidovits reinvigorated the area in the 1970s, and to him is attributed the paternity of the name 'geopolymers' [44].

The following section describes in detail the geopolymerisation process which leads to the formation of geopolymers, as this is useful to understand their macroscopic behaviour.

### 3.2.1. Geopolymerisation

Geopolymerization is the name given to the process which involves a chemical reaction between raw material alumino-silicate oxides, present in materials such as fly ash and metakaolin, and alkali metal silicate solutions under highly alkaline conditions, with the

formation of amorphous to semi-crystalline three-dimensional polymeric structures and crystalline Al-Si particles. The geopolymerization reaction is exothermic and takes place under atmospheric pressure at temperatures below 100 °C [45].

The exact mechanism which takes place during geopolymerization is not yet fully understood. One theory proposed by Glukhovsky in 1967, and then extended by studies of other authors [35, 46], describes a general model for the mechanisms that govern the alkali activation of aluminosiliceous materials, schematically shown in Figure 3.1. Glukhovsky divided the key processes occurring in the alkali activation of aluminosilicate materials into three main stages, which are largely coupled and occur concurrently [35, 36]: 1) destruction-coagulation; 2) coagulation-condensation; 3) condensation-crystallization. They are described in detail in the following three sections.

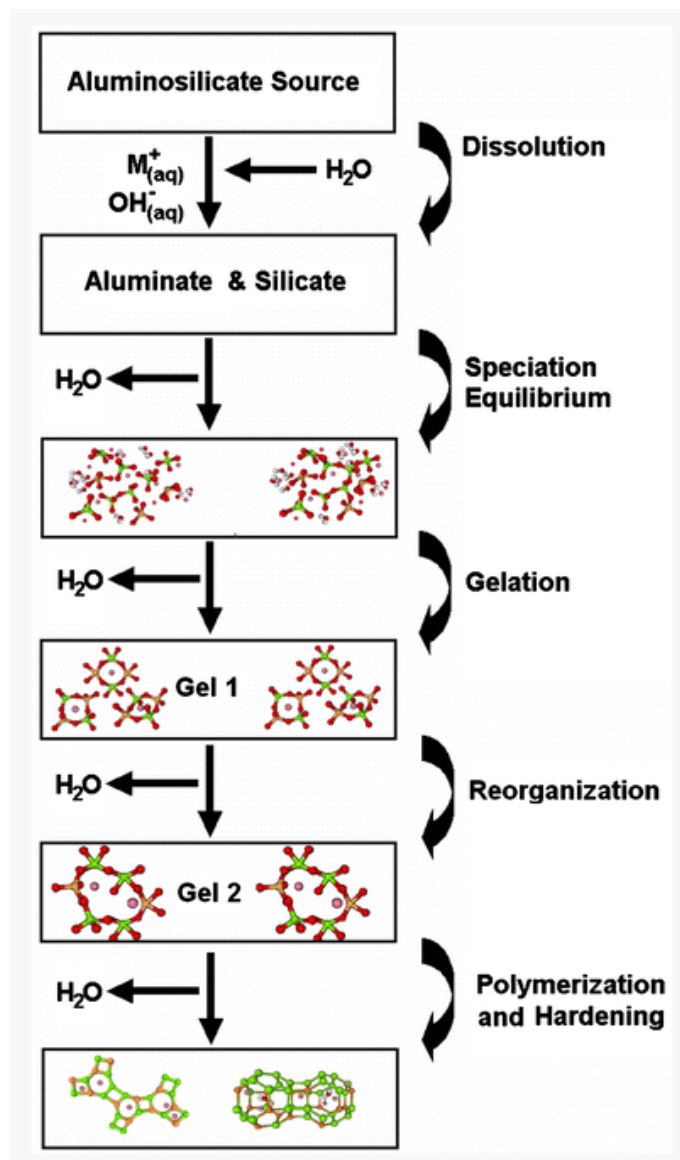


Figure 3.1 – Schematic representation of the conceptual model for geopolymerisation described by Glukhovskiy [35].

### 3.2.1.1. First stage: Destruction-Coagulation

In the first stage, known also as nucleation, the first disaggregation process consists of the severance of covalent bonds Si-O-Si, Al-O-Al and Al-O-Si in the starting raw material (e.g. fly ash). The  $OH^-$  ions coming from the alkaline solution initiate the rupture of the bonds, redistributing the electron density, and the presence of alkaline metal cations ( $M^+$ , most commonly  $Na^+$ ) neutralises the resulting negative charge: the  $OH^-$  ion acts as a reaction catalyst, and the alkaline metal cation ( $Na^+$ ) acts as a structure-forming element, balancing the negative charge of the tetrahedral aluminium. The first stage of reaction is controlled by the aptitude of the alkaline compound to dissolve the solid fly ash network and to produce small reactive species of silicates and aluminates. There is the formation of intermediate

complexes, called *oligomers*, that decompose into  $\text{Si}(\text{OH})_4$ ,  $\text{Al}(\text{OH})_4^-$ , anionic species containing  $\equiv \text{SiO}^-$  groups, and  $\equiv \text{Si} - \text{O} - \text{Na}^+$  which create conditions suitable for the transport of the reacting structural units and the development of the coagulated structure.

### 3.2.1.2. Second stage: Coagulation-Condensation

In the second stage, accumulation increases contact among the disaggregated products, forming a coagulated structure in which polycondensation takes place. The clusters formed by the polymerisation generate colloidal particles. Once in solution, the species released by dissolution are incorporated into the aqueous phase (which may already contain silicate present in the activation solution). This contributes to the formation of a complex mixture of silicate, aluminate and aluminosilicate species, and the speciation equilibria within these have been extensively studied [47, 48]: a supersaturated aluminosilicate solution is quickly created by the rapid dissolution of amorphous aluminosilicates at high pH. When a solution is so concentrated, the formation of a gel takes place, due to the condensation of oligomers in the aqueous phase. These form large networks, releasing the water that was consumed during dissolution, and starting the third stage.

### 3.2.1.3. Third stage: Condensation-Crystallization

In the third stage, the supersaturated aluminosilicate solution forms a continuous gel which varies considerably with raw material processing and synthesis conditions [49]. Initially, from the first few minutes to the first four or five hours, the formation of an aluminium-rich gel takes place, known as Gel 1 [50]. As the reaction progresses, there is a structural polymerisation process that determines the final composition of the polymer, pore microstructure and distribution in the material. This reorganisation process takes place when more Si-O groups of the initial solid source dissolve, increasing the silicon concentration in the medium. This forms a zeolite precursor gel, called Gel 2 [36]. After gelation, the system continues to rearrange and reorganize, as the connectivity of the gel network increases, forming the 3D aluminosilicate network typical of Geopolymers. When the nuclei reach a critical size, some crystallization starts to take place. The final geopolymer binders are mainly comprised by an X-ray amorphous gel with some unreacted raw material and some crystals. The degree of crystallinity is largely determined by product formulation and synthesis conditions.

The stage of geopolymerization in which crystals begin to develop is called growth, and it determines the microstructure and the pore distribution of geopolymers, and therefore also their physical properties. The microstructural development of the geopolymer system is also affected by the type of cation involved in the activation reaction and by the Si/Al ratio into the gel [51]. The following section describes the influence of alkaline solution on geopolymers' properties.

### 3.2.2. Alkaline solution

The choice of the type and the composition of the alkaline solution is very important for the structure of geopolymer binders. In particular, the apparent structural stability of geopolymers increases with addition of soluble silicon to the activating solution [35, 38]. By doing experiments using only NaOH as activator and other experiments by using a sodium silicate solution, it has been found that the presence of soluble silica in the activating solution plays an important role in microstructure development, mainly affecting the chemistry of phases and the kinetics, not the mechanism governing the reactions [43].

The alkali metal hydroxide solutions are usually indicated in general as MOH, where M can be Sodium (Na) or Potassium (K), corresponding respectively to Sodium Hydroxide (NaOH or SH) and Potassium Hydroxide (KOH or KS), the two most commonly used hydroxide solutions. KOH shows a greater extent of dissolution due to its higher level of alkalinity, but it has been shown that NaOH possesses a greater capacity to liberate silicate and aluminate monomers [35]. Therefore, NaOH is the most commonly used hydroxide activator in geopolymer synthesis, also because it is the cheapest and the most widely available among the alkali hydroxides [36]. The increase of NaOH concentration causes an acceleration to the dissolution reactions promoting the early stages of the geopolymerization process, and the increase of Si and Al concentrations in the aqueous phase enhances the hardening of the geopolymer system [45].

For all these reasons, a combination of Sodium Hydroxide (SH) and Sodium Silicate (SS) is the alkaline solution (L) used for the alkali activation of fly ash (A) in this work.

The chemistry and resulting wet / cured properties of the fly ash geopolymer are mainly defined by [41, 52]:

1. the mass ratio L/A;

2. the mass ratio SH/SS;
3. the molarity of the SH (which typically ranges from 8 -14 M).

While molarity can, to some extent, be selected based on safety considerations, the ratios L/A and SH/SS should be selected to match the chemical composition of the fly ash. This is a significant drawback for fly ash geopolymers, as: i) since fly ash is a waste product of coal combustion, fly ash composition can vary significantly between coal plant sources; and ii) unlike with Portland cement systems, at the time of writing, there are no simple numerical methods for geopolymer mix design, particularly for fly ashes [35, 53].

The ratios used in this work, outlined in section 4.3.2, were found through a process of trial and error over a testing matrix, and on the basis of literature findings, according to [54].

The following section is dedicated to the detailed description of fly ash geopolymers, used in this work.

### 3.2.3. Fly ash geopolymers

Geopolymers derived from fly ash, used in this work, offer a few key advantages over the other geopolymer precursors (such as those derived from metakaolin or blast-furnace slag), including:

- Higher workability, durability and strength: this is due to the lubricating and re-enforcing effect of unreacted fly ash particles [50, 51].
- Low cost: As fly ash is a by-product of coal combustion, it is cheap and available in large volumes around the world [50]. While there is a looming shortage of fly ash for use as a concrete additive [55], the availability for geopolymer coatings (a low volume application) is still high, as one billion tons of fly ash are still produced annually worldwide in coal-fired steam power plants [56].

In particular, the United Kingdom produces further 600,000 to 1 million tonnes of furnace bottom ash each year, and between 40% to 70% of the fly ash is utilised in beneficial applications. The remaining material is deposited in landfill [57].

As mentioned in the previous section, fly ash composition is an important parameter for the geopolymer mix design and depends on coal plant sources. The next section presents a detailed description of fly ash chemical composition and classification.

### 3.2.3.1. Fly Ash: chemical composition and classification

Coal is an organic sedimentary rock used as fuel in power stations to generate heat that is converted into electricity. The coal combustion process also produces fly ash, a waste product that forms a major constituent of fly ash geopolymers. The mineral composition of the coal burned and the combustion conditions has a significant impact on the constituents present in the fly ash and thus the properties of the final geopolymer [36]. As a base raw material, fly ash is variable for several reasons, including the sources of the coal, the efficiency of its pulverisation, the furnace in which the pulverised coal is burnt and the method of precipitating the ash from the combustion gases. In principle the furnace acts as a particle separator: about 20% of the ash particles either form together or combine into a form of clinker, which falls to the bottom of the furnace and is known as 'furnace bottom ash'; the remaining 80% is known as fly ash and this material is normally considered as an artificial pozzolan [58].

The chemical composition of fly ash is typically made up of elements with a high melting point, such as Si, Ca, Al, Fe, Mg and sulfur oxides along with carbon and various trace elements. Elements such as Fe, Ca, and Mg combine with oxygen in the air to form oxide minerals, such as magnetite ( $\text{Fe}_2\text{O}_3$ ), lime (CaO) and periclase (MgO). The mineral quartz ( $\text{SiO}_2$ ) survives the combustion process and remains as quartz in the coal ash. Other minerals decompose, depending on the temperature, and form new minerals. The clay minerals lose water and may melt, forming aluminosilicate crystalline and non-crystalline (glassy) materials. The most reactive glassy phases present in low calcium coal fly ashes are formed from the melting of clays present in the coal [36].

The distinction between crystalline and amorphous materials is important when considering dissolution behaviour in an alkaline solution, as it happens during the geopolymerization process. In fact, the crystalline phases (such as quartz and mullite) are considered unreactive, because the rate of their reaction in alkali-silicate solutions is extremely slow when compared to the amorphous phase. X-ray diffraction analysis (XRD) of fly ash allows to identify the major crystalline constituents of fly ash and the X-ray amorphous phases and to give a quantitative estimation of these [36, 45]. Other key factors

influencing the potential reactivity of fly ashes are: reactive silica content, vitreous phase content and particle size distribution [35].

Fly ash particles can be divided into different classes depending on their composition. Mehta [59, 60] classified fly ash into two categories based on calcium content: 1) fly ash resulting from combustion of anthracite and bituminous coal with CaO less than 5%; 2) fly ash resulting from combustion of lignite and sub-bituminous coal with CaO up to 15-35%.

Currently the system defined by the American Standard ASTM C 618 [61] is the most commonly used classification system for fly ash. It distinguishes two classes of fly ash, on the basis of the sum of the total Si, Al and Fe ( $\text{SiO}_2 + \text{Al}_2\text{O}_3 + \text{Fe}_2\text{O}_3$ ):

1. Class C, known as high calcium fly ash, since  $50\% \leq (\text{SiO}_2 + \text{Al}_2\text{O}_3 + \text{Fe}_2\text{O}_3) \leq 70\%$ ;
2. Class F, known as low calcium fly ash, since  $(\text{SiO}_2 + \text{Al}_2\text{O}_3 + \text{Fe}_2\text{O}_3) \geq 70\%$ .

In UK all fly ash is low calcium fly ash (class F).

BS EN 450 [58] is a harmonised European Standard for fly ash that replaced the former British Standard BS 3892: Part 1 in January 2007. Three categories of fly ash are permitted under BS EN 450. They are classified in dependence of Loss On Ignition (LOI) values <sup>5</sup>[58]:

- Category A: LOI not more than 5.0%;
- Category B: LOI 2.0% to 7.0%;
- Category C: LOI 4.0 to 9.0%;

Category C fly ash is not permitted in UK concrete, as the LOI upper limit under BS 8500 is 7.0% [62].

According to [58], there are two categories for fly ash fineness:

- Category N: not more than 40% retained on a 45 micron sieve and a limit of + 10% on the supplier's declared mean value is permitted.

---

<sup>5</sup> Loss on Ignition value is the mass obtained by a test which consists of strongly heating ("igniting") a sample of the material at a specified temperature, allowing volatile substances to escape, until its mass ceases to change. The LOI value is found by weighting the sample before and after the heating of the sample.

- Category S: not more than 12% retained on a 45 micron sieve.

The fly ash used in this work is low calcium fly ash, belongs to category B for LOI, and to category S for finesses.

All this information defines the characteristics and the formation process of the final geopolymer binder obtained from fly ash, which are described in the following section.

### 3.2.3.2. Fly ash geopolymers structural analysis

The review carried out by Provis et al. provides an overview on the existing results on the structure of geopolymer binders [35, 38]: the application of techniques such as X-ray Diffraction (XRD) analysis, Fourier-transform infrared (FTIR) spectroscopy, Nuclear Magnetic resonance (NMR), Scanning Electron Microscopes (SEM), and Optical Microscopy on geopolymers has provided valuable nanoscale information on geopolymer structure. Rheological and calorimetric analysis have brought additional insight [36].

The alkali activation of fly ash gives rise to the formation of crystalline phases identified as herschelite (Na-chabazite) and hydroxysodalite-type zeolites in fly ash geopolymer binders [63]. The transition of these materials from apparently amorphous to well-defined zeolitic structure has been observed by using NMR, FTIR spectroscopy, SEM and other techniques. It has been observed that the synthesis temperature and the aging are critical in determining the structure of the reaction products: even mild increases in synthesis temperature result in a readily observable increase in long-range ordering in geopolymers binders, by analysing XRD diffractograms of geopolymers [48]. The work of Palomo et al. (2004) [64] has demonstrated that time and temperature highly affect the mechanical development of geopolymer materials: as temperature increases, the mechanical strength development increases also [65]. This is important to take in mind in this work where, for the reasons highlighted in section 2.5, the geopolymer binder is cured at ambient temperature.

A recent study [45] used XRD analysis, FTIR spectroscopy and SEM to investigate the result of transformation of fly ash into geopolymer and the geopolymer structure. This study has revealed the existence of the major crystalline phases of fly ash and the fly ash phase transformations, as well as a new amorphous phase formation in the geopolymeric matrice, and undissolved fly ash particles in the final geopolymer. It has provided information on

micro and nano-structure of geopolymers as well. The results obtained can be synthesised in the following points [43, 45, 66, 67]:

- there is evidence of the dissolution of the amorphous phase of fly ash and the formation of a new amorphous aluminosilicate gel phase, observable from the shift toward higher values ( $2\theta=25^\circ-35^\circ$ ) in the XRD spectrum of geopolymer of the broad hump registered between  $2\theta=20^\circ$  and  $30^\circ$  in the fly ash XRD spectrum.
- the formation of new zeolites phases in the geopolymer ( $2\theta=5^\circ-15^\circ$ ).
- There is evidence of micro and nano-porosity, developed during the polycondensation stage and during the curing process.
- The undissolved solid particles of fly ash are very bonded within the amorphous geopolymeric framework, and the interface of insoluble fly ash particle with the amorphous geopolymeric framework is the most sensitive area of the geopolymer during the mechanical strength test.

All this information is important for the properties of the geopolymers to be used as repairs and sensors. The presence of crystalline zeolites phases and unreacted minerals, such as quartz and mullite, inside geopolymer binder will result in a higher mechanical strength, since these crystalline phases themselves show a Young Modulus of the order of GPa [68]. However, since the geopolymer binder manufactured in this work is cured at ambient temperature, it won't show high mechanical strength that it can be used as a structural repair, but this doesn't constitute a drawback for the technology, since it is conceived to play a non-structural role of protection and sensing of moisture and chloride content. On the other hand, porosity in geopolymers are known to cause a decrease in the mechanical strength [69]. Moreover, for the particular sensing application of this work of thesis, the presence of porosity in the material can affect its electrical properties: electrical conductivity increases in pores filled with pore solution (wet/saturated condition) or decreases in empty or partially empty pores (dry cases).

The main information provided in this section can be linked to two particular applications, which are of interest for this work of thesis:

1. geopolymers as protecting and repair coatings for concretes;
2. geopolymers as sensors for structural health monitoring.

A detailed overview and state of the art of the applications of geopolymer materials, with a particular focus on the first application above is presented in the following section, while the state on the art of geopolymer sensing applications is presented in chapter 5.

### 3.3. Geopolymer applications: state of the art

Geopolymer materials were originally developed as a fire-resistant alternative to organic thermosetting polymers following a series of fires in Europe in the 70s [70, 71], but the primary application for geopolymer binders has since shifted to uses in construction. Geopolymer technology has been regarded to be employed in concrete manufacturing, since the geopolymers' binders and concretes present a number of important advantages compared with the conventional cementitious materials and concretes, such as OPC concretes [72]. Advantages include abundant raw materials resources; energy saving and environment protection (since little CO<sub>2</sub> is emitted and less energy consumed in geopolymer production compared with OPC); simple preparation technique; good volume stability, since geopolymers have lower shrinkage than Portland cement; reasonable strength gain in a short time; excellent durability; high fire resistance and low thermal conductivity.

Another important field of application of geopolymer technology is the nuclear and radwaste management field and industry in particular. In fact, because of the great amount of remarkable properties, such as radiation resistance [16, 17], geopolymers are regarded as useful for immobilisation of low-level and intermediate-level nuclear waste [36]. They are also applied for the containment and immobilization of toxic and hazardous wastes, for advanced structural tooling and refractory ceramics, and as fire resistant composites used in buildings, aeroplanes, shipbuilding and racing cars [73].

Only recently some researchers have looked at geopolymer binders as 'smart cements' for structural health monitoring applications [2, 29-31, 33, 34]. Some of them take advantage of the 'electrolytic nature' of geopolymers. A detailed description of the electrical properties of the geopolymer material and the theory behind it will be presented in detail in chapter 5, together with a review on the use of geopolymers for structural health monitoring.

Another application connected to structural health is the use of geopolymers as reinforced concrete repair [23-28] and protective coatings [18-22].

The technology developed, tested and characterised in this work of thesis belongs to the last two application categories (sensing and repair/protection for concrete): it can be applied as skin-sensor onto concrete. Previous applications of geopolymer coatings as repair for concretes, reviewed in section 3.3.1 below, demonstrate that the system developed in this work can play also a maintenance, protective and repair role for concrete.

### 3.3.1. Geopolymers for concrete maintenance, repair and protection

Several authors have studied geopolymers as maintenance materials, repairing and protective coatings materials for marine concrete and transportation infrastructures. This is possible because of their high strength, corrosion resistance, water resistance, high temperature resistance. Besides, geopolymer properties, such as modulus of elasticity, Poisson's ratio and tensile strength, are similar to those of OPC concrete, thus making them compatible with OPC concrete [14, 27]. However, geopolymers' brittle nature limits their extensive applications [14], and research has focused on increasing their mechanical performance, and the bond strength between geopolymers and the concrete substrate [27].

Balaguru et al. [25] used geopolymer materials to bond carbon fabrics to reinforced concrete, for the strengthening of reinforced concrete structures. They demonstrated that geopolymers show a better performance in terms of adhesion than organic polymers originally used to bond the carbon fabrics to concrete. Huseien et al. [27] have made a comprehensive review on geopolymer mortars as repair materials for concrete compared with OPC and other commercial repair materials: the main advantages of geopolymer mortars are reported to be the relation between carbon dioxide footprint (less CO<sub>2</sub> emissions than OPC and other materials) and cost (7 times cheaper than the current repair methods), high durability, high early mechanical properties, frost resistance, resistance to both acid and salt environments, stiff workability behaviour (arising from the use of viscous compounds such as sodium silicate and sodium hydroxide). Phoo-ngernkham et al. [28] used high calcium fly ash geopolymer mortars containing OPC for use as an alternative materials for Portland cement concrete repair: they demonstrated sufficiently high shear bond and bending strengths compared with commercial repair binders. Hu et al. [26] demonstrated that geopolymer materials have better repair characteristics than cement-

based repair materials, and that the addition of steel slag improved significantly the abrasion resistance of the repair.

All these works make use of geopolymer binders (often as mortars or with fillers to increase their mechanical properties) for a structural function. On the other hand, other authors focused on the utilization of geopolymer materials as protective coatings and non-structural repairs for exposed concrete structures and infrastructures: surface deterioration of exposed concrete structures in most cases leads to structural problems because of the loss of cover and ensuing reinforcement corrosion, especially for concrete exposed in rigorous marine environment which is readily damaged by the erosive ocean-atmosphere and seawater. The coating material itself should be durable, should bond well to the parent surface, and be compatible with parent surface in terms of expansion/contraction during temperature changes.

Balaguru et al. [18] demonstrated that geopolymers are compatible with various concrete surfaces, steel, and wood and constitute an excellent promise for the application as protective and graffiti-resistant coatings on transportation infrastructures, providing durable coating, under wet-dry and freeze-thaw conditions. The geopolymer binders used consisted of alkaline solution, silicafume, carbon and organic fibers and water repellent agent. Zhang et al. [20-22] investigated the possibility of using geopolymers as inorganic coatings for marine concrete protection. They did a laboratory study, by evaluating setting time, permeability, anticorrosion, bond strength, volume stability, and pore structure of geopolymers. They used a metakaolin (MK) geopolymer with the addition of granulated blast furnace slag (GBFS), ordinary Portland cement (OPC), standard sand and polypropylene (PP) fibers. Geopolymers were chemically stable in sea water and in air, they made it difficult for sea water to penetrate and provided a sustainable protection for marine concrete structures.

All the reviewed works used fillers and additives to the geopolymer binders, and demonstrated excellent properties for the use of geopolymer binders as coating repair/protective coatings onto concretes for different scopes.

### 3.4. Summary

This chapter provided a general overview on the properties, advantages, theoretical background and applications of geopolymer materials, with a particular focus on fly ash geopolymers, used in this thesis. The key factors, useful in the experimental development and fully understanding of the geopolymer system proposed in this thesis, have been highlighted in this chapter. They can be summarised in the following points:

- the physical and structural properties of geopolymers are closely connected with their chemical composition and with the stages of the geopolymerisation process;
- the type and composition of the alkaline solution is very important for the structure of geopolymer binders;
- the presence of soluble silica in the activating solution plays an important role in the microstructure development;
- the increase of Si and Al concentrations in the aqueous phase enhances the hardening of the geopolymer system;
- sodium hydroxide possesses a greater capacity to liberate silicate and aluminate monomers than potassium silicate, is the cheapest and the most widely available among the alkali hydroxides;
- the increase of sodium hydroxide molarity promotes the early stages of the geopolymerization process;
- fly ash geopolymers, compared with metakaolin and blast furnace slag, show higher workability, durability and strength, and low cost;
- there are no simple numerical methods for geopolymer mix design, particularly for fly ashes (since fly ash composition can vary significantly between coal plant sources);
- crystalline and amorphous components of fly ash show a different dissolution behaviour in an alkaline solution: the reactions of amorphous phases are much faster than the case of crystalline phases (considered unreactive);

- key factors influencing the potential reactivity of fly ashes are: reactive silica content, vitreous phase content and particle size distribution;
- UK fly ash is only low calcium fly ash;
- the presence of crystalline phases and unreacted minerals inside a geopolymer binder may result in a higher mechanical strength;
- the synthesis temperature and the aging are critical in determining the structure of the reaction products;
- porosity in geopolymers causes a decrease in the mechanical strength and affects their electrical properties (depending on dry/wet/saturated conditions).

On the basis of this information, a process of trial and error was carried out to find the suitable geopolymer mix for this work, and an alkaline solution made of sodium hydroxide and sodium silicate was used, as shown in detail in chapter 4.

A review of the main applications of geopolymer materials demonstrated that the advantageous properties of geopolymers, such as high chemical and thermal stability, adhesive behaviour, high electrical conductivity, and affordability, made their use widespread in several different fields (military, nuclear, infrastructure rehabilitation, sensing, etc...). In particular, previous works demonstrated that geopolymer coatings with fillers and additives can play a maintenance, protective and repair role for concrete.

This work of thesis aims to develop a technology which is conceived to be applied to concrete containments of nuclear stores, air inlets and ducts in nuclear context. The introduction of heat sources to cure the geopolymer coatings in such a nuclear context is not allowed, and the presence of additives, such as plastic fibers, can compromise the operability of the technology in case of exposition to radioactive radiations. For all these reasons, the geopolymer binder used in this work is ambient cured and no additives are used, thus minimising the complexity of the manufacture process and the cost of production at the same time. This was challenging, a process of trial and error, and a laboratory testing study to face several issues were necessary. The next chapter demonstrates the ambient curing of fly ash geopolymers for use as protective coatings and non-structural repairs for concrete, with focus on challenges and achievements of the investigation.

## References

- [1] J. L. Provis, "Alkali-activated materials," *Cement and Concrete Research*, vol. 114, pp. 40-48, 2018.
- [2] J. He, G. Zhang, S. Hou, and C. Cai, "Geopolymer-based smart adhesives for infrastructure health monitoring: concept and feasibility," *Journal of Materials in Civil Engineering*, vol. 23, pp. 100-109, 2011.
- [3] M. P.G., R. C.A., and K. T., "Potential for Use of Alkali-Activated Silico-Aluminate Binders in Military Applications," Vicksburg, Mississippi WES/MP/GL-85-15,, 1986.
- [4] T. Glasby, J. Day, R. Genrich, and J. Aldred, "EFC geopolymer concrete aircraft pavements at Brisbane West Wellcamp Airport," *Concrete*, vol. 2015, pp. 1-9, 2015.
- [5] R. E. Lyon, P. Balaguru, A. Foden, U. Sorathia, J. Davidovits, and M. Davidovics, "Fire-resistant aluminosilicate composites," *Fire and materials*, vol. 21, pp. 67-73, 1997.
- [6] J. Giancaspro, P. Balaguru, and R. E. Lyon, "Use of inorganic polymer to improve the fire response of balsa sandwich structures," *Journal of materials in civil engineering*, vol. 18, pp. 390-397, 2006.
- [7] R. E. Lyon, "Fire Response of Geopolymer Structural Composites," FEDERAL AVIATION ADMINISTRATION WASHINGTON DC OFFICE OF AVIATION RESEARCH1996.
- [8] A. Buchwald, M. Hohmann, C. Kaps, H. Bettzieche, and J.-T. Kuhnert, "Stabilised foam clay material with high performance thermal insulation properties," in *Ceramic forum international*, 2004, pp. E39-E42.
- [9] V. Vaou and D. Panias, "Thermal insulating foamy geopolymers from perlite," *Minerals Engineering*, vol. 23, pp. 1146-1151, 2010.
- [10] M. M. Salahuddin, M. Norkhairunnisa, and F. Mustapha, "A review on thermophysical evaluation of alkali-activated geopolymers," *Ceramics International*, vol. 41, pp. 4273-4281, 2015.
- [11] W. M. Kriven, "Geopolymer porous nanoceramics for structural, for smart and thermal shock resistant applications," ILLINOIS UNIV AT URBANA DEPT OF MATERIALS SCIENCE AND ENGINEERING2011.
- [12] V. F. Barbosa and K. J. MacKenzie, "Synthesis and thermal behaviour of potassium sialate geopolymers," *Materials Letters*, vol. 57, pp. 1477-1482, 2003.
- [13] T.-W. Cheng and J. Chiu, "Fire-resistant geopolymer produced by granulated blast furnace slag," *Minerals engineering*, vol. 16, pp. 205-210, 2003.
- [14] S. Zhang, K. Gong, and J. Lu, "Novel modification method for inorganic geopolymer by using water soluble organic polymers," *Materials letters*, vol. 58, pp. 1292-1296, 2004.
- [15] Z. Li, Y. Zhang, and X. Zhou, "Short fiber reinforced geopolymer composites manufactured by extrusion," *Journal of materials in civil engineering*, vol. 17, pp. 624-631, 2005.
- [16] L. Leay, A. Potts, and T. Donoclift, "Geopolymers from fly ash and their gamma irradiation," *Materials Letters*, vol. 227, pp. 240-242, 2018.
- [17] C. Shi and A. Fernández-Jiménez, "Stabilization/solidification of hazardous and radioactive wastes with alkali-activated cements," *Journal of hazardous materials*, vol. 137, pp. 1656-1663, 2006.
- [18] P. Balaguru, "Geopolymer for protective coating of transportation infrastructures," 1998.

- [19] A. M. Aguirre-Guerrero, R. A. Robayo-Salazar, and R. M. de Gutiérrez, "A novel geopolymer application: Coatings to protect reinforced concrete against corrosion," *Applied Clay Science*, vol. 135, pp. 437-446, 2017.
- [20] Z. Zhang, X. Yao, and H. Zhu, "Potential application of geopolymers as protection coatings for marine concrete I. Basic properties," *Applied Clay Science*, vol. 49, pp. 1-6, 2010.
- [21] Z. Zhang, X. Yao, and H. Zhu, "Potential application of geopolymers as protection coatings for marine concrete: II. Microstructure and anticorrosion mechanism," *Applied clay science*, vol. 49, pp. 7-12, 2010.
- [22] Z. Zhang, X. Yao, and H. Wang, "Potential application of geopolymers as protection coatings for marine concrete III. Field experiment," *Applied Clay Science*, vol. 67, pp. 57-60, 2012.
- [23] C. Montes and E. Allouche, "Evaluation of the potential of geopolymer mortar in the rehabilitation of buried infrastructure," *Structure and Infrastructure Engineering*, vol. 8, pp. 89-98, 2012.
- [24] F. Pacheco-Torgal, Z. Abdollahnejad, S. Miraldo, S. Baklouti, and Y. Ding, "An overview on the potential of geopolymers for concrete infrastructure rehabilitation," *Construction and Building Materials*, vol. 36, pp. 1053-1058, 2012.
- [25] P. Balaguru, S. Kurtz, and J. Rudolph, "Geopolymer for repair and rehabilitation of reinforced concrete beams," *St Quentin, France, Geopolymer Institute*, vol. 5, 1997.
- [26] S. Hu, H. Wang, G. Zhang, and Q. Ding, "Bonding and abrasion resistance of geopolymeric repair material made with steel slag," *Cement and concrete composites*, vol. 30, pp. 239-244, 2008.
- [27] G. F. Huseien, J. Mirza, M. Ismail, S. Ghoshal, and A. A. Hussein, "Geopolymer mortars as sustainable repair material: A comprehensive review," *Renewable and Sustainable Energy Reviews*, vol. 80, pp. 54-74, 2017.
- [28] T. Phoo-ngernkham, V. Sata, S. Hanjitsuwan, C. Ridditirud, S. Hatanaka, and P. Chindaprasirt, "High calcium fly ash geopolymer mortar containing Portland cement for use as repair material," *Construction and building materials*, vol. 98, pp. 482-488, 2015.
- [29] M. Perry, M. Saafi, G. Fusiek, and P. Niewczas, "Hybrid optical-fibre/geopolymer sensors for structural health monitoring of concrete structures," *Smart Materials and Structures*, vol. 24, p. 045011, 2015.
- [30] M. S. Muntini and H. Ahmadi, "Performance of metakaolin geopolymer ceramic for fiber optic temperature sensor," *Materials Today: Proceedings*, vol. 5, pp. 15137-15142, 2018.
- [31] M. Perry, M. Saafi, G. Fusiek, and P. Niewczas, "Geopolymeric thermal conductivity sensors for surface-mounting onto concrete structures," 2016.
- [32] M. Saafi, L. Tang, J. Fung, M. Rahman, F. Sillars, J. Liggat, and X. Zhou, "Graphene/fly ash geopolymeric composites as self-sensing structural materials," *Smart materials and structures*, vol. 23, p. 065006, 2014.
- [33] M. Saafi, G. Piukovics, and J. Ye, "Hybrid graphene/geopolymeric cement as a superionic conductor for structural health monitoring applications," *Smart Materials and Structures*, vol. 25, p. 105018, 2016.
- [34] M. Saafi, A. Gullane, B. Huang, H. Sadeghi, J. Ye, and F. Sadeghi, "Inherently multifunctional geopolymeric cementitious composite as electrical energy storage and self-sensing structural material," *Composite Structures*, vol. 201, pp. 766-778, 2018.
- [35] A. F.-J. P. Duxon, J. L. Provis, G. C. Luckey, A. Palomo, J. S. J. Van Deventer, "Geopolymer technology: the current state of the art," vol. 42:2917-2933, 2007.
- [36] J. P. a. J. V. Deventer, "Geopolymers, structure, processing, properties and industrial applications," 2009.

- [37] J. L. Provis and J. S. J. Van Deventer, *Geopolymers: structures, processing, properties and industrial applications*: Elsevier, 2009.
- [38] J. L. Provis, Lukey, G. C. and Van Deventer, "Do geopolymers actually contain nanocrystalline zeolites? – A reexamination of existing results.," 2005.
- [39] J. Davidovits, "The need to create a new technical language for the transfer of basic scientific information," *Transfer and Exploitation of Scientific and Technical Information, EUR*, vol. 7716, pp. 316-320, 1982.
- [40] J. Davidovits, "Geopolymers: inorganic polymeric new materials," *Journal of Thermal Analysis and calorimetry*, vol. 37, pp. 1633-1656, 1991.
- [41] J. Davidovits, *Geopolymer chemistry and applications*: Geopolymer Institute, 2008.
- [42] L. K. Turner and F. G. Collins, "Carbon dioxide equivalent (CO<sub>2</sub>-e) emissions: A comparison between geopolymer and OPC cement concrete," *Construction and Building Materials*, vol. 43, pp. 125-130, 2013.
- [43] A. P. A. Fernández-Jiménez, M. Criado, "Microstructure development of alkali-activated fly ash cement: a descriptive model " 2005.
- [44] J. Xie and O. Kayali, "Effect of initial water content and curing moisture conditions on the development of fly ash-based geopolymers in heat and ambient temperature," *Construction and building materials*, vol. 67, pp. 20-28, 2014.
- [45] I. P. G. D. Parias, T. Perraki, "Effect of synthesis parameters on the mechanical properties of fly ash-based geopolymers," vol. 301 (2007) 246-254, 2007.
- [46] A. Fernández-Jiménez, A. Palomo, and M. Criado, "Microstructure development of alkali-activated fly ash cement: a descriptive model," *Cement and concrete research*, vol. 35, pp. 1204-1209, 2005.
- [47] T. W. Swaddle, J. Salerno, and P. A. Tregloan, "Aqueous aluminates, silicates, and aluminosilicates," *Chemical Society Reviews*, vol. 23, pp. 319-325, 1994.
- [48] T. W. Swaddle, "Silicate complexes of aluminum (III) in aqueous systems," *Coordination Chemistry Reviews*, vol. 219, pp. 665-686, 2001.
- [49] R. Aiello, F. Crea, A. Nastro, B. Subotić, and F. Testa, "Influence of cations on the physicochemical and structural properties of aluminosilicate gel precursors. Part 1. Chemical and thermal properties," *Zeolites*, vol. 11, pp. 767-775, 1991.
- [50] Z. Zhang, J. L. Provis, A. Reid, and H. Wang, "Fly ash-based geopolymers: the relationship between composition, pore structure and efflorescence," *Cement and concrete research*, vol. 64, pp. 30-41, 2014.
- [51] P. Duxson, A. Fernández-Jiménez, J. L. Provis, G. C. Lukey, A. Palomo, and J. S. van Deventer, "Geopolymer technology: the current state of the art," *Journal of materials science*, vol. 42, pp. 2917-2933, 2007.
- [52] S. Hanjitsuwan, S. Hunpratub, P. Thongbai, S. Maensiri, V. Sata, and P. Chindapasirt, "Effects of NaOH concentrations on physical and electrical properties of high calcium fly ash geopolymer paste," *Cement and Concrete Composites*, vol. 45, pp. 9-14, 2014.
- [53] E. Diaz, E. Allouche, and S. Eklund, "Factors affecting the suitability of fly ash as source material for geopolymers," *Fuel*, vol. 89, pp. 992-996, 2010.
- [54] S. Y. Oderji, B. Chen, and S. T. A. Jaffar, "Effects of relative humidity on the properties of fly ash-based geopolymers," *Construction and Building Materials*, vol. 153, pp. 268-273, 2017.

- [55] I. Diaz-Loya, M. Juenger, S. Seraj, and R. Minkara, "Extending supplementary cementitious material resources: Reclaimed and remediated fly ash and natural pozzolans," *Cement and Concrete Composites*, 2017.
- [56] A. M. Rashad, "A comprehensive overview about the influence of different admixtures and additives on the properties of alkali-activated fly ash," *Materials & Design*, vol. 53, pp. 1005-1025, 2014.
- [57] R. A. Carroll, "Coal combustion products in the United Kingdom and the potential of stockpile ash," in *Proceedings of the World of Coal Ash Conference, Nashville, TN, USA, 2015*, pp. 4-7.
- [58] B. EN, "450-1, Fly Ash for Concrete—Definition, Specifications and Conformity Criteria," *British Standards Institution*, 2012.
- [59] P. Mehta, "Effect of fly ash composition on sulfate resistance of cement," in *Journal Proceedings*, 1986, pp. 994-1000.
- [60] P. Mehta, "Standard Specifications for Mineral Admixtures--An Overview," *Special Publication*, vol. 91, pp. 637-658, 1986.
- [61] C. ASTM, "Standard specification for coal fly ash and raw or calcined natural pozzolan for use in concrete," ed, 2012.
- [62] BSI, "BS 8500-2: Concrete—complementary British standard to BS EN 206-1," *Part 2: Specification for constituent materials and concrete*, 2002.
- [63] A. Fernández-Jimenez, A. De La Torre, A. Palomo, G. López-Olmo, M. Alonso, and M. Aranda, "Quantitative determination of phases in the alkali activation of fly ash. Part I. Potential ash reactivity," *Fuel*, vol. 85, pp. 625-634, 2006.
- [64] A. Palomo, S. Alonso, A. Fernández-Jiménez, I. Sobrados, and J. Sanz, "Alkaline Activation of Fly Ashes: NMR Study of the Reaction Products," *J. Am. Ceram. Soc.*, 87 1141-1145, 2004.
- [65] L. Struble, E. Kim, and L. Gómez-Zamorano, "Overview of Geopolymer Cement," in *Geopolymer Binder Systems*, ed: ASTM International, 2013.
- [66] A. Fernández-Jiménez and A. Palomo, "Composition and microstructure of alkali activated fly ash binder: Effect of the activator," *Cement and concrete research*, vol. 35, pp. 1984-1992, 2005.
- [67] T. Bakharev, "Geopolymeric materials prepared using Class F fly ash and elevated temperature curing," *Cement and concrete research*, vol. 35, pp. 1224-1232, 2005.
- [68] F.-X. Coudert, "Systematic investigation of the mechanical properties of pure silica zeolites: stiffness, anisotropy, and negative linear compressibility," *Physical Chemistry Chemical Physics*, vol. 15, pp. 16012-16018, 2013.
- [69] Z. Kubba, G. F. Huseien, A. R. M. Sam, K. W. Shah, M. A. Asaad, M. Ismail, M. M. Tahir, and J. Mirza, "Impact of curing temperatures and alkaline activators on compressive strength and porosity of ternary blended geopolymer mortars," *Case Studies in Construction Materials*, vol. 9, p. e00205, 2018.
- [70] J. Davidovits, "years of successes and failures in geopolymer applications. Market trends and potential breakthroughs," in *Geopolymer 2002 Conference*, 2002, p. 29.
- [71] H. Cheng Yong, Y. M. Liew, M. M. Al Bakri Abdullah, and K. Hussin, "Fire resistant properties of geopolymers: A review," in *Key Engineering Materials*, 2015, pp. 39-43.
- [72] Z. Li, Z. Ding, and Y. Zhang, "Development of sustainable cementitious materials," in *Proceedings of international workshop on sustainable development and concrete technology, Beijing, China, 2004*, pp. 55-76.

- [73] K. Komnitsas and D. Zaharaki, "Geopolymerisation: A review and prospects for the minerals industry," *Minerals engineering*, vol. 20, pp. 1261-1277, 2007.

# 4. AMBIENT CURED FLY ASH GEOPOLYMERS AS COATINGS AND REPAIRS FOR CONCRETE

## 4.1. Introduction

Coating technologies are an effective means of protecting concrete structures from chemical attack and rebar corrosion. Inorganic coatings in particular have been widely applied as anticorrosive and decorative materials for concrete and steel structures [1-4]. These materials show a high long-term durability even under acid and alkali attack and at elevated temperatures [5].

Emerging solutions for concrete protection are based on alkali-activated materials, which show rapid setting and hardening, excellent bond strength and durability, low chloride permeability, and high freeze-thaw and chloride resistances [5-20]. Geopolymers are physically compatible with concrete substrates in most regards [21]. However, there are technical issues that are particular to geopolymer coatings on concrete substrates, particularly those cured at ambient temperatures.

Regardless of the application, a good coating for concrete should be free of cracks and defects. In the work presented in this chapter, the aim was to develop high-quality, ambient-temperature-cured fly ash geopolymer coatings, and assess their potential as non-structural repair materials for concrete. The goal was to achieve this with minimal additional

processing steps (such as fly ash grinding or the use of additives), so as to minimize manufacturing costs and complexity.

As already mentioned in previous chapters, the minimization of costs and complexity is not the only reason for the ambient curing of geopolymers and for the absence of additives, despite to the issues this introduces to the process. The main reasons are connected with the nuclear context: ambient curing avoids the introduction of heat sources to thermally cure geopolymers in radioactive environments, and additives are avoided since they can be damaged by gamma ( $\gamma$ ) irradiation (e.g. plastic fibers) and some of them can produce further  $\gamma$  radiation when irradiated. The ambient curing of geopolymers is challenging since they are typically cured at elevated temperatures to accelerate geopolymerisation, as rapid curing allows coatings to achieve a higher early-age strength [12, 22-25], but this can make geopolymers inconvenient to apply in the field, particularly in cooler climates.

For these reasons, some researchers have already been looking into ambient temperature curing of geopolymers [14, 22, 23, 26-28]. Somna [22], Temuujin [14] and others [29-31] ground fly ash particles to improve their reactivity and promote room-temperature curing. Some researchers have studied the effects of calcium rich additives, such as slag, on curing in ambient conditions [27, 32-37], while others have studied the effects of moisture [23].

These previous works have studied the ambient temperature curing of fly ash geopolymers cast in moulds. Their aim is to deliver geopolymers that serve a structural function. As such, they demonstrate high compressive strength and enhanced hardening, but at the expense of reduced workability and increased drying shrinkage [14]. The work presented in this thesis is distinct, as it outlines the development of fly ash geopolymer coatings, thus high workability and low shrinkage are key requirements, in addition to the performance requirements for non-structural repairs stated in the standard BS EN 1504-3:2005 [38].

The primary objective of this work is to investigate the development of a non-structural ambient-cured repair material that can be later developed for use as a sensor (chapter 5, 6 and 7), as in [39-43]. To achieve this, several experimental tests were conducted in order to: (i) obtain geopolymer coatings of high integrity; and (ii) test some of the mechanical properties of the material.

The notable contributions of this chapter are five-fold: i) we present an affordable process for ambient-temperature geopolymer synthesis that does not require additives or grinding; ii) we outline the influence of prolonged mixing times on coating quality (previous studies

use short mixing times under 10 minutes [22-25]); iii) we study the influence of concrete substrate age on geopolymer coating quality (previous work has studied coatings on mature concretes only [8, 44]), iv) we assess some of the mechanical properties of the geopolymer binder, in order to evaluate its potentiality as repair material, and v) perhaps most importantly, this chapter provides a frank discussion of the challenges faced during geopolymer development. In delivering these research contributions, the work makes the field application of geopolymer coatings in a nuclear storage context (and indeed many other contexts) much more viable.

The chapter begins with theory and state of the art on the factors affecting geopolymer coating integrity when placed onto concrete, and an outline of repair materials' properties, classification and requirements, in section 4.2. Section 4.3 describes the materials and methods used for geopolymer manufacture, the testing methods and the analysis conducted. Section 4.4 focuses on the results and discussion of the experiments and tests conducted to assess coating integrity of the specific geopolymer binders manufactured in this work, and their performance as repairs. Section 4.5 contains a further detailed discussion on the results. Finally a chapter summary and future work are presented in section 4.6.

## 4.2. Theory and state of the art

This section presents a paragraph on the main factors affecting the integrity of geopolymer coatings when they are placed onto concrete substrates (section 4.2.1), and a paragraph on the requirements and classification of repair materials (section 4.2.2).

### 4.2.1. Factors affecting geopolymer coatings on concrete substrates

One issue facing the development and practical application of geopolymers as coatings is that their integrity may significantly change when they are taken out of lab conditions and applied to concrete substrates in the field. Some common issues faced include cracking due to shrinkage, changes to setting times, and efflorescence [8, 45, 46]. These issues are particularly acute when geopolymers are used in field conditions which are at the extremes of humidity or moisture scales, such as those present in nuclear storage facilities. Note that the issues outlined in the following subsections are common across most geopolymer systems, not just those made with fly ash precursors.

#### 4.2.1.1. Shrinkage and curing

For geopolymer coatings cured on concrete at ambient temperatures, shrinkage is the most significant issue [47]. Shrinkage is defined as a reduction in the volume of the geopolymer because of a loss of water: this is predominantly due to drying, but it can also occur when water is used up during geopolymerisation [48].

Drying shrinkage is the result of a loss of water from the geopolymer's capillary pores. This loss of moisture causes the tension in the capillary pores to increase, resulting in a volume reduction in the specimen. When geopolymer coatings cure, they undergo this shrinkage while simultaneously binding to the underlying concrete substrate. The resulting confinement allows shrinkage strains to cause tensile and shear stresses. If significant shrinkage occurs before the coating has adequately cured, these stresses will exceed the strength of the geopolymer [49], leading to cracks and debonding that undermine coating integrity.

For geopolymer coatings, there are at least two major contributors to drying shrinkage, illustrated in Figure 4.1. The first, affecting all geopolymers regardless of substrate, is that a low environmental humidity encourages water loss through evaporation. Indeed, it is well known that drying shrinkage can be reduced by curing geopolymers in hermetically sealed conditions [49, 50]. The second mechanism for water loss, however, is the diffusion of water from the moist geopolymer layer into the drier, porous, concrete substrate. Control of the moisture content of the substrate is thus essential to control cracking [51].

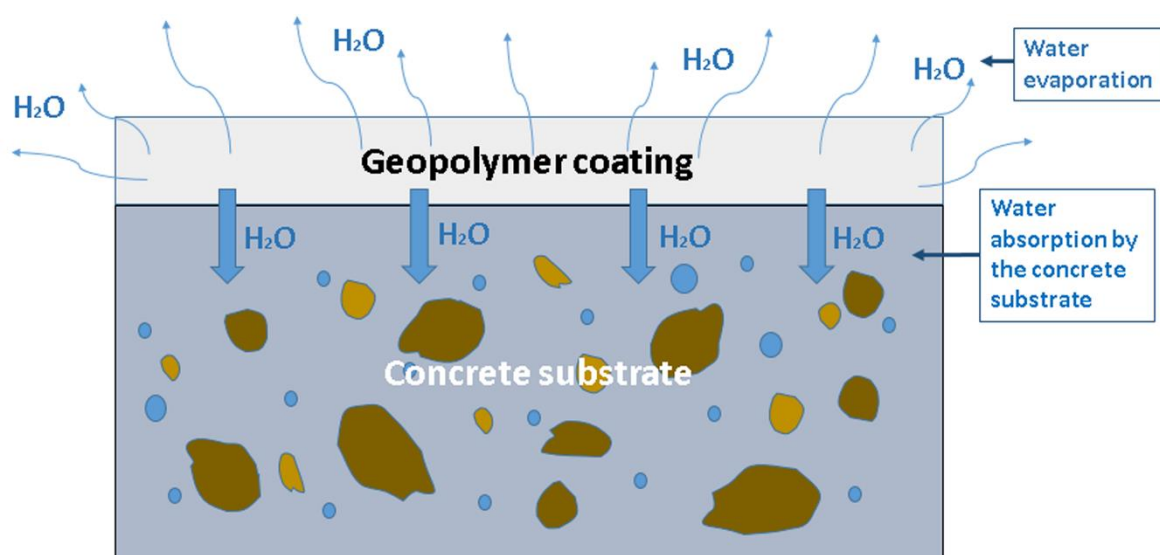


Figure 4.1 – Illustration of the main water loss mechanisms from geopolymer coatings on concrete substrates.

As both drying mechanisms are a surface-area dependent processes, the edges of geopolymer patches are particularly prone to cracking, as these edges can present an extra surface for evaporation.

One clear way of tackling this issue is to accelerate the curing rate of the geopolymer coating (and this is why elevated temperatures are often used). Grinding fly ash particles to improve their reactivity and allow room temperature curing, as in [22], may appear to be another solution, but this can in some cases lead to a higher shrinkage, due to the particle size being so fine that agglomerates form during mixing, resulting in a lower reaction rate which increases shrinkage [52]. It is worth noting that plastic fibers can reduce shrinking and cracking, especially for sealed curing conditions [50], but they are avoided in this work for reasons connected to the nuclear context. Plastics tend to swell, degrade and leach hydrogen under radiation, therefore their absence in geopolymer binders will improve radiation resistance, in addition to a reduction of the costs.

#### 4.2.1.2. Adhesion, workability and setting time

One of the most common ways to apply cementitious coatings to concrete in the field is by pumping and spray coating. There are also lab studies that demonstrate (as is shown in this work) the application of geopolymer coatings with a trowel [7], and even some that are coating using manufacturing methods such as 3D printing [41]. Regardless of the method used, one must consider the interplay between a geopolymer's adhesion to concrete, its workability and its setting time (and by extension, its behaviour during curing and shrinkage). Geopolymers are highly tuneable materials, but the majority of mixes will display:

- High surface tension: This plays a key role in the ability of the materials to bind and stay bound to substrates. A reduction in surface tension may, in some cases, be required to ensure good adhesion [53]. With respect to geopolymer microstructure formation, the water to solid ratio can significantly affect the process of geopolymerization and hence the properties of coatings, such as their workability and adhesion [5].
- Thixotropic Bingham plastic fluid behaviour: Most geopolymers show history-dependent rheological behaviour, and can be kept in fluid form if subjected to constant shearing [13, 54, 55]. Their rheological behaviour can also be tuned by

altering the molar concentration of the silicate and the ratio of silicate to hydroxide solutions [56].

- Setting times that are strongly dependent on chemical composition: The setting time of geopolymers can range from minutes to hours and depends on geopolymer composition. Setting times can be reduced by lowering Si/Al ratios, or by increasing calcium (Ca) content [47]. For systems with high Si/Al ratios, polymerisation is more likely to occur among silicate species, but when Si/Al ratios are lowered, polymerisation is more likely to occur between aluminate and silicate species. As condensation among silicate species is slower than that between aluminate and silicate species, setting is delayed with higher Si/Al ratios [57].

The impact this has on coatings is that it can be challenging to independently tune adhesion, rheology, setting time and shrinkage behaviour, as the properties of the system are highly interdependent. Previous work conducted at elevated temperatures may therefore not always map onto efforts to produce geopolymer coatings that cure in ambient conditions.

#### 4.2.1.3. The concrete substrate

Previous studies have found that the adhesion of coatings more generally is strongly influenced by the roughness of the substrate surface, its water content and the mix composition of the coating material [58-64]. Rough surfaces on concrete substrates are preferred as greater bond performance is ensured [62, 65]. Among the available surface preparation methods, a high bond strength can be achieved with sand-blasting and wire brushing [58]. Morgan [66] states that the degree of roughness and means of roughening both affect long-term performance. Before applying the geopolymer repair material Zanotti et al., for example, roughened the surface using the sandblasting technique [67].

Some authors [66, 68, 69] have shown the important role of the substrate during concrete-to-concrete repair work. A significant mismatch between substrate and repair concrete is a notable consideration if the repair is to resist the stresses induced by dimensional, mechanical and durability incompatibility. The surface of the substrate should have an open pore structure, to allow the absorption of the repair material into the substrate's pore structure, thus enhancing the bonding mechanism. In geopolymer coatings, this is at odds with the requirements for reducing drying shrinkage, as an excessively dry substrate with open pores may absorb too much water from the coating [70].

Today, opinions diverge about the most appropriate practice when coating and repairing concrete substrates. Even between international codes of practice, recommendations are contradictory. The AASHTO-AGC-ARTBA Joint Committee recommends a dry surface for concrete, except on dry and hot summer days, while the Canadian Standards Association Standard A23.1 recommends wetting the surface for at least 24 h before casting the new concrete [58]. In some studies, saturated, surface dry conditions are considered to be the best solution [70].

#### 4.2.1.4. Efflorescence

A final issue, which can be particularly prevalent in ambient temperature cured geopolymers, is efflorescence. Efflorescence is the formation of white salt deposits, and it can unfortunately occur during attempts to manipulate geopolymer shrinkage, adhesion, workability, and setting time. It has been found that efflorescence is due to many factors [46]: wet conditions, the reactivity of raw materials, the alkali metal type, and reaction conditions. In particular, a high alkali content in the activator solution causes efflorescence in partially wet conditions [45, 71]. Geopolymer efflorescence is thus common at high humidity, and this is important because humidity cannot always be controlled in the field. Ambient temperature curing also makes efflorescence more likely, because the low temperatures reduce the dissolution rate of the fly ash by the alkaline solution. Any excess alkaline solution is therefore more likely to crystallize on the surface [14].

#### 4.2.2. Repair materials, requirements and classification

In the field of concrete structure rehabilitation, cracking and spalling are the major causes of deterioration of concrete structures, and so coating or patching is a common repair method [72, 73]. BS EN 1504 is the European and British Standard of products and systems for the protection and repair of concrete structures [38]. It consists of 10 parts, which cover the test methods for material properties, specification for repair materials, and general principles for repair work. In particular, part 3 of the standard (BS EN 1504-3:2005) [38] lists the requirements and performance characteristics of structural and non-structural repair products. Table 3 of this standard lists the requirements for each structural and non-structural repair class. In this thesis only three out of the 12 required properties listed in table 3 of BS EN 1504-3:2005 have been tested, to give a preliminary evaluation of the geopolymer binder as a concrete repair: compressive strength, bond strength and thermal expansion coefficient. Table 4.1 below recalls the requirements listed in table 3 of BS EN

1504-3:2005, and the properties tested in this work are highlighted: compressive strength, bond strength and coefficient of thermal expansion (tested according to the standards BS EN 12190, BS EN 1542 and BS EN 1770:1998 respectively for each of the three tests).

Performance characteristic	Test method	Requirement			
		Structural		Non-structural	
		Class R4	Class R3	Class R2	Class R1
Compressive strength	EN 12190	≥ 45 MPa	≥ 25 MPa	≥ 15 MPa	≥ 10 MPa
Chloride ion content	EN 1015-17	≤ 0.05 %		≤ 0.05 %	
Adhesive bond	EN 1542	≥ 2.0 MPa	≥ 1.5 MPa	≥ 0.8 MPa * ≥ 0.5 MPa for cohesive failure	
Restrained shrinkage/expansion	EN 12617-4	Bond strength after test			No requirement
		≥ 2.0 Mpa	≥ 1.5 MPa	≥ 0.8 MPa	
Carbonation resistance	EN 13295	dk ≤ control concrete (MC(0,45))		No requirement	
Elastic modulus	EN 13412	≥ 20 GPa	≥ 15 GPa	No requirement	
Thermal compatibility: part 1 - freeze-thaw	EN 13687-1	Bond strength after 50 cycles			Visual inspection after 50 cycles
		≥ 2.0 Mpa	≥ 1.5 MPa	≥ 0.8 MPa	
Thermal compatibility: part 2 - thunder shower	EN 13687-2	Bond strength after 30 cycles			Visual inspection after 30 cycles
		≥ 2.0 Mpa	≥ 1.5 MPa	≥ 0.8 MPa	
Thermal compatibility: part 4 - dry cycling	EN 13687-4	Bond strength after 30 cycles			Visual inspection after 30 cycles
		≥ 2.0 Mpa	≥ 1.5 MPa	≥ 0.8 MPa	
Skid resistance	EN 13036-4	Class I: > 40 units wet tested Class II: > 40 units dry tested Class III: > 55 units wet tested		Class I: > 40 units wet tested Class II: > 40 units dry tested Class III: > 55 units wet tested	
Coefficient of thermal expansion	EN 1770	Declared value *or not required if tests 7, 8 or 9 are carried out		Declared value *or not required if tests 7, 8 or 9 are carried out	
Capillary/Absorption	EN 13057	≤ 0.5 Kg · m <sup>-2</sup> · h <sup>-0.5</sup>		≤ 0.5 Kg · m <sup>-2</sup> · h <sup>-0.5</sup>	No requirement

Table 4.1 - Performance requirements listed in table 3 of BS EN 1504-3:2005.

According to another standard BS EN 1542:1999 for measurement of bond strength by pull-off of repair materials, the bond strength value (load) measured at failure is valid for all combinations of failure type, except abnormal failures. According to BS EN 1542:1999, **abnormal failures**, shown in Figure 4.2, are respectively defined as: (a) adhesion failure between the last layer of the repair material and the adhesive layer; (b) cohesion failure in the adhesive layer; and (c) adhesion failure between the adhesive layer and the dolly. According to the same standard, the types of failure considered **valid** for the assessment of the bond strength, shown in Figure 4.3, are respectively: (a) cohesion failure in the concrete

substrate; (b) adhesion failure between the substrate and the first layer of the repair coating; (c) cohesion failure in the layers of the repair material itself.

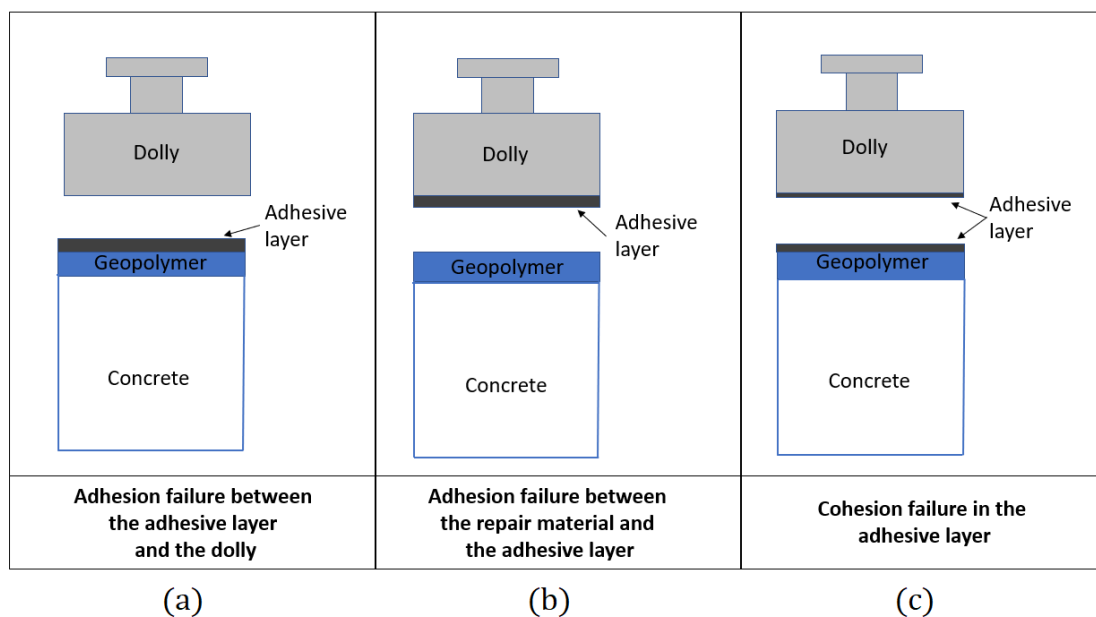


Figure 4.2 – Abnormal failure types of pull-out bond strength test: (a) adhesion failure between the adhesive layer and the dolly; (b) adhesion failure between the repair material and the adhesive layer; (c) cohesion failure in the adhesive layer.

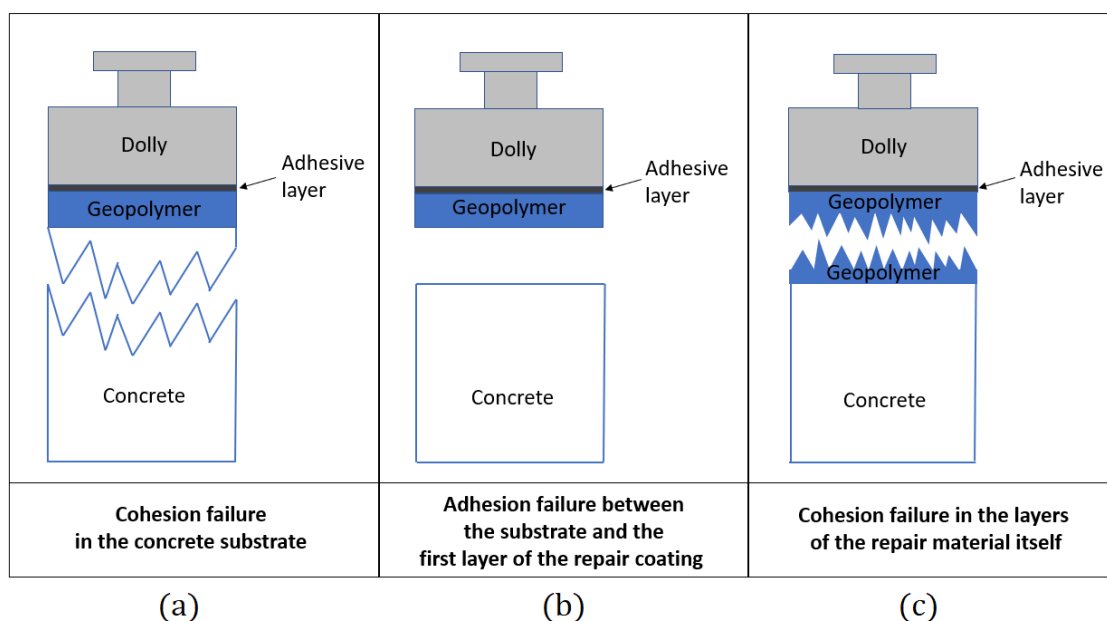


Figure 4.3 - Valid failure types of pull-out bond strength test: (a) cohesion failure in the concrete substrate; (b) adhesion failure between the substrate and the first layer of the repair coating; (c) cohesion failure in the layers of the repair material itself.

The materials commonly used for concrete repair have been categorized in three generic types [68, 74]: (i) Resinous materials; (ii) Polymer modified cementitious materials; and (iii) Cementitious materials. Geopolymers are categorized under the cementitious materials class [72]. Their potentially high durability, the highly versatile range of their physical properties, their endurance to extreme environmental conditions and their high adhesion to the substrate [75] make them a viable alternative to the most commonly used repair materials. The high adhesion to the substrate, in particular, is due to the fact that the concrete substrate chemically bonds to the geopolymeric phase by means of two processes [75]:

- (i) the ions  $\text{Ca}^{2+}$  coming from the OPC substrate balance the negative charge in the geopolymeric network cavities due to the presence of  $\text{Al}^{3+}$  ions;
- (ii) when the aggregate surface of concrete is subjected to the high alkaline activator in the geopolymer binder, there is a mechanical interlock yield by silica dissolution from aggregate surface.

Another property of geopolymer materials that impacts repair performance is the coefficient of thermal expansion ( $\alpha$ ) [66, 76]. According to Davidovits [77], formulations of castable geopolymer materials, without any additional filler, vary in degree of thermal expansion: the coefficient of thermal expansion values are a function of the Si/Al ratio, and range from  $4 \cdot 10^{-6}$  to  $25 \cdot 10^{-6} \text{ K}^{-1}$ . This range comprises the value of the coefficient of thermal expansion for concrete:  $13 \cdot 10^{-6} - 14 \cdot 10^{-6} \text{ K}^{-1}$  [133]. Similar thermal expansion properties between the coating material and the substrate are preferred for repairs [66].

This section has provided the theoretical background which was of key importance in the development of the experimental investigation for the achievement of: the coating integrity of ambient cured fly ash geopolymers, the solution of the issues outlined in section 4.2.1 above, and the evaluation of their mechanical properties for a preliminary repair performance evaluation, according to the requirements described in section 4.2.2. The experimental investigation is described in the following three sections: section 4.3 outlines the materials and the methodology used for the experiment, section 4.4 presents the results and discussion and section 4.5 provides a further discussion on the results obtained.

### 4.3. Materials and methods

This section provides the guidance needed to formulate and assess the integrity of fly ash geopolymer coatings onto concrete, as repair materials. Based on this guidance, a repair which meets the requirements of the BS EN 1504-3:2005, and the requirements needed by the nuclear storage application can be formulated.

#### 4.3.1. Materials

In this work, geopolymers were synthesized from low calcium fly ash. According to standard BS EN 450, the fly used was class B for loss on ignition (LOI 2.0% to 7.0%), and category S for fineness (no more than 12% retained on a 45 micron sieve). Under US notation, according to ASTM C 618-19, the fly ash used in this work would be considered class F. The chemical compositions of the fly ash used is given in Table 4.1, along with the information on the source of the ash and its median particle size, measured using a Mastersizer 2000.

Source	West Burton power station, Lincolnshire, England (UK)	
Supplier	CEMEX	
SiO <sub>2</sub>	52.70	
Al <sub>2</sub> O <sub>3</sub>	21.70	
Fe <sub>2</sub> O <sub>3</sub>	7.10	
CaO	4.10	
Loss of ignition	4.20	
Na <sub>2</sub> O	1.10	
K <sub>2</sub> O	2.50	
SO <sub>3</sub>	0.90	
MgO	1.80	
Total phosphate	0.58	
Free CaO	0.10	
Si/Al ratio	2.1	
Median particle size, $\mu\text{m}$	10.642	

Table 4.2 - Composition and properties of the fly ash used in this work.

Figure 4.4 shows the particle size distribution of the fly ash, measured as part of this work. The median value in Table 4.2 is the D50 or  $d(0, 5)$  value, defined as the intercept for 50% of the cumulative mass.

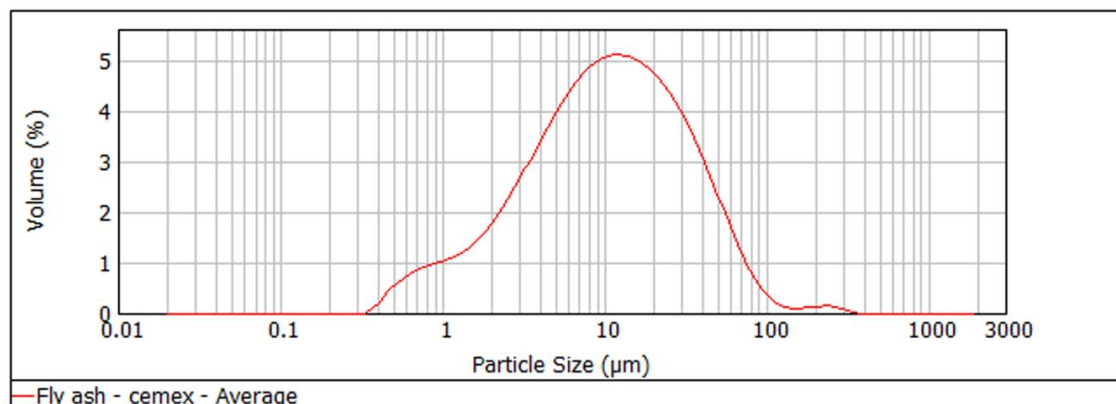


Figure 4.4 – Particle size distribution of the fly ash

The X-ray diffraction (XRD) spectrum of the fly ash is shown in Figure 4.5. It was acquired using the method which will be detailed in Section 4.3.6.3. The phases identified in the spectrum are: quartz (solid black line), mullite (dashed black line), maghemite (dotted black line), hematite (dot-dash line). The pattern shows an amorphous halo  $2\theta = [20^\circ, 35^\circ]$ , similar to [78]. Using Rietveld refinement (TOPAS v5, Bruker) on samples spiked with an internal standard (10 wt% silicon) the crystalline phases have been quantified: quartz is 33.58%, hematite is 2.18%, mullite is 59.51%, and magnetite is 4.73%. The amorphous content has not been quantified in this analysis. While the XRD spectra for magnetite is similar to maghemite (another iron oxide), the phase present is likely magnetite, as it is more common in UK fly ashes [24]. As mentioned in section 3.2.3.2, all this information on

fly ash composition is important for the resulting geopolymer binder. The XRD analysis of the geopolymer hardened binder will be presented in section 4.4.1.4.

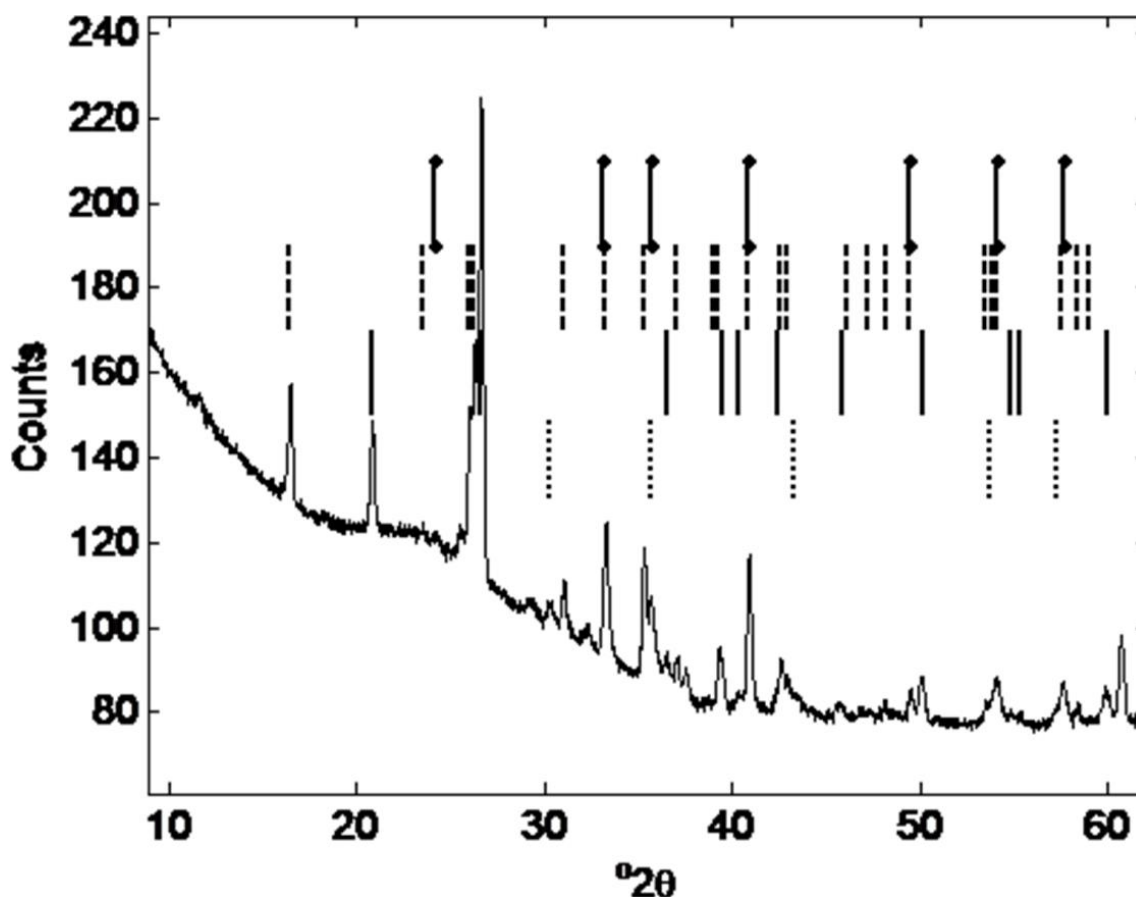


Figure 4.5 - XRD spectrum of Cemex Fly Ash. The legend of the figure is described here: Quartz (solid black line), mullite (dashed black line), magnetite (dotted black line), hematite (dot-dash line).

The alkaline activator used in this work was made by combining 10 wt% of 10 M sodium hydroxide solution (SH) and 24 wt% sodium silicate solution (SS), with the SH/SS ratio equal to 0.4. This is in accordance with [43], a work based on fly ash geopolymer coatings as skin sensors for concrete structural health monitoring (temperature and strain detection), coupled with optical fibers. The sodium silicate solution composition is made by 8.5 wt% Na<sub>2</sub>O and 27.8 wt% SiO<sub>2</sub>, in distilled water. The Na<sub>2</sub>O and SiO<sub>2</sub> concentrations of the alkaline activator are 12.7 wt% and 19.9 wt% respectively, and the remaining 67.4 wt% is

deionized water. The activator was made 24 hours prior mixing, to allow the heat of any exothermic reaction heat to dissipate.

### 4.3.2. Geopolymer synthesis

The geopolymer binder was fabricated by combining the fly ash with the activator solution, with a Liquid/Solid ratio ( $L/S$ ) = 0.5. The Si/Al ratio of the reactants of the geopolymer was 2.5. According to Nedelikovic et al.,  $L/S = 0.5$  improves workability, without having a significant effect on compressive strength [50]. A higher quantity of liquid also produces a less viscous slurry, which can penetrate more easily into the surface of a dry concrete substrate [79].

Figure 4.6 summarizes the steps taken to mix and apply geopolymers to concrete substrates. The mixing procedure consists of gradually adding the fly ash powder into a bowl containing the alkaline solution while continuously mixing (Figure 4.6 (a-c)). Samples were either mixed manually (Figure 4.6 (b)), or with an automatic mixer at  $500 \text{ min}^{-1}$  (Figure 4.6 (c-d)). Geopolymer binders were mixed for between 10 minutes and 1 hour before being applied to concrete substrates with a trowel (Figure 4.6 (e)).

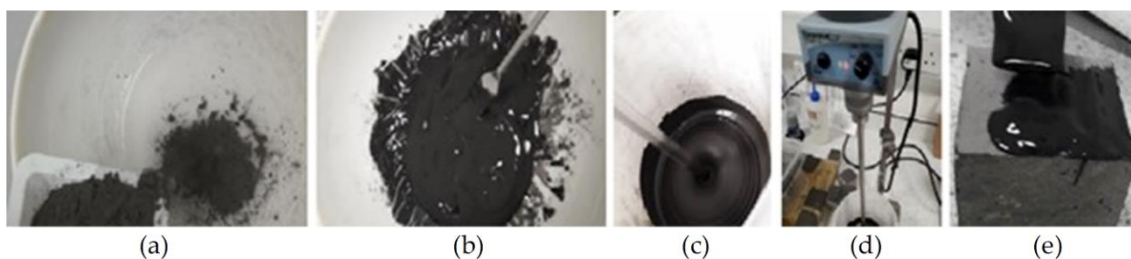


Figure 4.6 - Geopolymer synthesis process: (a) adding fly ash powder into alkaline solution; (b) manually mixing the geopolymer binder by means of a spatula; (c-d) automatic mixing of the binder; e) application of the binder onto concrete by means of a trowel.

For the bond strength test, the thermal expansion test and the compressive strength test, the binders were vibrated on a vibrating table for a couple of minutes before being applied onto the concrete substrate or being casted into the moulds for testing. These tests were conducted to provide comparison against BS EN 1504-3:2005. The binder was vibrated to remove air bubbles, because the presence of trapped air bubbles in cementitious binders can reduce their strength [80].

### 4.3.3. Application to substrate

Two thicknesses of geopolymer coatings were applied to concrete substrates in this work. Thin coatings were around  $m = 1$  mm high, and thicker coatings were  $m = 3$  mm high. These thicknesses were chosen in accordance with the requirements for sensing [43] and with the typical thicknesses for non-structural surface protective coatings for concrete (typically 0,1 mm – 5,0 mm, and only for particular applications  $> 5,0$  mm) outlined in standard BS EN 1504-2:2004 [81]. Structural repair coatings typically require much higher thicknesses (15 mm or 50 mm) [82].

To study any potential effects of the concrete substrate on coating integrity, geopolymer coatings were applied to concrete samples with varying age ranges:

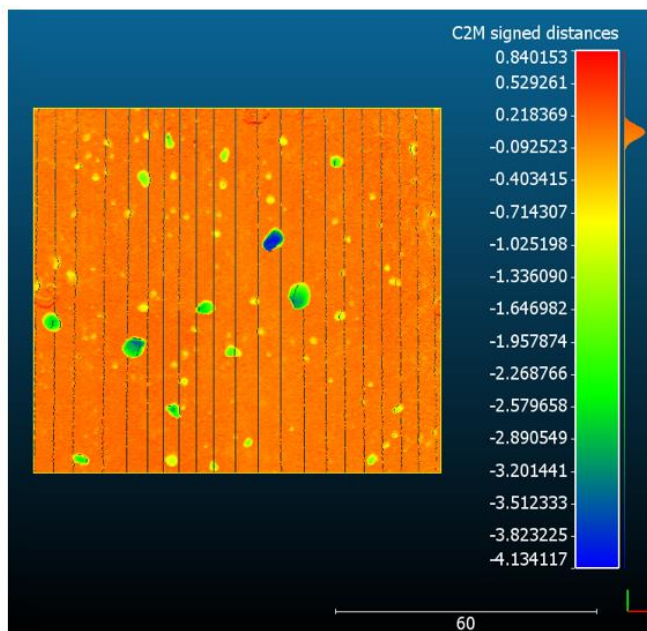
- Newly cast, or “young” concrete samples, left to cure for 1 - 5 months;
- Intermediate-aged concrete samples, 5 - 12 months of curing;
- Old concrete samples, over 1 year of curing.

The hypothesis was that the changing pore structure of the concrete substrate could affect moisture transport from the geopolymer layer, and thus coating integrity. As concrete matures, hydration progresses and capillary pore size and porosity decrease from the production of C-S-H and portlandite. Bentz et al. comment that when the volume fraction porosity has been reduced to c. 0.20, the pore space is no longer interconnected throughout the paste and that water transport is restricted, but the small gel pores ( $< 10$  nm in diameter) remain filled at RH values of 50% and higher [83, 84]. As a greater percentage of filled pores results in less capillary suction, the more mature concrete might be expected to drain less water from the geopolymer.

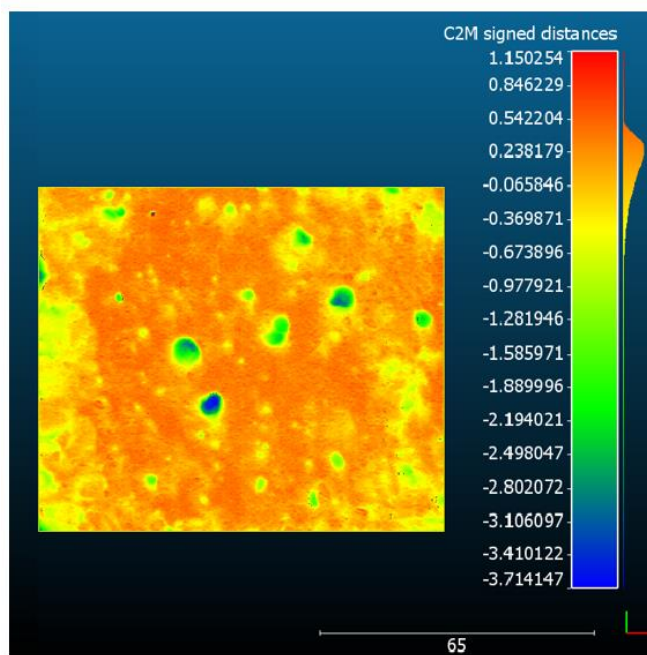
### 4.3.4. Concrete substrate roughness

The surface roughness of each concrete substrate used was measured by 3D laser scanning (using a Micro Epsilon Scan Control 2700-100, an exposure time of 1 msec, 56 profiles per second, and 1600 buffered profiles). Some surfaces of old concrete samples which were used for the pull-off test were prepared by roughening the surface with an electric brush with steel bristles, while the others were left untreated. The values for surface roughness were determined by analysing the root mean square deviation of the point cloud from a

mean plane, which represents the fitting plane of the cloud of points. The method is shown in Figure 4.7, where the two images represent the mapping of the distances between the cloud of points of a concrete surface and its mean fitting plane, respectively for a smooth (a) and a brushed (b) concrete surface.



(a)



(b)

Figure 4.7 – Graphic mapping of the distances between the cloud of points of the concrete surface and the mean fitting plane, for the calculation of the roughness as root mean square deviation method. (a) Example of an un-scored old concrete surface, and (b) example of a scoured old concrete surface.

Typical values of surface roughness for concrete samples are shown in Table 4.3. They are subjected to high variability depending on the presence of holes due to air bubbles on the concrete surface. The results in Table 4.3 are presented for surfaces with an intermediate configuration of holes (such as those shown in Figure 4.7). Values of the first three columns correspond to the average roughness of the smooth surface that one would expect from unscoured concrete [85], while the last column corresponds to the average roughness value of a brushed old concrete surface.

Age of concrete	Young	Intermediate	Old (untreated)	Old (brushed)
Surface roughness (mm)	0.097	0.053	0.091	0.353

Table 4.3 - Surface roughness values for each type of concrete used.

#### 4.3.5. Curing conditions for geopolymers

Geopolymer specimens were batched and placed within one of two curing conditions, summarized in Table 4.4. Both patches were cured at 20 °C, and the relative humidity of batch 1 and batch 2 were 50% and 95% respectively. Temperature and relative humidity (RH) were measured in lab conditions and shown to be relatively stable for batch 1, but they were not tightly controlled. Batch 2, meanwhile, was cured in an environmental chamber in controlled conditions. The high humidity range was chosen to emulate the actual conditions in the nuclear storage application, which are expected to be between 50% and 95% for most of the year, according to annual internal reports of temperature and RH data measured in the air corridors of the SPRS store in Sellafield.

All geopolymer specimens in the batches were left to cure for 28 days. While geopolymers do tend to cure much faster than Portland cement mixes, we opted to use a prolonged curing duration in this work to ensure that patches were fully cured and stabilized in ambient conditions.

Batch	Curing conditions	Temperature °C	Curing time (days)	Average RH %
1	Laboratory bench	20 ± 2	28	50
2	Environmental chamber	20 ± 1	28	95

Table 4.4 - Curing conditions of geopolymer coatings, divided in two batches.

### 4.3.6. Analysis methods

Several tests were carried out on the fly ash powder and the geopolymer binder to characterize their properties, before mixing, during curing and after curing. These are summarized in the following subsections.

#### 4.3.6.1. Vicat needle test

The setting time of geopolymer mixes was measured using the Vicat needle test, following the procedure outlined in BS EN 196, part 3 [86]. This test was conducted in order to define a suitable time to apply the geopolymer onto the concrete substrate, and to define the shelf life for our geopolymer mixes. While the Vicat needle test is a well-accepted and easy-to-use standard method used within ordinary Portland cement concrete mix design, it is less accurate than modern calorimetric and viscosity measurements and so results should be interpreted with caution.

#### 4.3.6.2. Isothermal calorimetry

A thermal analysis, together with an evaluation of setting time using the Vicat needle test, can be used to define an optimized time for applying geopolymer coatings to concrete substrates. In this work, an isothermal calorimeter (Calmetrix, I-CAL 4000 HPC) was used to measure the temporal dependence of the heat produced by the exothermic reactions occurring in the geopolymer from immediately after mixing up to 4 days. Tests were conducted three times for each geopolymer mix tested, with the averaged heat curve presented in the results.

#### 4.3.6.3. X-Ray diffraction analysis

X-ray diffraction (XRD) analysis was carried out on samples of fly ash, on geopolymer layers, and on geopolymer coatings which had demonstrated efflorescence. All XRD data was collected using a Bruker D8 Advance instrument. Data for Rietveld refinement was collected in Bragg-Brentano geometry in the range  $2\theta = [10^\circ - 60^\circ]$ , with an increment of  $0.02^\circ/\text{second}$  and a step time of 1 second. Motorized diverging slits were used fixed at 0.5mm to avoid beam spill onto the plastic sample holder. The sample was rotated to improve particle statistics.

The efflorescence was analysed intact on a sample of geopolymer. The efflorescence could not be easily removed for conventional powder analyses and was analysed in situ in the XRD using a Goebel mirror to reduce sample displacement error. Data was collected in the range  $2\theta = [10^\circ - 60^\circ]$ , with an increment of  $0.02^\circ/\text{second}$  and a step time of 8s. XRD data was analysed using Diffrac EVA, TOPAS software and MATLAB scripts.

#### 4.3.6.4. Compressive strength

Compressive strength tests were conducted with a small loading cell with the speed of 2 mm/min on geopolymer cubes of side 30 mm. Tests were conducted after 1 day, 2 days, 3 days, 4 days, 7 days, 14 days and 28 days for the non-vibrated binder used to assess the coating integrity of coatings. A further 56 day test was added for the test conducted on the vibrated binder. The intention here was to demonstrate the evolution of strength, rather than strictly comply with strength-testing standards.

#### 4.3.6.5. Visual inspection and quantification of cracks

A visual inspection was often enough to provide a binary “yes/no” assessment of whether a geopolymer coating had cracked after curing. However, to quantify the relative levels of cracking between specimens in a less subjective manner, a simple image processing technique, outlined in Figure 4.8, was developed.

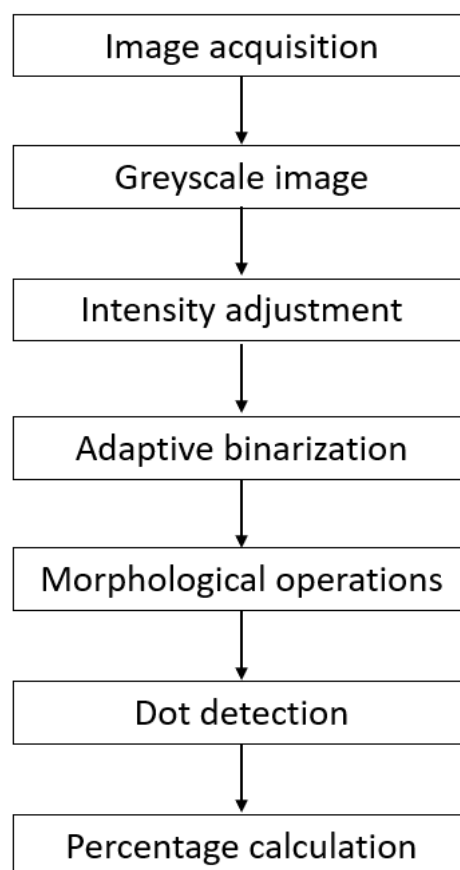


Figure 4.8 - Steps of the image processing method.

The original sample images were taken using a DSLR camera with a set distance between the sample and the focal lens. The image is then cropped so that all samples produce images of the same size for ease of comparison. The colour images obtained were converted to grayscale images. This eliminated colours during further processing, while preserving the intensity of each pixel in the image with a grayscale level.

In order to ensure that the cracks were the darkest part of the image, a pre-processing step of intensity adjustment was required. The bottom 1% and the top 1% of all pixel values were saturated to increase the contrast of the output image. By identifying and intensifying the pixels below the mean grayscale value in the image, a clearly distinguished foreground of cracks was obtained, as shown in Figure 4.9.



Figure 4.9 - (a) Original image and (b) grayscale image after intensity adjustment.

During the image acquisition step, an inconsistent amount of light in the background was difficult to avoid. In order to correct for this non-uniform illumination, adaptive binarization was used. By applying Bradley's method [87], each pixel in the integral image was compared to the average grayscale level of its surrounding pixels and set to a binary value accordingly.

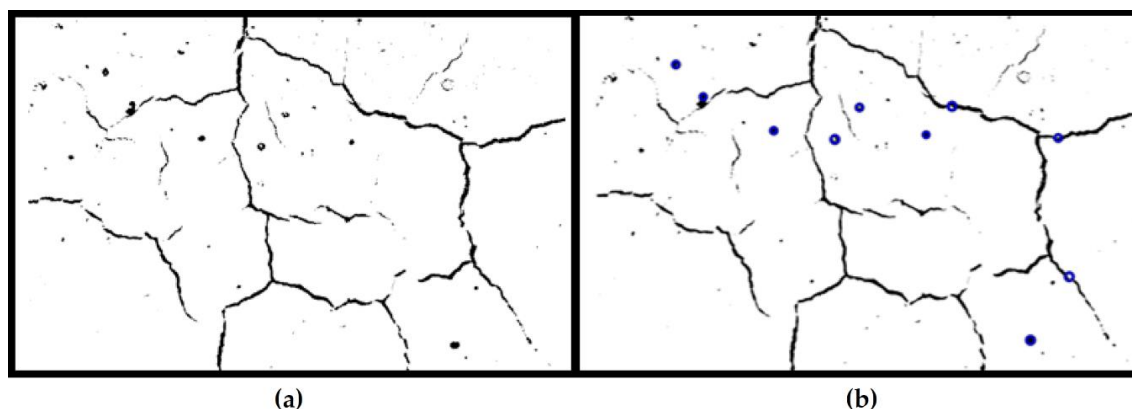


Figure 4.10 - Binary images: (a) morphological operation; (b) dot detection.

Due to the special characteristics of cracks in our samples, morphological operations and dot detection could be used to reduce noise that could interfere with the final quantification of cracking [88]. One pixel with more than 4-connected neighbourhoods is seen as one element. By removing elements that contain fewer than 10 pixels, more noise can be eliminated from the image. Dot detection was used since most of our samples had dark bubbles that were difficult to distinguish from real cracks in the previous step. By utilizing the circular Hough transform, the round objects could be identified and eliminated from the calculation. The Hough method is one of the standard methods for image recognition [89]. The images after morphological operations and dot detection are shown in Figure 4.10.

The final step was to calculate the percentage of dark pixels (cracks) over the area of the whole image, yielding a quantified and less subjective result for the levels of cracking in each sample. This result provided a percentage of the image that shows cracks.

#### 4.3.6.6. Bond strength test

The bond strength of the geopolymer coatings onto concrete surfaces was measured using a pull-off portable tester, the Elcometer 106-6, in accordance with the following National and International Standards: ASTM D 7234, BS 1881-207, EN1542, EN 12636. The Adhesion Tester employs a pull-off method to determine the force required to pull a test dolly of fixed area coated away from the concrete. The pull-off force is provided by the progressive compression of Belleville washers. The range of force measurable by the instrument is  $0\text{ MPa} - 3.5\text{ MPa}$ , and the accuracy is  $\pm 15\%$ . This accuracy is worse than that ( $\pm 2\%$ ) recommended by the standard BS EN 1542:1999 on the pull-out testing method for repair materials onto concrete. Besides, among the available methods for bond strength, it provides the most conservative results [90], and shows a larger scatter of results due to glue issues, eccentricity in the load application and damage during coring [59].

Nevertheless, the Elcometer has been chosen because it is a convenient and simple method which provides a preliminary evaluation of the in-service performance of the coatings. The method is useful because the patches manufactured in this work are thin (1-3 mm): it tests the bond strength of a coating, whereas other methods (such as slant shear tests, splitting tensile tests, among the others) investigate the bond between materials (for instance concrete and geopolymer) using the same volume for both.

The procedure used for the pull off test followed BS EN 1542:1999 [76] as closely as possible, and consisted of the following steps:

1. Some concrete specimens under examination were prepared by roughening the surface with an electric brush with steel bristles, while others were left with the smooth surface that one would expect from untreated concrete. Untreated and treated samples returned the average roughness values listed in Table 4.3.
2. A geopolymer coating of 1 mm was applied onto the surface with a trowel, and cured for 28 days in an environmental chamber at 20°C and 95% RH (batch 2 of Table 4.4).

3. After curing, the sample was drilled with a 50.8 mm diameter corer, by means of a diamond coring barrel to a depth of 5 mm into the concrete.
4. The day after, a test dolly made from high-tensile strength aluminium, with a diameter of 50 mm, was attached using an adhesive, after having prepared the surface of the dolly by roughening it with an abrasive paper. A two-part Araldite epoxy paste was used.
5. When the adhesive had cured (after about 24 hours at 25°C) and the adhesion tester claw engaged onto the dolly, the force was applied uniformly and without stopping, and the resulting stress recorded by means of a dragging indicator on an engraved scale.
6. The value was read from the position of the dragging indicator after the test was complete, and the face of the dolly was inspected, to assess the type of failure.

The concrete test specimens more than 3 years old used for the test were concrete cubes of side 150 mm. The 5 bond tests required by the standard BS EN 1542:1999 [76] were conducted on 5 cores, each of them in the centre of one face of the cubic concrete specimens. The final value for bond strength was calculated as the average of the 5 samples. An example of a sample specimen is shown in Figure 4.11, where (a) shows the old concrete cube with the fly ash geopolymer coating, and the drilled core in the centre of the face, (b) shows the dolly attached, and (c) shows with the pull-off Elcometer tester in testing position on the dolly.

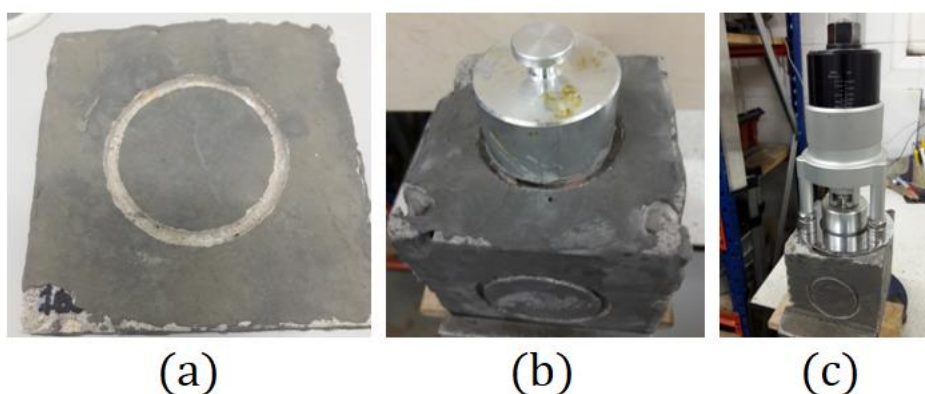


Figure 4.11 – An old concrete cube with fly ash geopolymer coating from the vibrated batch 2 of Table 4.4, and the drilled core in the centre of each face, (a) without and (b) with the dolly attached, and (c) with the pull-off Elcometer tester in testing position on the dolly.

#### 4.3.6.7. Thermal expansion measurement

The thermal expansion test of the ambient cured geopolymer manufactured in this work was conducted by following standard BS EN 1770:1998 [91] as closely as possible. The test was conducted on three geopolymer specimens, obtained from the binder manufactured as described in section 4.3.2, and then cast in cylindrical moulds with dimensions of 50 mm length and 25 mm diameter. The specimens were cured for 28 days in the environmental chamber at 20 °C and 95% RH (batch 2 of Table 4.4). After 28 days of curing, the specimens were drilled in 3 points along the vertical direction of the cylinder with three holes equally spaced, with a diameter of 3 mm and a horizontal depth of about 10 mm, as schematically shown in Figure 4.12 (a). The holes were made to accommodate three thermocouple probes in order to monitor the temperature of the sample in three different central points along its length.

Samples were then placed in a thermostated chamber, filled with mineral oil and cooled down with 12 Peltier cells. Temperature was reduced from 20 °C to 2°C. Thermal contraction was measured by means of an LVDT (Linear Variable Displacement Transducer). An image of the system in operation is shown in Figure 4.12 (b).

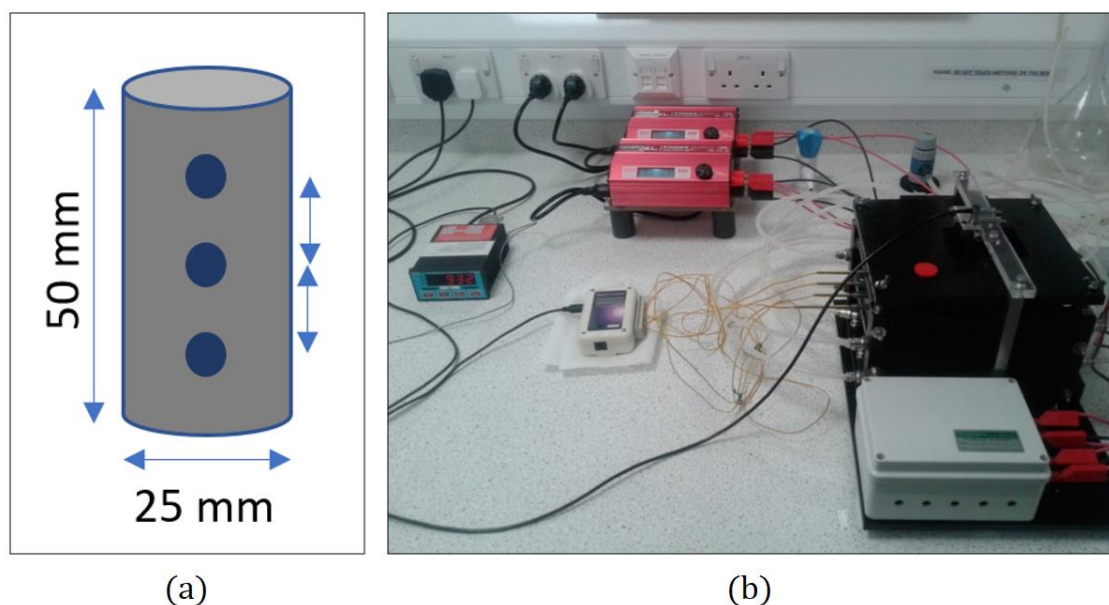


Figure 4.12 - (a) Schematic representation of a geopolymer cylindrical specimen for the thermal expansion test; (b) Image of the system prototype for thermal expansion, with the chamber in operation with the lid on the top.

A schematic representation of the chamber set-up with the sample, the LVDT and the tempocouples in the measurement position is shown in Figure 4.13.

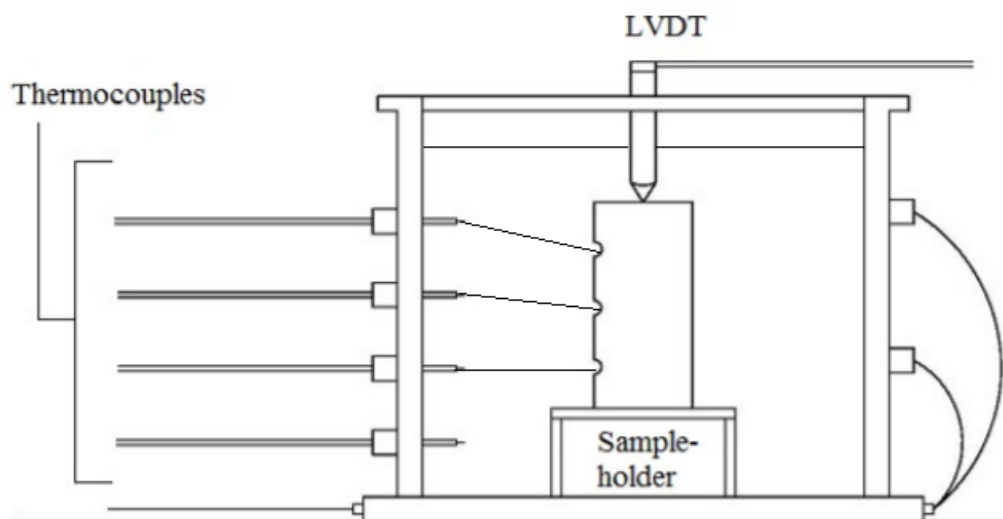


Figure 4.13 - Schematic representation of the thermostatic chamber with the LVDT, the mineral oil and the thermocouples.

The coefficient of thermal expansion,  $\alpha$ , for each geopolymer cylinder was then calculated by means of the formula[92]:

$$\alpha = \frac{\Delta L}{L} \cdot \frac{1}{\Delta T} \quad \text{Eq. 4.1}$$

where  $L$  is the length of the sample,  $\Delta L$  is the displacement measured by the LVDT (after the conversion from Volts to  $\mu\text{m}$  by means of a calibration equation for the LVDT), and  $\Delta T$  is the difference between the initial and the final temperature measured by averaging the values given by the thermocouples. The final value for  $\alpha$  was then obtained from the average of the values calculated for three specimens tested, and the respective error was obtained from the standard deviation of the three  $\alpha$  values.

#### 4.4. Results and discussion

The results of this work are presented in two sections, referring to the main tasks of the research work described in this chapter: achieving a high integrity low calcium ambient-cured geopolymer coating, and giving an indicative evaluation of the potential of these coatings for use as repairs for concrete substrates in nuclear containment environments.

#### 4.4.1. Coating Integrity

The main results on the integrity of the fly ash geopolymer coatings are outlined and discussed in the following subsections, where each factor affecting coating integrity has been tested.

##### 4.4.1.1. Coating thickness

The main finding of this investigation was related to the thickness of the geopolymer coatings applied onto the concrete specimens. These results are shown in Figure 4.14 and Figure 4.15 for 1 mm thick and 3 mm thick coatings respectively. Coatings with a thickness of  $m = 1$  mm (thin coatings), showed no cracks and a good layer integrity, regardless of the age of the concrete substrate, the mixing time or the curing conditions. The algorithm used to detect surface quality gave an average value of 0.001% defects for all samples. On the other hand, geopolymer coatings with a thickness of  $m = 3$  mm (thick coatings), tend to show cracking. The extent of the cracking depends on the mixing time, but is not strongly dependent of the age of concrete and the curing conditions. The percentage values generated by the crack detection algorithm are shown inset in each image in Figure 4.15.

1 mm thick		Batch 1 (50% RH)		Batch 2 (95% RH)	
M (mins)→		10	60	10	60
Concrete age	Young				
	Inter.				
	Old				

Figure 4.14 - Images of 1 mm thick geopolymer coatings on concrete. Results are shown as a function of i) geopolymer mixing time, M; ii) relative humidity during curing; and iii) concrete substrate age. All images shown cover a 40 mm × 40 mm area on the sample. The crack quantification algorithm found negligible cracking in all samples (typically 0.001%).

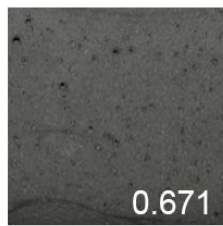
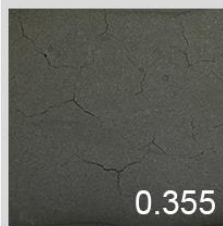
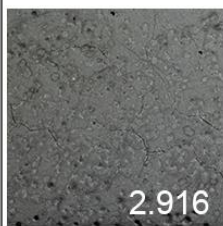
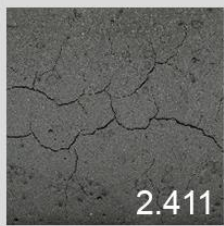
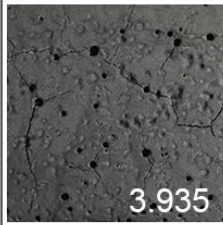
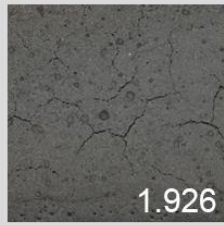
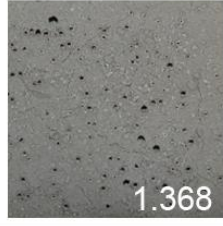
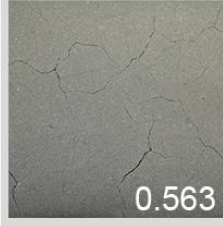
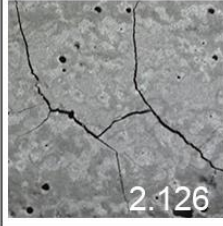
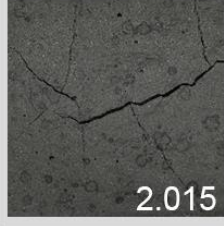
3 mm thick		Batch 1 (50% RH)		Batch 2 (95% RH)	
M (mins)→		10	60	10	60
Concrete age	Young				
	Inter.				
	Old				

Figure 4.15 - Images of 3 mm thick geopolymer coatings on concrete. Results are shown as a function of i) geopolymer mixing time, M; ii) relative humidity during curing; and iii) concrete substrate age. All images shown cover a 40 mm × 40 mm area on the sample. The numbers shown inset in each image are the crack percentages generated by the quantification algorithm.

This finding was initially surprising: the lower surface/volume ratio of the 3 mm thick coating should allow the geopolymer to retain more water. The result is also at odds with previous work by Zhang et al. [8], who concluded that increasing the thickness of the coatings from 3 mm to 5 mm reduced shrinkage. On the other hand, according to [64], the overall shrinkage of repair material increases with the repair volume, and this same result was found for concrete [93] and cementitious materials in general [94]. The explanation for these results could be that thicker layers show a higher drying shrinkage, since water is well-retained and evaporation takes place more gradually after the geopolymer matrix has slightly hardened (therefore generating stress). The water absorbed in thinner layers, meanwhile, is more likely to evaporate during the first few hours, while the geopolymer is still in a plastic state, and prior to any significant hardening.

#### 4.4.1.2. Setting and mixing time

The thicker coatings in Figure 4.15 show a relationship between coating quality and mixing time: coatings mixed for 10 minutes show numerous air bubbles on the surface (the black

spots). These could be a consequence of unreacted fly ash particles. When mixing times are increased to 1 hour, there are fewer air bubbles on the surface and no black spots (fewer unreacted particles). Cracks in thick coatings appear to be more extensive when the mixing time is longer. It could be that the agglomerates of unreacted fly ash particles are acting as 'micro aggregates' [83] for the coating, thus enhancing the strength of the coating. This hypothesis will, however, require testing in future work.

The reason for cracking in these coatings more generally can be explained using Figure 4.16, which shows the rate of heat release from the geopolymer (obtained using isothermal calorimetry analysis) over 4 days. The main extent of heat release occurs within the first hour after mixing. A similar result is seen in [50], for the same liquid to solid ratio. The absence of a second heat release peak in our results suggests that there are not a significant number of reaction products after the first hour [50]. According to [95] heat release can be associated with more shrinkage and cracking in coatings. For an ambient-cured geopolymer, mixing for 1 hour is preferable, as it allows the majority of the heat release to happen within the mixing bowl, it allows water to be used in geopolymerisation (rather than being lost to the substrate), and it allows unreacted fly ash particles to dissolve.

Figure 4.17 shows the cumulative heat release (calculated through cumulative trapezoidal numerical integration of Figure 4.16). These values grow more gradually than those found in previous work [50], and demonstrate that the reactions occurring in the ambient-cured geopolymer are more gradual. This hypothesis is also supported by the slower strength development (see section 4.4.2.1 and Figure 4.22).

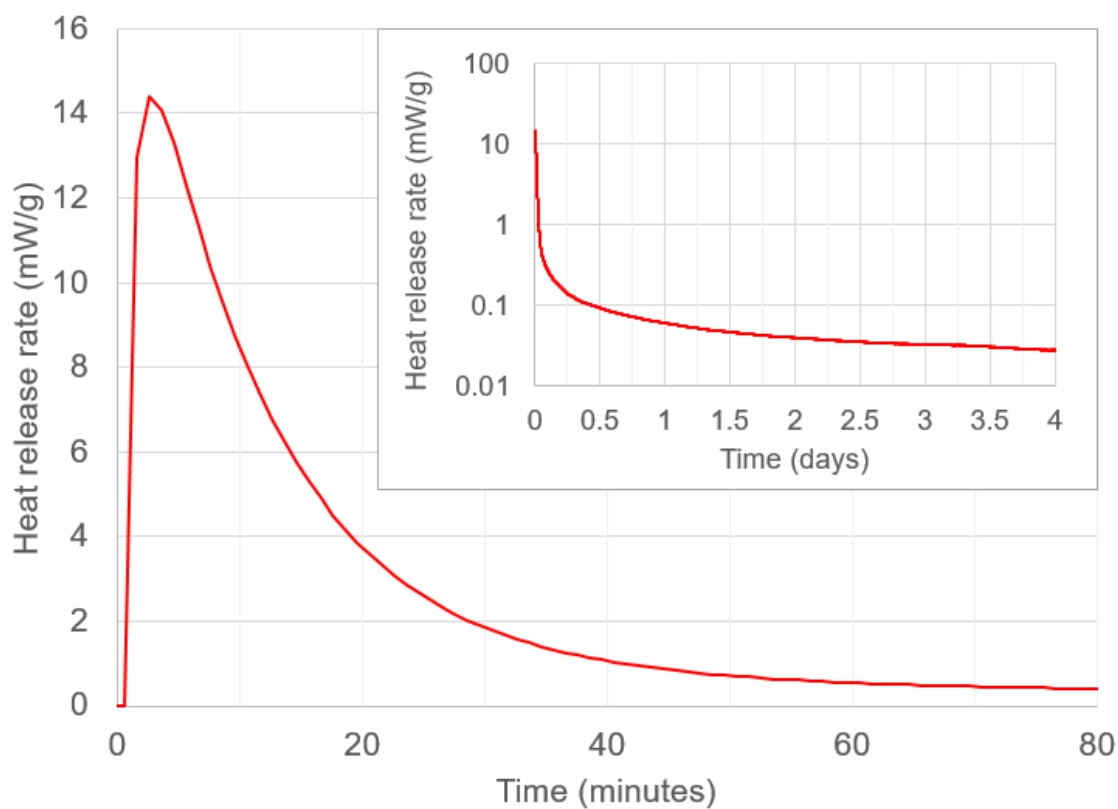


Figure 4.16 - The rate of heat release of the geopolymer over the first 80 minutes and (inset) over 4 days on a logarithmic scale.

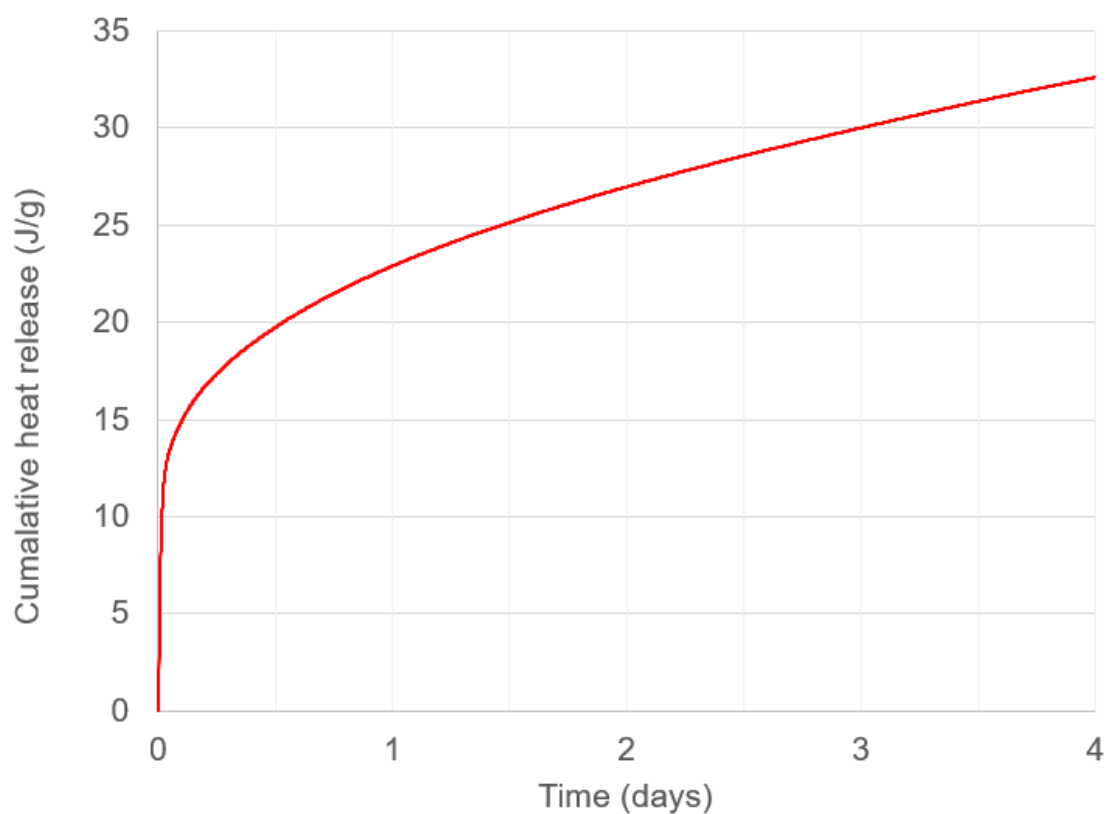


Figure 4.17 - Cumulative heat release of geopolymer binder over 4 days.

Finally, a Vicat Needle test produced the setting times shown in Figure 4.18. It appears that mixing for longer durations (1 hour, as opposed to 10 minutes) reduces the initial and final setting times, and this also supports the idea that a further extent of geopolymerisation can occur during prolonged mixing.

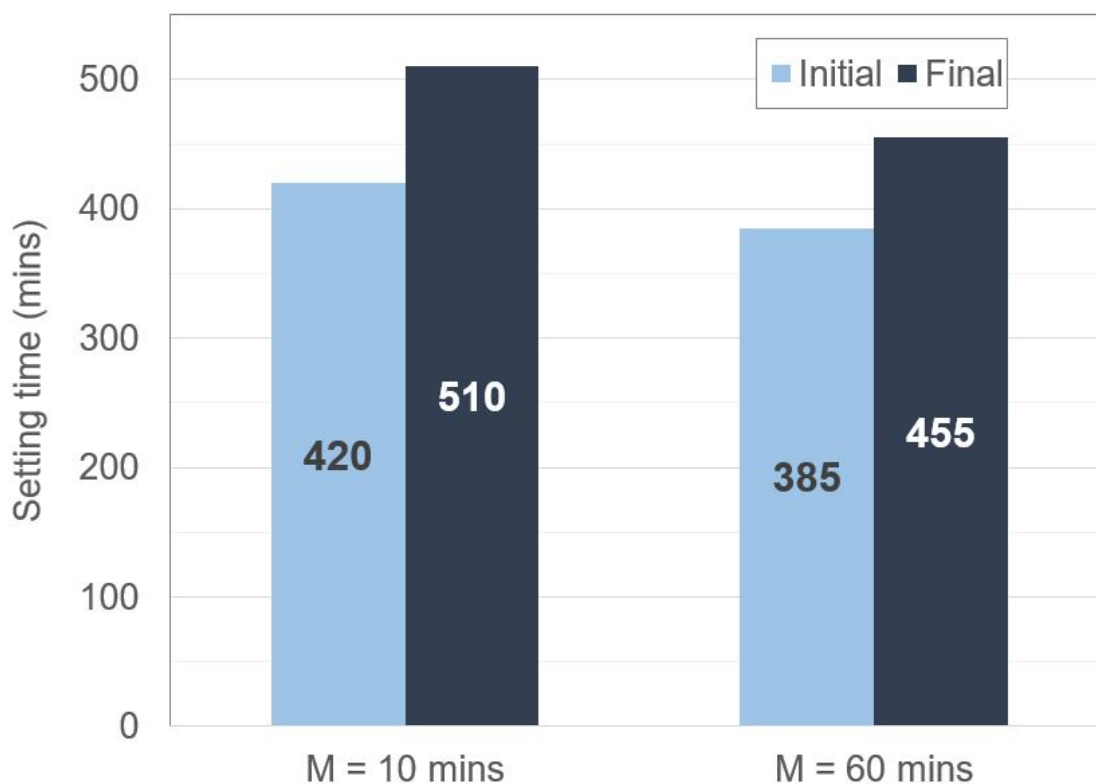


Figure 4.18 - Vicat Needle initial and final setting times of geopolymer samples mixed for M = 10 minutes and M = 60 minutes.

#### 4.4.1.3. Concrete age

The results in this work show that the age of the concrete substrate has little to no influence on the integrity of the coating layer: the coating thickness and the mixing time of the geopolymer are far more important factors. This does not rule out the effect of concrete age on water absorption from the geopolymer layer in all cases, however, as the rate-of-hydration and pore-size-change within concrete substrates is strongly dependent on the concrete's water/cement ratio, the cement particle size, and the curing conditions. Nevertheless, this result, together with the independence of the integrity of the coatings on the curing RH levels between 50% and 95%, is encouraging from the standpoint of application: geopolymer coatings can be applied to both new and old concrete assets, and at a wide range of humidity ranges. It could therefore be a promising technology for both existing and new built nuclear concrete containments.

#### 4.4.1.4. Efflorescence

The final issue faced in ambient curing of geopolymer coatings on concrete was efflorescence. The samples in batch 2 of Table 4.4 (high humidity curing) showed, in some

cases (mostly in case of thick layers), evidence of white crystals on the surface 3-8 weeks after application and curing. Efflorescence is a nucleated process, so its extent can change from one sample to the other, but the high humidity has increased the propensity for it to occur. Figure 4.19 shows that efflorescence can be accompanied by the presence of cracking, but it is likely that both efflorescence and cracking are both symptoms of moisture transport within the sample, mainly due to the drying process.

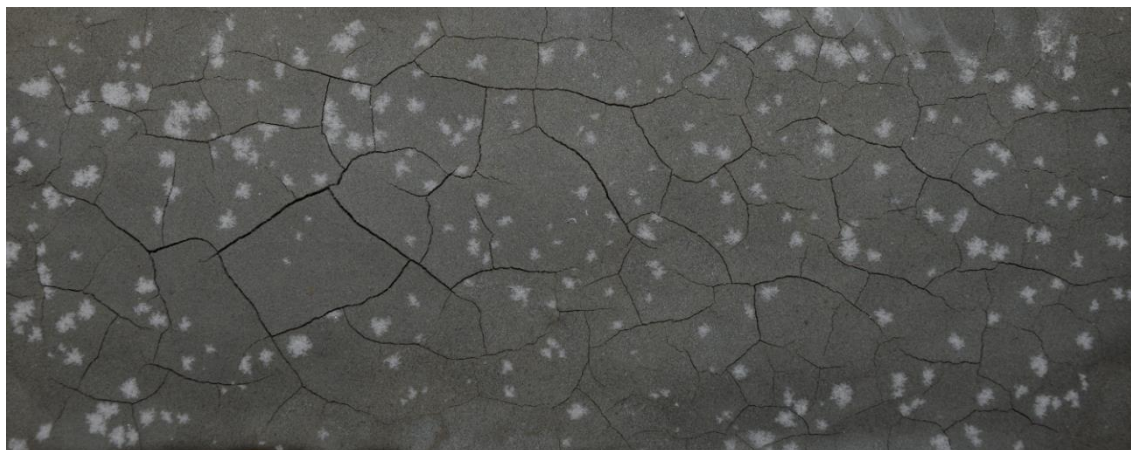


Figure 4.19 - An example of geopolymer coating in batch 2 which demonstrated efflorescence.

The samples with efflorescence crystals were analysed using XRD, as described in section 4.3.6.3. The results of the XRD analysis are shown in Figure 4.20. Solid black lines below the pattern are gaylussite ( $\text{Na}_2\text{Ca}(\text{CO}_3)_2 \cdot 5\text{H}_2\text{O}$ ), dotted lines are quartz and dashed lines are mullite. The background has been removed as the main feature of interest is the crystalline salt. The data is smoothed using a moving average method with a span of 9.

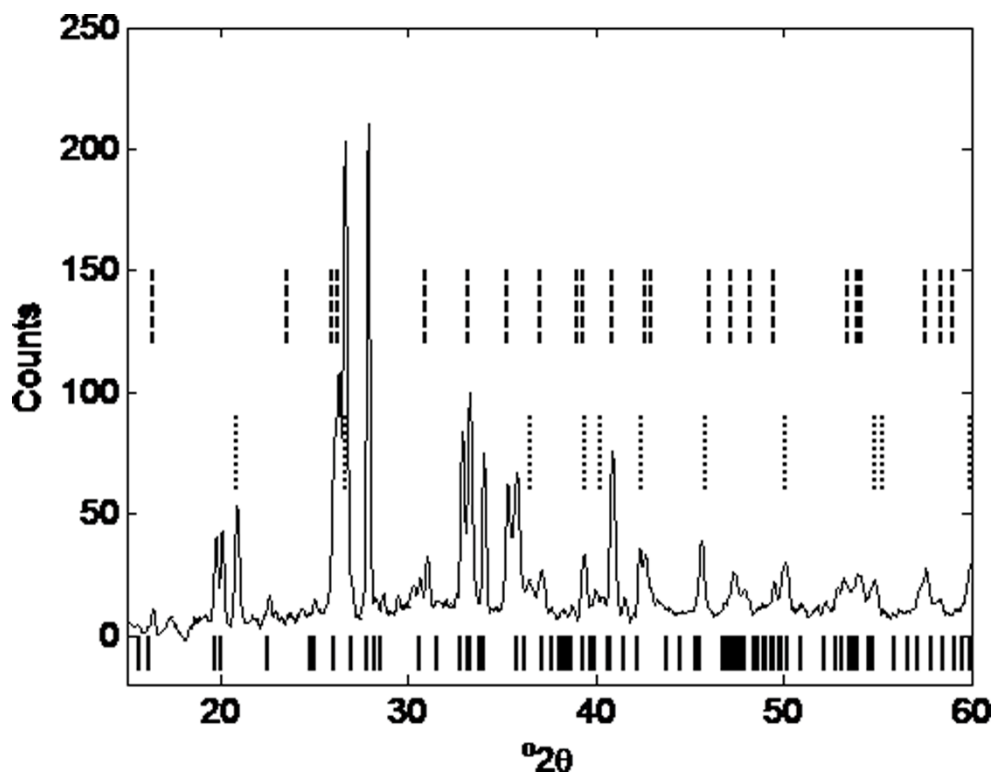


Figure 4.20 - XRD spectrum of geopolymer sample containing efflorescence crystals on the surface: Solid black lines below the pattern are gaylussite ( $\text{Na}_2\text{Ca}(\text{CO}_3)_2 \cdot 5\text{H}_2\text{O}$ ), dotted lines are quartz and dashed lines are mullite.

The results reflect the literature findings discussed in Section 4.2.1.4. Excess  $\text{Na}_2\text{O}$  is mobile and on the surface of the coating can react with atmospheric  $\text{CO}_2$  to form  $\text{Na}_2\text{CO}_3$  phases. In this case, the XRD analysis showed that the reaction product is gaylussite –  $\text{Na}_2\text{Ca}(\text{CO}_3)_2 \cdot 5\text{H}_2\text{O}$ . This result suggests that Ca has been dissolved from the cement substrate, forming with the  $\text{Na}_2\text{O}$ , by evaporation and reaction with atmospheric  $\text{CO}_2$ , the crystalline gaylussite phase at the geopolymer surface.

It is more likely that the Ca comes from the substrate, since in the geopolymer, as we can see from the XRD spectrum of a geopolymer sample of the same batch and under the same curing condition of the efflorescence sample (batch 2, Table 4.4), shown in Figure 4.21, no C-S-H is clearly present which is consistent with the low CaO content of the fly ash. In Figure 4.21, the amorphous halo is present from  $2\theta = 25^\circ$  and  $2\theta = 40^\circ$ , consistent with the formation of N-A-S-H, similar to [78, 96, 97]. TOPAS analysis of the geopolymer shows the following crystalline phases: 32.63% quartz, 0.16% hematite, 60.20% mullite, and 7.01% magnetite. The amorphous content has not been quantified in this analysis. Some of these crystalline phases decreased from the original quantities measured for the fly ash (such as hematite and magnetite), and others slightly increased (such as quartz and mullite). This is

consistent with the destruction of crystalline bonds during geopolymerisation, and with the fact that minerals such as quartz and mullite don't react during geopolymerization.

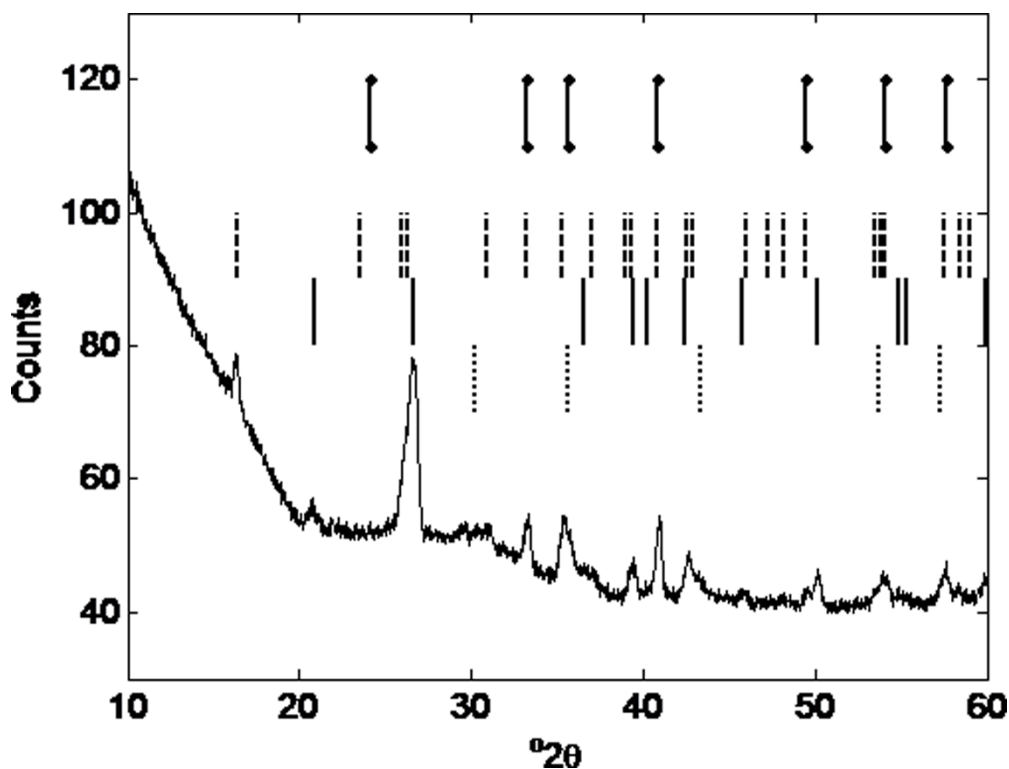


Figure 4.21 - XRD spectrum of geopolymer sample of batch 2, Table 4.4. The phases found are: Quartz (solid black line), mullite (dashed black line), magnetite (dotted black line), hematite (dot-dash line). The pattern shows an amorphous halo from c. 20 – 35 degrees 2theta.

#### 4.4.2. Preliminary repair performance evaluation

The results of compressive strength, bond strength and coefficient of thermal expansion tests and the indication they give on repair performance of the materials are outlined in the following sub-sections.

##### 4.4.2.1. Compressive strength

The evolution of the compressive strength of the geopolymer binder manufactured in this work is shown in Figure 4.22, with a non-linear fit obtained as outlined in detail in [98]. The fit follows concrete Carino's equation [99]:

$$S(t) = S_U \cdot \frac{k_{th} \cdot t}{1 + k_{th} \cdot t} \quad \text{Eq. 4.2}$$

where  $S_U$  is the limiting compressive strength of the concrete (at a theoretical ‘infinite age’) and  $k_{th}$  is a rate constant [ $days^{-1}$ ]. This equation accurately models the strength dependence of traditional OPC based concretes before 28 days, and then becomes less accurate for late stage strengths [98, 100]. It must be noted that this procedure is valid for concrete, but it has been found that it fits quite well also for the non-vibrated geopolymer binder manufactured in this work.

As expected, the evolution of strength is notably slower than for geopolymers cured at elevated temperatures. The mean value of compressive strength for 28 days in case of not vibrated binder has the potential to meet standard BS EN 1504-3:2005 [38] for a non-structural class R1 repair ( $\geq 10$  MPa), but there is a growing degree of strength variability in samples as they cure and it must be noted that the measurement was not strictly complying with the standard BS EN 12190 for compressive strength testing methods for repair materials.

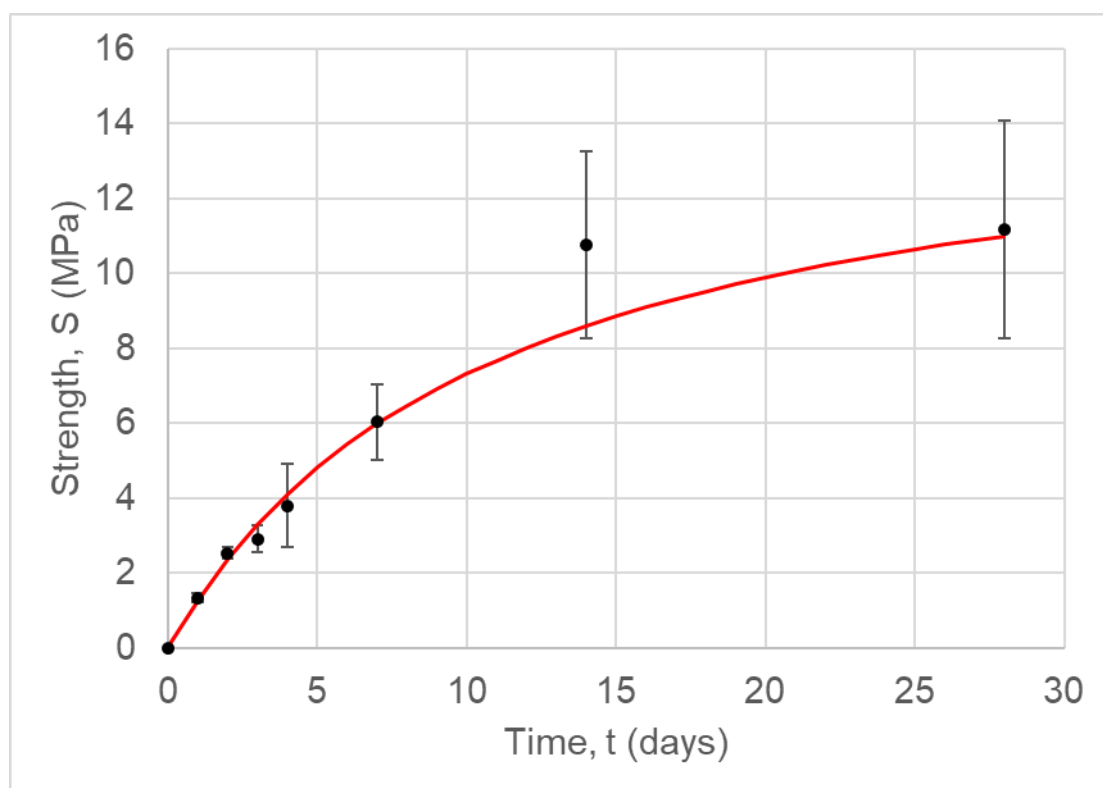


Figure 4.22 - Compressive strength values for non-vibrated geopolymer cubes as a function of time. Error bars show the standard deviation, taken over three cube tests at each time point

It is also interesting to investigate the compressive strength evolution over time in case of vibrated geopolymer binders before being casted into the cubic mould. In this case, the fit with Eq. 4.2 doesn't work well, and the results are shown in Figure 4.23 without fitting, over

56 days. In this case, the mean value of compressive strength for 28 days is between class R1 ( $\geq 10$  MPa) and class R2 ( $\geq 15$  MPa) for non-structural repair, while the mean value of compressive strength for 56 days it's between class R2 ( $\geq 15$  MPa) for non-structural repair, and class R3 ( $\geq 25$  MPa) for structural repair, according to the standard BS EN 1504-3:2005 [38].

These results show that air bubbles are a limiting strength factor on a non-vibrated mix. However, there is a growing degree of strength variability in samples as they cure, and so these results need to be taken with caution. Therefore, it is more safe to consider the material as a potential non-structural repair after 28 days. Moreover, it must be recalled here that the material, in order to be classified to one of the classes described in table 3 of the standard BS EN 1504-3:2005 [38] needs to satisfy the requirements for all the required performance properties. Therefore, the considerations made here need to be taken just as an indication of the repair potential of the ambient cured coatings tested in this work. Despite the coatings were not cured at elevated temperatures, the mechanical properties tested for the sample specimens could allow the material (vibrated and non-vibrated) to be classified as a non-structural repair of the standard BS EN 1504-3:2005.

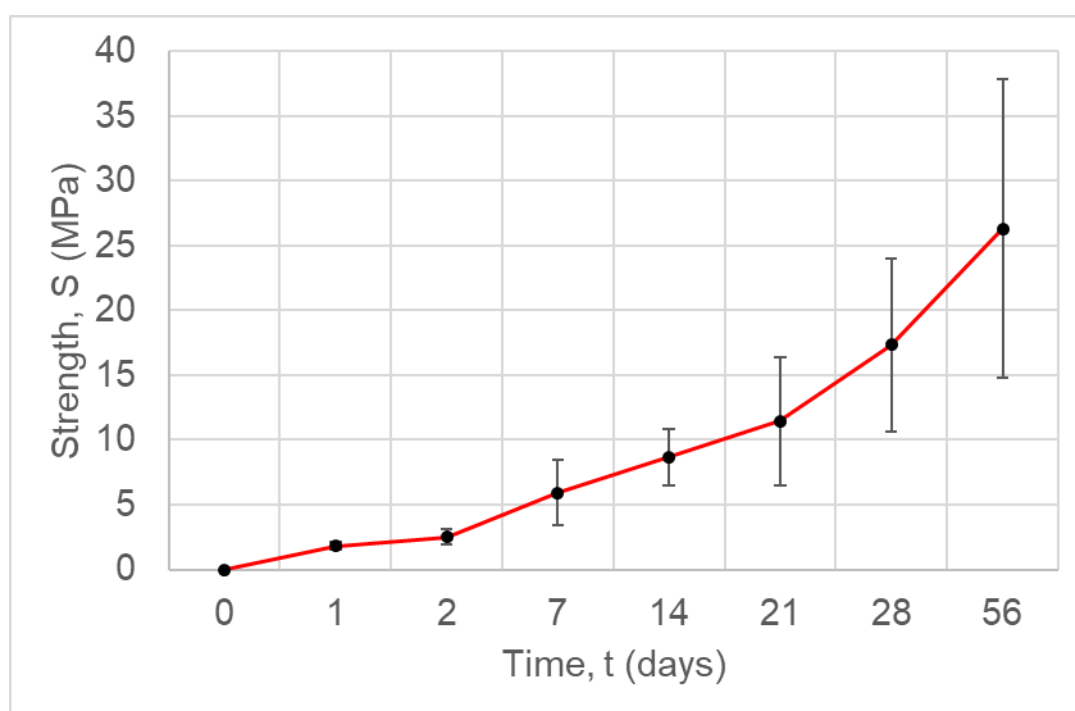


Figure 4.23 - Compressive strength values for geopolymer vibrated cubes as a function of time. Error bars show the standard deviation, taken over three cube tests at each time point

#### 4.4.2.2. Bond strength

The results for the bond strength test, conducted according to the method described in section 4.3.6.6 for vibrated geopolymer binders, are shown in Table 4.5. For roughened concrete surfaces (first row), an average strength value of  $1.82 \pm 0.67$  MPa has been found, while un-treated concrete surfaces (second row) show an average value of  $2.30 \pm 0.39$  MPa.

The two values are quite close if we consider the errors associated, but the coatings applied onto un-treated concrete surfaces show a slightly higher bond strength value than those applied onto roughened concrete surfaces. This result is opposite to that expected, since a roughened surface should create a better bond with the coating material. Besides, the measured values for roughness of both un-treated and treated old concrete surfaces, shown in Table 4.3, are quite different: treated surfaces are much more rough than smooth un-treated surfaces. However, the measure of roughness is given from a method where the average distance from the cloud of the concrete surface points is taken respect to a mean fitting plane of the surface.

From the observation of the two images in Figure 4.7, it is possible to see how the process of roughening makes the surface more rough, but contributes to smooth the depths of the holes in the surface. This means that un-scoured surfaces show deeper holes than scoured surfaces. For this reason, it is likely that less geopolymer binder can enter the holes of a scoured concrete surface, compared to the case of an un-scoured surface. Moreover, from the visual analysis of the types of failure in the two cases (see Table 4.5), one can see a higher percentage of cohesion failure in the concrete substrate in the case of scoured concrete surface specimens, and a prevalence of cohesion failure in the geopolymer coating, in the case of un-scoured surface specimens. The cohesion failure in concrete is an index of a better bond strength of the coating to concrete, and the lower result found for the first row's specimens of Table 4.5 may be due to slight uncertainties in the manual process of applying the loads. In any case, both the bond strength values found are  $\geq 0.8$  MPa, which is a requirement to classify a material as a non-structural repair.

The result found in this preliminary investigation of bond strength constitutes a promising result for the geopolymer coatings, since they are ambient cured and very thin (1 mm).

Further work needs to be done to assess the bond strength strictly according to standards, and the other 9 properties required by the standard, and not analysed in this work.

Type of substrate	Sample specimens					Bond strength [MPa]
	1	2	3	4	5	
Scoured concrete surface						$1.82 \pm 0.67$
Un-scoured concrete surface						$2.30 \pm 0.39$

Table 4.5 - Bond strength results for low calcium geopolymer binders vibrated before application onto scoured (first row) and un-scoured (second row) concrete substrates.

#### 4.4.2.3. Thermal expansion

The results for the coefficient of thermal expansion,  $\alpha$ , measured according to the procedure described in section 4.3.6.7, are shown in Figure 4.24. The graph shows the plots of the contraction of the three samples G1, G2 and G3, measured by the LVDT, as the temperature of the samples was lowered from 20 °C to 2 °C. The  $\alpha$  value for each sample was calculated from equation 4.1, where  $\Delta L$  is the displacement measured between  $T = 20$  °C and  $T = 2$  °C (the two extremities of the curves in Figure 4.24). This range of temperature was chosen because they are representative of the storage facility temperatures in ducts and air inlets, as internal reports for temperature and RH monthly measurements in the SPRS store in Sellafield show. The final value and error for  $\alpha$  is obtained from the average and standard deviation of the three values: it is  $\alpha = 10.6 \cdot 10^{-6} \pm 0.7 \cdot 10^{-6} K^{-6}$ . This result is in accordance with the range of variation of the coefficient of thermal expansion for geopolymer materials, already reported in section 4.2.2. It is also close to the known values for concrete ( $13 \cdot 10^{-6} - 14 \cdot 10^{-6} K^{-6}$  [101]).

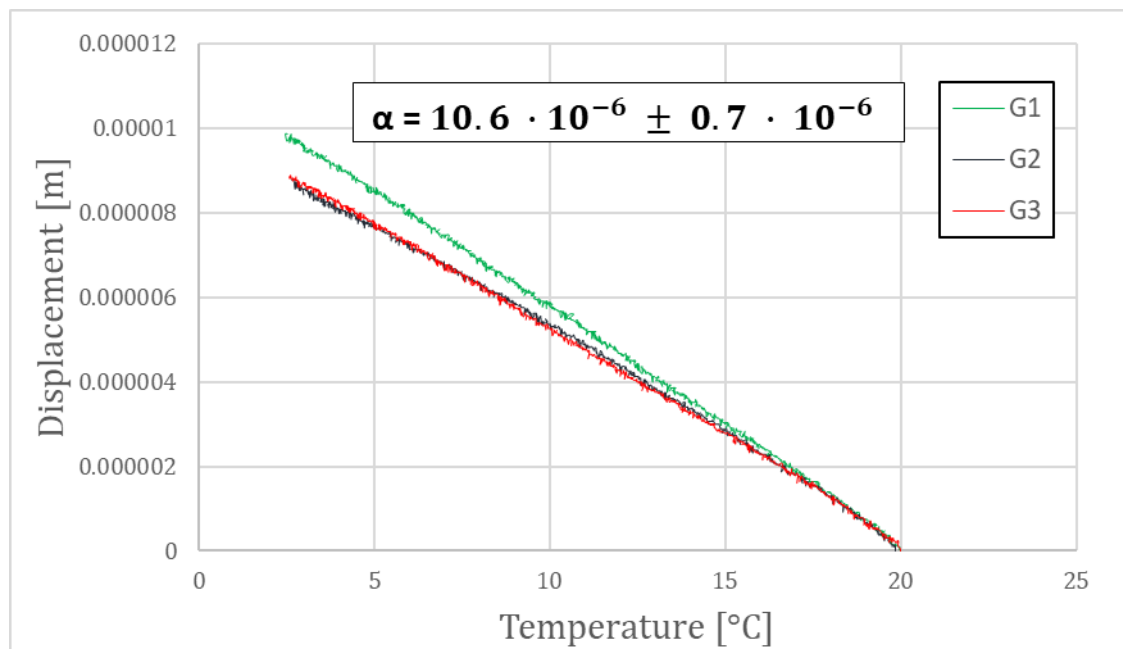


Figure 4.24 – Displacement measured by the LVDT over a range of temperature 2 °C – 20 °C, for three cylindrical geopolymer samples, and the average value of the coefficient of thermal expansion  $\alpha$ .

#### 4.5. Further discussion

The challenge of ambient-cured geopolymer coatings is by no means easy to solve, due to the several competing and interconnected reactions and water transport processes: as the geopolymer cures, more NASH gel is produced, thus resulting in smaller pores, and in some cases in closed pores, and this will change the permeability of the geopolymer and so the water transport inside the geopolymer coating [102].

The Si/Al ratio of the reactants of the geopolymer in this work was 2.5. The actual compositional ratio Si/Al depends on how much aluminosilicate precursor has reacted and on the final product, since a link has been demonstrated between precursor characterization and extent of the reaction [103]. In order to have an idea of the Si/Al ratio of the final geopolymer, a detailed characterization of the geopolymer sample after curing is required, described in [103]. This is beyond the scope of this thesis, but it could be taken into consideration within future work.

Coating thickness was found to play a role in coating integrity. The thickness of cementitious coatings on concrete assets can play a direct role on their overall performance for their intended use. The thickness of patches has also been reported to affect the sensing capabilities of cement-based self-sensing coatings for loading applications. Baeza et al.

reported thinner patches had higher sensing capacity [104] whereas Wang et al. stated that thicker patches gave a higher fractional increase in resistance than thinner patches which was attributed to greater crack propagation in thicker patches compared to thinner ones [105]. While it is yet rather unclear which of the two provide greater sensing capabilities, it can be assumed that the thickness of self-sensing coatings impacts sensing capabilities. Sensing characterization will be discussed in detail in chapters 5, 6 and 7.

Repairs require high strain capacity to resist strain and thus subsequently cracks [66]. Morgan [66] has stated that an ideal repair material should display a similar modulus of elasticity and thermal expansion to the parent substrate and that it should be compatible with the existing structure (in terms of its adhesion strength, capillary water absorption, dilatation properties and durability). The bond strength and thermal expansion of the ambient-cured mix outlined in this thesis are factors that still require some further investigation. In particular, they should be tested also for non-vibrated geopolymer binders, and strictly according to the methods required by the standard for non-structural and structural repairs. Despite this, the preliminary results obtained in this work are promising: the measured value for the coefficient of thermal expansion is similar to the one for concrete; the bond strength value measured satisfies the requirement for a non-structural repair. As the aim of this work is to demonstrate a non-structural repair, for the time being, measurements of elastic modulus are not required (according to BS EN 1504-3:2005 [38]).

## 4.6. Summary and future work

The work presented in this chapter has demonstrated that fly ash geopolymer coatings can be cured at room temperature and high humidities without any additional grinding steps, or additives. While ambient-cured coatings do take longer to cure, they are touch-dry within one day, and are strong enough to have the potential to form a non-structural class R1 repair from 28 days. For vibrated binders, they can reach a non-structural class R2 repair. Accelerants (such as heat or calcium additives) may be required if the application demands more rapid strength development.

It has been found that the main factors which affect coating integrity are related to the retention of water in the geopolymer during its prolonged curing at ambient temperatures. These are:

- Coating thickness: coatings with thickness = 1 mm show no cracks, regardless of mixing times and RH levels between 50% and 95%. Coatings with higher thickness show cracks, the extent of which is dependent on the mixing time;
- Mixing time: for the mix described in this chapter, the optimal mixing time was 1 hour, to allow the main extent of geopolymerisation reactions to occur without loss of water or thermal stress, and to ensure that only small extent of fly ash particles is unreacted. Optimising mixing time can allow geopolymer coatings to overcome water-loss induced cracking and to show a homogeneous surface without voids and bubbles.
- Maturity of concrete: the results show that coating integrity doesn't depend on concrete maturity. This is an important consideration if geopolymer coatings and linings are to be applied to newly cast concrete structures, and not only to old structures which need repair.
- Efflorescence: for low-temperature, but humid curing and prolonged storage conditions (above 70% RH) efflorescence is likely, as excess alkaline solution crystallizes on the surface of the coating. Efflorescence is less likely for relative humidities at or below 50%.

In conclusion, this chapter has outlined the manufacture of ambient-cured geopolymer coatings for concrete, without the use of additives, that may be restricted in a nuclear context. The most important consideration was the interaction between water-transport processes and the geopolymerisation reaction processes responsible for strength gain. While the geopolymer coatings took longer to cure than a thermally cured specimen, they remain a promising choice for retrofitted concrete repairs, rehabilitation and sensing.

Work in future should focus on further research in order to investigate and comply with the following points:

- solutions to the issues of efflorescence in humid environments;
- the influence of a concrete substrate water saturation;
- durability under exposure to a variety of environmental conditions;

- define methods for studying the relationship between coating thickness, shrinkage and integrity after prolonged geopolymer mixing;
- testing all the required properties for the assessment of non-structural repairs strictly according to the methods required by the specific standard, and for vibrated and not vibrated binders.

Moisture and chloride sensing feasibility and characterisation of the ambient cured low calcium fly ash geopolymer binders investigated in this chapter are demonstrated respectively in chapter 5 and chapter 6. The results for chloride sensing and characterisation are preliminary, and further work is required. The final task of this research work is to use the ambient cured low calcium fly ash geopolymer binders developed in this chapter as skin sensors for moisture and chloride sensing in concrete. A very preliminary investigation of moisture and chloride sensing feasibility for coatings will be described in chapter 7.

Next chapter outlines the experimental characterisation of the geopolymer-based moisture sensor developed in this work, providing a literature review on the existing moisture sensing methods for structural health monitoring, and investigates the use of geopolymer binders as sensors, providing a literature review on the state of the art of geopolymers used for sensing applications, and the theory behind the sensing system developed in this work of thesis.

## References

- [1] K. Gobakis, D. Kolokotsa, N. Maravelaki-Kalaitzaki, V. Perdikatsis, and M. Santamouris, "Development and analysis of advanced inorganic coatings for buildings and urban structures," *Energy and Buildings*, vol. 89, pp. 196-205, 2015.
- [2] J. Yang, L.-l. Xu, L. Wang, Z.-b. Zhang, and F. Liu, "Study on new inorganic coating for outdoor," *Journal of Nanjing University of Technology (Natural Science Edition)*, vol. 1, p. 016, 2008.
- [3] H. Y. Moon, D. G. Shin, and D. S. Choi, "Evaluation of the durability of mortar and concrete applied with inorganic coating material and surface treatment system," *Construction and Building Materials*, vol. 21, pp. 362-369, 2007.
- [4] G. Batis, P. Pantazopoulou, and A. Routoulas, "Synergistic effect of corrosion inhibitor and inorganic coating on reinforcement corrosion," *Anti-Corrosion methods and materials*, vol. 48, pp. 107-116, 2001.
- [5] S. Mu, J. Liu, W. Lin, Y. Wang, J. Liu, L. Shi, and Q. Jiang, "Property and microstructure of aluminosilicate inorganic coating for concrete: Role of water to solid ratio," *Construction and Building Materials*, vol. 148, pp. 846-856, 2017.
- [6] A. F.-J. P. Duxon, J. L. Provis, G. C. Luckey, A. Palomo, J. S. J. Van Deventer, "Geopolymer technology: the current state of the art," vol. 42:2917-2933, 2007.
- [7] Z. Zhang, X. Yao, and H. Zhu, "Potential application of geopolymers as protection coatings for marine concrete: II. Microstructure and anticorrosion mechanism," *Applied clay science*, vol. 49, pp. 7-12, 2010.
- [8] Z. Zhang, X. Yao, and H. Wang, "Potential application of geopolymers as protection coatings for marine concrete III. Field experiment," *Applied Clay Science*, vol. 67, pp. 57-60, 2012.
- [9] F. Pacheco-Torgal, J. B. de Aguiar, Y. Ding, W. Tahri, and S. Baklouti, "Performance of alkali-activated mortars for the repair and strengthening of OPC concrete," in *Handbook of Alkali-Activated Cements, Mortars and Concretes*, ed: Elsevier, 2015, pp. 627-641.
- [10] A. T. Pinto and E. Vieira, "Repairing of damaged stone in monuments and stone buildings," in *Proceedings of the World Congress Geopolymer*, 2005, pp. 173-176.
- [11] W. Yodsudjai, "Application of fly ash-based geopolymer for structural member and repair materials," in *Advances in Science and Technology*, 2014, pp. 74-83.
- [12] T. Bakharev, "Geopolymeric materials prepared using Class F fly ash and elevated temperature curing," *Cement and concrete research*, vol. 35, pp. 1224-1232, 2005.
- [13] M. Criado, A. Palomo, A. Fernández-Jiménez, and P. Banfill, "Alkali activated fly ash: effect of admixtures on paste rheology," *Rheologica Acta*, vol. 48, pp. 447-455, 2009.
- [14] J. Temuujin, R. Williams, and A. Van Riessen, "Effect of mechanical activation of fly ash on the properties of geopolymer cured at ambient temperature," *Journal of materials processing technology*, vol. 209, pp. 5276-5280, 2009.
- [15] Y. Zarina, M. M. Al Bakri Abdullah, H. Kamarudin, I. Khairul Nizar, and R. Abd Razak, "Reviews on the geopolymer materials for coating application," in *Advanced Materials Research*, 2013, pp. 958-962.
- [16] H. Zhu, G. Liang, J. Xu, Q. Wu, and J. Du, "Surface-modification of fly ash and its effect on strength and freezing resistance of slag based geopolymer," *Construction and Building Materials*, vol. 199, pp. 574-580, 2019.

- [17] M. Babae and A. Castel, "Chloride diffusivity, chloride threshold, and corrosion initiation in reinforced alkali-activated mortars: Role of calcium, alkali, and silicate content," *Cement and Concrete Research*, vol. 111, pp. 56-71, 2018.
- [18] J. Osio-Norgaard, J. P. Gevaudan, and W. V. Srubar III, "A review of chloride transport in alkali-activated cement paste, mortar, and concrete," *Construction and Building Materials*, vol. 186, pp. 191-206, 2018.
- [19] H. Yoon, S. M. Park, and H.-K. Lee, "Effect of MgO on chloride penetration resistance of alkali-activated binder," *Construction and Building Materials*, vol. 178, pp. 584-592, 2018.
- [20] S. A. Bernal, E. D. Rodríguez, R. M. de Gutiérrez, M. Gordillo, and J. L. Provis, "Mechanical and thermal characterisation of geopolymers based on silicate-activated metakaolin/slag blends," *Journal of materials science*, vol. 46, pp. 5477-5486, 2011.
- [21] G. F. Huseien, J. Mirza, M. Ismail, S. Ghoshal, and A. A. Hussein, "Geopolymer mortars as sustainable repair material: A comprehensive review," *Renewable and Sustainable Energy Reviews*, vol. 80, pp. 54-74, 2017.
- [22] K. Somna, C. Jaturapitakkul, P. Kajitvichyanukul, and P. Chindaprasirt, "NaOH-activated ground fly ash geopolymer cured at ambient temperature," *Fuel*, vol. 90, pp. 2118-2124, 2011.
- [23] J. Xie and O. Kayali, "Effect of initial water content and curing moisture conditions on the development of fly ash-based geopolymers in heat and ambient temperature," *Construction and building materials*, vol. 67, pp. 20-28, 2014.
- [24] J. Davidovits, *Geopolymer chemistry and applications*: Geopolymer Institute, 2008.
- [25] I. P. G. D. Parias, T. Perraki, "Effect of synthesis parameters on the mechanical properties of fly ash-based geopolymers," vol. 301 (2007) 246-254, 2007.
- [26] P. Wattanachai and T. Suwan, "Strength of Geopolymer Cement Curing at Ambient Temperature by Non-Oven Curing Approaches: An Overview," in *IOP Conference Series: Materials Science and Engineering*, 2017, p. 012014.
- [27] G. Fang, H. Bahrami, and M. Zhang, "Mechanisms of autogenous shrinkage of alkali-activated fly ash-slag pastes cured at ambient temperature within 24 h," *Construction and Building Materials*, vol. 171, pp. 377-387, 2018.
- [28] M. C. Bignozzi, S. Manzi, M. E. Natali, W. D. Rickard, and A. Van Riessen, "Room temperature alkali activation of fly ash: The effect of Na<sub>2</sub>O/SiO<sub>2</sub> ratio," *Construction and Building Materials*, vol. 69, pp. 262-270, 2014.
- [29] S. Hsu, M. Chi, and R. Huang, "Effect of fineness and replacement ratio of ground fly ash on properties of blended cement mortar," *Construction and Building Materials*, vol. 176, pp. 250-258, 2018.
- [30] H. Fanghui, W. Qiang, and F. Jingjing, "The differences among the roles of ground fly ash in the paste, mortar and concrete," *Construction and Building Materials*, vol. 93, pp. 172-179, 2015.
- [31] G. Mucsi, S. Kumar, B. Csőke, R. Kumar, Z. Molnár, Á. Rácz, F. Máda, and Á. Debreczeni, "Control of geopolymer properties by grinding of land filled fly ash," *International Journal of Mineral Processing*, vol. 143, pp. 50-58, 2015.
- [32] F. Puertas, S. Martínez-Ramírez, S. Alonso, and T. Vazquez, "Alkali-activated fly ash/slag cements: strength behaviour and hydration products," *Cement and Concrete Research*, vol. 30, pp. 1625-1632, 2000.
- [33] S. A. Bernal, J. L. Provis, B. Walkley, R. San Nicolas, J. D. Gehman, D. G. Brice, A. R. Kilcullen, P. Duxson, and J. S. van Deventer, "Gel nanostructure in alkali-activated binders based on slag and fly ash, and effects of accelerated carbonation," *Cement and Concrete Research*, vol. 53, pp. 127-144, 2013.

- [34] P. Nath and P. K. Sarker, "Effect of GGBFS on setting, workability and early strength properties of fly ash geopolymer concrete cured in ambient condition," *Construction and Building Materials*, vol. 66, pp. 163-171, 2014.
- [35] P. S. Deb, P. Nath, and P. K. Sarker, "The effects of ground granulated blast-furnace slag blending with fly ash and activator content on the workability and strength properties of geopolymer concrete cured at ambient temperature," *Materials & Design (1980-2015)*, vol. 62, pp. 32-39, 2014.
- [36] G. Fang, W. K. Ho, W. Tu, and M. Zhang, "Workability and mechanical properties of alkali-activated fly ash-slag concrete cured at ambient temperature," *Construction and Building Materials*, vol. 172, pp. 476-487, 2018.
- [37] P. S. Deb, P. Nath, and P. K. Sarker, "Drying shrinkage of slag blended fly ash geopolymer concrete cured at room temperature," *Procedia Engineering*, vol. 125, pp. 594-600, 2015.
- [38] B. EN, "1504-3 (2005) Products and systems for the protection and repair of concrete structures. Definitions, requirements, quality control and evaluation of conformity. Structural and non-structural repair," *British Standard Institute*.
- [39] M. Saafi, G. Piukovics, and J. Ye, "Hybrid graphene/geopolymeric cement as a superionic conductor for structural health monitoring applications," *Smart Materials and Structures*, vol. 25, p. 105018, 2016.
- [40] L. Biondi, M. Perry, C. Vlachakis, and A. Hamilton, "Smart cements: repairs and sensors for concrete assets," in *Sensors and Smart Structures Technologies for Civil, Mechanical, and Aerospace Systems 2018*, 2018, p. 105982U.
- [41] C. Vlachakis, L. Biondi, and M. Perry, "3D printed smart repairs for civil infrastructure," in *9th European Workshop on Structural Health Monitoring Series (EWSHM)*, 2018, pp. 1-12.
- [42] M. Perry, M. Saafi, G. Fusiek, and P. Niewczas, "Geopolymeric thermal conductivity sensors for surface-mounting onto concrete structures," 2016.
- [43] M. Perry, M. Saafi, G. Fusiek, and P. Niewczas, "Hybrid optical-fibre/geopolymer sensors for structural health monitoring of concrete structures," *Smart Materials and Structures*, vol. 24, p. 045011, 2015.
- [44] S. Hu, H. Wang, G. Zhang, and Q. Ding, "Bonding and abrasion resistance of geopolymeric repair material made with steel slag," *Cement and concrete composites*, vol. 30, pp. 239-244, 2008.
- [45] Z. Zhang, H. Wang, J. L. Provis, and A. Reid, "Efflorescence: a critical challenge for geopolymer applications?," in *Concrete Institute of Australia's Biennial National Conference 2013*, 2013, pp. 1-10.
- [46] Z. Zhang, J. L. Provis, A. Reid, and H. Wang, "Fly ash-based geopolymers: the relationship between composition, pore structure and efflorescence," *Cement and concrete research*, vol. 64, pp. 30-41, 2014.
- [47] L. Struble, E. Kim, and L. Gómez-Zamorano, "Overview of Geopolymer Cement," in *Geopolymer Binder Systems*, ed: ASTM International, 2013.
- [48] P. Lura, O. M. Jensen, and K. van Breugel, "Autogenous shrinkage in high-performance cement paste: An evaluation of basic mechanisms," *Cement and concrete research*, vol. 33, pp. 223-232, 2003.
- [49] R. M. Vijayakumar, "Evaluating shrinkage of fly ash-slag geopolymers," University of Illinois at Urbana-Champaign, 2013.
- [50] M. Nedeljković, M. Luković, K. van Breugel, D. Hordijk, and G. Ye, "Development and application of an environmentally friendly ductile alkali-activated composite," *Journal of cleaner production*, vol. 180, pp. 524-538, 2018.
- [51] J. Zhou, G. Ye, and K. van Breugel, "Cement hydration and microstructure in concrete repairs with cementitious repair materials," *Construction and Building Materials*, vol. 112, pp. 765-772, 2016.

- [52] Y. C. Zheng, "Shrinkage behaviour of geopolymer," 2009.
- [53] C. Montes and E. Allouche, "Rheological Behavior of Fly-Ash-Based Geopolymers," in *Geopolymer Binder Systems*, ed: ASTM International, 2013.
- [54] A. Palomo, P. Banfill, A. Fernández-Jiménez, and D. Swift, "Properties of alkali-activated fly ashes determined from rheological measurements," *Advances in Cement Research*, vol. 17, pp. 143-151, 2005.
- [55] M. Palacios, P. F. Banfill, and F. Puertas, "Rheology and setting of alkali-activated slag pastes and mortars: effect of organic admixture," *ACI Materials Journal*, vol. 105, p. 140, 2008.
- [56] A. I. Laskar and R. Bhattacharjee, "Rheology of Fly-Ash-Based Geopolymer Concrete," *ACI Materials Journal*, vol. 108, 2011.
- [57] P. Suraneni, S. Puligilla, E. H. Kim, X. Chen, L. J. Struble, and P. Mondal, "Monitoring setting of geopolymers," *Advances in Civil Engineering Materials*, vol. 3, pp. 177-192, 2014.
- [58] E. N. Julio, F. A. Branco, and V. t. D. Silva, "Concrete-to-concrete bond strength. Influence of the roughness of the substrate surface," *Construction and Building materials*, vol. 18, pp. 675-681, 2004.
- [59] H. Beushausen and M. Alexander, "Bond strength development between concretes of different ages," *Magazine of concrete research*, vol. 60, pp. 65-74, 2008.
- [60] A. D. Espeche and J. León, "Estimation of bond strength envelopes for old-to-new concrete interfaces based on a cylinder splitting test," *Construction and Building Materials*, vol. 25, pp. 1222-1235, 2011.
- [61] L. Courard, J.-F. Lenaers, F. Michel, and A. Garbacz, "Saturation level of the superficial zone of concrete and adhesion of repair systems," *Construction and Building Materials*, vol. 25, pp. 2488-2494, 2011.
- [62] L. Courard, T. Piotrowski, and A. Garbacz, "Near-to-surface properties affecting bond strength in concrete repair," *Cement and Concrete Composites*, vol. 46, pp. 73-80, 2014.
- [63] M. Mohammadi, R. M. Moghtadaei, and N. A. Samani, "Influence of silica fume and metakaolin with two different types of interfacial adhesives on the bond strength of repaired concrete," *Construction and Building Materials*, vol. 51, pp. 141-150, 2014.
- [64] J. Qian, C. You, Q. Wang, H. Wang, and X. Jia, "A method for assessing bond performance of cement-based repair materials," *Construction and Building Materials*, vol. 68, pp. 307-313, 2014.
- [65] F. Pacheco-Torgal, Z. Abdollahnejad, S. Miraldo, S. Baklouti, and Y. Ding, "An overview on the potential of geopolymers for concrete infrastructure rehabilitation," *Construction and Building Materials*, vol. 36, pp. 1053-1058, 2012.
- [66] D. Morgan, "Compatibility of concrete repair materials and systems," *Construction and building materials*, vol. 10, pp. 57-67, 1996.
- [67] C. Zanotti, P. H. Borges, A. Bhutta, and N. Banthia, "Bond strength between concrete substrate and metakaolin geopolymer repair mortar: Effect of curing regime and PVA fiber reinforcement," *Cement and Concrete Composites*, vol. 80, pp. 307-316, 2017.
- [68] N. Emberson and G. Mays, "Significance of property mismatch in the patch repair of structural concrete Part 1: Properties of repair systems," *Magazine of Concrete Research*, vol. 42, pp. 147-160, 1990.
- [69] N. Emberson and G. Mays, "Significance of property mismatch in the patch repair of structural concrete Part 2: Axially loaded reinforced concrete members," *Magazine of Concrete Research*, vol. 42, pp. 161-170, 1990.
- [70] R. Emmons, *CONCRETE REPAIR AND MAINTENANCE ILLUSTRATED. PROBLEM ANALYSIS. REPAIR STRATEGY. TECHNIQUES*, 1993.

- [71] H. Szklorzová and V. Bílek, "Influence of alkali ions in the activator on the performance of alkali-activated mortars," in *3rd International Symposium on Non-traditional Cement and Concrete. Brno: Czech Republic, 2008*.
- [72] A. Warid Wazien, M. M. Al Bakri Abdullah, M. Mohd Remy Rozainy, M. F. M. Tahir, and K. Hussin, "Potential of Geopolymer Mortar as Concrete Repairing Materials," in *Materials Science Forum, 2016*.
- [73] A. Shash, "Repair of concrete beams—a case study," *Construction and Building Materials*, vol. 19, pp. 75-79, 2005.
- [74] J. Mirza, M. Mirza, and R. Lapointe, "Laboratory and field performance of polymer-modified cement-based repair mortars in cold climates," *Construction and Building Materials*, vol. 16, pp. 365-374, 2002.
- [75] F. Pacheco-Torgal, J. Castro-Gomes, and S. Jalali, "Alkali-activated binders: A review: Part 1. Historical background, terminology, reaction mechanisms and hydration products," *Construction and Building Materials*, vol. 22, pp. 1305-1314, 2008.
- [76] B. EN, "1542—Products and systems for the protection and repair of concrete structures-Test methods-Measurement of bond strength by pull-off," *British Standard Institution, London, 1999*.
- [77] J. Davidovits, "Geopolymers: inorganic polymeric new materials," *Journal of Thermal Analysis and calorimetry*, vol. 37, pp. 1633-1656, 1991.
- [78] M. Criado, W. Aperador, and I. Sobrados, "Microstructural and mechanical properties of alkali activated Colombian raw materials," *Materials*, vol. 9, p. 158, 2016.
- [79] L. Courard, "Adhesion of repair systems to concrete: influence of interfacial topography and transport phenomena," *Magazine of Concrete Research*, vol. 57, pp. 273-282, 2005.
- [80] H. Koh, D. Yeoh, and S. Shahidan, "Effect of re-vibration on the compressive strength and surface hardness of concrete," in *Materials Science and Engineering Conference Series, 2017*, p. 012057.
- [81] B. EN, "1504-2: 2004—Products and systems for the protection and repair of concrete structures," *Definitions, requirements, quality control and evaluation of conformity—Part, vol. 2, 2004*.
- [82] C. Pellegrino, F. da Porto, and C. Modena, "Rehabilitation of reinforced concrete axially loaded elements with polymer-modified cementitious mortar," *Construction and Building Materials*, vol. 23, pp. 3129-3137, 2009.
- [83] Z. Zuhua, Y. Xiao, Z. Huajun, and C. Yue, "Role of water in the synthesis of calcined kaolin-based geopolymer," *Applied Clay Science*, vol. 43, pp. 218-223, 2009.
- [84] D. P. Bentz, K. A. Snyder, and P. E. Stutzman, "Hydration of Portland cement: The effects of curing conditions," in *Proceedings of the 10th International Congress on the Chemistry of Cement, 1997*.
- [85] A. Garbacz, L. Courard, and B. Bissonnette, "A surface engineering approach applicable to concrete repair engineering," *Bulletin of the Polish Academy of Sciences: Technical Sciences*, vol. 61, pp. 73-84, 2013.
- [86] BSI, "BS EN 196-1: 2005: Methods of testing cement. Determination of strength," ed: BSI London, UK, 2005.
- [87] D. Bradley and G. Roth, "Adaptive thresholding using the integral image," *Journal of graphics tools*, vol. 12, pp. 13-21, 2007.
- [88] M. Seul, M. J. Sammon, and L. O'Gorman, "Practical Algorithms for Image Analysis Description," *Examples, and Code, ISBN*, vol. 521660653, 2000.

- [89] D. Ioannou, W. Huda, and A. F. Laine, "Circle recognition through a 2D Hough transform and radius histogramming," *Image and vision computing*, vol. 17, pp. 15-26, 1999.
- [90] A. Momayez, M. Ehsani, A. Ramezani-pour, and H. Rajaie, "Comparison of methods for evaluating bond strength between concrete substrate and repair materials," *Cement and concrete research*, vol. 35, pp. 748-757, 2005.
- [91] "Products and systems for the protection and repair of concrete structures. Test methods. ," in *Determination of the coefficient of thermal expansion*, ed: BSI, 1998, p. 14.
- [92] P. A. Tipler and G. Mosca, *Physics for Scientists and Engineers*: W. H. Freeman, 2007.
- [93] W. Piasta and B. Zarzycki, "The effect of cement paste volume and w/c ratio on shrinkage strain, water absorption and compressive strength of high performance concrete," *Construction and Building Materials*, vol. 140, pp. 395-402, 2017.
- [94] B. t. Bissonnette, P. Pierre, and M. Pigeon, "Influence of key parameters on drying shrinkage of cementitious materials," *Cement and Concrete Research*, vol. 29, pp. 1655-1662, 1999.
- [95] G. Ma and L. Wang, "A critical review of preparation design and workability measurement of concrete material for largescale 3D printing," *Frontiers of Structural and Civil Engineering*, vol. 12, pp. 382-400, 2018.
- [96] I. García-Lodeiro, A. Palomo, A. Fernández-Jiménez, and D. Macphee, "Compatibility studies between NASH and CASH gels. Study in the ternary diagram Na<sub>2</sub>O–CaO–Al<sub>2</sub>O<sub>3</sub>–SiO<sub>2</sub>–H<sub>2</sub>O," *Cement and Concrete Research*, vol. 41, pp. 923-931, 2011.
- [97] T. Phoo-ngernkham, P. Chindaprasirt, V. Sata, S. Hanjitsuwan, and S. Hatanaka, "The effect of adding nano-SiO<sub>2</sub> and nano-Al<sub>2</sub>O<sub>3</sub> on properties of high calcium fly ash geopolymer cured at ambient temperature," *Materials & Design*, vol. 55, pp. 58-65, 2014.
- [98] M. Perry, G. Fusiek, P. Niewczas, T. Rubert, and J. McAlorum, "Wireless concrete strength monitoring of wind turbine foundations," *Sensors*, vol. 17, p. 2928, 2017.
- [99] N. J. Carino, "The maturity method: theory and application," *Cement, concrete and aggregates*, vol. 6, pp. 61-73, 1984.
- [100] M. A. Elsageer, S. G. Millard, and S. J. Barnett, "Strength development of concrete containing coal fly ash under different curing temperature conditions," in *World of Coal Ash (WOCA) Conference, Lexington, KY, USA*, 2009.
- [101] A. GOULDSTONE, W. CHOI, W. CHI, Y. WU, and S. SAMPATH, "Mechanical, thermal and electrical properties of cold sprayed coatings," in *The Cold Spray Materials Deposition Process*, ed: Elsevier, 2007, pp. 245-263.
- [102] Y. Ma, J. Hu, and G. Ye, "The pore structure and permeability of alkali activated fly ash," *Fuel*, vol. 104, pp. 771-780, 2013.
- [103] A. Van Riessen, W. Rickard, R. Williams, and G. Van Riessen, "Methods for geopolymer formulation development and microstructural analysis," *Journal of Ceramic Science and Technology*, vol. 8, pp. 421-431, 2017.
- [104] F. Baeza, O. Galao, E. Zornoza, and P. Garcés, "Multifunctional cement composites strain and damage sensors applied on reinforced concrete (RC) structural elements," *Materials*, vol. 6, pp. 841-855, 2013.
- [105] W. Wang, H. Dai, and S. Wu, "Mechanical behavior and electrical property of CFRC-strengthened RC beams under fatigue and monotonic loading," *Materials Science and Engineering: A*, vol. 479, pp. 191-196, 2008.

# 5. GEOPOLYMER-BASED MOISTURE SENSORS

## 5.1. Introduction

The economic and social effects of aging, deterioration and extreme events on concrete infrastructures have led to the awareness of the need for advanced structural health monitoring and damage detection technologies [1]. Reinforced concrete structures can employ a network of optical or electronic sensors to monitor the main causes of deterioration [1, 2], and automated measurements of strain, temperature or chemical contamination have been previously used to provide assessments of structural health. The goal of these techniques is to allow in-operation monitoring, in order to optimise maintenance and inspection [3]. This has been also demonstrated by integrating smart material technology into health-monitoring systems [3, 4]. Smart materials are defined as materials with built-in sensing and/or actuation functions [5]. They can serve as sensors, with the advantage that they can be placed with different sizes even in remote and inaccessible locations of various types of structures [3].

In particular, moisture plays a critical role in reinforced concrete corrosion, underpinning structural degradation which costs the global economy a staggering \$2.3 trillion per year (3.4% GDP, 2013)[6, 7]. This growing sum must be added to the significant social and environmental costs of continually maintaining concrete, especially as it underpins most

public services and utilities. Both moisture sensors and repair materials that limit water ingress are required, but monitoring and maintenance are often viewed as separate challenges.

Sensors for locating and quantifying moisture in concrete are key because water plays a leading role in reinforced concrete corrosion, accelerating the infiltration of carbonation, chloride attack and freeze-thaw damage [8-10], as already discussed in detail in chapter 2. As moisture data can support degradation models and proactive asset management strategies [2, 11], moisture sensors are naturally a topic of prime interest within concrete health monitoring [12-21]. The level of interest is particularly keen within industries with significant inventories of safety-critical coastal, marine and riverside concrete assets, such as nuclear, transport, and off-shore energy generation sectors. This is the context in which the technology developed and characterised in this work has been conceived, as already seen in detail in chapter 2: nuclear concrete containments.

This chapter outlines a first-time demonstration of moisture sensors based on low calcium fly ash geopolymers. As already seen in chapters 3 and 4, such materials are a class of cementitious materials, which can be used as repairs for concrete. As shown in the previous chapter, they exhibit similar thermal and mechanical properties to ordinary Portland cement and adhere strongly to concrete substrates [22]. Geopolymers are also chemically stable and show electrical conductivities in the range  $10^{-6} - 10^{-2}$  S/cm depending on mix design [23-25]. The electrical conductivity of geopolymers is due to the presence of the alkali metal ions ( $\text{Na}^+$ , in the case of this work) introduced by the activator solution. This has allowed to utilize them as ionic conductors, to correlate their electrical properties with physical and chemical measurands. For this reason, geopolymers are highly suited to concrete monitoring and maintenance applications, as ‘smart materials’: they have already been developed as sensors for strain and temperature based on impedance measurements [25-29]. At the time of writing, no literature has been found on geopolymer sensors for water and chloride content. This constitutes one major novelty of this thesis: the study outlined in this chapter and in chapter 6 demonstrates the feasibility of moisture and chloride sensing using geopolymers, and furthers the current understanding of the role of moisture and chloride in the ionic conductivity of alkali-activated materials.

In this chapter, electrochemical impedance spectroscopy and equivalent circuit models are used to understand and optimize the electrical response of geopolymer sensors to water content and temperature. This work is anticipated to be the first stage in developing 2D,

distributed sensor-repairs for concrete structures, and other chemical sensors that support concrete structural health monitoring and prognostics.

Numerous methods for continuous moisture monitoring in concrete have already been proposed by previous authors, including: fibre-optic sensors [30, 31]; concrete electrical resistance/conductivity/impedance measurements [32-43]; dielectric permittivity and capacitive sensors [44]; and NEMS/MEMS (nano-/micro- electro-mechanical systems) sensors [45]. It must be noted that most of these methods are directly applied onto concrete, and they often consist of embedding electrodes or other sensing systems (such as optical fibres) directly into concrete. A more detailed overview on the state of the art of existing moisture sensing methods is provided in section 5.2.2. Each of these approaches can be viable in the face of a specific application.

The low calcium fly ash geopolymer sensors proposed in this work of thesis do, however, offer unique benefits: i) they do not directly embed electrodes into concrete; ii) they are multi-functional, offering both sensing and repair capability; and iii) they can be applied as 2-dimensional skin sensors, and so could support the distributed sensing of parameters [46]. Before distributed moisture sensing can be explored, one must first demonstrate that moisture sensing using geopolymers is feasible. This is the aim of the work outlined in this chapter. The work outlined here achieves this aim by developing a sensor prototype and characterising its response and performance under temperature and moisture cycling.

The remainder of this chapter is organised as follows:

- Section 5.2 provides a review on the state of the art of geopolymer sensors for structural health monitoring in general (section 5.2.1), and a review of the existing methods for monitoring moisture in concrete, by highlighting their advantages and weaknesses (section 5.2.2);
- section 5.3 describes the theory behind the principle of geopolymer sensing, with a particular focus on moisture sensing;
- section 5.4 describes the materials and methods used for the geopolymer moisture sensing characterisation;
- section 5.5 presents the results and discussion of this system characterisation,
- Section 5.6 concludes the chapter with a summary, and outlines future work.

## 5.2. State of the art

Geopolymers have been already used for strain and temperature sensing applications applied to structural health monitoring: some authors used them as smart materials/adhesives coupled with fiber optics sensors [2, 47, 48], while other authors took advantage of their electrolyte nature [2, 25-29]. The direct piezoelectric effect in geopolymers has made them suitable to be explored also as self-sensing materials. At the time of writing, no previous literature is found on geopolymer moisture sensing, and most of the existing methods to monitor moisture have been directly applied to concrete specimens. This work represents the first time demonstration of moisture sensing for geopolymer materials. A detailed review on the existing methods to monitor moisture in concrete for structural health monitoring is presented in section 5.2.2, while section 5.2.1 below provides a review on the existing geopolymer-based sensing applications applied to structural health monitoring (SHM).

### 5.2.1. Previous geopolymer-based sensor applications

The research into low-cost, durable sensors for SHM has led to the use of piezoresistive strain sensors based on conductive composites (typically polymers) or self-sensing cementitious materials, in most cases with the addition of conductive fillers, such as carbon fibers/nanotubes/nanofibers and graphene [49-55]. In these sensors, mechanical deformation causes a change in electrical properties. They have been successfully developed for several SHM applications, for their low cost, chemical stability, good durability and good compatibility with host structures. Some authors have developed these sensors using geopolymer binders, patches and concrete, both as conductive composites to couple with concrete structures, and self-sensing cementitious materials. Geopolymer was demonstrated to possess a direct piezoresistive effect originating from the migration of mobile hydrated cations in the pores of the geopolymeric structure under loading [56, 57]. A preliminary study conducted on both Portland cement and geopolymer concrete [58] demonstrated the superior conductance of geopolymer concrete. Most of the authors have used conductive fillers to improve further geopolymer conductivity. It has been demonstrated that the incorporation of conductive fillers has provided a conductive network which can greatly improve the self-sensing capability of a geopolymeric material

[57, 59]. The following table summarises the main geopolymer-based sensing applications and studies, by classifying them depending on the measurands investigated.

<b>Measurands</b>	<b>Shown in</b>
<b>Strain</b>	[2, 25, 28, 57, 59-61]
<b>Temperature</b>	[2, 28, 48]
<b>Moisture</b>	No previous literature
<b>Chloride</b>	No previous literature
<b>Thermal conductivity</b>	[27]

Table 5.1 – Review of physical and chemical measurand investigated in previous applications of geopolymers to structural health monitoring.

As shown in Table 5.1 only temperature, strain and thermal conductivity geopolymer sensors have been investigated so far. The two main sensing methods are based on optical fiber sensors and impedance measurements. Optical fiber sensors require geopolymers as adhesives to be fixed onto concrete, and as shielding materials. Despite their advantages, such as high accuracy and resolution among the others, optical fibers show the technical challenge of providing affordable, long-term packaging to the fibers.

Impedance based sensors can be both self-sensing geopolymer composites and geopolymer patches applied onto concretes. Despite the fact that geopolymers are themselves conductive, thanks to the metal cations introduced by the alkaline activator in the pore solution of the material, the works reviewed in Table 5.1 used conductive fillers such as carbon fibers (CFs), carbon nanotubes/nanofibers (CNTs/CNFs) and graphene to further improve conductivity and piezoresistive effect in geopolymers. This has been done also for other less conductive cementitious materials for structural health monitoring applications [26, 28, 53-55]. However, it must be noted that large-scale deployment of conductive fillers in cementitious composites is limited due to serious issues including poor dispersibility, incompatibility with the host materials, costs and health risks [25]. Moreover, the addition of such fillers in safety-critical applications, such as those in nuclear context, introduces a further issue, connected with the interaction of those materials with ionising radiation. For this reason, no conductive fillers have been introduced in the fly ash geopolymer binders developed in this work of thesis: the newly developed sensing technology for moisture and chloride sensing in nuclear context relies on the conductivity of the only geopolymer pore solution.

The work presented in this thesis represents the first time demonstration in literature of geopolymers as moisture and chloride sensors. The aim of this chapter is to demonstrate

the feasibility of such system and its sensing performances for moisture sensing. Before this is done, a detailed review on the existing methods to monitor moisture for structural health monitoring in literature is outlined in the following section.

### 5.2.2. Moisture monitoring methods for structural health: a review

Several methods have been used in previous works to monitor water content or water content profiles into concrete structures. They have been mentioned and referenced in the introduction above, and recalled here: fiber-optic sensors [30, 31]; concrete electrical resistance/conductivity/impedance measurements [32-43]; capacitive sensors [44]; and NEMS/MEMS (nano-/micro- electro-mechanical systems) sensors [45].

A summary with the main advantages and disadvantages of each technique is shown in the following Table 5.2. In the following sub-sections, these methods are described in detail.

	Advantages	Disadvantages
<b>Fiber-optic sensors</b>	Small dimensions Lightweight Sufficiently high resolution and accuracy Able to transmit signal over a long distance Immune to electromagnetic wave interference	Technical challenge of providing affordable, long-term packaging Invasive: Mostly embedded into concrete
<b>Concrete conductivity/resistivity/impedance measurements</b>	Simple procedure that uses cheap equipment	Less accurate Invasive: Mostly embedded onto concrete
<b>Capacitive sensors</b>	Accuracy $\pm 1 - 1.7$ % RH for early age samples Affordable	Reduced accuracy, for RH > 90% Measurement time from 3 hours to weeks Invasiveness: Drilled holes into concrete Measurement of Relative Humidity, not water content
<b>NEMS/MEMS</b>	Small and robust integrated technology Moisture and temperature monitoring	Invasiveness: A number of devices embedded into concrete More suitable for early age concretes

Table 5.2 – Advantages and disadvantages of the main moisture sensing methods in literature, used for Structural Health Monitoring.

### 5.2.2.1. Capacitive sensors

Capacitive sensors are mainly used as relative humidity (RH) sensors. They are small capacitors consisting of a hygroscopic dielectric material (typically a polymer or plastic material) placed between two electrodes, where the absorption of moisture results in an increase in sensor capacitance. This type of sensor relies on the relationship between relative humidity, the amount of moisture present in the sensor, and sensor capacitance. A hygrometer which utilises a capacitive sensor typically consists of the sensor itself, a probe,

a cable and the related electronics. This type of sensors is also generally affordable, but presents a reduced accuracy at RH values exceeding 90% [32].

Molina et al. [44] used a capacitive hygrometer to assess the moisture state of cementitious materials, by drilling measurement holes in the material. The authors preferred this method to other methods because of the universal value of RH for any different materials, material degree of maturity, and influence of other adjacent materials. However, depending on external conditions and thickness of the material, the measurement time ranges from 3 hours (for early age materials) to weeks, and in some cases the insertion of test tubes directly after casting is recommended to avoid longer times. Moreover, if the climatic conditions at the measurement site are difficult, it is preferable to measure the RH on material specimens taken in situ. Therefore, this method presents some disadvantages, since it requires holes to be drilled into the substrate material, it takes even weeks in the worst case scenario, while only for early age materials it needs about 3 hours for the measurement. Moreover, relative humidity (RH) of concrete is not equivalent to moisture content, even if it can be related to it. All these points make the use and application of this type of sensor less direct and easy, despite for early age samples measurements it showed an accuracy of up to  $\pm 1 - 1.7 \% RH$ .

#### 5.2.2.2. NEMS/MEMS (nano-/micro- electro-mechanical systems) sensors

Nano-/micro- electro-mechanical systems are devices made of nano and micro components and usually consist of a central unit that processes data (an integrated circuit chip such as microprocessor) and several components that interact with the surroundings (such as microsensors) [62, 63]. Their small dimensions allow them to be used in devices for structural health monitoring. From hundreds to millions of them can be distributed throughout a structure. They are produced in batch processes, robust, easy to use and can be embedded into concrete. Integrated technologies are needed for sensing, powering, wireless communication, device location, computation, interrogation, storage and data analysis.

Norris et al. [45] proposed MEMS sensors to simultaneously measure temperature and moisture in concrete. This sensor consisted of a Wheatstone Bridge piezoresistor circuit coupled with microcantilever beams with a vapor-sensitive nanopolymer film designed to

expand and contract under water vapour exposition. The deflection of the beams is measured as resistance change in the embedded strain gauges. The Wheatstone Bridge circuit provides output voltages linearly proportional to RH and to temperature. Although the many advantages of NEMS and MEMS sensors, embedding a great number of devices into concrete may affect the mechanical and physical properties of the hardened material, depending on size, and type of the structure, and on the environmental conditions. Moreover, since such devices need to be embedded into concrete, they are more suitable for newly casted structures, than for existing structures. This makes the technology difficult to be applied to existing safety-critical structures, such as those in nuclear context, where the store structure construction needs to follow strict requirements.

### 5.2.2.3. Fiber-optic sensors

Fiber-optic-based humidity sensors measure moisture absorption in concrete by means of a fiber Bragg grating (FBG) coated with a moisture sensitive polymer. The polymer-coated FBG sensor detects moisture through the strain induced on the device as a result of the polymer swelling caused by moisture absorption. A direct indication of the humidity level within a concrete sample where such a sensor is embedded is given by the shift of the Bragg wavelength caused by the expansion of the humidity-sensitive material coated on the fiber.

The FBG-fiber optic sensor utilizes the shifting of the Bragg wavelength ( $\Delta\lambda_B$ ) caused by the change of strain ( $\Delta\varepsilon$ ) which was caused in turn by the expansion of the humidity-sensitive material coated on the fiber. Bragg wavelength  $\lambda_B$  is a function of the core refractive effective index of optical fiber ( $n$ ) and the lattice period ( $\Lambda$ ) of the grating. A schematic representation of a FBG is shown in Figure 5.1: the impact of external environment on lattice, i.e. strain induced by the humidity-sensitive material, will change the Bragg wavelength, as a consequence of the change of  $\Lambda$  and  $n$ .

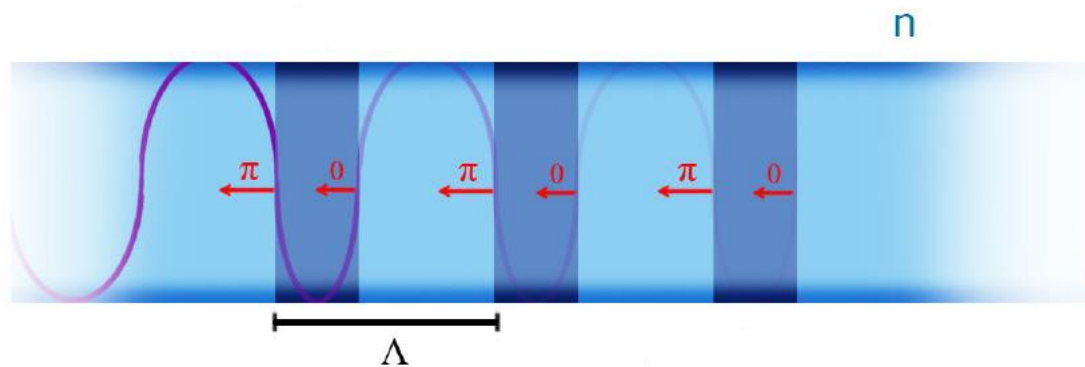


Figure 5.1 – Schematic representation of a Fiber Bragg Grating (FBG) [2].

The equation which relates  $\lambda_B$  to  $\Lambda$  and  $n$  is:

$$\lambda_B = 2 \cdot n \cdot \Lambda \quad \text{Eq. 5.1}$$

An optical interrogator emits a broadband light. The light is guided within the fiber, meets the grating, and a narrow distribution of wavelengths are back-reflected towards the optical interrogator.

Yeo et al. [30, 31] demonstrated that optical-fiber-based humidity sensors of this type can determine the changes in the moisture content in different concrete samples, and react to the ingress of water, detecting the moisture migrating through concrete. Some works previous to those of Yeo, such as [64], developed optical fiber sensors capable of detecting the beginning of composite failure in aircraft structures, such as delamination and moisture ingress issues. These sensors were embedded directly into the composite part during manufacturing and based on a Bragg grating system, or on a long period grating system.

Fiber optic sensors have several advantages: small dimensions, lightweight, sufficiently high resolution and accuracy, and an excellent ability to transmit signal over a long distance, are immune to electromagnetic wave interferences and may incorporate a series of interrogated sensors multiplexed along a single fiber [47, 65]. On the other hand, the technical challenge of providing affordable, long-term packaging to the fibers often represents a barrier to their widespread use [2, 66]. Electronic sensors, on the other hand, despite their lower resolution and accuracy, provide a more established, cost-effective route for health evaluation [2, 65]. Besides, the optical fiber-based sensors reviewed here present the drawback of being embedded inside the concrete structure, thus limiting the application to newly casted structures. The same thing applies to moisture sensors which are based on

the measurement of the electrical properties of concrete. Most times they directly apply electrodes into the concrete system [34, 35, 38-43, 67]. They are reviewed in the following section.

#### 5.2.2.4. Concrete electrical resistance/conductivity/impedance measurements

Previous works have applied electrodes directly to concrete in order to measure water content and/or water ingress by measuring changes in the electrical conductivity of the concrete itself, and thus in its resistance and impedance. Indeed, as it will be shown in section 5.3.3, electrical conductivity of concrete and cementitious materials in general mainly stems from the electrolytic solution within concrete pores, which highly depends on water content.

Spencer et al. [68] and Woelfl et al. [35] demonstrated that electrical resistance can be used to measure the moisture content of concrete: their study showed that electrical resistance increases as moisture content decreases. In [35], the electrical resistivity of concrete was measured by using a Wheatstone bridge circuit, with a three electrodes configuration, and electrodes embedded within the concrete. An alternating current at frequencies above 50 Hz was applied to minimize the polarization effects and thus facilitate the accurate measurement of electrical resistivity. Although other techniques for measuring moisture content of concrete are more accurate (i.e. fiber optics), the use of electrical resistance has the advantage of being a relatively simple procedure that uses cheap equipment.

Saleem et al. [34] measured the resistance of cylindrical concrete specimens by applying a square wave current through copper plates and measuring a voltage drop by means of two copper pin electrodes. They demonstrated an exponential decrease in the electrical resistivity with moisture content. Nguyen et al. [43] used four point probes (as shown in Figure 5.2) to measure the moisture content of concrete by means of concrete electrical resistivity measurements. They obtained an experimental power law between the resistivity of concrete and its moisture content.

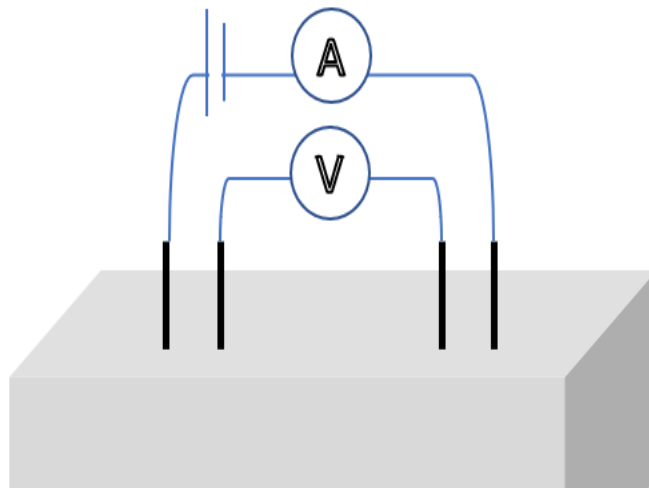


Figure 5.2 – Schematic representation of four point probes resistivity measurement of a concrete slab, as in [43]

Sanchez et al. [39] used impedance spectroscopy to study the water distribution in concrete samples. Rajabipour et al. [42] studied the potentiality of in-situ electrical property measurements to assess moisture transport in concrete.

These existing studies and applications of moisture sensing in concrete at the moment of writing apply resistance, conductivity or impedance measurements directly to concrete, thus becoming more invasive and preferable for newly casted concretes. These methods rely on the electrical and electrolytic conductivity of concrete, when its pores are filled with water. Some authors have tested and demonstrated the feasibility and performance of those methods by adding conductive fillers to concrete samples in order to further improve their conductivity [33].

In this thesis, a sensing solution based on a separate conductive medium acting as sensor for moisture content and temperature is developed: low calcium fly ash geopolymer materials are used. As shown in section 5.2.1, previous studies demonstrated that geopolymers are more conductive than concrete and have already been used for self-sensing applications and as sensing patches for concretes to monitor strain and temperature. This work represents the first time demonstration of their moisture sensing capability. In order to understand the sensing principle of the system characterised in this chapter, next section provides some useful theory on impedance-based geopolymer sensors.

## 5.3. Theory: impedance-based geopolymer sensors

A detailed description of geopolymer electrical properties and geopolymer sensors based on impedance measurements is presented in this section, with a particular focus on the theory behind the sensing system prototype developed in this work of thesis (see sections 5.3.2.1 and 5.3.3).

### 5.3.1. Geopolymer's conductivity

The electrical conductivity of geopolymers stems from the alkali metal cations ( $Na^+$  in the case of this work) introduced by the activator solution [22, 23]. A proportion of the population of these cations is actively bonded to the negatively charged aluminosilicate matrix. The remaining ions are mobile, able to move through the matrix, partly because it is disordered (rather than crystalline) [69]. They increase the ionic content of the water inside the cured material's pores, migrating along the pore network and acting as carriers of electrical current under an applied voltage [24]. Geopolymers are therefore often referred to as solid electrolytes, electrolytic conductors, or ionic conductors.

Measured changes in the electrical properties of geopolymers at varying of physical and chemical measurands allow these materials to be employed as sensors [2, 25-28]: some authors have already measured resistance, conductivity and impedance changes in geopolymer binders to sense physical properties such as strain and temperature [70]. In this work, Electrochemical Impedance Spectroscopy (EIS) is employed to use geopolymer samples as moisture sensors. The following section provides a theoretical description of the electrochemical impedance spectroscopy technique applied to geopolymers.

### 5.3.2. Electrochemical impedance spectroscopy (EIS)

Geopolymers can be electrically interrogated using metal electrodes, which are embedded prior to curing. This produces a sensor cell, as the one developed during the work outlined in this thesis, shown in Figure 5.3.

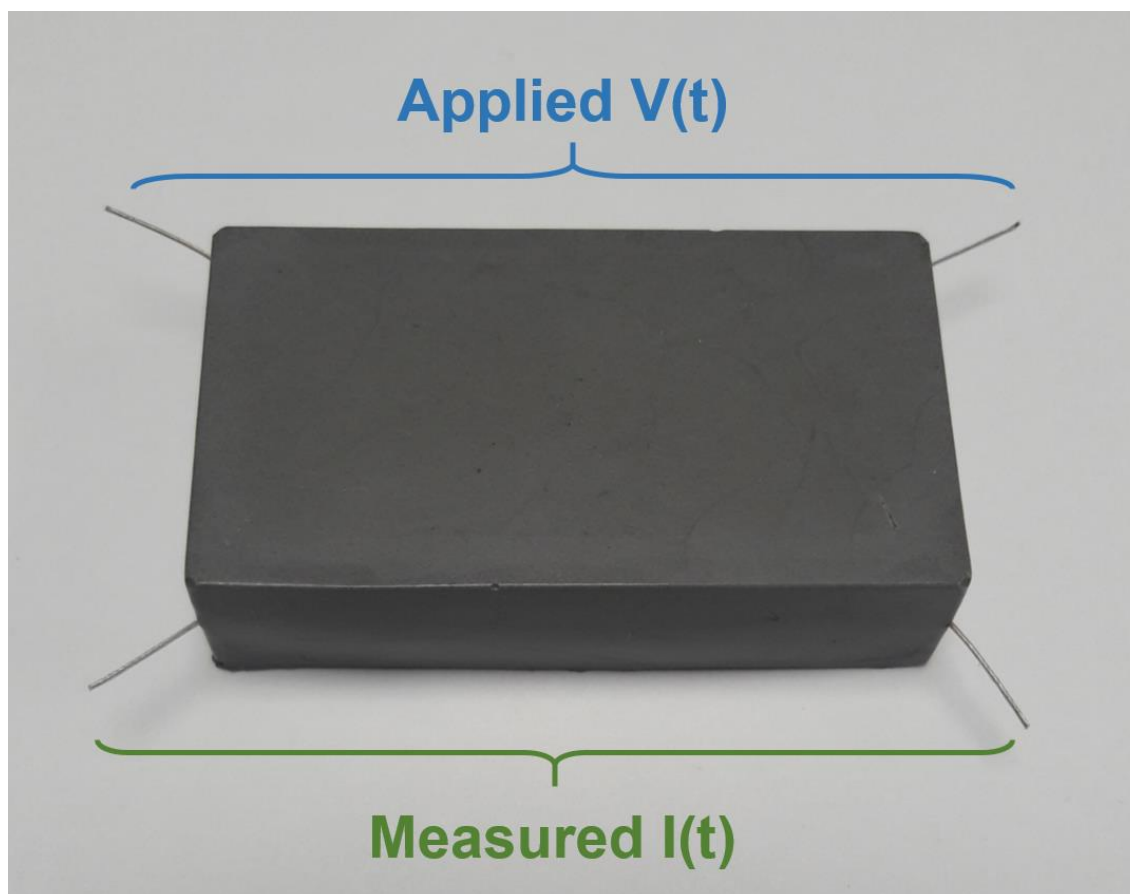


Figure 5.3 - Photograph of geopolymer sensor cell showing electrodes used for sensor interrogation.

While standard circuits are comprised mainly of electronic conductors, geopolymer sensors are a composite of electronic conductors (the metal electrodes) in contact with an ionic conductor (the geopolymer). They are therefore classed as an electrochemical system, and exhibit behaviours that are not present in most standard electronic sensors. As geopolymers behave as electrolytes, they cannot be reliably interrogated using a dc current/voltage, since dc current causes electrolysis in electrolytes. For this reason, geopolymers are interrogated by applying ac current/voltage, and the frequency of this ac current/voltage can be altered (and the cell's response measured) by means of the Electrochemical Impedance Spectroscopy (EIS) technique. As the response of the cell is dependent on the ac frequency, sweeping the frequency provides a rich dataset which can be used to improve our understanding of sensing behaviour or the underlying electrochemical processes occurring in the cell.

EIS is a non-destructive technique that can be used to analyse electrochemical systems both at rest and in response to external measurands. EIS can be Galvanostatic, when an ac current is applied to the electrochemical system, and an ac voltage is measured, or Potentiostatic, when an ac voltage is applied to the electrochemical system and an ac current is measured. In this work, a Potentiostatic EIS was used. The reason for this is that the Potentiostatic EIS is self-limiting, avoids electrical breakdowns and applies voltage, which is easier to apply than current using electronics. In Potentiostatic EIS, the frequency-dependent current response of the sensor cell,  $I(t)$ , is measured during an applied, time-varying voltage excitation,  $V(t)$  [71]:

$$V(t) = V_0 \cos(\omega t), \quad \text{Eq 5.2}$$

$$I(t) = I_0 \cos(\omega t - \varphi(\omega)).$$

Here,  $V_0$  and  $I_0$  are the amplitudes of the applied voltage and measured current respectively,  $\varphi(\omega)$  is the frequency-dependent phase difference between  $V(t)$  and  $I(t)$ , and  $\omega = 2\pi f$  is the radial frequency of applied ac voltage. The electrical impedance of the cell,  $Z$ , which is a complex quantity, can be defined using Euler notation as [71]:

$$Z = \frac{V(t)}{I(t)} = Z_{mod}(\cos(\varphi) + i\sin(\varphi)) = Z_{mod}e^{i\varphi}, \quad \text{Eq. 5.3}$$

Where  $i$  is the imaginary unit,  $Z_{mod}(\omega) = |Z|$  is the frequency-dependent magnitude or modulus of the impedance, and  $\varphi = \arg(Z)$  is the phase angle between real and imaginary components. The real component of the impedance,  $Z_{real} = \text{Re}(Z)$ , is the electrical resistance of the cell, while the imaginary component,  $Z_{imag} = \text{Im}(Z)$ , is its reactance. Inductive elements in a sensor cell,  $L$ , cause current changes to lag behind applied voltage, as  $Z_{imag} = i\omega L$ . Capacitive elements,  $C$ , meanwhile, cause current changes to lead the voltage as  $Z_{imag} = -\frac{i}{\omega C}$ . Acquired EIS impedance data are typically assessed using a combination of Bode plots (plots of  $Z_{mod}$  and  $\varphi$  against swept frequency), and Nyquist plots (plots of  $Z_{imag}$  against  $Z_{real}$ ).

### 5.3.2.1. The electrical impedance of geopolymers

The impedance response of electrolytic cells can be modelled using equivalent circuits comprised of resistors, capacitors and inductors in series and/or parallel. Previous studies [72, 73] have shown that electrolytic cells made using alkali activated binders can be modelled using the equivalent circuit shown in Figure 5.4 a). The elements in this circuit include the:

- Resistance of the Electrolyte,  $R_e$ : the resistance of the liquid electrolyte within the geopolymer pores. This resistance depends on the number of ions (i.e. the ion concentration and volume of the cell, both of which are often constant), and the mobility of the ions (a function of ion concentration, metal ion type, and temperature) [74].
- Connected pore resistance,  $R_c$ , and unconnected pore resistance,  $R_{uc}$ : the resistance of the ion conducting pathways between the connected (percolating) and unconnected pores in the geopolymer matrix [75].
- Solid phase, or bulk capacitance,  $C_b$ : the dielectric capacitance associated with the solid phase of the geopolymer between the electrodes. This will be comprised of hardened geopolymer paste and unreacted fly ash particles.
- Interface resistance,  $R_i$ , and double layer capacitance,  $C_i$ , at the specimen-electrode interface: a single layer of  $Na^+$  ions in the geopolymer will adhere to the negatively charged surface of the metal electrode. This layer acts as a dielectric, separating the electrons in the metal electrode from the  $Na^+$  in the geopolymer.
- Pore wall capacitance,  $C_p$ : a double layer capacitance present between the unconnected pores of the pore solution.

In the present work, modifications have been made to this standard model to produce a new equivalent circuit shown in Figure 5.4 b). The changes are justified as follows:

1. The solid phase capacitance is described by:

$$C_b = \epsilon_0 \frac{A_e}{d}, \quad \text{Eq. 5.4}$$

where  $\varepsilon_0$  is the effective dielectric constant of the solid phase of the geopolymer cell,  $A_e$  is the shared area between the electrodes in the specimen, and  $d$  is the separation between the electrodes. In the present work, the electrodes embedded in the geopolymer cell are stainless steel wires of diameter 0.4 mm, embedded at a depth of 7.5 mm, and their separation  $d = 55$  mm. This set up, specific to our sensor design, means that  $A \ll d$ , and  $C_b \approx 0F$ . Capacitor  $C_b$  is therefore removed.

2. Double layer capacitances in electrolytic systems can be modelled using constant phase elements (CPEs), represented as elements Q in Figure 5.4 b). In this work, all double-layer capacitances are modelled using CPEs which have an impedance described by:

$$Z_{cpe} = \frac{1}{Y_0} \frac{1}{(i\omega)^{\alpha'}}, \quad \text{Eq. 5.5}$$

where  $Y_0$  and  $\alpha' = [0, 1]$  are fitting parameters. While the use of CPEs in electrochemical circuit modelling is common, it is a slightly controversial approach as  $Y_0$  and  $\alpha'$  do not have widely accepted physical meanings. However, it is accepted that equation 5.5 describes the net result of ion dynamics in electrochemical systems [69, 76]. When ions make forward hops between vacant sites in the geopolymer, they make a positive contribution to conductivity. However, because ion movements within geopolymers are highly correlated, forward hops are often soon followed by backwards ionic hops which cancel out the conductivity contribution. This is why CPEs describe a low conductivity at low EIS frequencies. At high EIS frequencies, there is no time for backwards ionic hops before the polarity of the electrodes switches, so all ionic hops are forwards, and all contribute positively to conductivity.

3. Electrolytic cells often exhibit inductive loops at high frequencies. While inductances are commonly attributed to experimental artefacts such as electrode cross-talk, particularly when measured currents are small, some research has suggested that it could also stem from genuine electrochemical processes, such as

relaxation of adsorbates on the electrodes [77]. Regardless of the cause, inductive effects were seen in our system, and so an inductance term,  $L$ , and corresponding resistance,  $R_L$ , was added to the equivalent circuit.

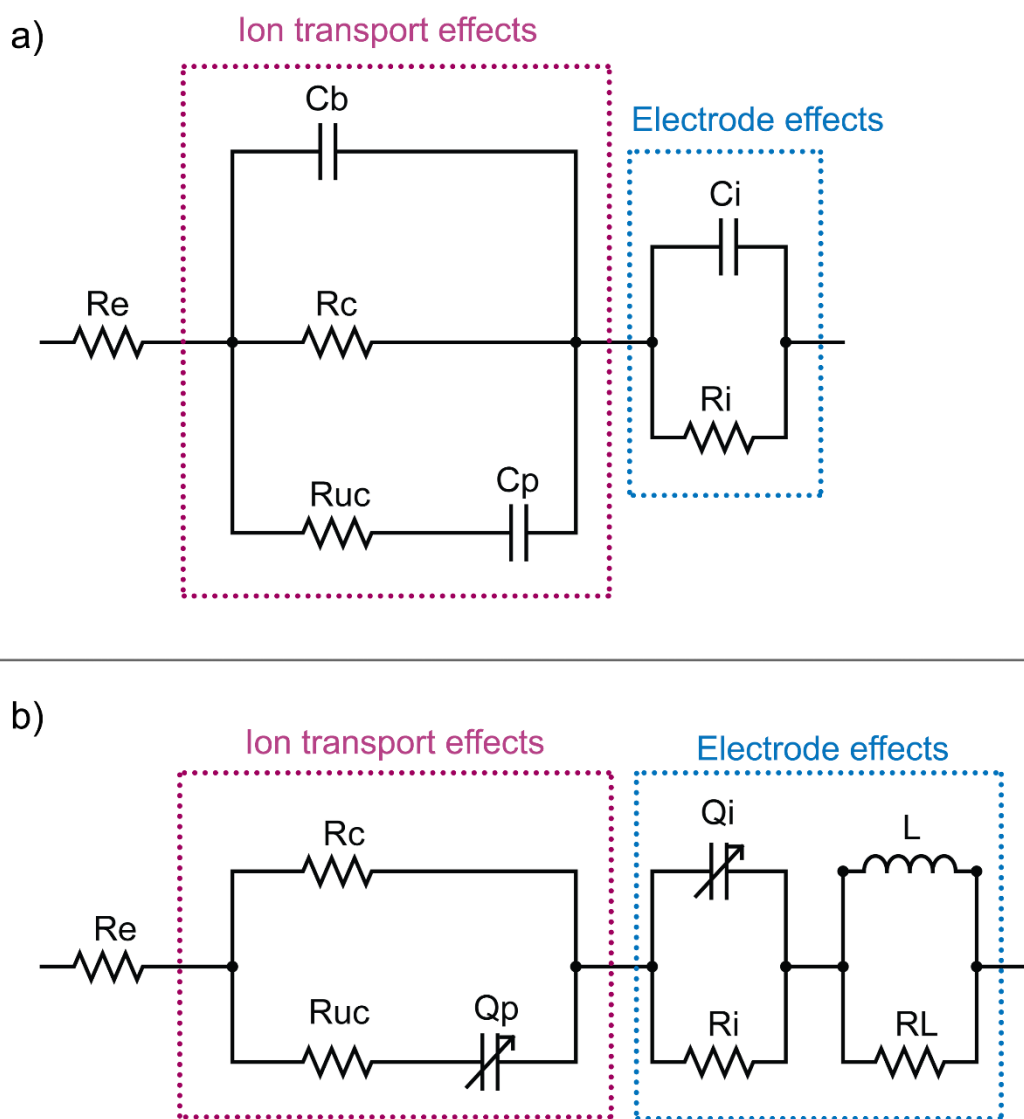


Figure 5.4 - a) The equivalent circuit previously used to describe alkali-activated materials. b) The equivalent circuit used to describe the geopolymer cells in this work.

The overall impedance response of the geopolymer sensor modelled by the circuit shown in Figure 5.4 b) is:

$$Z = R_e + Z_{transport} + Z_{electrode}, \quad \text{Eq. 5.6}$$

where  $Z_{transport}$  and  $Z_{electrode}$ , found through parallel sums of components, capture the total impedance of ion transport and electrode effects respectively.

After this theoretical description of the electrical impedance for the sensor cell prototype in Figure 5.3, the following section introduces the moisture and temperature sensing principle.

### 5.3.3. Temperature and moisture sensing principle of geopolymer system

Previous work has already outlined geopolymer strain and temperature sensing, as shown in section 5.2.1. For a geopolymer cell consisting of metal electrodes (copper, stainless steel, etc...), connected to an EIS interrogation system, the equation for the magnitude of the impedance,  $Z_{mod}$ , is:

$$Z_{mod} = |Z| = \frac{|V|}{|I|} = \frac{\rho \cdot L}{A} \quad \text{Eq. 5.7}$$

where  $A$  is the contact area of each electrode with the geopolymer,  $L$  is the distance between the electrodes in the geopolymer material and  $\rho$  is the resistivity of the geopolymer material. Assuming no changes in strain and ion concentration are happening, fractional changes in impedance are induced by changes in moisture and temperature, as described by the following equation:

$$\frac{\Delta Z_{mod}}{Z} = p(\Delta W) + q(\Delta T) \quad \text{Eq. 5.8}$$

where  $p$  and  $q$  are two functions, which describe the geopolymer sensor's moisture and temperature sensitivity respectively,  $\Delta W$  is the change in moisture, and  $\Delta T$  is the change in temperature.

However, no previous literature is available on geopolymer-based moisture sensors, so far. As such, the theoretical sensing principle for geopolymer moisture sensors that we use must begin by drawing on the literature for concrete and other similar cementitious materials.

Bulk electrical conductivity in cementitious materials is a function of the conductivity of the pore solution,  $\sigma_0$ , the volume of the pore network filled with pore solution,  $\varphi_{con}$ , and the connectivity factor of the pore network,  $\beta$  [42]:

$$\sigma = \sigma_0 \varphi_{con} \beta. \tag{Eq. 5.9}$$

If geopolymers follow this same principle, then their conductivities,  $\sigma$ , will depend on measurands which alter the three factors on the right hand side of equation 5.9.

Increasing the temperature of a geopolymer enhances ion mobility and encourages electrolytic dissociation, both of which increase  $\sigma_0$ . Therefore, provided there is no evaporation of water at high temperatures, the relationship between geopolymer conductivity,  $\sigma$ , and temperature,  $T$ , is expected to follow one similar to that of other cement systems [78]:

$$\ln(\sigma) = \frac{D_1}{T} + D_2 T + D_3, \tag{Eq. 5.10}$$

where  $D_1$ ,  $D_2$  and  $D_3$  are constants.

The admittance of a geopolymer sensor is defined as the inverse of impedance:

$$A = \frac{1}{Z}. \tag{Eq. 5.11}$$

For a fixed cell geometry, the modulus of admittance,  $A_{mod} = |A|$ , is proportional to conductivity,  $\sigma$ .

While the first term in equation 5.10, i.e.  $D_1/T$ , has been used on its own to describe the 'Arrhenius dependence' of geopolymer conductivity on temperature in previous literature [2, 27, 28], in this work the full form of equation 5.10 is used.

Water content within the geopolymer, meanwhile, can affect all three factors in equation 5.9. It reduces the conductivity of the pore solution,  $\sigma_0$ , by diluting it, but meanwhile increases pore fill volume,  $\varphi_{con}$ , and connectivity,  $\beta$  [40]. At very low water contents, conductivity can decrease dramatically as the liquid electrolyte cannot cover the internal surfaces of the pores [40]. Given the lack of previous literature on geopolymer moisture sensors, a reference to previous studies of ordinary Portland cement systems is made. In most of these studies, electrical conductivity was found to have an exponential dependence on water content [34], which can be described by the following equation:

$$\sigma = a_1 * e^{a_2 \cdot W} \quad \text{Eq. 5.12}$$

where  $\sigma$  is the conductivity of concrete,  $W$  is the water content and  $a_1$  and  $a_2$  are constants.

In this work, the decreasing of impedance with water content was found to be described by equation 5.13, which provides a good fit to the impedance experimental data, as shown in section 5.5:

$$Z_{mod} = a_3 * e^{\frac{a_4}{W}} \quad \text{Eq. 5.13}$$

where  $Z_{mod}$  is the impedance modulus of the geopolymer cell,  $W$  is the water content and  $a_3$  and  $a_4$  are constants.

Equation 5.13 can be re-expressed as:

$$\ln(Z) = \frac{D_4}{W} + D_5, \quad \text{Eq. 5.14}$$

where  $D_4$  and  $D_5$  are constants.

Equations 5.10, 5.11 and 5.14, can then be combined to produce a characterization equation for the geopolymer sensor:

$$\ln\left(\frac{Z_{mod}}{Z_{mod,0}}\right) = \frac{G_1}{T} + G_2 T + \frac{G_3}{W} + G_4 T \frac{1}{W} + G_5, \quad \text{Eq. 5.15}$$

where  $G_{1, \dots, 5}$  are constant. Equation 5.15 includes an additional cross-dependence term between moisture and temperature ( $G_4 T/W$ ). The equation considers shifts in the modulus of the impedance only, and furthermore normalizes all  $Z_{mod}$  values by  $Z_{mod,0}$ , where  $Z_{mod,0}$  is the impedance of the sensor in ambient conditions (in this work, defined as a water content of 60wt% and at a temperature of 20 °C). This normalization makes the

characterization equation less sensitive to variations in sensor geometry. These equations have been used in the results section for the moisture and temperature characterization of the sensor prototype.

Next section describes the materials used and the methodology of the moisture and temperature sensor characterisation experiment.

## 5.4. Materials and Methods

This section presents a detailed description of the materials and methods used for the manufacture, set-up, characterisation and testing of a newly developed low calcium fly ash geopolymer moisture and temperature sensor prototype.

### 5.4.1. Sensor fabrication

The geopolymer binder used in this work was synthesized from low calcium fly ash and an alkaline solution made from sodium hydroxide (SH) and sodium silicate (SS), with a liquid to solid ratio,  $L/S = 0.5$ , and  $SH/SS = 0.4$ . A detailed description of the geopolymer binder's fabrication, its mechanical properties and suitability as a repair is described in chapter 4. The mixed binder was poured into rectangular silicon moulds (dimensions 55mm x 30mm x 15mm) with electrodes penetrating 2 mm into the corners to cast the geopolymer cells shown in Figure 5.3, and schematically shown in Figure 5.5. The electrodes were 7-wire braided stainless steel wires of diameter 0.4 mm. The geopolymer cells were cured for 30 days at 20 °C and 95% relative humidity in an environmental chamber prior to testing. The reasons for this choice were detailed in chapter 4, and are related with the nuclear context where the sample is going to be deployed in future.

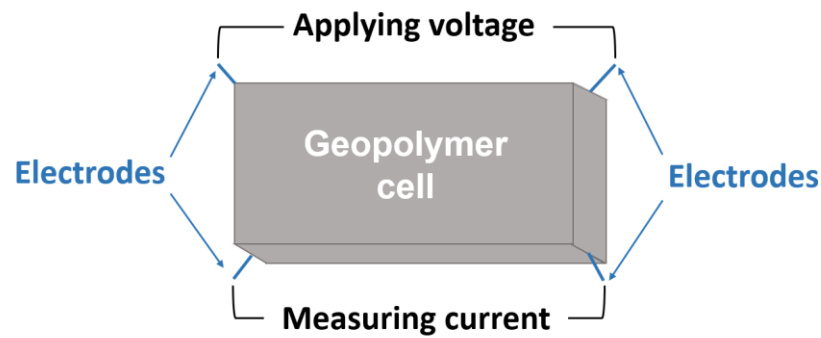


Figure 5.5 – Schematic representation of the geopolymer cell shown in Figure 5.3.

The four-electrode configuration shown in Figure 5.3 and in Figure 5.5 is known as Van Der Pauw configuration. It minimizes lead and contact resistance effects, and the influence of electrode polarization at low frequencies [79, 80]. It was also found in preliminary work that this configuration reduces stress and the probability of micro-cracking in the samples at the electrode-geopolymer interface as samples cure and shrink, partly because it maximizes the distance between adjacent electrodes.

#### 5.4.2. Interrogation system

During potentiostatic EIS a 10mV voltage was applied to geopolymer cells. The low magnitude of the voltage produces a pseudo-linear current response, allowing impedance to be calculated more conveniently [71, 81]. The frequency of the applied voltage was swept over the range 10 Hz –100 kHz during impedance characterization.

#### 5.4.3. Calibration methods

The procedure for the moisture and temperature calibration is summarized as a flowchart in Figure 5.6:

1. The geopolymer sensor cell was immersed in deionized water for 24 hours to reach a high water content.
2. Surface water was removed from the cell, and its wet mass,  $M_{i,1}$ , was measured.
3. Geopolymer cells were sealed in a box for 24 hours to allow water within the pores to equilibrate and homogenize, as shown in Figure 5.7. This ensured that moisture measurements were conducted in a steady state regime. The sealed sample was placed in an environmental chamber and connected to the interrogation system. A

separate data logger was placed within the box to verify temperature and relative humidity measurements (resolution of 0.5 °C and 0.5% RH). The schematic representation of this experimental set-up is shown in Figure 5.8.

4. Temperatures within the chamber were cycled in  $\sim 5^\circ\text{C}$  steps from  $\sim 5^\circ\text{C}$  to  $\sim 30^\circ\text{C}$  and back to  $\sim 5^\circ\text{C}$ . For each temperature point, temperatures were held for 2 hours to allow the system to reach thermal equilibrium. Once thermal equilibrium was reached, impedance spectra were measured twenty times over a 20 minutes duration, to allow an average to be taken.
5. After temperature cycling, the geopolymer sensor was taken out of the sealed container and its wet mass,  $M_{i,2}$ , was weighed a second time. The wet mass  $M_i$  was then defined as the mean value of  $M_{i,1}$  and  $M_{i,2}$ , while the variation was used to establish an error in moisture content.
6. The sensor was placed in a desiccator with silica gel to drive water out of the sample through evaporation. The sensor was regularly weighed until a new target mass (target moisture level) was reached. This cycle was repeated for all target moisture contents. Some samples underwent several drying and wetting cycles and several temperature cycles to assess sensor repeatability. Once the characterization was complete, each sample was completely dried in an oven at  $105^\circ\text{C}$  for 24 hours and its dry mass  $M_d$  was measured. This allowed the gravimetric water content  $W_i$  of the samples to be quantified [82]:

$$W_i(\text{wt}\%) = \frac{M_i - M_d}{M_d} \times 100 \quad \text{Eq. 5.16}$$

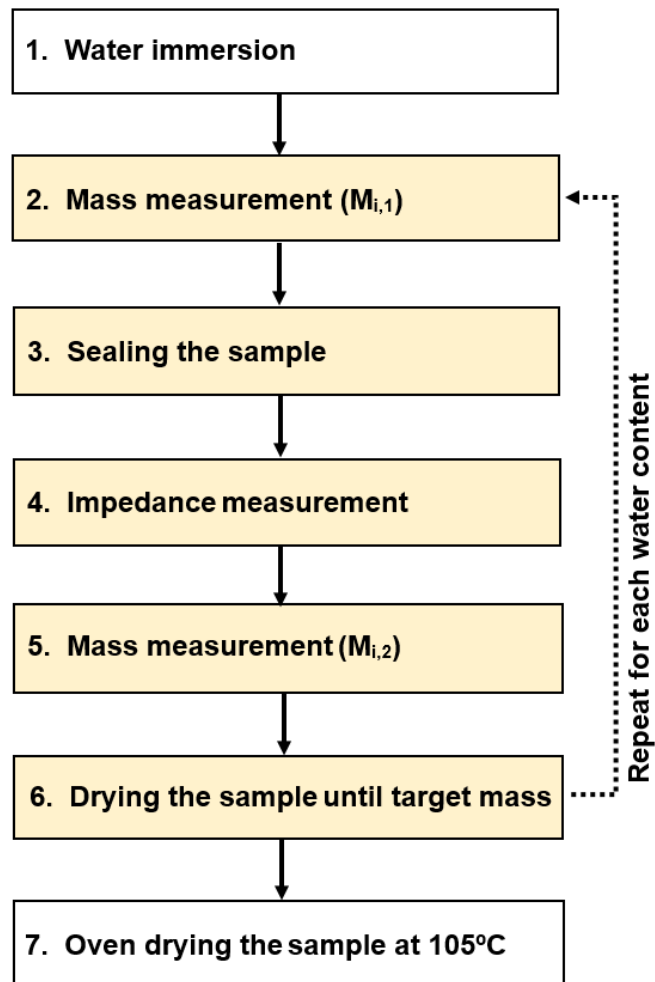


Figure 5.6 - Flowchart showing the steps in the water and temperature characterization experiment.

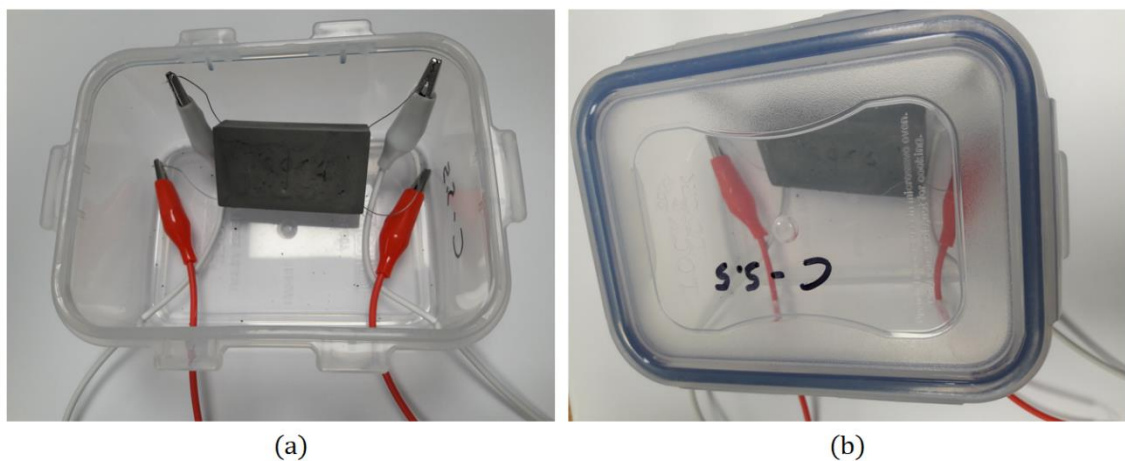


Figure 5.7 - (a) Geopolymer cell inside the plastic box, connected to the electrodes of the interrogation system, before sealing; (b) geopolymer cell inside the sealed plastic box.

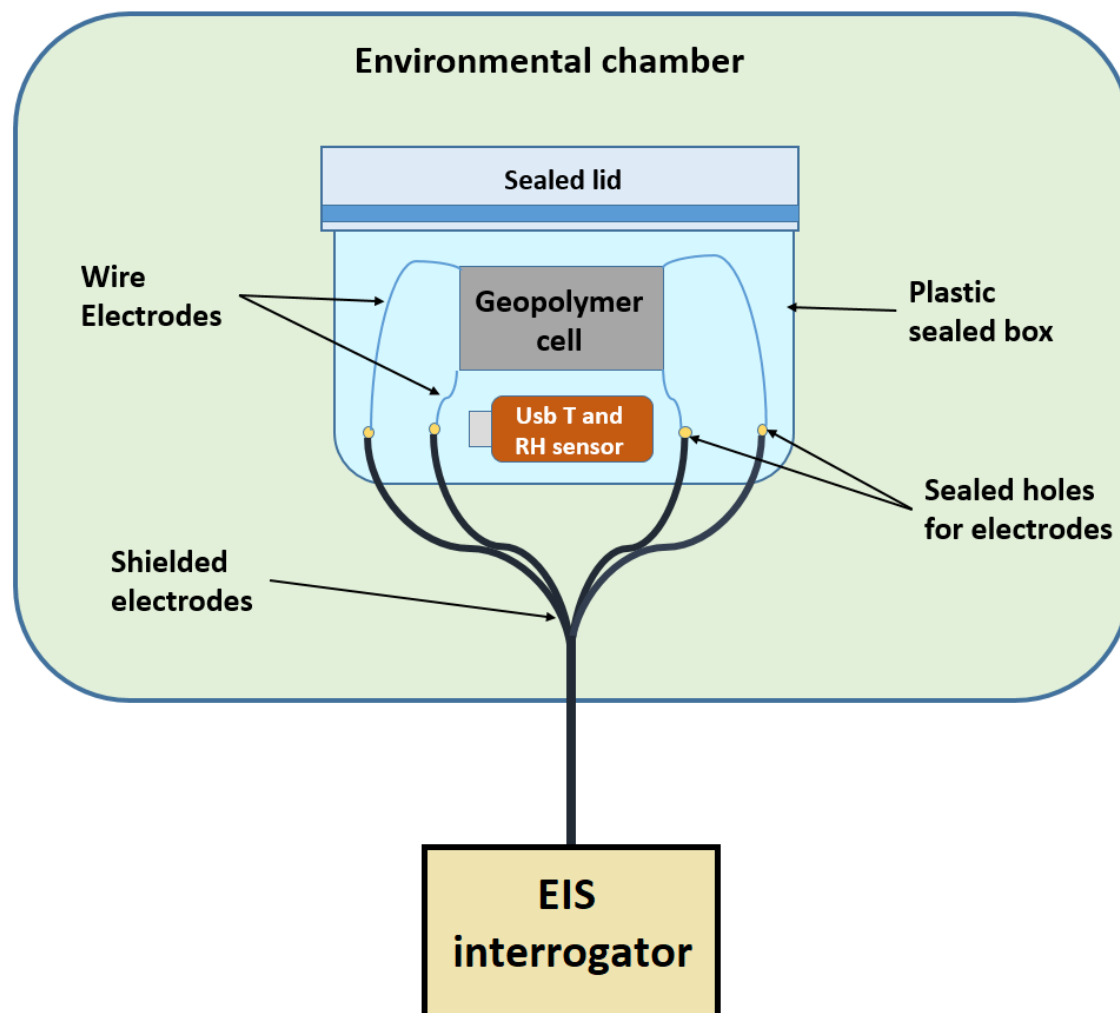


Figure 5.8 – Scheme of the experimental set-up for the EIS measurement of the geopolymer cell sample at each water content.

#### 5.4.4. Post-mortem examination of ion leaching

The drying and wetting cycles could cause  $Na^+$ ,  $Si^+$  and  $Cl^-$  ions from the geopolymer to leach from samples, reducing their ionic conductivity over time. To assess this, inductively coupled plasma optical emission spectrometry (ICPOES) and ion chromatography (IC) were used to measure ionic leaching from geopolymer cells. Sensors were immersed three consecutive times in 1.1 L of deionized water for 24 hours. After each wash, water samples were collected and filtered with a 0.45  $\mu m$  pore size filter prior to analysis of ion content.

## 5.5. Results and discussion

### 5.5.1. Geopolymer cell impedance response

Figure 5.9 shows a typical Bode plot of phase  $\varphi$  and  $Z_{mod}$  for a geopolymer sensor, taken at a water content of  $W = 88\%$  and temperature of  $T = 20\text{ }^{\circ}\text{C}$ . The fits shown use the equivalent circuit model given in Figure 5.4 b), and the values for each component are given in Table 5.3. The fits of Figure 5.9 show that the circuit model in Figure 5.4 b) well describes the geopolymer cell.

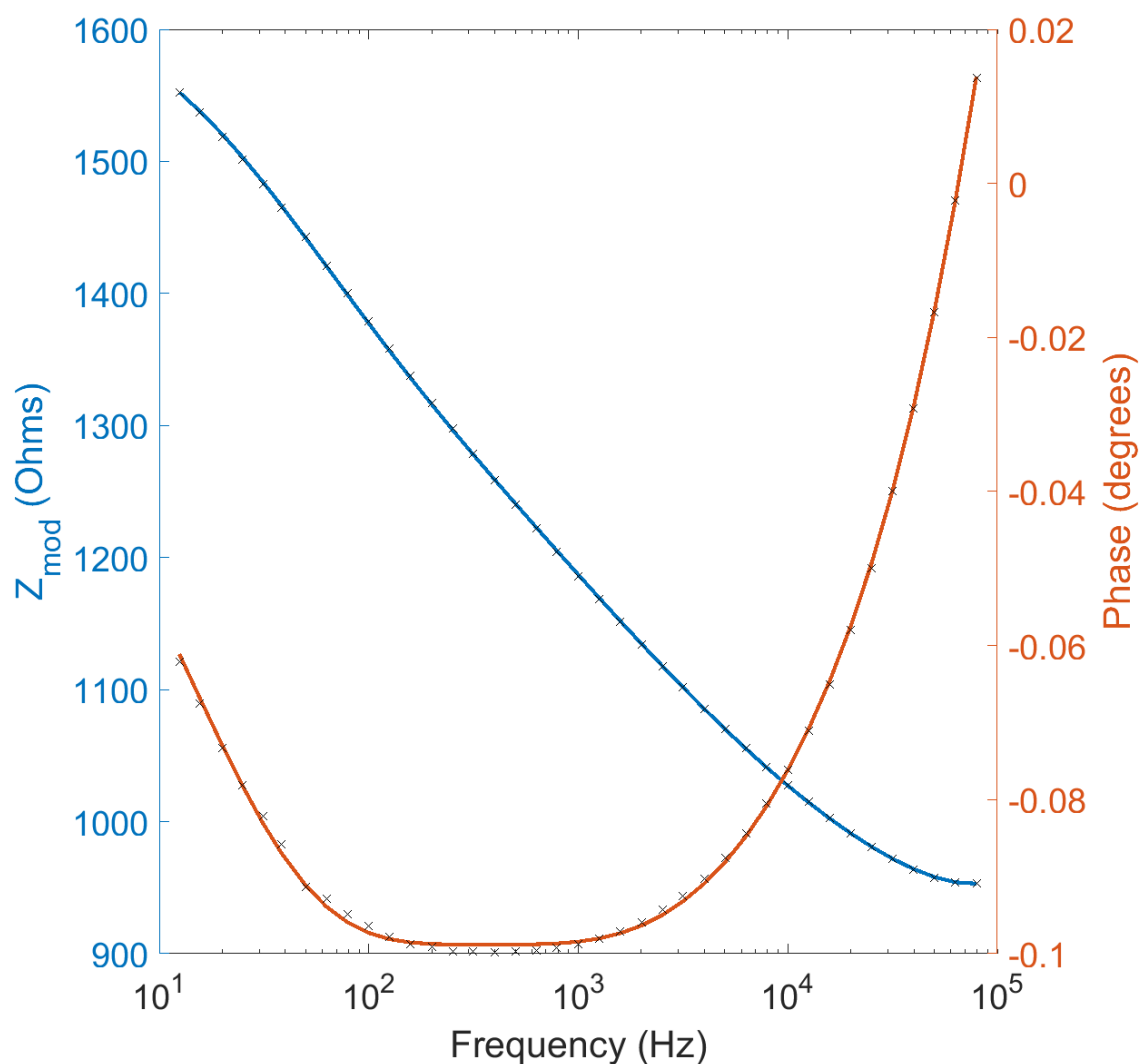


Figure 5.9 – Bode plot for  $Z_{mod}$  and phase  $\varphi$  obtained for sensor at  $W = 88\%$  and  $T = 20\text{ }^{\circ}\text{C}$ .

Circuit element	$R_e$ [ $\Omega$ ]	$R_c$ [ $\Omega$ ]	$R_{uc}$ [ $\Omega$ ]	$Y_p$ [ $\mu\text{F}$ ]	$\alpha_p$	$R_i$ [ $\Omega$ ]	$Y_i$ [ $\mu\text{F}$ ]	$\alpha_i$	L [ $\mu\text{H}$ ]	$R_L$ [ $\Omega$ ]
Value	108	57	33	50	0.7	63	74	0.5	0.7	5

Table 5.3 – Values of parameters used in the equivalent circuit model of Figure 5.4 b) for impedance data shown in Figure 5.9.

### 5.5.2. Temperature dependence of impedance

Figure 5.10 shows Bode plots for sensors at temperatures ranging from 6 °C to 30 °C. In this figure, isotherms have been plotted on the y-axis by taking the product of the modulus of admittance and temperature, or  $A_{mod} \cdot T$ .

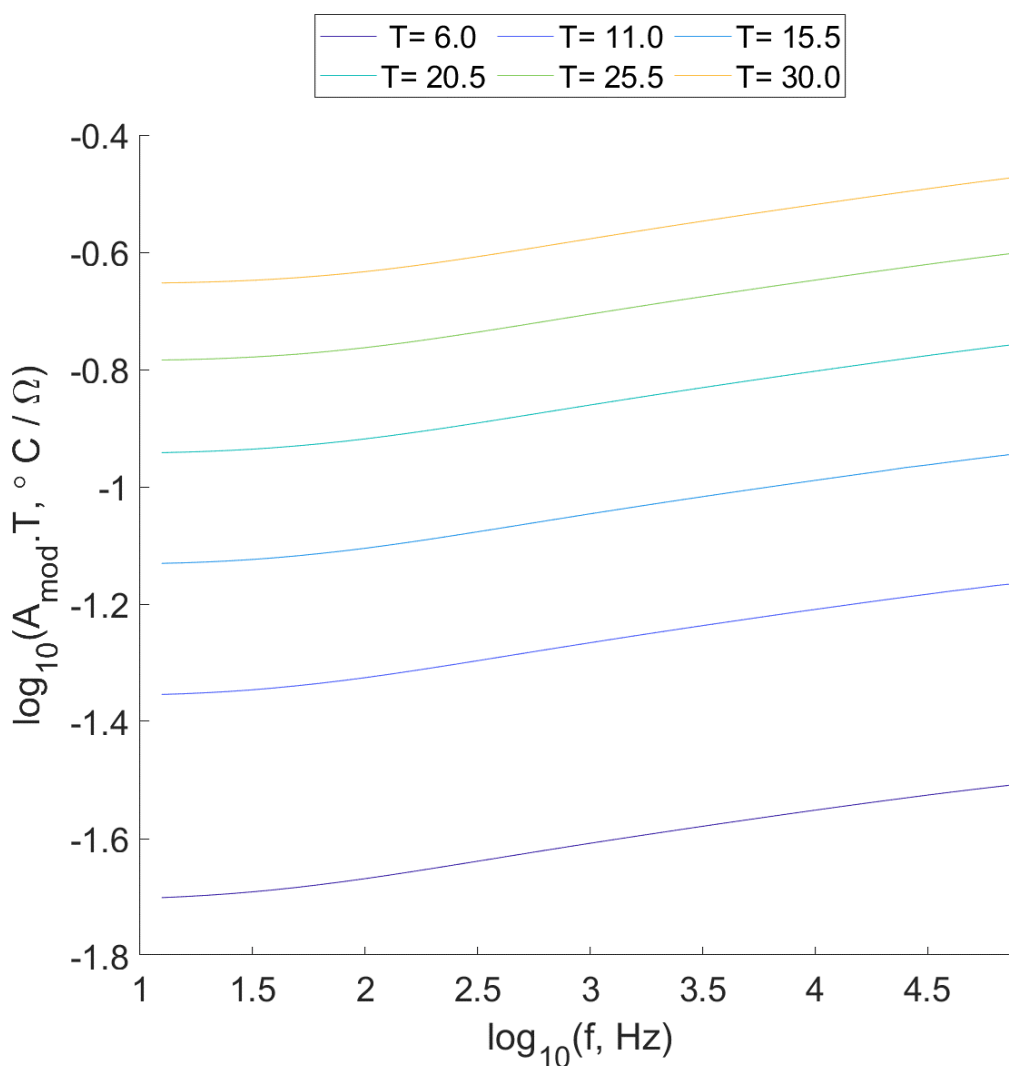


Figure 5.10 – Bode plots of isotherms of  $A_{mod} \cdot T$ . Data shown is for samples at a constant water content of  $W = 77\%$ .

Figure 5.10 demonstrates that the geopolymer sensors obey a scaling law typical of ionic conductors known as Summerfield scaling [69]: the shape of each Bode plot is independent of temperature (e.g. the  $T = 11\text{ }^{\circ}\text{C}$  line can be shifted up or down to superimpose onto any other temperature line). This means that we can define a master curve, arbitrarily defining a baseline frequency of  $f_0 = 100\text{ Hz}$ , and a baseline admittance at  $100\text{ Hz}$  of  $A_{0,mod} = A_{mod}(100\text{Hz})$  for each line. This allows us to plot all of the data shown in Figure 5.10 onto a single scaled Summerfield plot, which is shown in Figure 5.11.

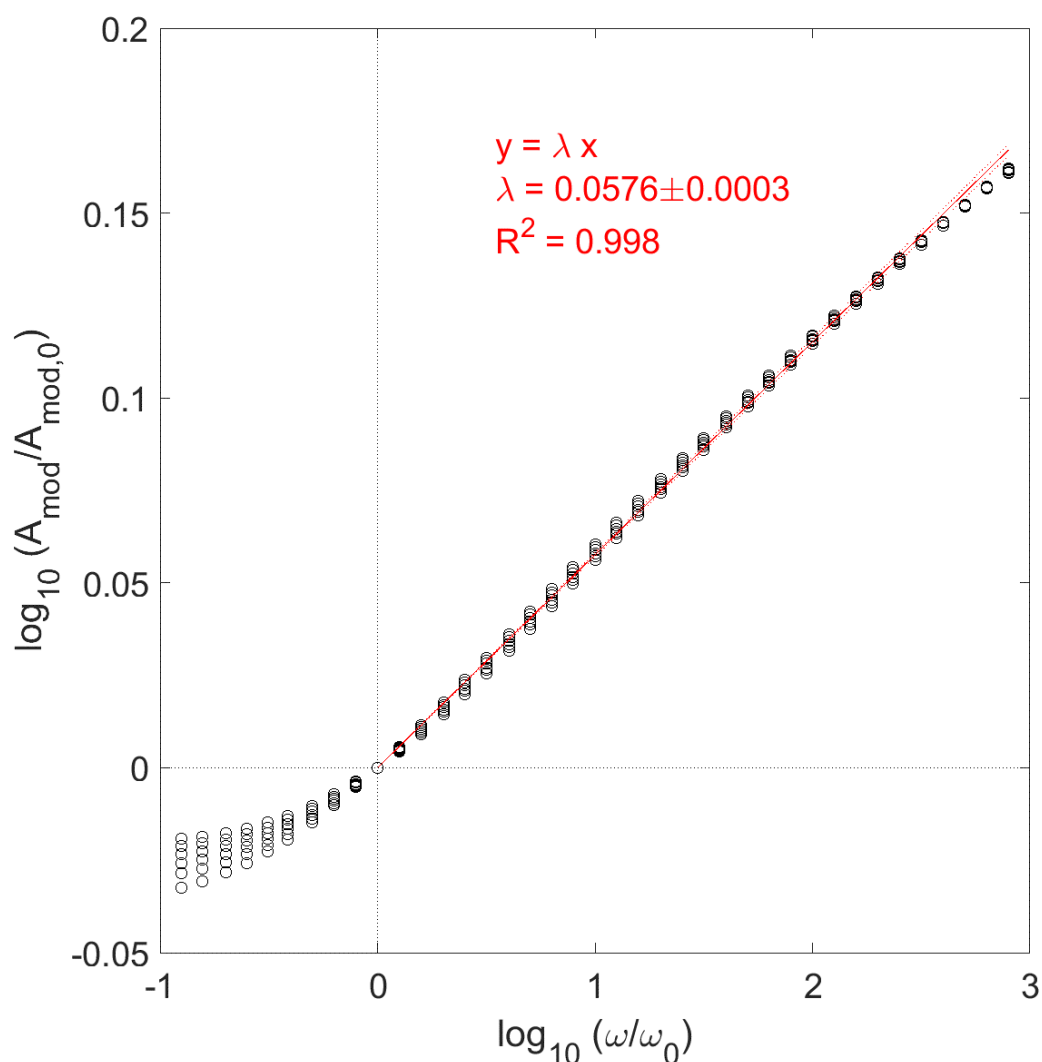


Figure 5.11 – Scaled Summerfield plot representing all data in Figure 5.10 in a single data series.

The overlap of the isotherms in Figure 5.11 shows that the number of mobile ions is unchanged between temperature cycles. The linear relationship, meanwhile, supports the

notion of time-temperature superposition in geopolymers [69]. To conduct an electrical current, an ion within the geopolymer must hop from its existing site to an adjacent site, and this adjacent site must relax to accommodate the ion. The longer it takes for an ion to be accommodated, the higher the probability for a backwards hop. Increasing temperature speeds up relaxation, and so essentially speeds up the ion hopping process (hence time temperature superposition).

Figure 5.10 and Figure 5.11 have consequences for temperature sensing. In order to monitor temperature using geopolymers, it is possible to choose almost any excitation frequency in the linear region of Figure 5.11. It is not prudent to use frequencies that are too low, as this can encourage electrolysis, driving gradual ion migration to one electrode, thus causing corrosive chemical reactions (and, as might be expected given the theory above, corrosion at low interrogation frequencies is particularly pronounced at higher temperatures).

### 5.5.3. Moisture dependence of impedance

Figure 5.12 shows Nyquist plots for the geopolymer cell at water contents ranging from  $W = 51\text{wt}\%$  to  $W = 88\text{wt}\%$ , and at a constant temperature of  $T = 20^\circ\text{C}$ . As the water content decreases, impedance increases as expected. Resistive and inductive circuit elements in the modelled system all increase in magnitude as the water content decreases (Table 5.3).

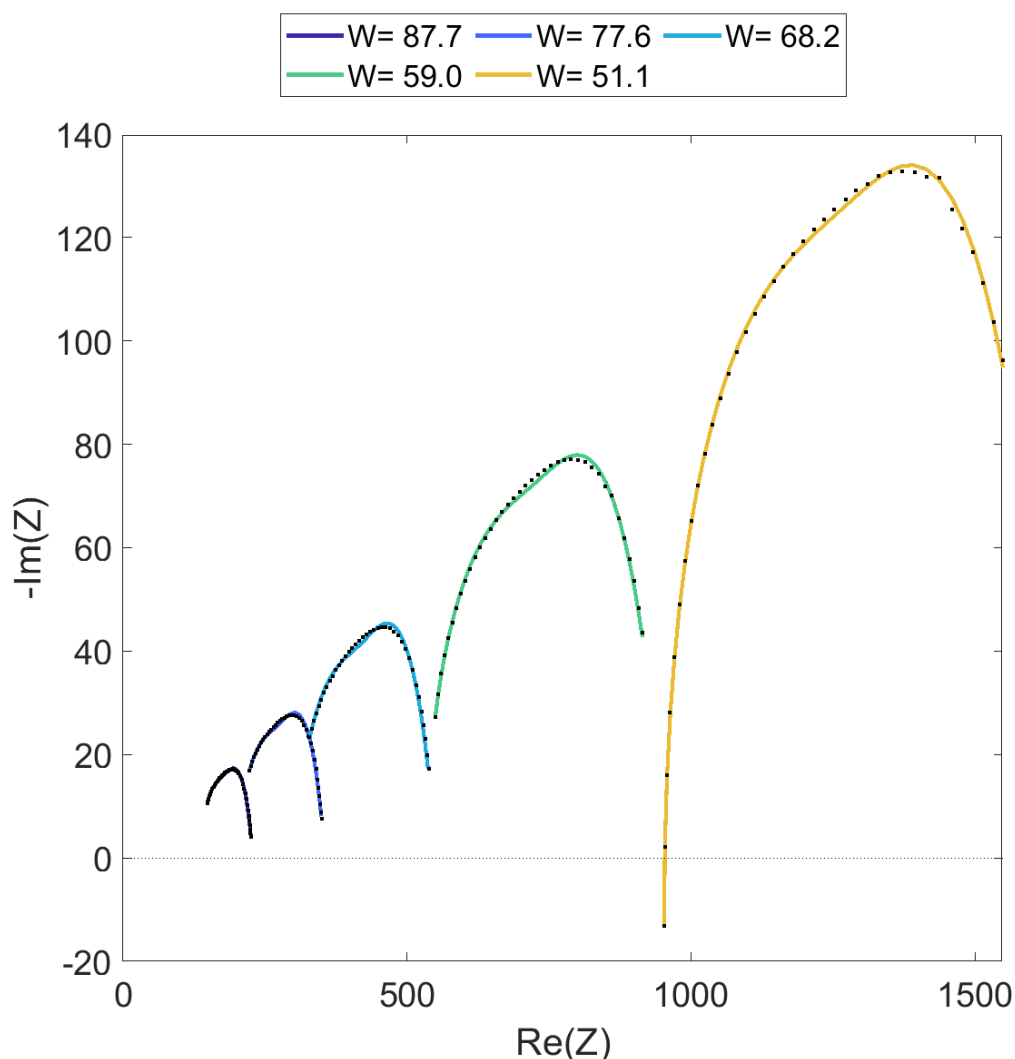


Figure 5.12 – Nyquist plots from 10 Hz to 100 kHz, for a geopolymer sample system at 20°C for different water contents. Fits are obtained using the equivalent circuit model shown in Figure 5.4 b).

Repeating the scaled Summerfield plot process for water contents produces the plot shown in Figure 5.13. The trend is similar to Figure 5.11, but there is more scatter in the results. It is clear that water, like temperature, speeds up the ion hopping process. This makes physical sense: as described by equation 5.9, water increases the connectivity of the pore network and the volume of the pore network filled with electrolyte solution. It is possible to hypothesise that the added scatter in the Summerfield plot could be due to an added non-linear effect: the dilution of the pore solution. A more detailed discussion of the scatter in the moisture Summerfield scaled plot, together with a critical comparison with the scatter in the Summerfield plots for temperature and NaCl concentration, is postponed to section 6.4.2 of chapter 6.

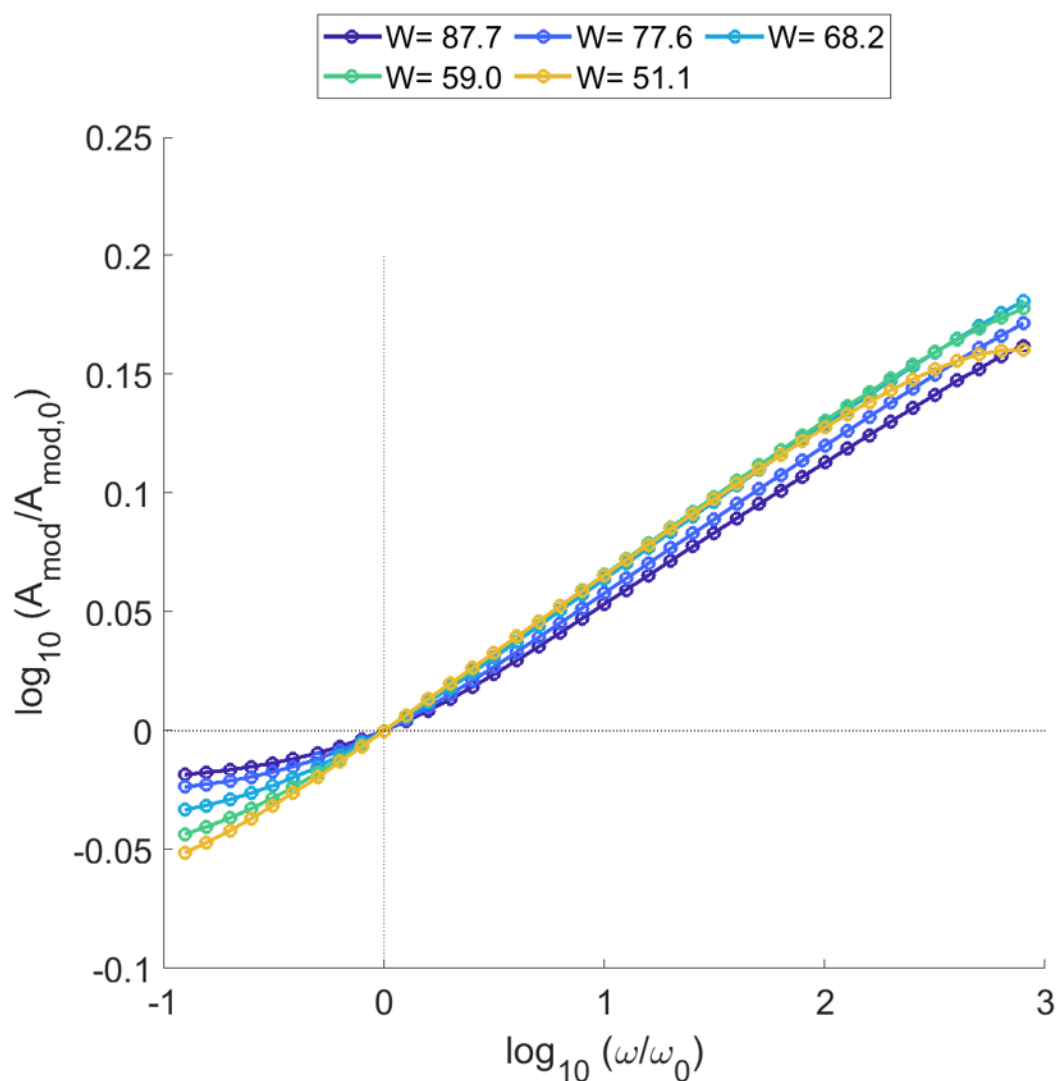


Figure 5.13 – Scaled Summerfield plots for water as a colorized set of series for each water content value.

From the perspective of sensing, the increased scatter in results at higher frequencies suggests that this could be a more sensitive region for sensing moisture contents and distinguishing them from temperature shifts. It has therefore been selected a single frequency of 10 kHz for the remainder of the sensor characterization described in this chapter. As shown by Figure 5.9, this frequency also corresponds to the region where phase angles tend to be at their highest values, but the frequencies are not so high to see the influence of the inductance that is currently not possible to fully explain.

#### 5.5.4. Sensor response

Figure 5.14 shows plots of sensor response at 10 kHz to a) temperature and b) moisture contents. Here the sensor response has been defined as  $\frac{Z_{mod}}{Z_{mod,0}}$ , where  $Z_{mod,0}$  is the modulus of impedance of the sensor in ambient conditions (i.e. at a water content of 60% and at a temperature of 20 °C). As shown, equations 5.10 and 5.14 provide good non-linear fits to the data.

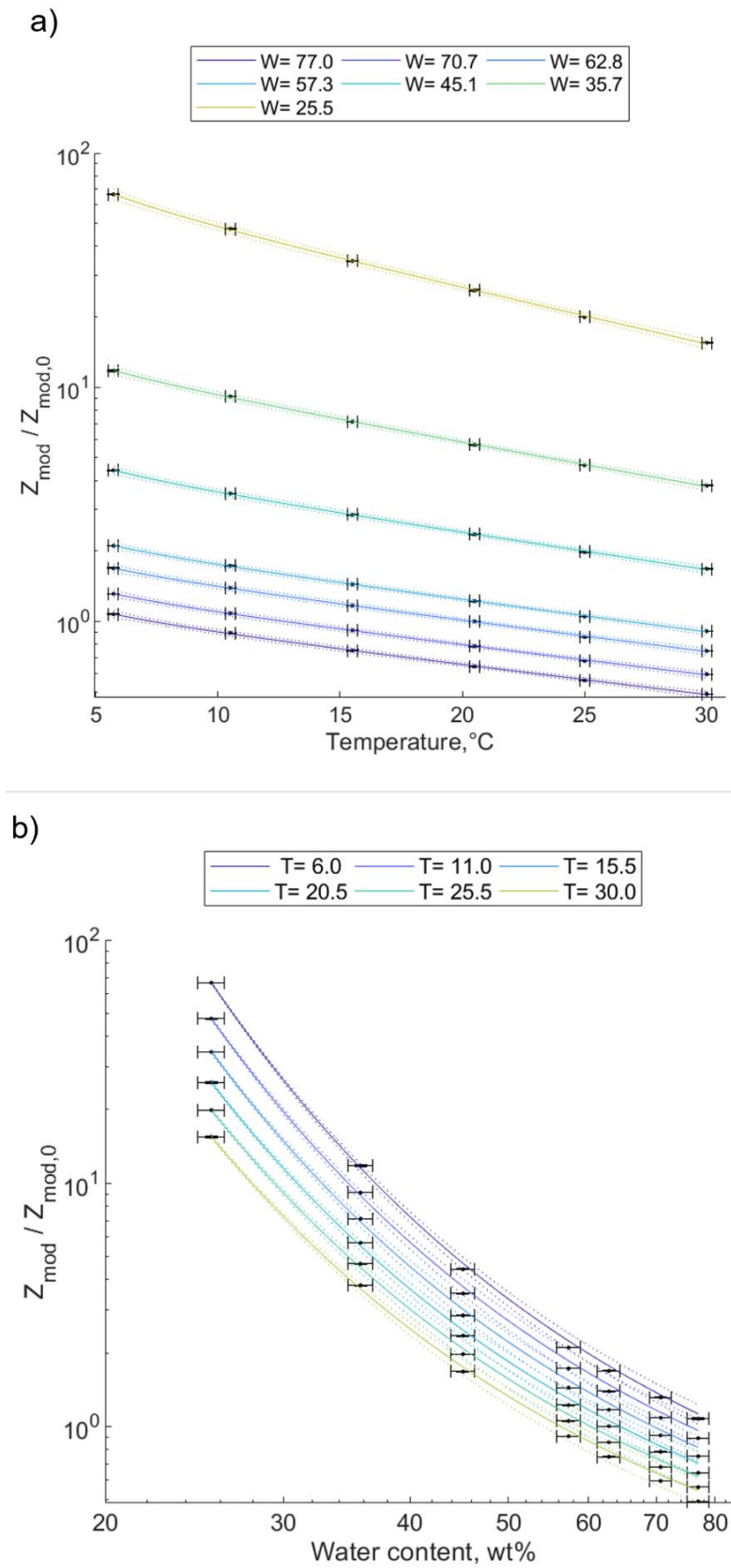


Figure 5.14 – a) Plots of  $Z_{mod}/Z_{mod,0}$  versus temperature for each water content. Non-linear fits use equation 5.10. b) Plots of  $Z_{mod}/Z_{mod,0}$  versus water content for each temperature. Non-linear fits use equation 5.14.

The overall response of the sensor for any general water/temperature combination is better characterized by fitting temperature and moisture simultaneously, using equation 5.15. Figure 5.15 shows the data from Figure 5.14 on a 3D scatterplot. Here the “dryness” of the sample has been defined as the inverse of its moisture content, or  $1/W$ . This allows to fit a surface described by equation 5.15, where the parameters of the fit and their standard errors are given in Table 5.4.

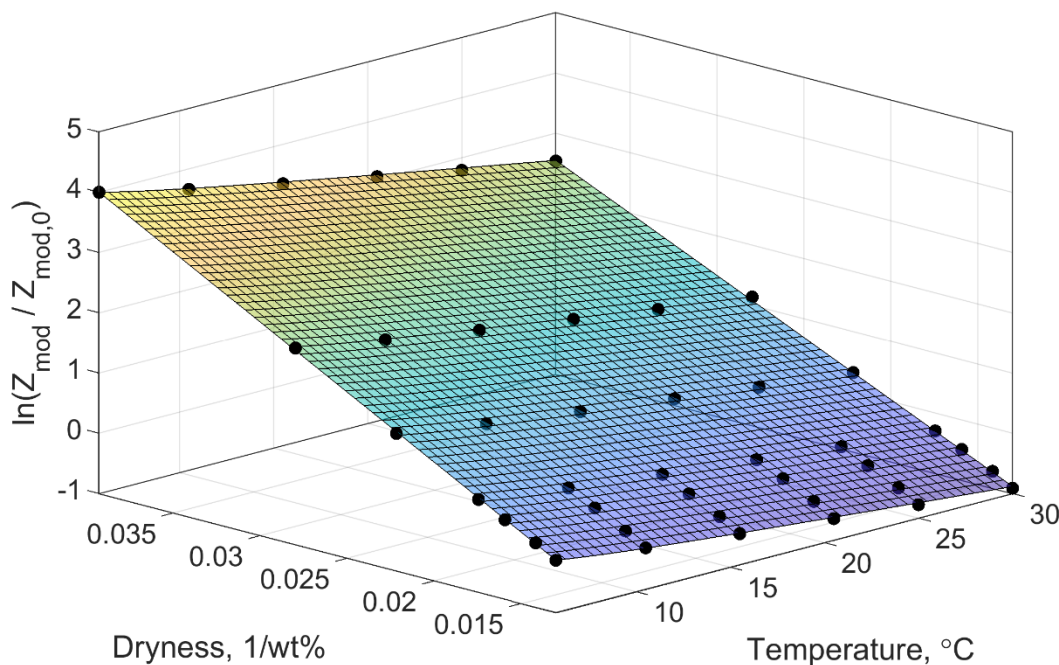


Figure 5.15 - 3D plot of calibration curve for sensor as a function of both moisture and temperature. The surface of best fit shown is described by equation 5.15.

Parameter	$G_1$	$G_2$	$G_3$	$G_4$	$G_4$
Value	0.82	-0.012	163.2	-1.09	-2.24
<b>95% confidence bounds</b>					
Lower	0.44	-0.016	161.1	-1.20	-2.32
Upper	1.20	-0.001	165.4	-0.97	-2.16

Table 5.4 - Parameters and their 95% confidence bounds for the plane of best fit, equation 5.15, shown in Figure 5.15.

Using these parameterization constants, the water content of a sample can be ascertained if a second reference sensor (a nearby thermocouple) is used for temperature compensation as:

$$W = \frac{G_3 + G_4 T}{\ln\left(\frac{Z_{mod}}{Z_{mod,0}}\right) - \frac{G_1}{T} - G_2 T - G_5} \tag{Eq. 5.17}$$

### 5.5.5. Sensor precision

The non-linear dependence of the sensor from water content and temperature means that the precision is not fixed for all water contents and temperatures. In general, precision is higher when the changes in impedance are large, i.e. when the conductivity of the sample is high, at high temperatures and moisture contents. Nevertheless, the precision can be calculated by mapping the impedance fluctuations of the EIS interrogator onto the moisture and temperature axes, using the calibration surface shown in Figure 5.15. These calculations are shown in detail in Appendix 1 (sections A-1.1 and A-1.2). The fractional errors in the impedance values measured using the interrogator are typically 0.1 – 0.8 %.

As such, the results of this exercise, shown in Table 5.5, demonstrate that, even in worse case conditions, the precision of the sensor is acceptable, at  $\delta W = 0.3 \text{ wt}\%$  and  $\delta T = 0.2 \text{ }^\circ\text{C}$ . In typical conditions, precisions of  $\delta W = 0.1 \text{ wt}\%$  and  $\delta T = 0.1 \text{ }^\circ\text{C}$  are achievable.

	Moisture precision $\delta W, \text{ wt}\%$	Temperature precision $\delta T, \text{ }^\circ\text{C}$
<b>Worst case</b>	0.26	0.18
<b>Typical case</b>	0.09	0.10
<b>Best case</b>	0.02	0.06

Table 5.5 – Worst case, best case and typical precisions for moisture and temperature sensing.

### 5.5.6. Sensor repeatability

Figure 5.16 and Figure 5.17 demonstrate the excellent repeatability of the sensors in response to temperature and wetting cycles. However, in order to quantitatively evaluate this repeatability, Pooled Repeatability of the temperature and wetting cycles measurements has been calculated. The mathematical formulation of Pooled Repeatability is found in Appendix 2. For the two temperature cycles shown, the response has been found to be repeatable to within a maximum deviation of 1 – 2%. For moisture, sensor pooled repeatability between all three wetting cycles is 3 – 4%. This corresponds to a repeatability in moisture measurement of 0.2 – 1.5 wt%.

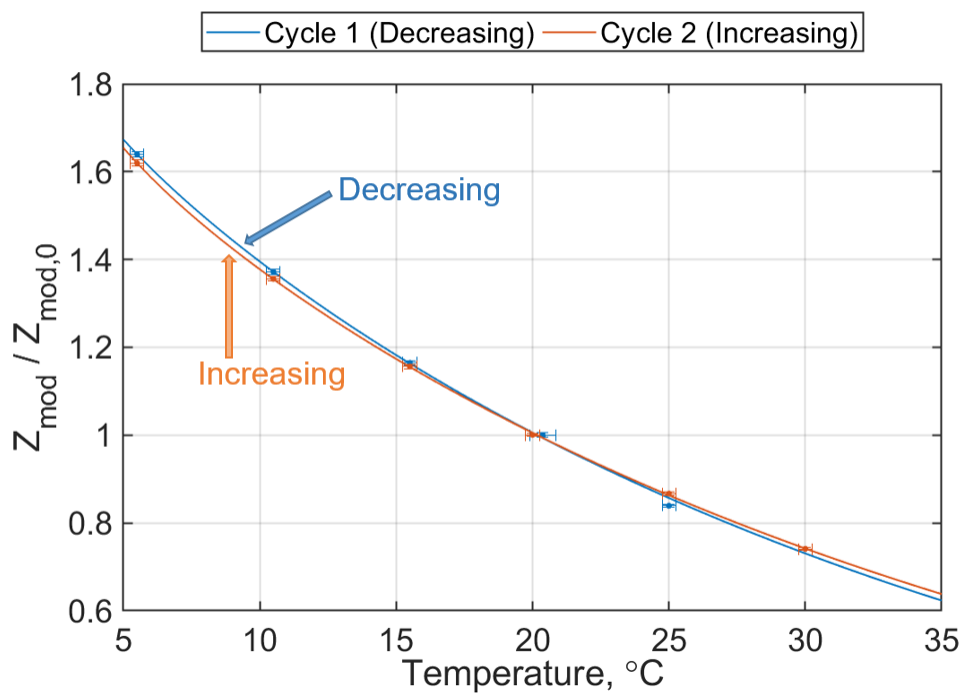


Figure 5.16 – Sensor response for increasing and decreasing temperature cycles for  $w = 89$  wt%. Non-linear fits use equation 5.10 for  $Z$ .

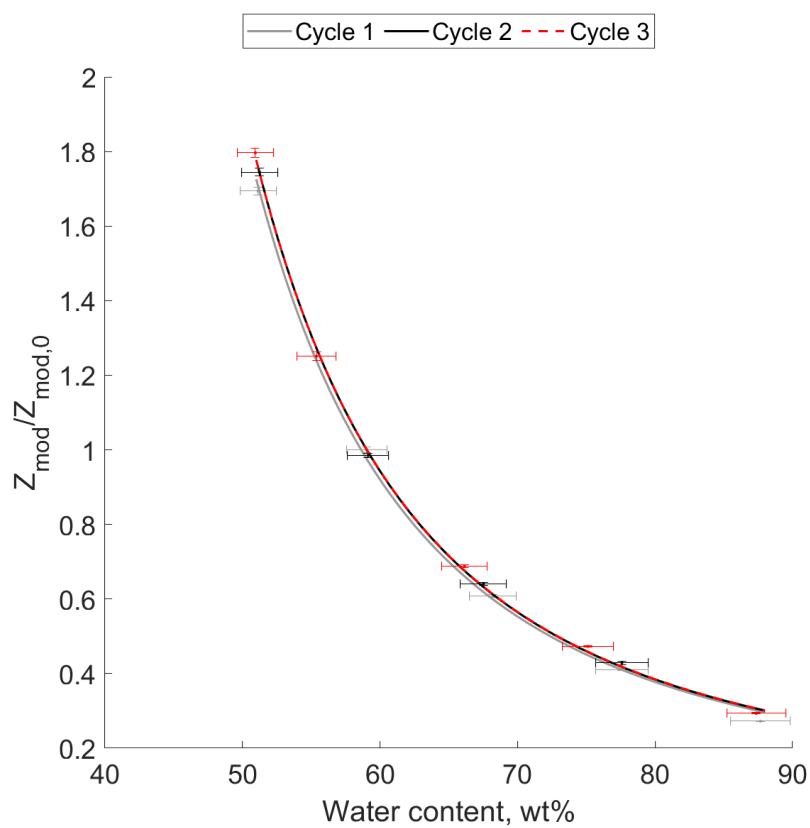


Figure 5.17 – Sensor response for three consecutive wetting-drying cycles. Non-linear fits use equation 5.13 for  $Z$ .

### 5.5.7. Critical comparison with other sensors

The moisture content values quoted as wt% in this work can be converted to vol% by multiplying by the relative bulk density of the geopolymer matrix (measured to be RD=1.535). This allows the precision and repeatability of the sensor to be compared to other common moisture sensors for soils reviewed in [83]. As shown in Table 5.6, the precision of the geopolymer sensor compares favourably with competing methods, with a comparable or lower repeatability.

	Precision (vol%)	Repeatability (vol%)	Continuous measurement?
Neutron scattering	0.01–4	0.02	No
Time-domain reflectometry	1–3	0.2	Yes
Frequency domain reflectometry	1–3	0.2	Yes
Geopolymer sensor	0.03–0.5	0.2–2	Yes

Table 5.6 – Critical comparison of sensor developed in this work with other common moisture monitoring techniques from [83].

### 5.5.8. Ion leaching

The good repeatability of the impedance response with moisture shown in Figure 5.17 suggests that ion leaching is minimal. However, ICP and IC analyses were conducted to assess long-term moisture sensing performance. The results, shown in Table 5.7, suggest that Na<sup>+</sup> ions do leach in small quantities from the geopolymer when it is submerged in water, along with silicon and chloride ions. Despite this, their percentages are thought to be a small fraction of the sodium that the geopolymer binder contains. Whether Na<sup>+</sup> exists in the bulk pore solution or adsorbed onto the pore walls is unknown and beyond the scope of this work but the very low levels of Na<sup>+</sup> being leached during the wash cycles (15–51 mg/L) shown in Table 5.7 is an encouraging sign for the long term performance of the sensor.

Wash cycle	Na <sup>+</sup> [%]	Si <sup>+</sup> [%]	Cl <sup>-</sup> [%]
1 <sup>st</sup> wash	0.06496	0.00393	0.00062
2 <sup>nd</sup> wash	0.03716	0.00262	0.00018
3 <sup>rd</sup> wash	0.12294	0.01382	0.00031

Table 5.7 – Percentage of Na<sup>+</sup>, Si<sup>+</sup> and Cl<sup>-</sup> ions leached from the geopolymer sample into deionized water.

### 5.5.9. Sensor drift

Another important parameter to investigate is the long-term stability of the sensor's response. Low frequency changes in the sensor response (sensor drift) were extracted independently of high frequency changes (noise), using a low-pass filter: the signal was smoothed with a 20 sample (20 minute) period moving average with a window of 5 minutes. The drift is defined as the maximum fractional shift in this smoothed signal. Using this approach allowed to extract a drift indicator for all temperature and moisture points over a total sampling period of 28 days. The result, shown in Figure 5.18, shows that sensor drift is usually negative, and worst at high temperatures and low moisture contents, but is always  $< 3\%$  over each 20 min period.

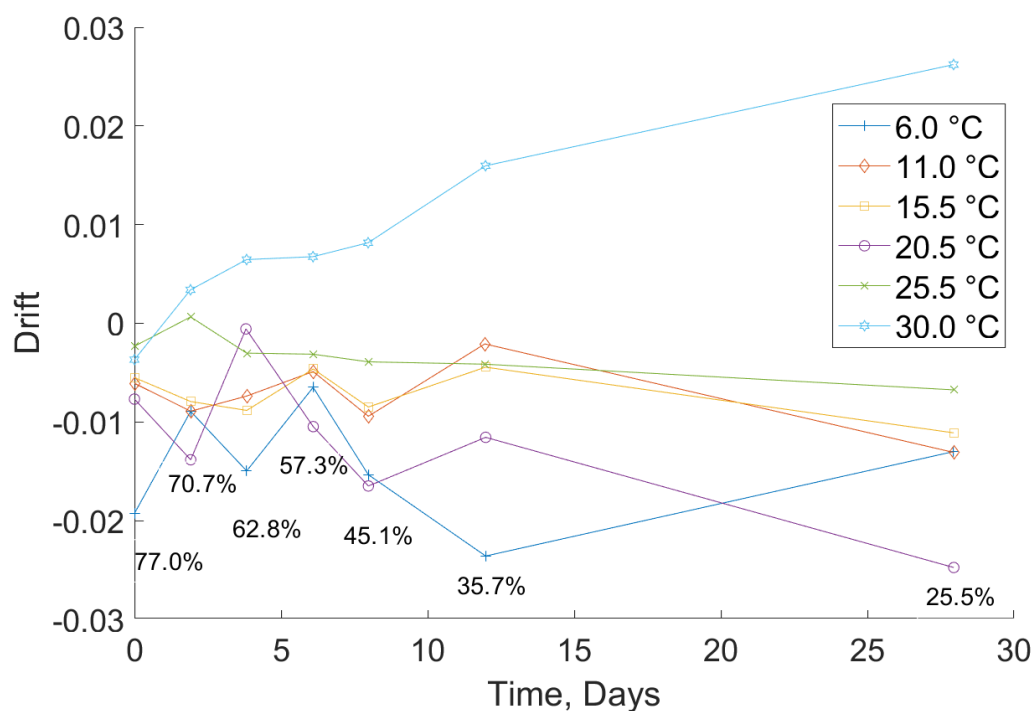


Figure 5.18 - Sensor drift as a function of time, temperature and moisture. Data labels show each moisture content as samples were dried over 28 days. Meanwhile, each temperature is plotted as a new series. The data shown here cover the same data points plotted in Figure 5.15.

## 5.6. Summary and future work

This chapter has provided the first time demonstration in literature of the viability of monitoring moisture content in low calcium fly ash geopolymers. In this work, a sensor prototype was developed. It is made of a geopolymer block with stainless steel electrodes

in a Van Der Pauw configuration, coupled with an electrical interrogation system to measure electrical impedance. A laboratory experimental campaign of impedance measurements was conducted in order to characterize the sensor and assess its performance (precision, repeatability, and drift) at varying moisture contents and temperatures.

The results showed that, as expected from theory, changes in water content of the geopolymer cell result in changes in impedance, with an exponential dependence. It was demonstrated that it is possible to find the water content of the geopolymer cell prototype for each impedance value measured and for each given temperature, through a calibration equation which describes a 3D fit surface for the experimental points. This result constitutes a remarkable scientific result, and at the same time demonstrates the capability of such sensor to detect water contents and temperatures which are in the range of those found in nuclear storage structures, such as SPRS. Moreover, ion leaching analyses showed that a high sensor repeatability stemmed from the fact that relatively low levels of  $\text{Na}^+$  (the main ionic charge carrier in the sensor) are leached during wetting/washing cycles.

It was found that, in general, sensor performance is lower at low moisture contents (25 wt%). Electrical conductivity (and so sensitivity) decreases as the sensor is dried, and this leads to a lower achievable precision. Low moisture combined with high temperature (30 °C) was meanwhile found to lead to a higher sensor drift. This may partly be due to some change in the physical mechanisms behind geopolymer electrical conductivity when pore connectivity is low and ion mobility is high. The affordability of the technique outlined in this work is on par with direct measurements of concrete impedance, but the higher electrical conductivity of geopolymers could allow for monitoring over a broader range of moisture contents with affordable electronics. The sensor prototype outlined constitutes a solution for structural health monitoring applications in damp, critical environments, such as nuclear repositories, where the sensors could be deployed and either routinely monitored or continuously interrogated with a wireless system.

Future work will characterize the response time of the sensor, investigate field deployment methods, and explicitly demonstrate that moisture can be ascertained independently of temperature when a second reference sensor (a nearby thermocouple) is used for temperature compensation.

The same sensor prototype developed and characterised for moisture and temperature in this chapter can be used for chloride sensing. As for moisture, there is no literature so far

on geopolymer-based chloride sensors. A preliminary work on the feasibility and characterisation of geopolymer sensors for chloride is described in next chapter.

## References

- [1] P. C. Chang, A. Flatau, and S. Liu, "Health monitoring of civil infrastructure," *Structural health monitoring*, vol. 2, pp. 257-267, 2003.
- [2] M. Perry, M. Saafi, G. Fusiek, and P. Niewczas, "Hybrid optical-fibre/geopolymer sensors for structural health monitoring of concrete structures," *Smart Materials and Structures*, vol. 24, p. 045011, 2015.
- [3] G. Park, H. H. Cudney, and D. J. Inman, "Impedance-based health monitoring of civil structural components," *Journal of infrastructure systems*, vol. 6, pp. 153-160, 2000.
- [4] D. Inman, "Smart structures solutions to vibration problems," in *PROCEEDINGS OF THE INTERNATIONAL SEMINAR ON MODAL ANALYSIS*, 1998, pp. 1-12.
- [5] C. Boller, "Composites for sensors and actuators," 2001.
- [6] G. Koch, J. Varney, N. Thompson, O. Moghissi, M. Gould, and J. Payer, "International measures of prevention, application and economics of corrosion technologies study (impact)," Technical report. NACE international 2016.
- [7] G. H. Koch, M. P. Brongers, N. G. Thompson, Y. P. Virmani, and J. H. Payer, "Corrosion cost and preventive strategies in the United States," United States. Federal Highway Administration 2002.
- [8] L. Bertolini, B. Elsener, P. Pedferri, E. Redaelli, and R. Polder, *Corrosion of steel in concrete* vol. 392: Wiley Online Library, 2013.
- [9] M. Torres-Luque, E. Bastidas-Arteaga, F. Schoefs, M. Sánchez-Silva, and J. F. Osma, "Non-destructive methods for measuring chloride ingress into concrete: State-of-the-art and future challenges," *Construction and building materials*, vol. 68, pp. 68-81, 2014.
- [10] B. Conde, S. Del Pozo, B. Riveiro, and D. González-Aguilera, "Automatic mapping of moisture affectation in exposed concrete structures by fusing different wavelength remote sensors," *Structural Control and Health Monitoring*, vol. 23, pp. 923-937, 2016.
- [11] N. Buenfeld, R. Davies, A. Karimi, and A. Gilbertson, "Intelligent monitoring of concrete structures," 2008.
- [12] S. Sikarwar and B. Yadav, "Opto-electronic humidity sensor: A review," *Sensors and Actuators A: Physical*, vol. 233, pp. 54-70, 2015.
- [13] Z. Rittersma, "Humidity sensor," *Encycl. Sens*, vol. 4, pp. 481-509, 2006.
- [14] C.-Y. Lee and G.-B. Lee, "Humidity sensors: a review," *Sensor Letters*, vol. 3, pp. 1-15, 2005.
- [15] N. Yamazoe and Y. Shimizu, "Humidity sensors: principles and applications," *Sensors and Actuators*, vol. 10, pp. 379-398, 1986.
- [16] J.-R. Huang, M.-Q. Li, and J.-H. Liu, "A novel conductive humidity sensor based on field ionization from carbon nanotubes," *Sensors and Actuators A: Physical*, vol. 133, pp. 467-471, 2007.
- [17] R. Fenner and E. Zdzankiewicz, "Micromachined water vapor sensors: a review of sensing technologies," *IEEE Sensors Journal*, vol. 1, pp. 309-317, 2001.

- [18] J. Kim and P. Reucroft, "Solid state water vapor sensor for robotics applications," in *Proceedings. 1988 IEEE International Conference on Robotics and Automation*, 1988, pp. 1302-1303.
- [19] O. Vancauwenberghe, J. Short, E. Giehler, P. Bildstein, P. Ancey, and M. Gschwind, "Design of the interface electronics for an integrated microsensor for the preventive detection of water condensation," in *Proceedings of the International Solid-State Sensors and Actuators Conference-TRANSDUCERS'95*, 1995, pp. 835-838.
- [20] K. V. Heber, "Humidity measurement at high temperatures," *Sensors and actuators*, vol. 12, pp. 145-157, 1987.
- [21] B. Yadav, R. Srivastava, C. Dwivedi, and P. Pramanik, "Moisture sensor based on ZnO nanomaterial synthesized through oxalate route," *Sensors and Actuators B: Chemical*, vol. 131, pp. 216-222, 2008.
- [22] F. Pacheco-Torgal, J. Castro-Gomes, and S. Jalali, "Alkali-activated binders: A review: Part 1. Historical background, terminology, reaction mechanisms and hydration products," *Construction and Building Materials*, vol. 22, pp. 1305-1314, 2008.
- [23] S. Hanjitsuwan, P. Chindaprasirt, and K. Pimraksa, "Electrical conductivity and dielectric property of fly ash geopolymer pastes," *International Journal of Minerals, Metallurgy, and Materials*, vol. 18, pp. 94-99, 2011.
- [24] X.-M. Cui, G.-J. Zheng, Y.-C. Han, F. Su, and J. Zhou, "A study on electrical conductivity of chemosynthetic Al<sub>2</sub>O<sub>3</sub>-2SiO<sub>2</sub> geopolymer materials," *Journal of Power Sources*, vol. 184, pp. 652-656, 2008.
- [25] M. Saafi, A. Gullane, B. Huang, H. Sadeghi, J. Ye, and F. Sadeghi, "Inherently multifunctional geopolymeric cementitious composite as electrical energy storage and self-sensing structural material," *Composite Structures*, vol. 201, pp. 766-778, 2018.
- [26] M. Saafi, L. Tang, J. Fung, M. Rahman, F. Sillars, J. Liggat, and X. Zhou, "Graphene/fly ash geopolymeric composites as self-sensing structural materials," *Smart materials and structures*, vol. 23, p. 065006, 2014.
- [27] M. Perry, M. Saafi, G. Fusiek, and P. Niewczas, "Geopolymeric thermal conductivity sensors for surface-mounting onto concrete structures," 2016.
- [28] M. Saafi, G. Piukovics, and J. Ye, "Hybrid graphene/geopolymeric cement as a superionic conductor for structural health monitoring applications," *Smart Materials and Structures*, vol. 25, p. 105018, 2016.
- [29] M. Saafi, K. Andrew, P. L. Tang, D. McGhon, S. Taylor, M. Rahman, S. Yang, and X. Zhou, "Multifunctional properties of carbon nanotube/fly ash geopolymeric nanocomposites," *Construction and Building Materials*, vol. 49, pp. 46-55, 2013.
- [30] T. Yeo, M. Cox, L. Boswell, T. Sun, and K. Grattan, "Optical fiber sensors for monitoring ingress of moisture in structural concrete," *Review of scientific instruments*, vol. 77, p. 055108, 2006.
- [31] T. Yeo, D. Eckstein, B. McKinley, L. Boswell, T. Sun, and K. Grattan, "Demonstration of a fibre-optic sensing technique for the measurement of moisture absorption in concrete," *Smart materials and structures*, vol. 15, p. N40, 2006.
- [32] Z. C. Grasley, D. A. Lange, M. D. D'Ambrosia, and S. Villalobos-Chapa, "Relative humidity in concrete," *Concrete international*, vol. 28, pp. 51-57, 2006.
- [33] R. M. Chacko, N. Banthia, and A. A. Mufti, "Carbon-fiber-reinforced cement-based sensors," *Canadian Journal of Civil Engineering*, vol. 34, pp. 284-290, 2007.
- [34] M. Saleem, M. Shameem, S. Hussain, and M. Maslehuddin, "Effect of moisture, chloride and sulphate contamination on the electrical resistivity of Portland cement concrete," *Construction and Building Materials*, vol. 10, pp. 209-214, 1996.

- [35] G. Woelfl and K. Lauer, "The electrical resistivity of concrete with emphasis on the use of electrical resistance for measuring moisture content," *Cement, concrete and Aggregates*, vol. 1, pp. 64-67, 1979.
- [36] G. Monfore, "A small probe-type gage for measuring relative humidity," 1963.
- [37] P. Schie, L. Breot, and M. Raupach, "Investigations into the effect of coatings on water distribution in concrete using multi-ring electrodes," *Special Publication*, vol. 151, pp. 119-134, 1994.
- [38] A. Schießl, W. Weiss, J. Shane, N. Berke, T. Mason, and S. Shah, "Assessing the moisture profile of drying concrete using impedance spectroscopy," *Concrete Science and Engineering(France)*, vol. 2, pp. 106-116, 2000.
- [39] I. Sánchez, C. Antón, G. De Vera, J. M. Ortega, and M. Climent, "Moisture distribution in partially saturated concrete studied by impedance spectroscopy," *Journal of Nondestructive Evaluation*, vol. 32, pp. 362-371, 2013.
- [40] K. Brantervik, A. Berg, G. Niklasson, B. Hedberg, and L.-O. Nilsson, "Percolation effects in the electrical conductivity of porous cement mortar," *EPL (Europhysics Letters)*, vol. 13, p. 549, 1990.
- [41] W. J. McCarter, G. Alaswad, and B. Suryanto, "Transient moisture profiles in cover-zone concrete during water absorption," *Cement and Concrete Research*, vol. 108, pp. 167-171, 2018.
- [42] F. Rajabipour, J. Weiss, and D. M. Abraham, "Insitu electrical conductivity measurements to assess moisture and ionic transport in concrete (A discussion of critical features that influence the measurements)," in *Proceedings of the International RILEM Symposium on Concrete Science and Engineering: A Tribute to Arnon Bentur*, 2004.
- [43] A. Nguyen, G. Klysz, F. Deby, and J.-P. Balayssac, "Evaluation of water content gradient using a new configuration of linear array four-point probe for electrical resistivity measurement," *Cement and Concrete Composites*, vol. 83, pp. 308-322, 2017.
- [44] L. Molina, *Measurement of high humidity in cementitious material at an early age*: Swedish cement and concrete research institute, 1990.
- [45] A. Norris, M. Saafi, and P. Romine, "Temperature and moisture monitoring in concrete structures using embedded nanotechnology/microelectromechanical systems (MEMS) sensors," *Construction and Building Materials*, vol. 22, pp. 111-120, 2008.
- [46] Y. Yao and B. Glisic, "Sensing sheets: Optimal arrangement of dense array of sensors for an improved probability of damage detection," *Structural Health Monitoring*, vol. 14, pp. 513-531, 2015.
- [47] J. He, G. Zhang, S. Hou, and C. Cai, "Geopolymer-based smart adhesives for infrastructure health monitoring: concept and feasibility," *Journal of Materials in Civil Engineering*, vol. 23, pp. 100-109, 2011.
- [48] M. S. Muntini and H. Ahmadi, "Performance of metakaolin geopolymer ceramic for fiber optic temperature sensor," *Materials Today: Proceedings*, vol. 5, pp. 15137-15142, 2018.
- [49] I. Kang, M. J. Schulz, J. H. Kim, V. Shanov, and D. Shi, "A carbon nanotube strain sensor for structural health monitoring," *Smart materials and structures*, vol. 15, p. 737, 2006.
- [50] P. Dharap, Z. Li, S. Nagarajaiah, and E. Barrera, "Nanotube film based on single-wall carbon nanotubes for strain sensing," *Nanotechnology*, vol. 15, p. 379, 2004.
- [51] Z. Jing, Z. Guang-Yu, and S. Dong-Xia, "Review of graphene-based strain sensors," *Chinese Physics B*, vol. 22, p. 057701, 2013.
- [52] A. Deepak, N. Srinivasan, V. Karthik, S. Ramya, V. Ganesan, and P. Shankar, "Graphene based polymer strain sensors for non-destructive testing," in *Advanced Materials Research*, 2015, pp. 314-317.

- [53] X. Fu, W. Lu, and D. Chung, "Improving the strain-sensing ability of carbon fiber-reinforced cement by ozone treatment of the fibers," *Cement and concrete research*, vol. 28, pp. 183-187, 1998.
- [54] X. Yu and E. Kwon, "A carbon nanotube/cement composite with piezoresistive properties," *Smart Materials and Structures*, vol. 18, p. 055010, 2009.
- [55] F. Azhari and N. Banthia, "Cement-based sensors with carbon fibers and carbon nanotubes for piezoresistive sensing," *Cement and Concrete Composites*, vol. 34, pp. 866-873, 2012.
- [56] C. Lamuta, S. Candamano, F. Crea, and L. Pagnotta, "Direct piezoelectric effect in geopolymeric mortars," *Materials & Design*, vol. 107, pp. 57-64, 2016.
- [57] S. Bi, M. Liu, J. Shen, X. M. Hu, and L. Zhang, "Ultrahigh self-sensing performance of geopolymer nanocomposites via unique interface engineering," *ACS applied materials & interfaces*, vol. 9, pp. 12851-12858, 2017.
- [58] S. Vaidya, "Applications of electricity in the rehabilitation and health monitoring of concrete structures," 2009.
- [59] D. Chung, "Carbon materials for structural self-sensing, electromagnetic shielding and thermal interfacing," *Carbon*, vol. 50, pp. 3342-3353, 2012.
- [60] S. Vaidya and E. N. Allouche, "Strain sensing of carbon fiber reinforced geopolymer concrete," *Materials and structures*, vol. 44, pp. 1467-1475, 2011.
- [61] J. He, G. Zhang, S. Hou, and C. Cai, "Geopolymer-based smart adhesives for infrastructure health monitoring: concept and feasibility," *Journal of Materials in Civil Engineering*, vol. 23, pp. 100-109, 2010.
- [62] M. Gad-el-Hak, *MEMS: introduction and fundamentals*: CRC press, 2005.
- [63] J.-B. Waldner, *Nanocomputers and swarm intelligence*: John Wiley & Sons, 2013.
- [64] A. Trego, "An update on monitoring moisture ingress with fiber optic sensors," in *Sixth Pacific Northwest Fiber Optic Sensor Workshop*, 2003, pp. 94-101.
- [65] B. Lee, "Review of the present status of optical fiber sensors," *Optical fiber technology*, vol. 9, pp. 57-79, 2003.
- [66] A. Mendez, "Fiber Bragg grating sensors: a market overview," in *Third European Workshop on Optical Fibre Sensors*, 2007, p. 661905.
- [67] L. Parrott, "Moisture profiles in drying concrete," *Advances in cement research*, vol. 1, pp. 164-170, 1988.
- [68] R. Spencer, "Measurement of the moisture content of concrete," in *Journal Proceedings*, 1937, pp. 45-64.
- [69] K. Funke and R. D. Banhatti, "Ionic motion in materials with disordered structures," *Solid State Ionics*, vol. 177, pp. 1551-1557, 2006.
- [70] S. Vaidya and E. N. Allouche, "Experimental evaluation of electrical conductivity of carbon fiber reinforced fly-ash based geopolymer," *Smart Structures and Systems*, vol. 7, pp. 27-40, 2011.
- [71] A. Lasia, "Electrochemical impedance spectroscopy and its applications," in *Modern aspects of electrochemistry*, ed: Springer, 2002, pp. 143-248.

- [72] D. Ravikumar and N. Neithalath, "An electrical impedance investigation into the chloride ion transport resistance of alkali silicate powder activated slag concretes," *Cement and Concrete Composites*, vol. 44, pp. 58-68, 2013.
- [73] R. D. Miron, L. Emilio, and D. A. Koleva, *Concrete durability: cementitious materials and reinforced concrete properties, behavior and corrosion resistance*: Springer, 2017.
- [74] V. S. Bagotsky, *Fundamentals of electrochemistry* vol. 44: John Wiley & Sons, 2005.
- [75] M. Cabeza, P. Merino, A. Miranda, X. Nóvoa, and I. Sanchez, "Impedance spectroscopy study of hardened Portland cement paste," *Cement and Concrete Research*, vol. 32, pp. 881-891, 2002.
- [76] M. S. Abouzari, F. Berkemeier, G. Schmitz, and D. Wilmer, "On the physical interpretation of constant phase elements," *Solid State Ionics*, vol. 180, pp. 922-927, 2009.
- [77] P. Cordoba-Torres, M. Keddam, and R. P. Nogueira, "On the intrinsic electrochemical nature of the inductance in EIS: A Monte Carlo simulation of the two-consecutive-step mechanism: The flat surface 2 D case," *Electrochimica Acta*, vol. 54, pp. 518-523, 2008.
- [78] N. Van Meurs, "Temperature dependence of the conductivity of electrolyte solutions," *Nature*, vol. 182, p. 1532, 1958.
- [79] Z. Moroń and T. Grysiński, "Experimental investigations of van der Pauw method applied for measuring electrical conductivity of liquids," in *19th IMEKO World congress fundamental and applied metrology*, 2009, pp. 1640-1644.
- [80] C. Chaparro, L. Herrera, A. Meléndez, and D. Miranda, "Considerations on electrical impedance measurements of electrolyte solutions in a four-electrode cell," in *Journal of Physics: Conference Series*, 2016, p. 012101.
- [81] G. Instruments, "Basics of electrochemical impedance spectroscopy," *G. Instruments, Complex impedance in Corrosion*, pp. 1-30, 2007.
- [82] R. F. Craig, *Craig's soil mechanics*: CRC press, 2004.
- [83] S. L. SU, D. Singh, and M. S. Baghini, "A critical review of soil moisture measurement," *Measurement*, vol. 54, pp. 92-105, 2014.

# 6. GEOPOLYMER-BASED CHLORIDE SENSORS

## 6.1. Introduction

Degradation of reinforced concrete structures is a problem of primary importance for the ageing population of structures of many developed countries, and for safety-critical structures, such as those in nuclear context. One of the major causes of reinforced concrete degradation is chloride ingress [1-3], together with moisture content. Exposure of concrete structures to chloride-bearing solutions such as sea water or de-icing salts can lead to corrosion of steel reinforcement, thus causing concrete degradation [4].

According to statistics, many reinforced concrete structures and infrastructures were damaged by chloride penetrating from the surrounding environment, over longer duration of exposure, especially in tidal zones and coastal areas [4-8]. Corrosion induced by chloride has led to very high repair costs, which sometimes overcome the initial construction cost, and when left under-maintained in extreme situations can result in the collapse of the structure [9]. For this reason, chloride and water ingress into reinforced concrete structures requires measurement, control and mitigation. This is particularly valid for safety critical structures, such as those in a nuclear context, where concrete assets are usually coastal, and often play the crucial role of containment of radioactive packaged materials.

Section 2.4.1 outlined that no chloride content monitoring inside concrete has been applied to reinforced concrete nuclear stores so far. The techniques used so far in nuclear store

structures, such as steel sample plates and chloride candles measuring atmospheric salt content [10], are giving representative surface salt deposition measurements. They don't provide a value for the chloride content of the concrete. As already seen in chapter 2, the absence of air filtering mechanisms in some of those structures makes the need for forefront monitoring technologies even more urgent and fundamental.

Chloride monitoring is challenging. Some techniques for measuring chloride content in reinforced concrete have already been investigated. Some of them are destructive or semi-destructive, time-consuming and costly, such as potentiometric and Volhard methods, which measure free and total chlorides in concrete cores extracted from in service structures [2]. Currently, there is a growing interest for non-destructive techniques (NDT) to measure chloride content in reinforced concrete, such as Ion selective electrodes (ISE) [11-16], Optical fiber sensors (OFS) [17-19] and Electrical resistivity (ER) [20-26]. These methods consist of external or embedded equipment to concrete or other cementitious materials to which they are applied [11, 27]. Embedded sensors have been used to monitor the initiation of corrosion of steel reinforcement with time, and measure the open circuit potential and polarisation of steel reinforcement, humidity inside the concrete, chloride content and other properties [4]. Among these techniques, electrochemical impedance spectroscopy (EIS) has been used for corrosion assessment [28], and for chloride diffusion coefficient estimation [29-31] in laboratory concrete specimens. Most of the existing applications of these techniques present the drawback of needing the sensor to be embedded into concrete (which requires forethought or drilling). More detail on these competing sensor methods is provided in section 6.2.1 of this thesis.

This chapter represents a first time demonstration of geopolymer-based chloride sensors. In this system, Electrochemical Impedance Spectroscopy is applied to low calcium fly ash geopolymer binders, rather than directly to concrete. This solution takes advantage of the electrolytic nature of geopolymers, which show higher conductivities than concrete, as already shown in the previous chapter. This allows them to be used without the need of conductive additives. Another advantage of applying EIS to geopolymers is given by the advantageous chemical and physical properties of such materials and their strong adhesion to concrete, as already shown in chapters 3, 4 and 5. Moreover, in chapter 4 it has been demonstrated that geopolymer binders cured at room temperature and high Relative Humidity (RH) levels, and manufactured without any additive or grinding processes, can be applied as thin coatings onto concrete, and achieve mechanical properties which make them

suitable to be used as non-structural repair. Avoiding heating and additives, such as plastic fibers, makes this system suitable to be used in safety-critical applications, in a nuclear context.

This sensing system can be produced as both skin sensors applied onto concrete (a preliminary laboratory characterisation of such system is provided in chapter 7) or independent sensor prototypes to be deployed near concrete structures. The moisture sensing capability of geopolymers has already been demonstrated in chapter 5. The work outlined in this chapter has the aim of demonstrating the chloride sensing capability of geopolymers. It investigates the chloride sensing capability of the same geopolymer sensor prototype described in chapter 5. This study constitutes the first step in the development of a system which has the future aim of being applied as a distributed geopolymer skin sensor for concrete structures.

The remainder of this chapter starts with section 6.2, where the state of the art of the existing chloride sensing methods for structural health monitoring is presented in detail (section 6.2.1), the new chloride sensing system proposed in this work is introduced (section 6.2.2) and the theory behind the sensing principle of the chloride sensor presented and characterised in this chapter is outlined (section 6.2.3). Section 6.3 describes the materials and methods used for the experimental characterisation of the sensor. The results of the experiment and the relative discussion are presented in section 6.4. Finally, conclusions and future work are found in section 6.5.

## 6.2. Theory and state of the art

A review on the existing methods to measure chloride in concrete for structural health monitoring (SHM), the chloride sensing system characterised in this chapter, and the theory behind its sensing principle are presented respectively in section 6.2.1, in section 6.2.2 and in section 6.2.3.

### 6.2.1. State of the art: chloride monitoring methods for SHM

According to the critical review made by Torres-Luque et al. [2], the most common chloride content measurement techniques have been broadly classified as field and laboratory

techniques. Some lab techniques characterize concrete before it is used in the field: they determine the concrete’s chloride diffusion coefficient to predict the rate of diffusion processes, and are useful for decision-making. Field destructive tests, meanwhile, take samples from in-service structures and determine chloride profiles by using chemical or physical lab techniques. Destructive techniques are mostly used for short term decision making (e.g., urgent, reactive repairs and maintenance). Since the ‘90s, some non-destructive techniques have been developed and applied to chloride content measurement in reinforced concrete structures: they consist of external techniques and embedded sensors. All the mentioned techniques are shown in Table 6.1, and classified by measurement output (i.e. what the techniques directly measure), method (use of lab specimens/destructive/non-destructive), and type (laboratory/field).

Measurement techniques	Measurement output	Method	Type
Rapid chloride permeability test (RCPT)	Chloride penetrability	Specimens	Laboratory
Non steady state diffusion test	Chloride diffusion coefficient		
Electrical migration test			
Electrochemical Impedance Spectroscopy (EIS)			
Ponding test	One-dimensional chloride ingress profile		
Volhard method	Total chloride content	Destructive chemical	Field
Potentiometric evaluation	Free chlorides	Destructive Physical	
Quantitative X-Ray Diffraction analysis			
Ion-selective electrode	Chloride content	Non Destructive	
Electrical resistivity			
Optical fiber			

Table 6.1 - Common techniques for measuring chloride content, chloride ingress and estimating diffusion coefficient in concrete specimens and structures, according to [2]

Recent interest has focused more on non-destructive techniques, which are of interest for this work. For this reason, the following three sub-sections present a detailed description of the most promising non-destructive techniques for chloride sensing in concrete: Ion selective electrodes (ISE) [11-16], Optical fiber sensors (OFS) [17-19] and Electrical resistivity (ER) [20-26].

#### 6.2.1.1. Ion selective electrodes (ISE) device

An ion selective electrode (ISE) is a transducer that converts the activity of a specific ion dissolved in a sample into an electrical potential. The ISE selects a specific ion by a selective

membrane, which can be of four types [32, 33]: glass, solid state, liquid based, and compound electrode. The Ion selective electrode is coupled with a reference electrode (RE) (which is usually a calomel electrode<sup>6</sup>). These embedded sensors determine free chloride concentration near the rebar by measuring changes in the potential difference. Those potential difference changes are related to chemical activity and chloride ion concentration by Nernst equation[2]:

$$\Delta V = V - V_0 = \frac{RT}{nF} \cdot \ln(a_{Cl^-}) - V_{ref} \quad \text{Eq. 6.1}$$

where  $V$  is the measured potential,  $V_0$  is the standard electrode potential,  $R$  is the gas constant,  $T$  is the absolute temperature,  $n$  is the number of electrons,  $F$  is the Faraday constant,  $a_{Cl^-}$  is the chemical activity of chloride ions, and  $V_{ref}$  is the standard potential of the reference electrode.

Elsener et al. [11] used an ISE commercial sensor element to monitor the chloride uptake into mortar specimens. The sensor element was a silver wire coated with electrochemically deposited silver chloride (AgCl), with an internal glass reference electrode. They demonstrated advantages of the sensor, such as good reproducibility and long term stability, but also some issues, such as a questionable long term stability of the reference electrode over several years, and the influence of electric fields on the potential readings of the sensors. Atkins et al. [12, 13] demonstrated the use of silver/silver chloride electrodes as a chloride-monitoring device in concrete, to determine free chloride ion concentration in pressure-extracted cement pore water and in concrete. Some issues were found to be: errors due to the difference in temperature between the measurement and reference electrode; an over estimation of bromide in seawater; potential shifts due to the potential field between the Luggin probe (a small tube which represents the sensing point for the reference electrode near the working electrode) and the silver/silver chloride electrode. Duffò et al. [14, 15] demonstrated that laboratory-made Ag/AgCl electrodes embedded in concrete are chloride-sensitive, and the feasibility of an integrated, embedded into concrete and cost-effective sensor system able to monitor the state of reinforced concrete structures from the corrosion point of view, and to measure the chloride ions concentration and the temperature inside the concrete structure.

---

<sup>6</sup> A calomel electrode is a type of half-cell in which the electrode is mercury coated with calomel ( $Hg_2Cl_2$ ) and the electrolyte is a solution of potassium chloride and saturated calomel.

The general advantages and disadvantages of ISE devices can be summarised and listed in the following Table 6.2:

<b>Advantages</b>	<b>Disadvantages</b>
<ul style="list-style-type: none"> <li>• Chemical stability in aggressive Environments</li> <li>• Easy fabrication</li> <li>• It can be used to sense other parameters, such as temperature</li> <li>• It has been widely used in Electrochemistry</li> </ul>	<ul style="list-style-type: none"> <li>• Temperature can lead to measurement shifts (since they are sensitive to temperature changes)</li> <li>• High alkalinity of pore solution can interfere with the potentiometric response</li> <li>• The presence of electrical fields produces shifts in the potential difference measurement</li> <li>• A prior calibration of the reference electrode is necessary, since not in any experimental conditions it shows long term stability</li> <li>• The sensors need to be embedded directly into concrete samples or structures</li> </ul>

Table 6.2 – Advantages and disadvantages of Ion Selective Electrode sensors, according to [2].

#### 6.2.1.2. Fiber optic sensors

Fiber optic sensors (FOSs) have been developed to detect changes in chloride concentration of concrete. This is possible because a change in the chloride concentration of concrete results in a change in the refractive index of the surrounding medium, and in the refractive index of the cladding [34]. An ultraviolet or laser incident light is sent through the fiber, and the output light is analysed by an optical spectrum analyser, which gives back the value of the central wavelength,  $\lambda_m$ , which is related to both the refractive index of the surrounding medium and of the cladding. Fuhr et al. [17] monitored chloride penetration in a steel bridge in Vermont, US, with FOSs embedded at various points along the bridge: the chloride sensor was based on the interaction between the chloride ions and a sol-gel film, which was positioned between the input-output fiber. Some authors [18, 19] have improved the sensitivity of fiber optics sensors for chloride detection by using gold nanoparticles deposited on the active grating surface of the fibers: they measured chloride ions in a typical concrete sample immersed in salt water solutions with different weight concentrations, by using low-cost long-period fiber grating (LPG) sensors. LPG is an optical fiber structure with the properties periodically varying along the fiber: it couples light from a guided mode into forward propagating cladding modes where it is lost due to absorption and scattering. The loss is spectrally selective, since the coupling from the guided mode to cladding modes is wavelength dependent. The period of such a structure is much larger than the wavelength, and this makes easier their manufacture. The transmission spectrum has dips at the

wavelengths corresponding to resonances with various cladding modes. It was demonstrated [18] a linear decrease in the transmission loss and resonance wavelength shift when the concentration increased, with an accuracy of 0.6%.

Advantages and disadvantages for FOSs are summarised in Table 6.3:

Advantages	Disadvantages
<ul style="list-style-type: none"> <li>• Sensitive to small chloride concentrations</li> <li>• Measurements are not affected by electromagnetic fields</li> <li>• The long and thin geometry can make the distribution of this sensor more convenient for some large structural applications</li> </ul>	<ul style="list-style-type: none"> <li>• They need adequate protection during casting and service life</li> <li>• They need additional protection to isolate the fiber from corrosive environments and high temperatures</li> <li>• They are sensitive to temperature changes;</li> <li>• High cost</li> <li>• Power requirements of the interrogation systems</li> </ul>

Table 6.3 - Advantages and disadvantages of Fiber optic sensors (FOSs), according to [2].

### 6.2.1.3. Electrical Resistivity (ER)

Electrical resistivity measurements have been applied to the estimation of chloride profiles, since chloride presence in concrete increases electrical current, and reduces concrete resistivity [2]. By applying a voltage  $V$  and measuring a current  $I$ , Ohm's law allows the resistance of the material to be found:

$$R = \frac{V}{I} \tag{Eq. 6.2}$$

Which is related to resistivity  $\rho$  by the following equation:

$$R = \frac{A}{l} \cdot \rho \tag{Eq. 6.3}$$

where  $A$  is the electrode area, and  $l$  is the distance between the electrodes.

Four different configurations have been mostly used for the Electrical Resistivity method to assess corrosion and/or chloride content [2]: (a) Wenner array configuration [35]; (b) Disc configuration [25]; (c) Embedded electrodes configuration [26, 36]; (d) Multi-electrode resistivity probes [37]. They are schematically shown in Figure 6.1.

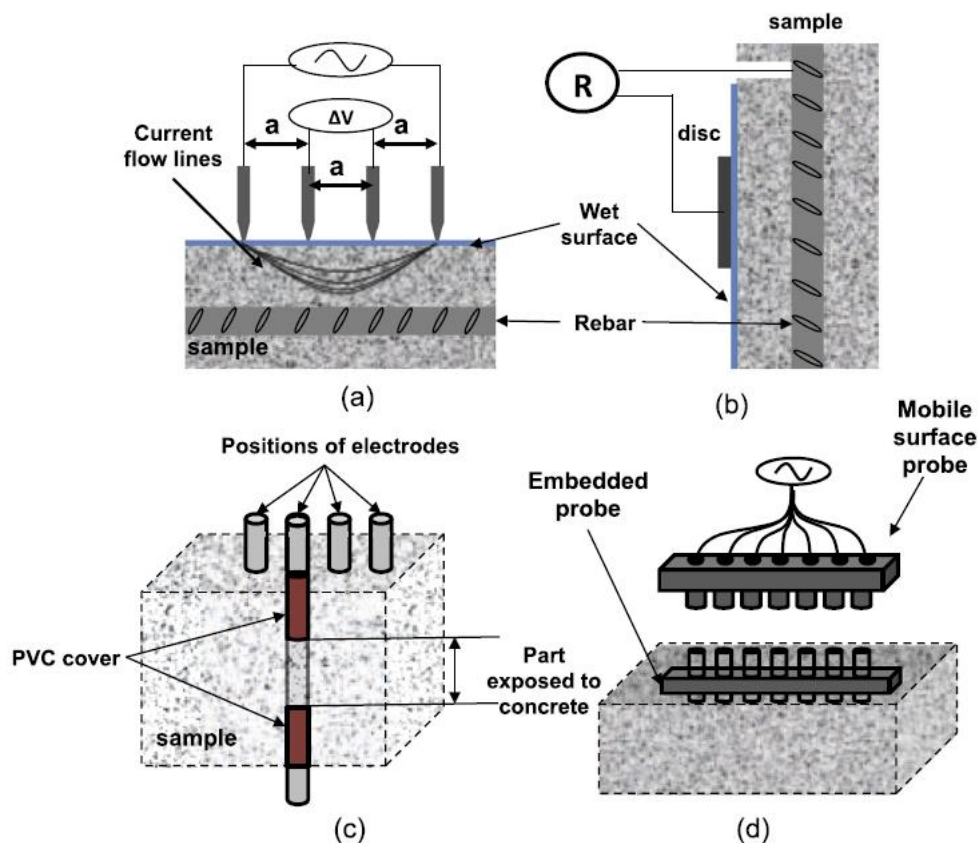


Figure 6.1 – Schematic representation of the four configurations of the Electrical Resistance technique [2]: (a) Wenner array; (d) disc; (c) Embedded electrodes; (d) Multi-electrodes resistivity probes.

Some authors [22] demonstrated that resistivity not only depends on the geometry, but also on the capillary connectivity, level of pore saturation, and concentration and mobility of ions in the pore solution. For this reason, concrete is wet for most of electrical resistivity measurements, in order to improve the effectiveness of the technique. The concrete surfaces shown in Figure 6.1 (a) and (b) are intended to be wet, as the blue colour on the surface symbolises. All the four configurations above consist of directly applying electrodes onto the concrete substrate.

The work of Basheer et al. [26] applied ER measurements to different concrete mixes subjected to a cyclic ponding regime with 0.55 M sodium chloride solution and the changes in concrete. Pairs of stainless steel electrodes were embedded in the concrete at different depths from the exposed surface and the test was continued for nearly one year. This experiment has shown that, in concretes with alternative cementitious materials (ACM), resistivity can change also because of continued hydration of concrete [26]. Fares et al. [20] used Electrical Resistivity Tomography (ERT) in a Wenner configuration to measure resistivities and obtain resistivity profiles versus chloride and versus depth for each type of

concrete. There are also some authors which have made use of the ER technique by applying a thin film on the concrete surface: Park et al. [21] developed a thin-film screen printed Ag paste and iron powder sensor. The task of their work was to monitor chloride penetration in concrete mortars at different depths. This was possible because the thin sensor film reacted to chloride ions in cement mortars at different salinity levels, in a similar manner to a steel reinforcement. They measured the change in electrical resistance of the sensor as it corroded with salinity penetration from the mortar surface over time. However, this method doesn't give an estimation of chloride content, but only on its penetration in the mortar.

A summary of the advantages and disadvantages of the ER technique for chloride content and penetration measurement is found in Table 6.4.

Advantages	Disadvantages
<ul style="list-style-type: none"> <li>• Good sensitivity to chloride ions</li> <li>• Can be used to determine chloride diffusion coefficients and chloride penetration in concrete</li> </ul>	<ul style="list-style-type: none"> <li>• Very sensitive to moisture content</li> <li>• Measurements depend on the geometry and the reinforcing configuration (rebar presence and corners can modify the electrical field)</li> <li>• Not enough information about the durability of these devices in field</li> <li>• In most of the cases, directly embedded onto concrete</li> </ul>

Table 6.4 - Advantages and disadvantages of Electrical resistivity sensors, according to [2]

### 6.2.2. Development of a new geopolymer chloride sensor for nuclear stores

All the methods reviewed above show some advantages, such as the good chemical stability in aggressive environments for the ISE, the good sensitivity to the chloride presence for the ER and OFS, but also some disadvantages, such as issues related with the sensitivity to changes in the concrete structure environmental conditions (temperature, relative humidity, pH), interference due to electrical fields, additional costs for protective packaging for FOSs, and first of all the fact that the sensors most of the times need to be embedded directly onto concrete. The same thing applies to the existing works on the use of the Electrochemical Impedance Spectroscopy (EIS) technique for the chloride diffusion

coefficient estimation in both mortars samples in laboratory [29, 30] and concrete structures [38, 39], where electrodes are directly applied onto concrete.

All these methods present a certain level of invasiveness for concrete, since they are directly embedded or parts of them are directly applied (i.e. by means of drilling holes) to concrete. This makes these methods more suitable for new build structures, and not suitable for retrofitting within nuclear stores. This section introduces the development of a new geopolymer chloride sensor, which is based on EIS measurements, is able to measure chloride content in concrete and is non-invasive for concrete and thus more suitable to be applied in nuclear stores than the other reviewed existing techniques.

As already mentioned in detail in chapter 2, there is a growing demand for easy to apply, affordable, multifunctional, non-destructive technologies to monitor chloride content in concrete structures, especially in a safety-critical context, such as nuclear store buildings. Nuclear store buildings, such as the SPRS detailed described in section 2.3.4, are existing structures, intended to last for 100 years, placed in coastal locations and made of reinforced concrete. Embedding electrodes directly onto those structures is not recommended as it would undermine function and structural integrity. The ideal sensing system to be applied to concrete surfaces of such structures (i.e. nuclear store's concrete surfaces of ducts and air corridors) would be a non-invasive system, where the electrodes could be applied to another highly conductive medium. The technology proposed in this work of thesis, and already introduced in chapter 5 for moisture sensing, belongs to this category.

The future aim of this work is to develop a distributed system of geopolymer skin sensors based on EIS measurements and applied onto concrete surfaces for moisture and chloride content monitoring. The electrodes of such a system will be applied to the geopolymer layer, and no drilling will be required. At the same time, the geopolymer coating will act also as a protection and a repair for the concrete itself.

In comparison with the existing reviewed methods, the sensor proposed in this PhD project is affordable, sensitive to both chloride and moisture, applicable to any surface and shape, non-invasive, and it combines a monitoring and maintenance technology. The advantages of this technology for the application in nuclear stores, compared with the existing reviewed chloride sensing technologies, are summarised in detail in the following Table 6.5.

<b>Geopolymer chloride sensor</b>	<b>Other chloride sensing technologies</b>
<ul style="list-style-type: none"> <li>• Not invasive</li> <li>• Cheap: the cost per patch could be less than £10 (geopolymer material costs are almost negligible)</li> <li>• Minimal manufacturing and deployment steps (no thermal curing, no fly ash grinding, no additives)</li> <li>• The possibility to make different sizes of patches and samples: can be applied to structures of any shape and size</li> <li>• Sensor patch also acts as a maintenance technology</li> <li>• Could offer convenient distributed sensing with the use of tomography over a patch</li> </ul>	<ul style="list-style-type: none"> <li>• Invasive installation during retrofit, or requires new build</li> <li>• Tend to be more expensive</li> <li>• More complicated manufacture and deployment</li> <li>• Limitation given by the use of standardised shape and size of elements (such as the reference electrode for ISE, the embedded FBG for FOSs, the drilled holes for electrodes in concrete for ER)</li> <li>• Measurement technologies only</li> <li>• Typically only offer point, or quasi-distributed sensing</li> </ul>

Table 6.5 – Advantages of the geopolymer chloride sensor compared with the existing chloride sensing methods

For all the sensors, also for the system presented in this work, the sensitivity to changes of environmental conditions, such as temperature and moisture, can lead to unpredictable measurement shifts in most cases. For this reason, the response of the system has been calibrated also for water content and temperature, so external thermometers and moisture sensors will allow to correct changes due to moisture and temperature fluctuations.

This chapter provides a preliminary study on geopolymer chloride sensing capability by using the same rectangular geopolymer sensor prototype used for moisture sensing in chapter 5, and shown in Figure 6.2.

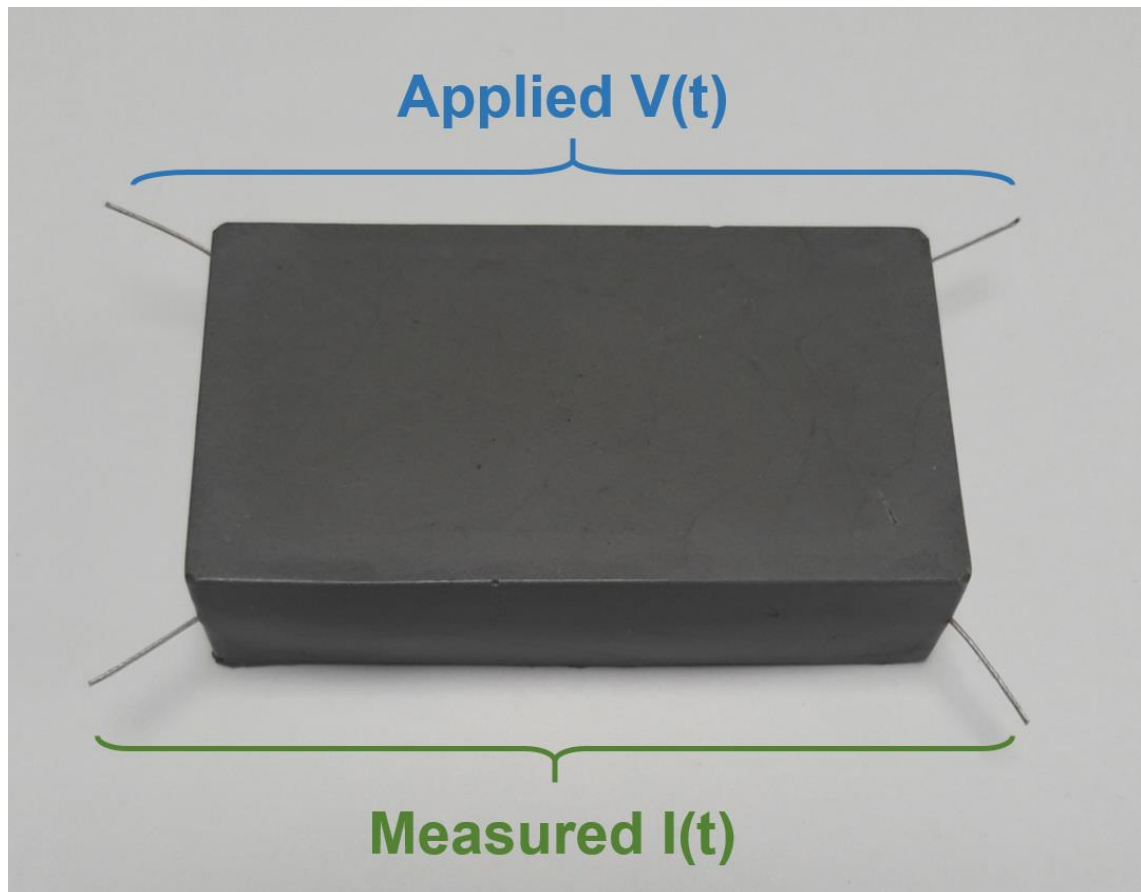


Figure 6.2 – Photograph of geopolymer rectangular sensor prototype cell used for chloride and moisture calibration, showing electrodes used for sensor interrogation in a Van Der Pauw configuration.

An Electrical Impedance Spectroscopy (EIS) interrogation system applies an ac voltage  $V(t)$  through two electrodes, and measures an ac current  $I(t)$  through the other two electrodes, as shown in Figure 6.2.

This sensor prototype can be easily deployed nearby concrete structures and constitute an alternative to the skin sensor solution. In this work it has been used for calibration and characterization.

The theory behind the sensing principle of the system characterised in this chapter is outlined in the following section.

### 6.2.3. Theory: geopolymer chloride sensor

As already outlined in chapter 5, both geopolymer and concrete pore solutions are comprised of ionic electrolytes in which electrical conduction is due to the migration of ions and cations under an electrical potential gradient.

In the geopolymers discussed in this thesis, the major ionic species in the pore solution, and main carriers of ionic current, are sodium ions ( $Na^+$ ). The hypothesis for using the geopolymer as a sodium chloride sensor is thus: when geopolymer samples are soaked in sodium chloride (NaCl) solutions, the number of  $Cl^-$  and  $Na^+$  inside the pore solution will increase. More ions will result in more ionic conductivity, particularly when ion mobility is high at high moisture contents.

However, at very high concentrations, the mobility of each ion is adversely affected by the Coulomb interaction between the ion and the surrounding ions. In a state of infinite dilution (when ionic concentration equal to zero with the exception of a single ion), the motion of the lone ion is limited only by its interactions with the surrounding solvent molecules, since there are no other ions within a finite distance. At higher concentrations, the ionic interactions result in a molecular mean field acting on each ion, and this may play a limitation effect on ionic motion [40, 41]. Less mobility could result in less conductivity gain. A more detailed discussion of the ion mobility in electrolytes is behind the scope of this work of thesis, and can be found in [40].

### 6.2.3.1. Sensing principle

This work constitutes the first time demonstration of a geopolymer-based chloride sensor. For this reason, the theory behind this sensor comes from a combination of: (i) previous works on Electrical Resistivity measurements on concrete; (ii) analogy of electrical properties of geopolymers with those of concrete (as already done in section 5.3.3); and (iii) the experimental evidence in this work.

The moisture and temperature dependence of geopolymer impedance has already been described in detail in section 5.3.3. Previous works on electrical resistivity measurements of concrete have demonstrated an exponential dependence of resistivity on chloride content [20]. The experimental results of this investigation, outlined in section 6.4, show that also for geopolymers the impedance dependence on chloride content is exponential. It can be described by the following equation:

$$\frac{Z_{mod}}{Z_{mod,0}} = b_1 * e^{-b_2 \cdot c} + b_3 \quad \text{Eq. 6.4}$$

where  $Z_{mod}$  is the modulus of the impedance at different NaCl concentrations,  $Z_{mod,0}$  is the modulus of the geopolymer sample before the soaking into the NaCl solution,  $c$  is the concentration of NaCl inside the pore solution of the geopolymer sample, and  $b_{1,\dots,N}$  are constants. Note that equation 6.4 is normalised ( $\frac{Z_{mod}}{Z_{mod,0}}$ ) to eliminate the dependence on the geometry and the specific geopolymer sample.

Assuming the contributions to the impedance from each term in equation 6.4 are independent allows the equation to be re-expressed as:

$$\ln\left(\frac{Z_{mod}}{Z_{mod,0}}\right) = E_1 * c + E_2 \quad \text{Eq. 6.5}$$

where  $E_1$  and  $E_2$  are constants.

Also in this case, the water dependence of impedance is described by the following equation:

$$\frac{Z_{mod}}{Z_{mod,0}} = a_5 * e^{\frac{a_6}{W}} \quad \text{Eq. 6.6}$$

where  $a_5$  and  $a_6$  are constants,  $W$  is the water content percentage and  $Z_{mod,0}$  is the modulus of the geopolymer sample before the soaking into the NaCl solution, as before.

Also this equation can be re-expressed as:

$$\ln\left(\frac{Z_{mod}}{Z_{mod,0}}\right) = \frac{D_6}{W} + D_7 \quad \text{Eq. 6.7}$$

where  $D_6$  and  $D_7$  are constants.

By combining equations 6.5 and 6.7, the following characterization equation for the geopolymer sensor is obtained:

$$\ln\left(\frac{Z_{mod}}{Z_{mod,0}}\right) = H_1 + H_2 * c + \frac{H_3}{W} + \frac{H_4}{W} * c \quad \text{Eq. 6.8}$$

where  $H_{1,\dots,N}$  are constants. Also equation 6.8, as equation 5.15, includes an additional cross-dependence term between moisture and NaCl concentration,  $\frac{H_4}{W} * c$ , although as seen in the results, there seems to be little cross-dependence between Cl and Moisture.

Equation 6.8 doesn't fully capture the non-linear behaviour due to the saturation of sensor response at high concentration contents, and for this reason a better description of this behaviour is given by the following equation:

$$\ln\left(\frac{Z_{mod}}{Z_{mod,0}}\right) = H_1 + H_2 * c + \frac{H_3}{W} + H_4 * c^2 \quad \text{Eq. 6.9}$$

where  $H_{1,...,N}$  are constants. In this equation, the relatively weak cross dependence term of equation 6.8 is replaced by the term ' $H_4 * c^2$ '. The experiments were run at a constant temperature, so a T term is not required in the equation.

These equations have been used in the results section for the moisture and chloride characterization of the sensor prototype. Next section describes the materials used and the methodology of the moisture and chloride sensor characterisation experiment.

### 6.3. Materials and methods

This section presents a detailed description of the materials and methods used for the manufacture, set-up, preliminary characterisation and testing of the newly developed low calcium fly ash geopolymer chloride sensor prototype.

#### 6.3.1. Sensor fabrication

The sensor prototype developed and tested in this work is the geopolymer cell already described in chapter 5, and shown in Figure 6.2. The description of the prototype has already been described in section 5.4.1, and it is here recalled: the prototype is a geopolymer rectangular sample (dimensions 55mm × 30mm × 15mm), with 4 -wire braided stainless steel wire electrodes penetrating 2mm into the corners, in a Van Der Pauw configuration.

The geopolymer binder, as for the case of the experiment described in chapter 4 and for the case of the moisture and temperature sensing characterisation outlined in chapter 5, was synthesized from low calcium fly ash and an alkaline solution made of sodium Hydroxide (SH) and sodium silicate (SS), with a liquid (L) to solid (S) ratio,  $L/S = 0.5$ , and the ratio between sodium hydroxide and sodium silicate,  $SH/SS = 0.4$ . Also in this case, the

geopolymer cells were cured for 30 days at 20°C and 95% relative humidity in an environmental chamber prior to testing.

### 6.3.2. Interrogation system

As for the case of moisture and temperature sensing calibration, Electrochemical Impedance Spectroscopy (EIS) was applied to the geopolymer cells in a potentiostatic mode: a 10mV voltage was applied to geopolymer cells, and the resulting pseudo-linear current response was measured, thus obtaining the impedance of the system. The frequency of the applied voltage was swept over the range 10Hz – 100kHz during impedance characterization.

### 6.3.3. Sodium Chloride solutions

In order to calibrate the sensor prototype for chloride sensing, NaCl solutions with nine different concentrations were used, plus nanopure water for the case of 0% NaCl concentration. The solutions were made by adding a certain amount of NaCl salt into nanopure water by using a volumetric flask of 1 liter. The concentrations of these solutions are called ‘applied concentrations’, since the geopolymer cells were soaked in them for 24 hours. After the oven drying of the geopolymer samples, which is the last step of the calibration procedure outlined in section 6.3.4, the amount of salt in each sample was measured by the Ion Chromatography analysis (IC): each cell was crushed in powder, and leached in nanopure water that was then analysed by means of the IC device to find the quantity of  $Cl^-$  ions leached. This provides a measurement of the actual chloride concentration within the sample. This differs from the applied concentration because the geopolymer sample itself contains water prior to soaking, and the leaching of chloride into the sample is a time-dependent process.

The measured mass of salt from the leaching IC analysis,  $m_{salt}$ , the mass measurements of the geopolymer cells after soaking,  $m_{saturation}$ , and the geopolymer cell mass after oven drying,  $m_{dry}$ , were used to calculate the actual internal NaCl concentration,  $c$ , in the pore solution of each cell, as:

$$c = \frac{m_{salt}}{m_w} \quad \text{Eq. 6.10}$$

where  $m_w$  is the mass of water inside the geopolymer cell after soaking in the solution. This mass is given by:

$$m_w = m_{saturation} - m_{dry} \quad \text{Eq. 6.11}$$

The error associated with each actual concentration value,  $c$ , is given by the propagation of errors formula:

$$Error_c = c \cdot \sqrt{\left(\frac{Error(m_{salt})}{m_{salt}}\right)^2 + \left(\frac{Error(m_{saturation})}{m_{saturation}}\right)^2 + \left(\frac{Error(m_{dry})}{m_{dry}}\right)^2} \quad \text{Eq. 6.12}$$

The applied NaCl concentration,  $c_a$ , and the corresponding actual internal NaCl concentration,  $c$ , just after soaking are listed in Table 6.6.

Applied NaCl concentration $c_a$ [wt%]	Actual internal NaCl concentration $c$ [wt%]	
	Value	Error
<b>0</b>	0.002	$0.002 \cdot 10^{-2}$
<b>0.520</b>	0.139	$0.809 \cdot 10^{-3}$
<b>1.202</b>	0.473	0.003
<b>2.169</b>	0.939	0.006
<b>3.412</b>	1.371	0.008
<b>5.293</b>	2.507	0.015
<b>8.041</b>	3.327	0.020
<b>12.002</b>	5.676	0.034
<b>16.175</b>	10.032	0.064
<b>28.568</b>	15.266	0.103

Table 6.6 – NaCl applied and actual internal concentrations

The actual internal NaCl concentrations for each drying point (calculated by equation 6.10, where  $m_w$  is the mass of the water inside the sample at each drying point) and the corresponding water content calculated by the gravimetric formula 6.13 are listed respectively in Table A 1 and in Table A 2 of Appendix 3.

#### 6.3.4. Calibration method

The procedure for the chloride and moisture calibration is summarized as a flowchart in Figure 6.3:

1. NaCl solutions of different concentrations (listed in the first column of Table 6.6 above) were made by dissolving solid NaCl into nanopure water. Each solution was

poured into sealed containers, each of them containing the volumes of solution listed in Table A 3 of Appendix 3;

2. The geopolymer cells were removed from the curing environmental chamber, and their initial mass,  $M_{i,0}$ , was measured;
3. Sample cells were placed into empty sealed boxes, placed inside a Faraday cage at 20°C and connected to the interrogation system (Figure 6.4), in order to measure the initial impedance value,  $Z_{mod,0}$ : the EIS cycle was run and the impedance spectra were measured five times over a 5 minute duration to allow an average to be taken;
4. Each geopolymer sample was then soaked in a different NaCl solution inside the sealed containers for 24 hours to reach a high solution content;
5. After soaking, the samples were taken out of the solution, wiped to remove excess solution from the surfaces, and their mass,  $M_{i,1}$ , was measured;
6. Then, the samples were sealed in empty boxes (as shown in Figure 5.7 of chapter 5) for 24 hours to allow the solution inside the pores to equilibrate and homogenise;
7. The sealed box containing the sample was placed inside a Faraday cage at 20°C and connected to the interrogation system (Figure 6.4), and the EIS cycle was run and the impedance spectra were measured five times over a 5 minute duration to allow an average to be taken;
8. After the EIS measurement, each geopolymer sensor was taken out of the sealed container and its wet mass,  $M_{i,2}$ , was weighed a second time. The wet mass  $M_i$  was then defined as the mean value of  $M_{i,1}$  and  $M_{i,2}$ , while the variation was used to establish an error in moisture content.
9. The sensor was placed in a desiccator with silica gel to drive water out of the sample through evaporation. The sensor was regularly weighed until a new target mass (target moisture level) was reached. This cycle was repeated for all target moisture contents.
10. Once the characterization was complete, each sample was completely dried in an oven at 105 °C for 24 hours and its dry mass  $M_d$  was measured.  $M_d$  is the mass of the solid geopolymer plus the mass of the NaCl salt inside the sample ( $M_d = M_{solid} +$

$M_{salt}$ ). This allowed the gravimetric water content  $W_i$  of the samples to be quantified by means of the equation:

$$W_i = \frac{M_i - M_d}{M_d} \times 100 \quad \text{Eq. 6.13}$$

A different geopolymer cell was used for each NaCl concentration value. In order to remove the dependence on the specific geopolymer cell, and to compare the measured values of impedance for different NaCl concentrations, the normalized values  $\frac{Z_{mod}}{Z_{mod,0}}$  were used: the value of impedance modulus  $Z_{mod}$  of each cell was divided by the initial value of impedance of the same cell before being soaked in the solution,  $Z_{mod,0}$  (impedance value of the sample just after curing, corresponding to a water content of  $\sim 77 \pm 1\%$  and  $20 \pm 1^\circ\text{C}$ , without any NaCl content).

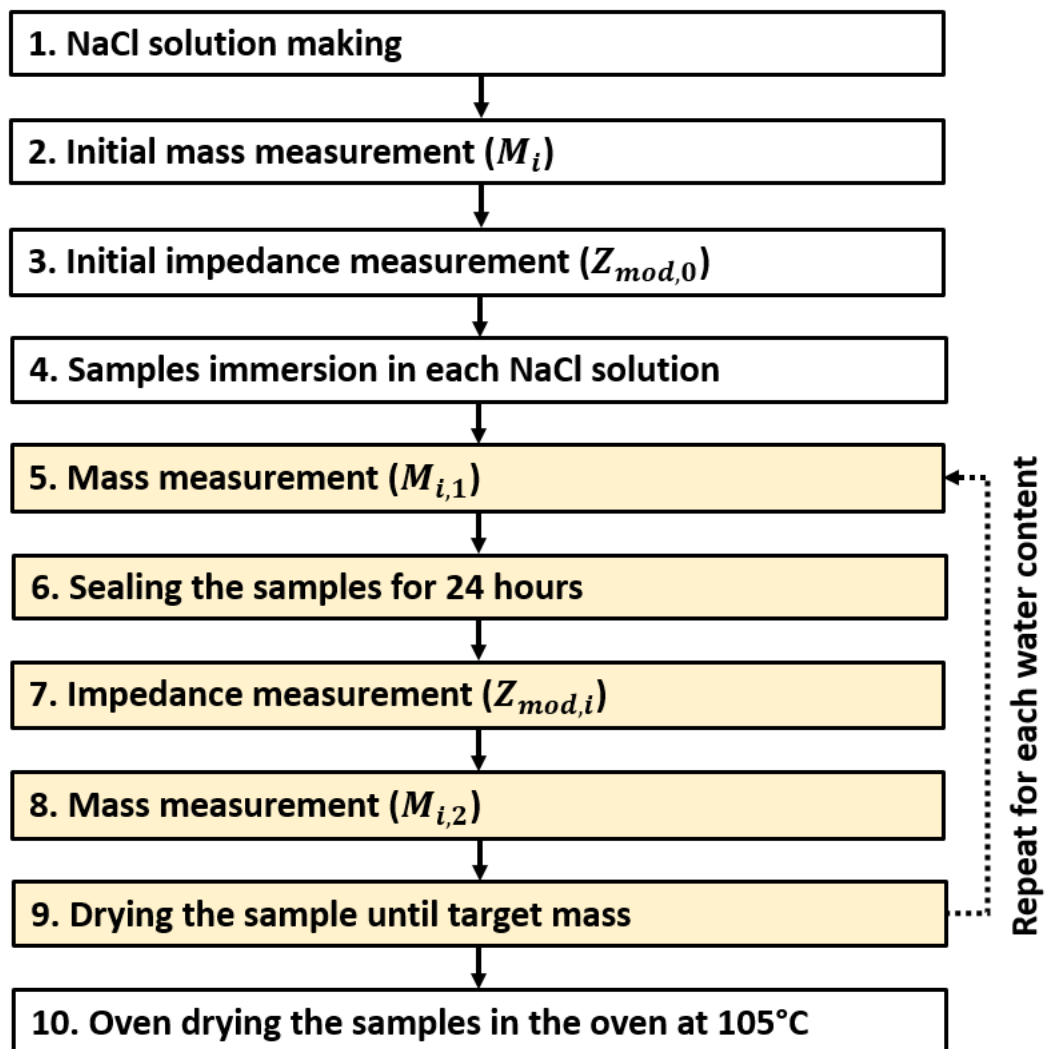


Figure 6.3 - Flowchart showing the steps in the chloride and moisture characterization experiment.

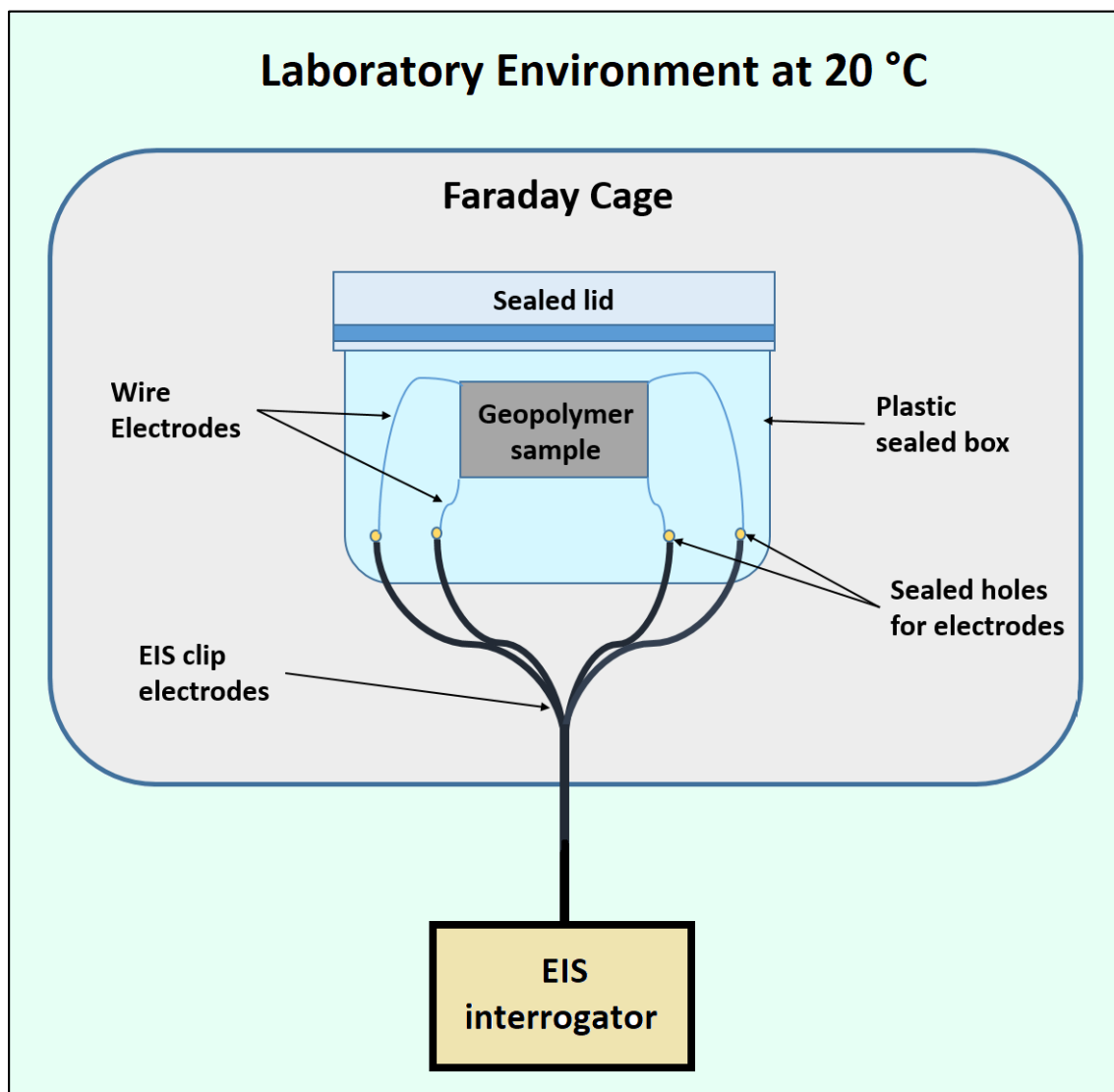


Figure 6.4 - Scheme of the experimental set-up for the EIS measurement of the geopolymer cell sample at each water content and NaCl concentration.

## 6.4. Results and discussion

This section outlines the results of the chloride and moisture sensing calibration experiment of the geopolymer cell prototype in Figure 6.2. The results are preliminary because the main task of this work is to demonstrate the feasibility of a geopolymer-based chloride sensor at 20°C, while a more complete calibration would take into consideration also a chloride and temperature calibration for each moisture level, and a repeatability evaluation. The EIS measurements were also taken over 5 minutes time (5 measurements), while a more

complete evaluation of the stability and drift of the sensor system would need an average over a longer time.

The remainder of this section starts with subsection 6.4.1, which describes the impedance response of the sensor cell when it contains NaCl solutions at different concentrations for the investigated frequency range. Subsection 6.4.2 outlines the chloride and frequency dependence of impedance, and the sensor response and sensor precision are described in subsections 6.4.3 and 6.4.4 respectively.

### 6.4.1. Impedance response of the sensor cell plus NaCl solution

Figure 6.5 and Figure 6.6 show the typical Bode plots of phase  $\varphi$  and  $Z_{mod}$  for a geopolymer sensor cell with 2.5wt% and 15.3wt% actual internal NaCl concentration respectively. The EIS measurements were taken at a water content  $W \sim 86 \pm 1 \text{ wt}\%$  and temperature  $T = 20 \pm 1 \text{ }^\circ\text{C}$ . The fits made use of the equivalent circuit model given in Figure 5.4 b) and the values for each component of the circuit are given in Table A 4 of Appendix 4. For all the other concentrations in Table 6.6, the Bode plots, their fits with the equivalent circuit model given in Figure 5.4 b), and the values for each component of the circuit can be found in Appendix 4.

The results show that the geopolymer sample cells containing NaCl solution can be well-modelled by the same circuit model given in Figure 5.4 b) of chapter 5. This perhaps should be expected because the physical geopolymer matrix itself is not changing: all that is changing is the electrolyte concentration, i.e. the number of  $Na^+$  ions and the presence of  $Cl^-$  ions inside the geopolymer pore solution, so there is no reason why the electrochemical description of the system should not remain valid.

By comparing the  $Z_{mod}$  values for a geopolymer sample with no NaCl in Figure 5.9, with the  $Z_{mod}$  values in Figure 6.5, for a geopolymer cell with an actual internal concentration of 2.7 wt%, it is possible to see lower values in case of NaCl presence inside the pore solution of the samples (i.e. at a frequency of 1 kHz,  $Z_{mod}(no \ NaCl) \sim 900 \text{ Ohms}$  and  $Z_{mod}(2.7\% \ NaCl) \sim 120 \text{ Ohms}$ ). Besides,  $Z_{mod}$  values decrease at the increasing of NaCl concentration, as is expected from the presence of more charge carriers. This is shown in the following section 6.4.2, where the results of the dependence of impedance on NaCl concentration are presented.

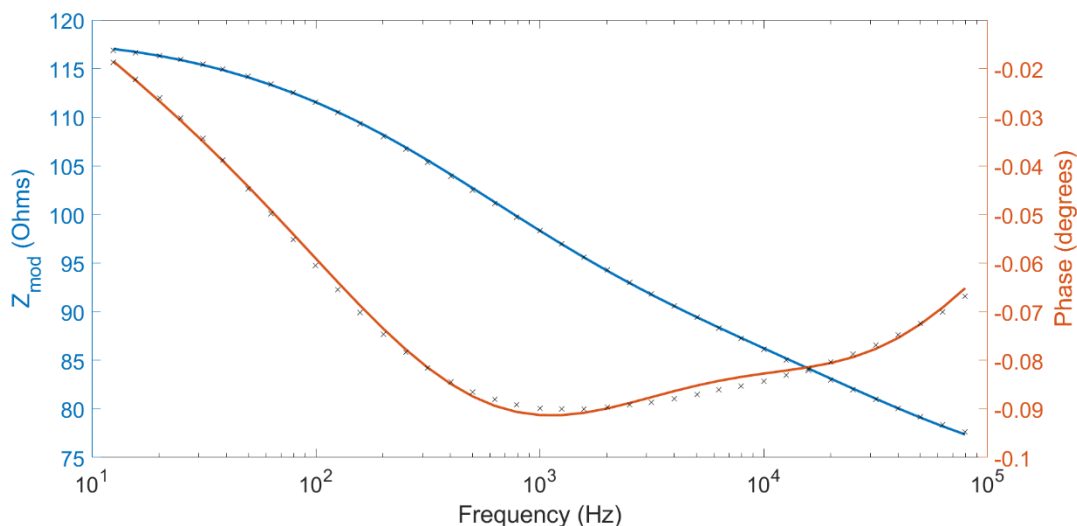


Figure 6.5 – Bode plots for  $Z_{mod}$  and phase  $\varphi$  obtained for a geopolymer sensor cell with 2.5 wt% actual internal NaCl concentration (applied NaCl concentration = 5.3 wt%), at water content  $W \sim 86 \pm 1 \text{ wt}\%$  and temperature  $T = 20 \pm 1 \text{ }^\circ\text{C}$ . The fits use the equivalent circuit model given in Figure 5.4 b).

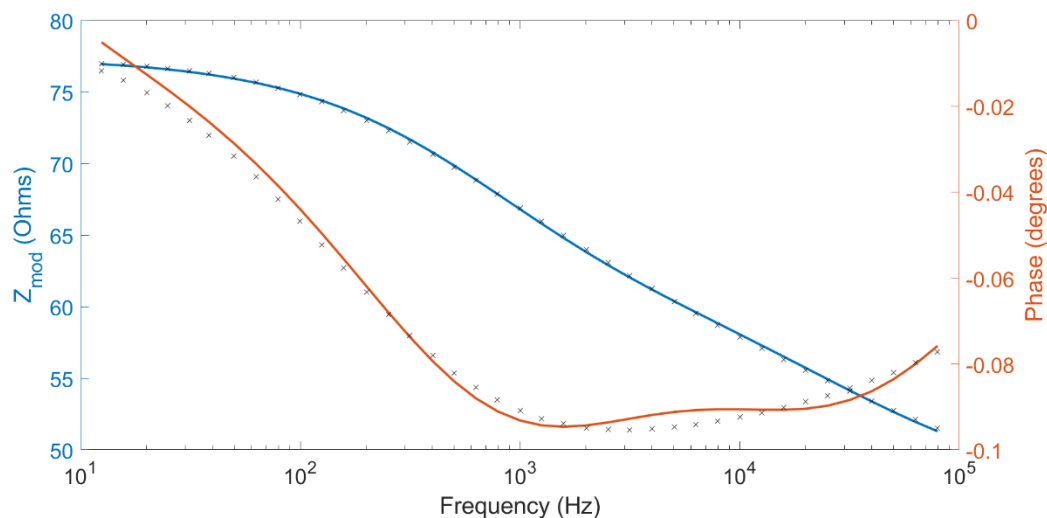


Figure 6.6 - Bode plots for  $Z_{mod}$  and phase  $\varphi$  obtained for a geopolymer sensor cell with 15.3 wt% actual internal NaCl concentration (applied NaCl concentration = 28.6 wt%), at water content  $W \sim 86 \pm 1 \text{ wt}\%$  and temperature  $T = 20 \pm 1 \text{ }^\circ\text{C}$ . The fits use the equivalent circuit model given in Figure 5.4 b).

### 6.4.2. Chloride and frequency dependence of impedance

Figure 6.7 shows Nyquist plots for the geopolymer cells at water content  $W \sim 86 \pm 1 \text{ wt}\%$  and temperature  $T = 20 \pm 1 \text{ }^\circ\text{C}$ , for the actual internal NaCl concentrations  $c$  listed in

Table 6.6. The data in Figure 6.7 are the same of section 6.4.1: the circuit model for the fitting Nyquist curves is the circuit model in Figure 5.4 b), as per Figure 6.5 and Figure 6.6, and the values of the circuit parameters are given in Table A 4 of Appendix 4. Figure 6.7 shows that impedance increases as NaCl concentration  $c$  decreases, as expected. The overlap of some lines in Figure 6.7 can be eliminated once the correction for the initial impedance of each sample,  $Z_{mod,0}$ , is applied, as it is shown in Figure 6.12, where  $\frac{Z_{mod}}{Z_{mod,0}}$  is plotted against NaCl concentrations  $c$ .

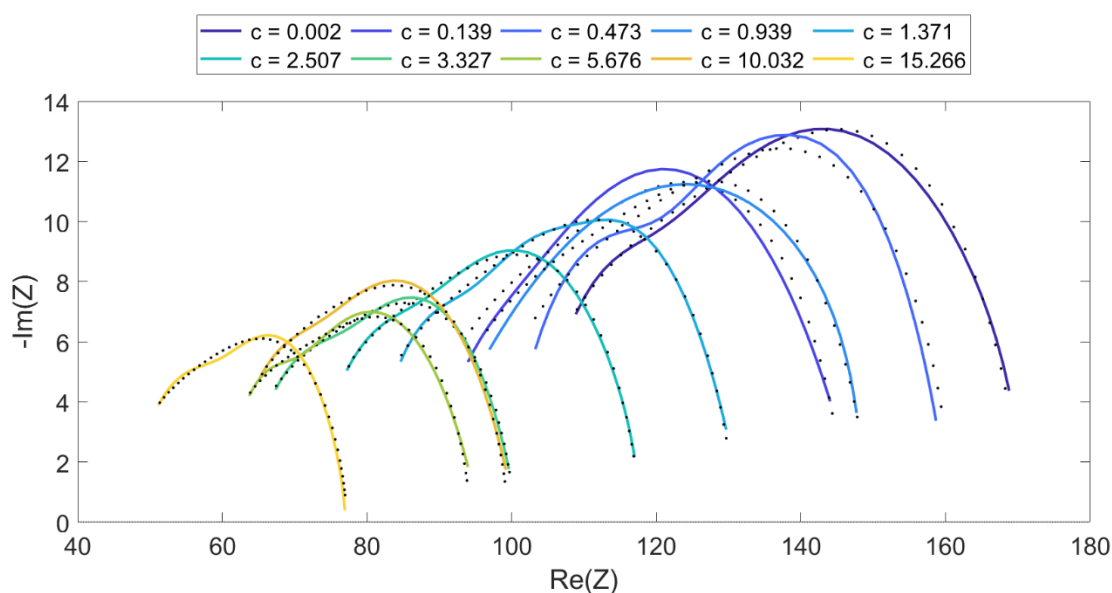


Figure 6.7 - Nyquist plots from 10 Hz to 100 kHz, for geopolymer sample cells at a temperature of  $20 \pm 1^\circ\text{C}$ , a water content of  $86 \pm 1\%$  and for the different NaCl actual internal concentrations listed in Table 6.6. Fits are obtained using the equivalent circuit model shown in Figure 5.4 b).

Figure 6.8 shows Bode plots for sensors soaked in the NaCl solutions of Table 6.6, where in the y-axis there is  $A_{mod} \cdot c$ , which is the product of the modulus of admittance,  $A_{mod}$ , and the NaCl actual internal concentrations after saturation,  $c$ . Water contents for each sample are  $\sim 86 \pm 1 \text{ wt}\%$ , and all measurements were conducted at a constant temperature of  $20 \pm 1^\circ\text{C}$ .

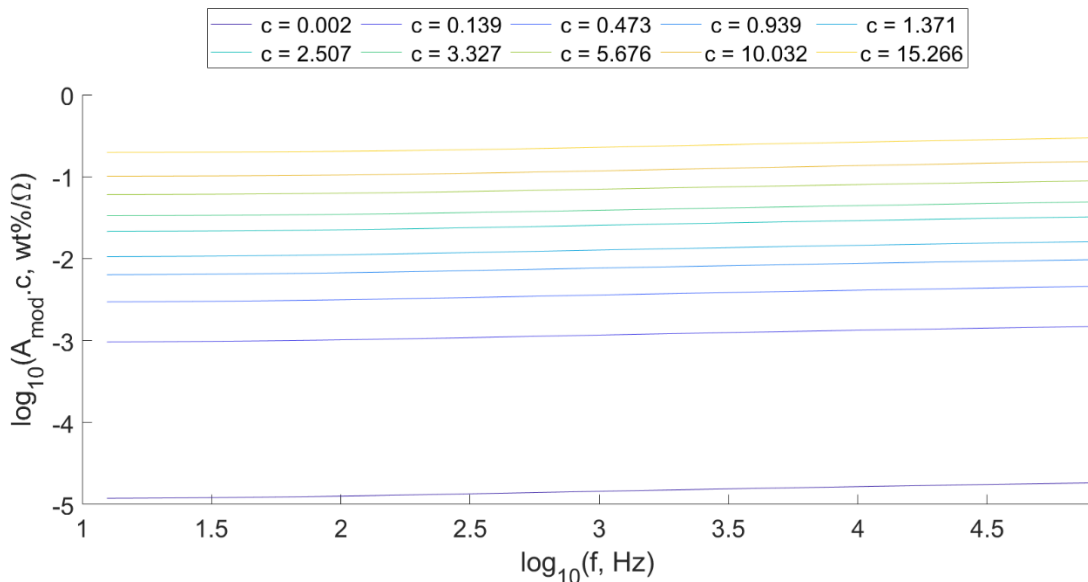


Figure 6.8 - Bode plots of isotherms of  $A_{mod} \cdot c$ . Data shown is for samples at a water content of  $\sim 86 \pm 1\%$ , and temperature  $T = 20 \pm 1^\circ\text{C}$ .

From the observation of Figure 6.8, it is possible to hypothesise that also in this case, as for moisture and temperature, the sensors can follow the Summerfield scaling [42]: the shape of each Bode plot in Figure 6.8 seems to be not too dependent on chloride concentration (e.g. the  $c = 2.7 \text{ wt}\%$  line can be shifted up or down to superimpose onto any other  $c$  line). Also in this case, the data shown in Figure 6.8 can be plotted onto a scaled coloured Summerfield plot, shown in Figure 6.9, by arbitrarily defining a baseline frequency of  $f_0 = 100 \text{ Hz}$ , and a baseline admittance at  $100 \text{ Hz}$  of  $A_{0,mod} = A_{mod}(100\text{Hz})$  for each line.

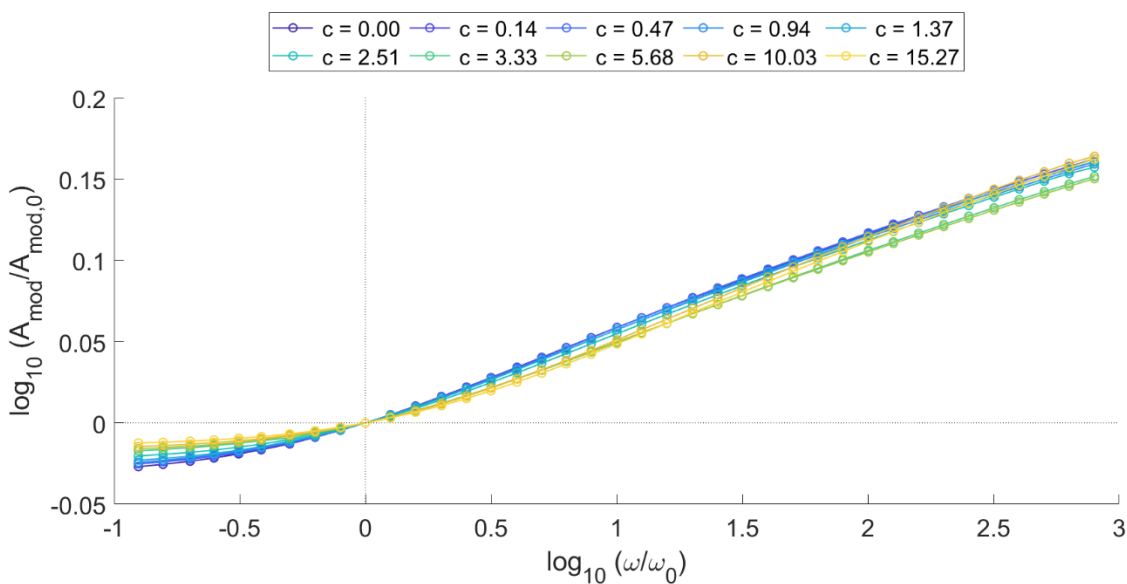


Figure 6.9 - Scaled Summerfield bode plots for NaCl concentrations as a colored set of series for each NaCl concentration value  $c$ .

The colorization of the data points for each NaCl concentration  $c$  in Figure 6.9 shows that for high frequencies  $>1$  kHz, the curves corresponding to the highest concentrations ( $c > 9$  wt%), tend to follow the lower concentration curves. This effect is more visible in Figure 6.10, where the curves of Figure 6.9 are limited to the range of frequencies between 100 Hz and 10 kHz. No overlap is found for frequencies up to 1 kHz. Therefore, this could be a more sensitive region for sensing NaCl concentrations and distinguishing them from moisture shifts. It has therefore been selected a single frequency of 1 kHz for the remainder of the sensor characterization described in this chapter.

As shown by Figure 6.5 and in Figure 6.6, a 1 kHz frequency also corresponds to the region where phase angles tend to be at their minimum values, so in this region the capacitive effects, due to the electrodes and the unconnected pores of the pore solution, are less important, and the frequencies are not so high to see the influence of inductive effects.

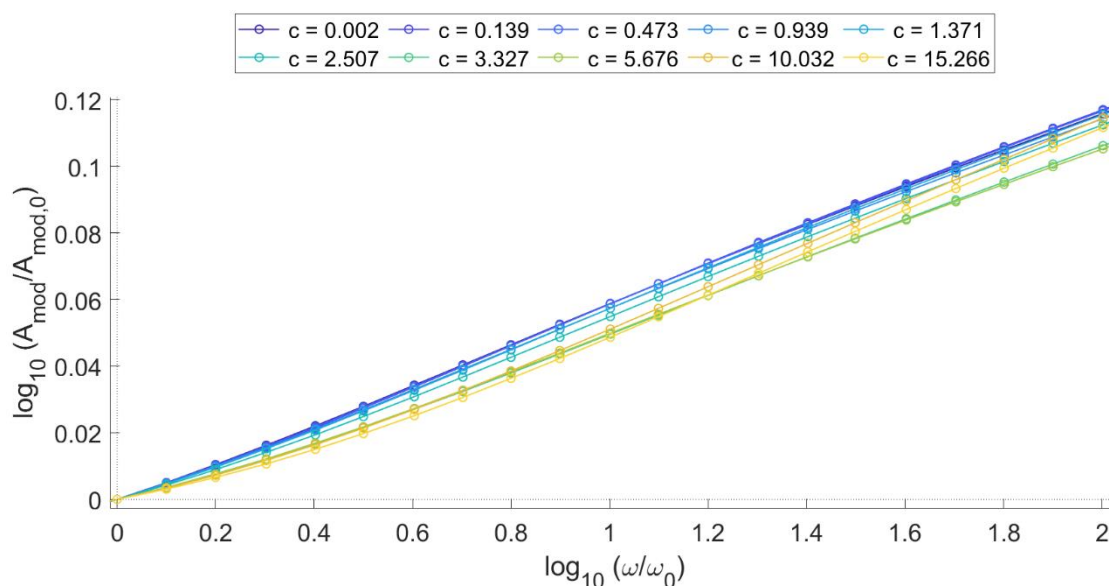


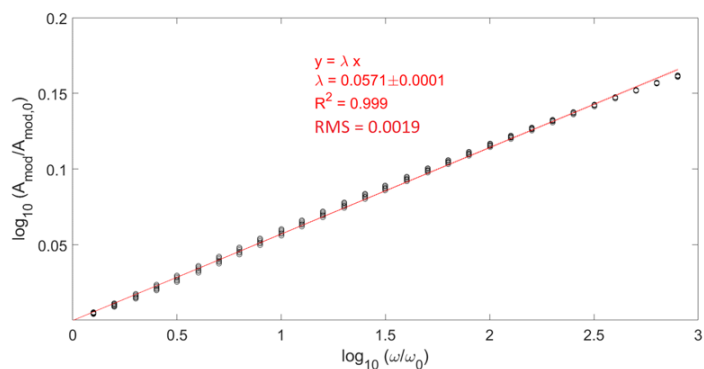
Figure 6.10 - Scaled Summerfield plots for NaCl as a colorized set of series for each NaCl concentration value, in the range of frequencies from 100 Hz to 10 kHz.

An interesting exercise, at this point, is to compare the scatter in the Summerfield scaled plots for NaCl concentration (data in Figure 6.9), with those for temperature (data in Figure 5.10) and moisture (data in Figure 5.13) found in chapter 5. To do this, for each case, all the points are considered as a unique single series, and a linear fit through these points is performed. The linearity of the scatter of the points is quantified by means of the Root Mean Square (RMS) parameter of the fit. The three graphs obtained are shown in Figure 6.11,

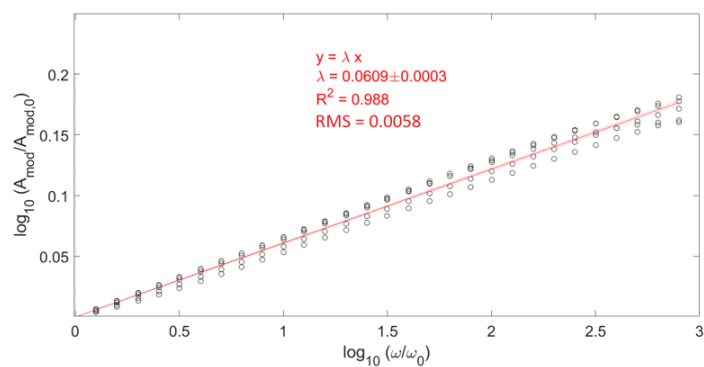
along with the RMS parameter value for each of them: (a) temperature series (from data of Figure 5.10 of chapter 5); (b) moisture series (from data of Figure 5.13 of chapter 5); (c) NaCl concentration series (data in Figure 6.9). The RMS values for each series are listed in Table 6.7.

	Temperature	Water content	NaCl concentration
RMS	0.0019	0.0058	0.0041

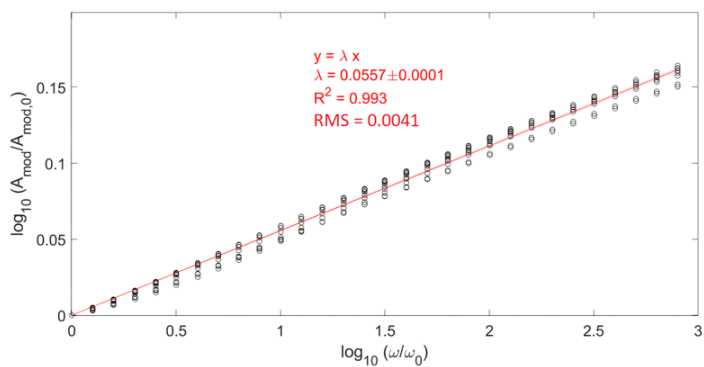
Table 6.7 – RMS values for the linear fit goodness evaluation of the series in Figure 6.11 (a), (b) and (c).



(a)



(b)



(c)

Figure 6.11 - Scaled Summerfield plots as a single data series for: (a) temperature (data in Figure 5.10); (b) moisture (data in Figure 5.13); and (c) NaCl concentration (data in Figure 6.9),

From the observation of Figure 6.11 and Table 6.7, it is evident that the temperature series shows the lowest scattering, the moisture series shows the highest scattering, while the NaCl concentration series shows an intermediate scattering between the other two series. According to [43], for the Summerfield Scaling Theory, the scaled Summerfield plot  $\sigma_0 T$  versus frequency is linear if:

$$N_0 p q^2 \xi^2 = \text{const} \quad \text{Eq. 6.14}$$

where  $N_0$  is the total ion concentration,  $p$  is the fraction of the ions which are mobile,  $q$  is the charge of the ions, and  $\xi$  is the diffusion length scale of the ions.

Although the Summerfield Scaling is defined for temperature [42-44], the use of this tool here also for moisture and NaCl concentration allows to further distinguish the response of the sensor to these three parameters (temperature, moisture and NaCl concentration).

In the case of the temperature series (Figure 6.11 (a)), the ion hopping process is sped up with temperature, and the linearity is guaranteed by time-temperature superposition, as already seen in section 5.5.2. Moreover, equation 6.14 is valid, since the concentration of the ions, their diffusion length scale and the number of mobile ions should not change in the range of temperatures investigated in chapter 5 (from 5 to 30 °C). This further explains the linearity of the plot and the RMS low value.

In the case of the moisture series (Figure 6.11 (b)), where from one curve to the other the number of  $Na^+$  ions is the same, the concentration of ions in the pore solution,  $N_0$ , and their diffusion length scale,  $\xi$ , change with the decreasing of the water content, since the ion atmosphere surrounding each ion becomes more dense, thus introducing a non-linearity in the plot.

Finally in the case of the NaCl concentration series (Figure 6.11 (c)), where from one curve to the other the concentration of the  $Na^+$  and  $Cl^-$  ions in the pore solution changes,  $N_0$  and the ions diffusion length scale  $\xi$  change. The density of the ions in the pore solution increases, thus increasing the number of the charge carriers, but limiting their mobility path, for the influence of the surrounding ions (as seen in section 6.2.3).

The higher scattering in the case of moisture variation may be interpreted as a slightly better sensitivity of the sensing system to moisture. This can be explained perhaps with equation 5.9, that can be recalled here:

$$\sigma = \sigma_0 \varphi_{con} \beta \quad \text{Eq. 6.15}$$

where  $\sigma$  is the bulk electrical conductivity,  $\sigma_0$  is the conductivity of the pore solution,  $\varphi_{con}$  is the volume of the pore network filled with pore solution, and  $\beta$  is the connectivity factor of the pore network [45]. The water content plays a critical role in all the three factors of the right hand side of equation 6.15: the connectivity factor of the pore network, the volume of the pore network filled with pore solution, and the conductivity of the pore solution, since it depends on the concentration and mobility of the ions in the pore solution. On the other hand instead, NaCl concentration plays a critical role only on  $\sigma_0$ . These results may warrant further investigation in future work.

### 6.4.3. Sensor response

Figure 6.12 shows the plot of the sensor response at 1 kHz to the actual internal chloride concentrations  $c$  listed in Table 6.6, for saturation water content only ( $\sim 86 \pm 1$  wt%), and at a constant temperature of  $20 \pm 1$  °C. Here the sensor response has been defined as  $\frac{Z_{mod}}{Z_{mod,0}}$ , where  $Z_{mod,0}$  is the modulus of impedance of the sensor before soaking in NaCl solution, at a water content of  $77 \pm 1$  wt% and a temperature of  $20 \pm 1$  °C. As shown, equation 6.4 provides a good fit to the data. The data points further from the curve can be attributed to experimental noise in temperature, water content values or chloride concentrations.

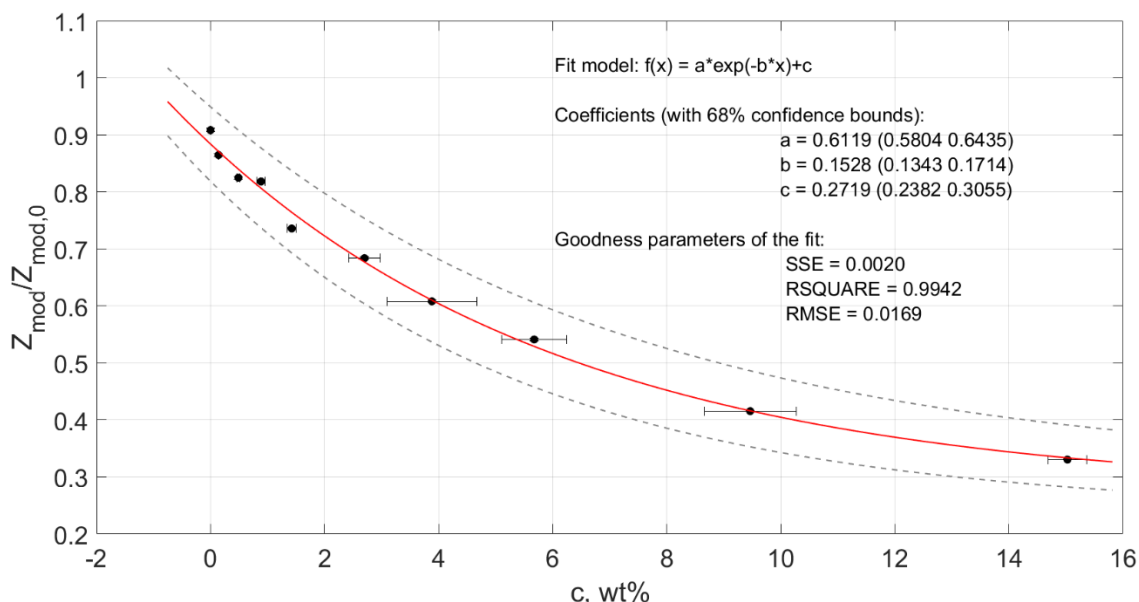


Figure 6.12 – Plot of  $\frac{Z_{mod}}{Z_{mod,0}}$  versus actual internal NaCl concentrations  $c$  (Table 6.6). Non-linear fit uses equation 6.4.

Figure 6.13 shows the sensor response as a function of water content for each chloride concentration. As shown, the exponential fit (equation 6.6) used for moisture calibration is still valid for each sample (each starting actual internal NaCl concentration  $c$ ). The parameters of the fit in Figure 6.13 and their standard errors are given in Table A 7 of Appendix 5.

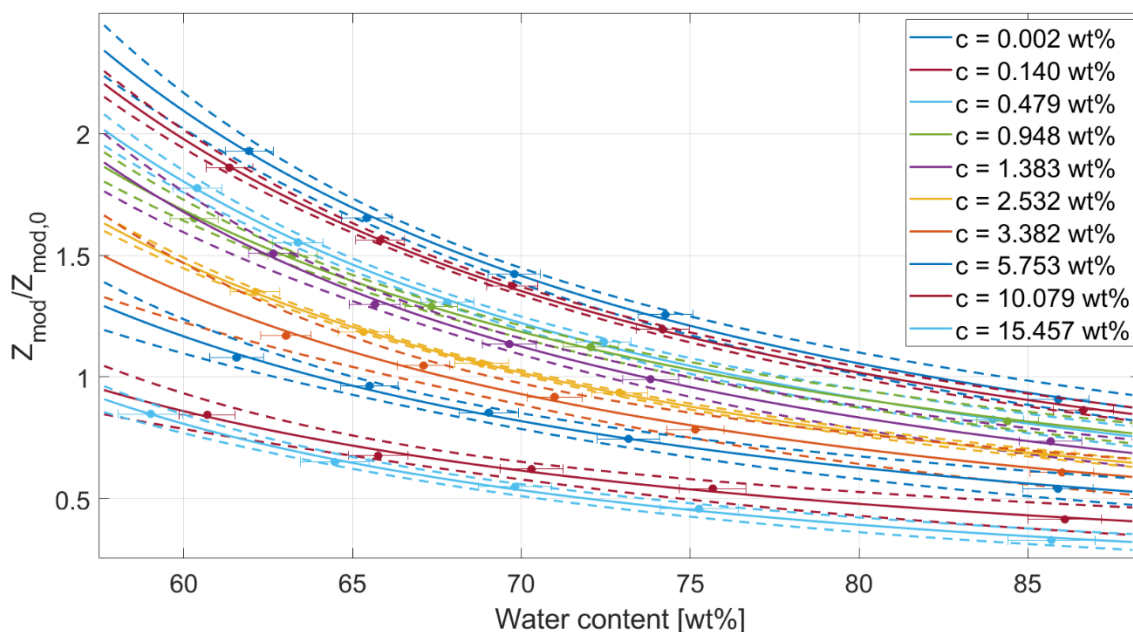


Figure 6.13 - Plots of  $\frac{Z_{mod}}{Z_{mod,0}}$  versus water content for each actual internal NaCl concentration  $c$ . Non-linear fits use equation 6.6.

The overall response of the sensor for any general water/NaCl concentration combination is better characterized by fitting moisture and NaCl simultaneously, as shown in Figure 6.14, where the “dryness” of the sample has been defined as the inverse of its moisture content, or  $1/W$ . Here equation 6.9 is found to be matching with the experimental data trend in the range of water contents from  $\sim 86 \text{ wt}\%$  up to  $\sim 60 \text{ wt}\%$ , since it well-describes the saturation of the sensor up to high NaCl concentrations, shown in Figure 6.14. When water content decreases in the pore solution by evaporation, the NaCl concentration increases, while on the other hand the decreasing of water causes a decrease in the connectivity between the pores. Therefore, a saturation behaviour is seen. The parameters of the fit in Figure 6.14 and their standard errors are given in Table 6.8.

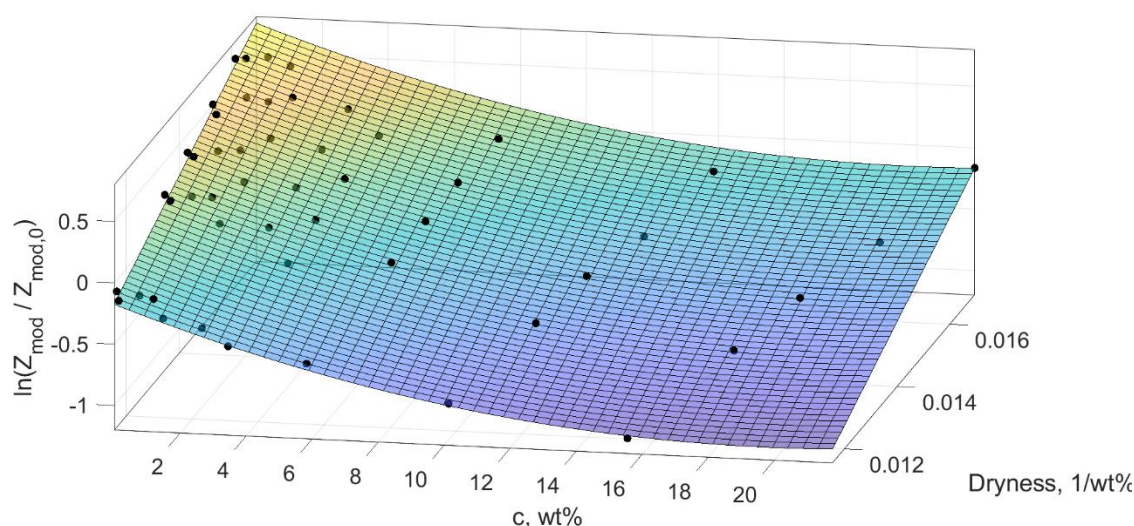


Figure 6.14 - 3D plot of calibration curve for sensor as a function of both NaCl concentration and moisture. The surface of best fit shown is described by equation 6.9.

Parameter	$H_1$	$H_2$	$H_3$	$H_4$
Value	-2.140	-0.09311	170.2	0.002359
<b>95% confidence bounds</b>				
Lower	-2.239	-0.09931	163.4	0.002028
Upper	-2.041	-0.08690	177.0	0.002689

Table 6.8 - Parameters and their 95% confidence bounds for the surface of best fit, equation 6.9, shown in Figure 6.14.

However, it is possible to completely remove the water content dependence from the data shown in Figure 6.14. This can be done because drying a sample which contains NaCl causes the NaCl concentration in the sample to increase: thus each stage of drying can be viewed as increasing the chloride concentration. This has been found to be valid in the range of water contents investigated in this chapter (90wt% - 60wt%). The steps in removing the water dependence are as follows:

- the water dependence fitting curve in Figure 6.13 for  $c = 0 \text{ wt\%}$  (0.002wt%) is used to find the interpolated impedance values  $\frac{Z_{mod}}{Z_{mod,0,c=0,interpol}}$  for each water content;
- Since the impedance values of the data points with  $c = 0 \text{ wt\%}$  are independent of NaCl, a further normalization is applied to each impedance value  $\frac{Z_{mod}}{Z_{mod,0}}$  of Figure 6.14 by dividing it for the  $\frac{Z_{mod}}{Z_{mod,0,c=0,interpol}}$  value of the corresponding water content;
- These operations result in the plot shown in Figure 6.15. The new normalised impedance values are defined as:

$$Z_{modNorm_w}(c) = \frac{\frac{Z_{mod}(W,c)}{Z_{mod,0}}}{\frac{Z_{mod}}{Z_{mod,0,c=0,interpol}}(W)} \quad \text{Eq. 6.16}$$

where  $Z_{modNorm_w}$  is dependent only on the actual internal concentration  $c$ .

The fit equation used for the fit in Figure 6.15 is still the exponential equation 6.4, which can be re-written as:

$$Z_{modNorm_w} = b_1 * e^{-b_2 \cdot c} + b_3 \quad \text{Eq. 6.17}$$

The parameters of the fit in Figure 6.15 and their standard errors are given in Table 6.9. By using the parameterization constants in Table 6.9, the actual internal NaCl concentration of a geopolymer cell can be ascertained as:

$$c = -\frac{1}{b_2} \cdot \ln\left(\frac{Z_{modNorm_w} - b_3}{b_1}\right) \quad \text{Eq. 6.18}$$

if a second reference sensor is used for water content compensation in  $Z_{modNorm_w}$ .

Parameter	$b_1$	$b_2$	$b_3$
Value	0.5940	0.1730	0.3655
95% confidence bounds	Lower	0.5656	0.3363
	Upper	0.6225	0.3946

Table 6.9 - Parameters and their 95% confidence bounds for the line of best fit, equation 6.17, shown in Figure 6.15

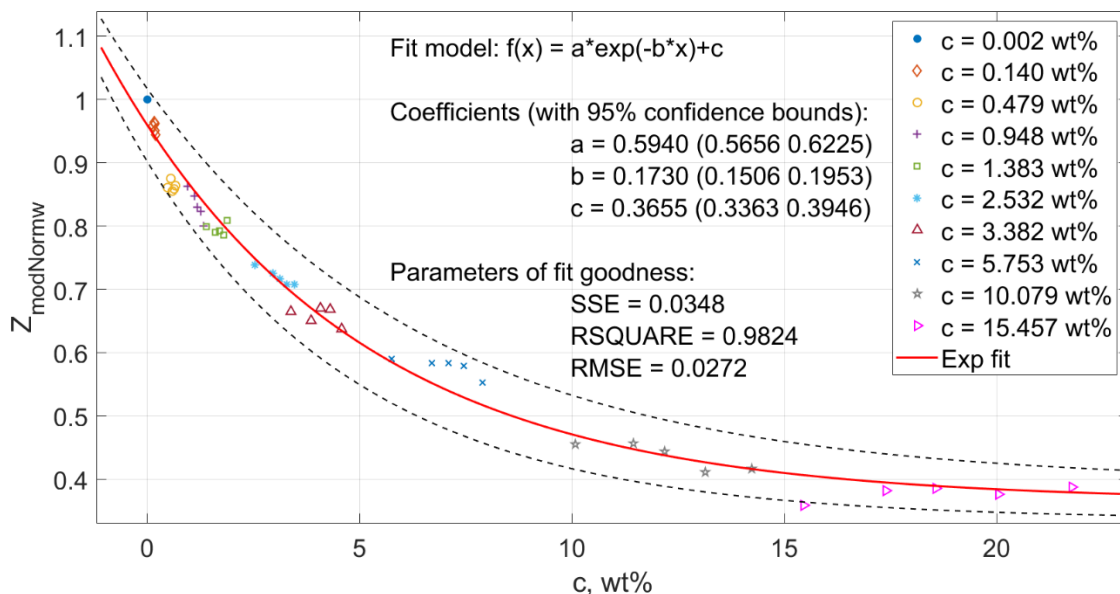


Figure 6.15 - Plot of the new normalised  $Z_{modNorm_w}$  values versus the actual internal NaCl concentrations  $c$  (Table 6.6). Non-linear fit uses equation 6.17. The colorization/shape of the data points indicates a different sample with its starting actual internal concentration value.

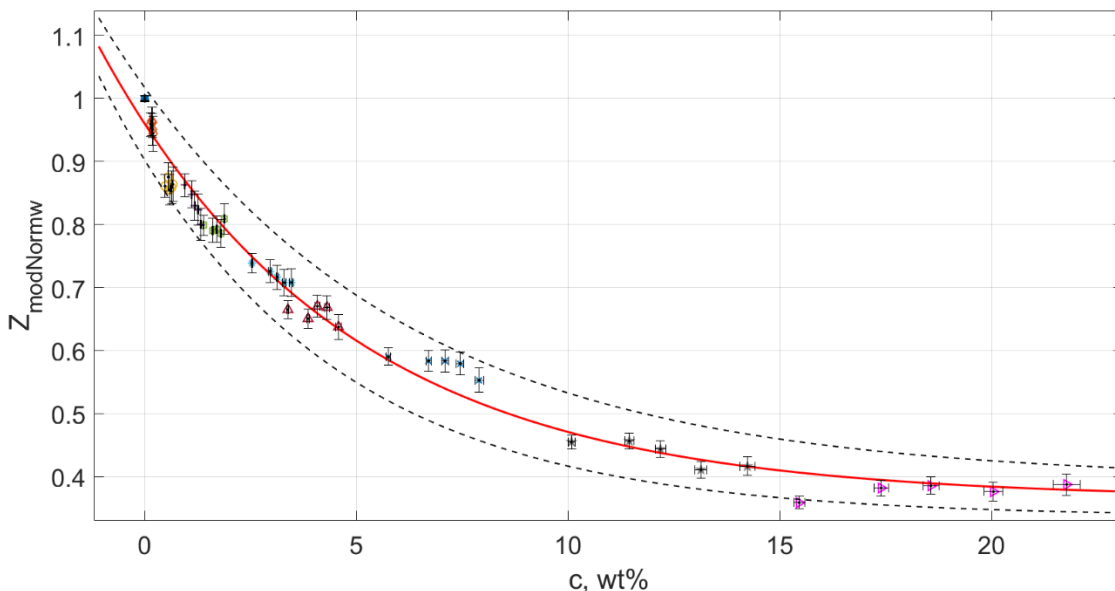


Figure 6.16 - Plot of Figure 6.15 with error bars

This result confirms that equation 6.4 is valid not only in the solution saturation case, but for all the water contents, by using the normalization equation 6.16. The colorization/shape of the data points in Figure 6.15 allows the samples to be distinguished according to the starting actual internal NaCl concentration  $c$  values. The five data points plotted in Figure 6.15 for each sample show that internal NaCl concentration  $c$  increases as the sample dries. The usefulness of Figure 6.15 is the possibility to see only the variation in internal NaCl

concentration, so it could be used to ascertain how much NaCl has actually leached into a concrete system (not just how much it is exposed to).

Figure 6.15 does show some fluctuations of the points around the fitting curve, with the furthest points that can be more likely attributed to experimental noise in temperature, water content values or chloride concentrations, and to the error associated to the interpolation process from the fitting curve  $c = 0wt\%$  ( $0.002wt\%$ ) of Figure 6.13, for water content compensation. Figure 6.16 shows the plot in Figure 6.15 with error bars for each data point. This shows that all the error bars are inside the 95% confidence bounds of the fit, except for one point at high concentrations, which remains just outside the bottom confidence limit, and can be considered an experimental outlier.

Figure 6.15 and Figure 6.16 clearly show the saturation of the sensor response for high NaCl concentrations, which suggests that the low concentration region  $<5wt\%$  is a better region for chloride sensing. Moreover, this saturation behaviour could be linked to the ion interaction molecular mean field which at high concentrations has a limiting effect on the ionic motion, as mentioned in the theory section 6.2.3.

#### 6.4.4. Sensor precision

The non-linear dependence of the sensor in response to water content and NaCl concentration means that the precision is not fixed for all water contents and NaCl concentrations. In this work, precision can be calculated by mapping the impedance fluctuations of the EIS interrogator onto the NaCl concentration axes, using the calibration fitting curve shown in Figure 6.15, and equation 6.17. The calculations are shown in detail in Appendix 1 (section A-1.3). The method for precision calculation can be graphically schematised as in Figure 6.17: A and B are the extremities of the error bars of the data point, and A' and B' are the corresponding points in the fitting curve, calculated by using equation 6.17. A'' and B'' are the corresponding points of A' and B' in the NaCl concentration axes, found by using equation 6.18. Precision is calculated as:

$$Precision = \frac{B'' - A''}{2} \quad \text{Eq. 6.19}$$

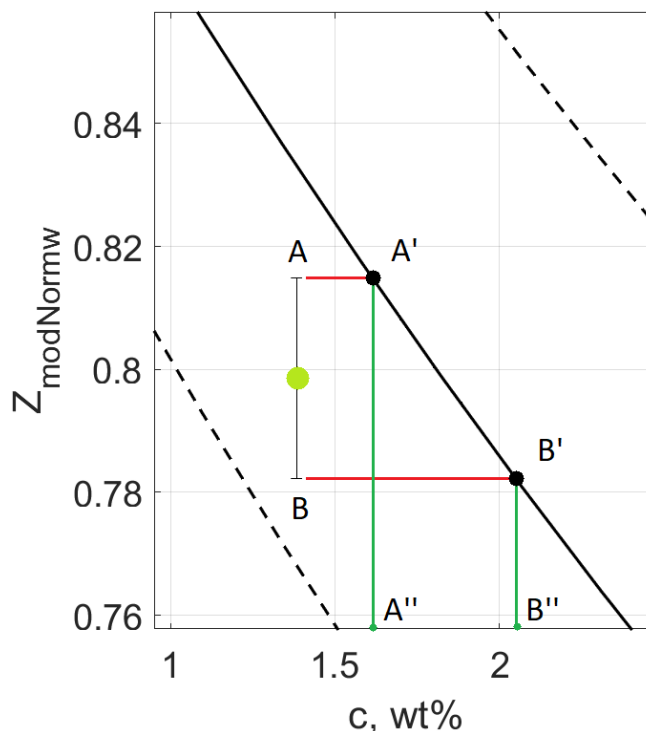


Figure 6.17 – Schematization of the method for NaCl concentration precision calculation, by using the data point with  $c = 1.383\text{wt}\%$ , and  $W \sim 85\text{wt}\%$ , its vertical error bars, and the fitting curve from the plot in Figure 6.16.

The fractional errors in the  $Z_{modNormw}$  response are in the range 0.01 – 0.04 %. They take into account the error in  $Z_{mod}$  and also the error coming from the interpolation process for the water content compensation. The precision results are shown in Table 6.10.

The fluctuations of the experimental data points observed in Figure 6.15 and the sensor saturation at high concentrations mean that the values for sensor precision for NaCl concentration are worse than those for moisture and temperature characterization (found in section 5.5.5 and listed in Table 5.5). These values demonstrate that typical sensor precision is  $\delta c \sim 0.85\text{wt}\%$  in the range of NaCl concentrations  $1 < c < 5\text{wt}\%$ . The worst case precision of  $\delta c = 5.84\text{wt}\%$  occurs in the region where the sensor response shows saturation, and the best case precision  $\delta c = 0.21\text{wt}\%$  corresponds to low concentrations,  $0.2\text{wt}\% < c < 1\text{wt}\%$ , where the sensor shows a better sensitivity to  $c$  changes. Note that concentrations  $c < 0.2\text{wt}\%$  produce negative estimations of impedance. On the other hand, the horizontal red lines in Figure 6.17 for experimental points located below the saturating part of the fitting curve of Figure 6.15 (at concentrations  $c > 15\text{wt}\%$ ) may not intersect with such fitting curve, making it impossible to define the relative precision. Therefore, the useful range for precision definition is  $0.2 < c < 15\text{wt}\%$ , which is also the region of operation of the sensor.

	$\delta c, wt\%$
<b>Worst case</b>	5.84
<b>Typical case</b>	0.85
<b>Best case</b>	0.21

Table 6.10 - Worst case, best case and typical precisions for NaCl sensing in the range of actual internal NaCl concentrations between 0 and 15 wt%, in the range of water content percentage between 86-61wt% and at a temperature of 20°C.

## 6.5. Summary and future work

This chapter has provided a first time demonstration of the viability of monitoring NaCl concentration in the pore solution of low calcium fly ash geopolymers at 20°C. In this work, the same sensor prototype developed in chapter 5 was used: a geopolymer block with stainless steel electrodes in a Van Der Pauw configuration, coupled with an electrical interrogation system to measure electrical impedance. The results show that, as expected from theory, changes in NaCl concentration inside the pore solution of the geopolymer cell result in changes in impedance, with an exponential dependence. The calibration equation found in chapter 5 for impedance dependence on moisture was confirmed to hold for the case of NaCl contamination.

An experimental campaign of impedance measurements was conducted to characterize the geopolymer cell for chloride sensing. Fifty different actual internal NaCl concentrations covering the range 0 wt% – 22wt% were used. Sensor response showed saturation for internal NaCl concentrations beyond 5wt%. The most sensitive region for NaCl concentration sensing was found in the range 0.2 – 5 wt%, with typical precisions of  $\delta c \sim 0.8$  wt%, while at higher concentrations the saturation led to lower precision. Worst case precision  $\delta c \sim 5.8$  wt% corresponds to high concentration values ( $c \geq 10$  wt%), while the best case precision corresponds to concentration values  $0.2 < c < 1$  wt%. This result is worse than those obtained for moisture and temperature calibration in the previous chapter. This may partly be due to some change in the physical mechanisms behind geopolymer ion conductivity when ion density in the solution is high, and to fluctuations in temperature and water content.

The range of NaCl concentrations covered in the sensor calibration meets all the possible chloride contamination values and water contents in the range of those found in nuclear storage structures, such as SPRS: from the case of initial contamination ( $\sim 0.2\%$ ) to the

worst case contamination (applied contamination corresponding to chloride saturation in water, 35 g of salt/litre of solution alias 28 g of salt/g of solution).

Future work will need a more complete calibration of the sensing system, which requires: (a) a temperature calibration for each NaCl concentration; (b) a higher measurement time for each impedance measurement (about 20 minutes) which would allow an evaluation of sensor stability and drift; and (c) a repeatability evaluation.

Besides, another piece of future work is to explore system dynamics: how the chloride concentration inside the sample changes as the sensor is exposed to chloride outside of the sample, and how this affects drift in the sensor response.

In future work, an environmental chamber is preferred to the faraday cage for a future sensor cell characterization, in order to reduce fluctuations in temperature values.

This work, together with the work outlined in the previous chapter, constitutes only the first step of the development of a distributed network of geopolymer skin sensors for structural health monitoring. Next step in the preliminary characterization of such technology is to evaluate the feasibility of temperature, moisture and chloride sensing in case of geopolymer coatings on concrete specimens, which is outlined in next chapter.

## References

- [1] F. P. Glasser, J. Marchand, and E. Samson, "Durability of concrete—Degradation phenomena involving detrimental chemical reactions," *Cement and Concrete Research*, vol. 38, pp. 226-246, 2008.
- [2] M. Torres-Luque, E. Bastidas-Arteaga, F. Schoefs, M. Sánchez-Silva, and J. F. Osma, "Non-destructive methods for measuring chloride ingress into concrete: State-of-the-art and future challenges," *Construction and building materials*, vol. 68, pp. 68-81, 2014.
- [3] C. Andrade, M. Castellote, and R. d'Andrea, "Measurement of ageing effect on chloride diffusion coefficients in cementitious matrices," *Journal of Nuclear Materials*, vol. 412, pp. 209-216, 2011.
- [4] H. S. Lee, M. A. Ismail, J. K. Singh, and J. H. Shin, "Embedded sensor system to detect chloride permeation in concrete: an overview," *Corrosion Engineering, Science and Technology*, vol. 52, pp. 373-382, 2017.
- [5] P. Mehta, "Concrete durability-fifty years progress," in *Proceedings of the 2nd International Conference on Concrete Durability, Montreal, QC, Canada, 1991*, p. 132.
- [6] R. E. Melchers and C. Q. Li, "Phenomenological modeling of reinforcement corrosion in marine environments," *ACI Materials Journal*, vol. 103, p. 25, 2006.
- [7] G. Glass and N. Buenfeld, "Chloride-induced corrosion of steel in concrete," *Progress in Structural Engineering and Materials*, vol. 2, pp. 448-458, 2000.
- [8] M. K. Kassir and M. Ghosn, "Chloride-induced corrosion of reinforced concrete bridge decks," *Cement and Concrete Research*, vol. 32, pp. 139-143, 2002.
- [9] M. Montemor, A. Simoes, and M. Ferreira, "Chloride-induced corrosion on reinforcing steel: from the fundamentals to the monitoring techniques," *Cement and Concrete Composites*, vol. 25, pp. 491-502, 2003.
- [10] I. O. f. Standardization, *Corrosion of Metals and Alloys: Corrosivity of Atmospheres: Measurement of Environmental Parameters Affecting Corrosivity Atmospheres*: ISO, 2012.
- [11] B. Elsener, L. Zimmermann, and H. Böhni, "Non destructive determination of the free chloride content in cement based materials," *Materials and Corrosion*, vol. 54, pp. 440-446, 2003.
- [12] C. Atkins, J. Scantlebury, P. Nedwell, and S. Blatch, "Monitoring chloride concentrations in hardened cement pastes using ion selective electrodes," *Cement and Concrete Research*, vol. 26, pp. 319-324, 1996.
- [13] C. Atkins, M. Carter, and J. Scantlebury, "Sources of error in using silver/silver chloride electrodes to monitor chloride activity in concrete," *Cement and Concrete Research*, vol. 31, pp. 1207-1211, 2001.
- [14] G. Duffò, S. Farina, and C. Giordano, "Characterization of solid embeddable sensor to monitor the corrosion process of new and existing reinforced concrete structures," *Construction and building materials*, vol. 23, pp. 2746-2751, 2009.
- [15] G. S. Duffó and S. B. Farina, "Development of an embeddable sensor to monitor the corrosion process of new and existing reinforced concrete structures," *Construction and Building Materials*, vol. 23, pp. 2746-2751, 2009.
- [16] G. De Vera, M. Climent, C. Antón, A. Hidalgo, and C. Andrade, "Determination of the selectivity coefficient of a chloride ion selective electrode in alkaline media simulating the cement paste pore solution," *Journal of Electroanalytical Chemistry*, vol. 639, pp. 43-49, 2010.

- [17] P. L. Fuhr and S. J. Spammer, "Fiber optic sensors in the Waterbury bridge," in *Fourth Pacific Northwest Fiber Optic Sensor Workshop*, 1998, pp. 124-129.
- [18] J.-L. Tang and J.-N. Wang, "Measurement of chloride-ion concentration with long-period grating technology," *Smart materials and structures*, vol. 16, p. 665, 2007.
- [19] C. C. C. Lam, R. Mandamparambil, T. Sun, K. T. Grattan, S. V. Nanukuttan, S. E. Taylor, and P. M. Basheer, "Optical fiber refractive index sensor for chloride ion monitoring," *IEEE Sensors Journal*, vol. 9, pp. 525-532, 2009.
- [20] M. Fares, G. Villain, S. Bonnet, S. P. Lopes, B. Thauvin, and M. Thiery, "Determining chloride content profiles in concrete using an electrical resistivity tomography device," *Cement and Concrete Composites*, vol. 94, pp. 315-326, 2018.
- [21] W.-J. Park, H.-S. Lee, S.-H. Joh, and H.-S. Lee, "Monitoring method for the chloride ion penetration in mortar by a thin-film sensor reacting to chloride ion," *Construction and Building Materials*, vol. 53, pp. 403-410, 2014.
- [22] W. J. McCarter and Ø. Vennesland, "Sensor systems for use in reinforced concrete structures," *Construction and Building Materials*, vol. 18, pp. 351-358, 2004.
- [23] W. J. McCarter, T. Chrisp, G. Starrs, A. Adamson, E. Owens, P. Basheer, S. Nanukuttan, S. Srinivasan, and N. Holmes, "Developments in performance monitoring of concrete exposed to extreme environments," *Journal of infrastructure systems*, vol. 18, pp. 167-175, 2012.
- [24] R. B. Polder, "Test methods for on site measurement of resistivity of concrete—a RILEM TC-154 technical recommendation," *Construction and building materials*, vol. 15, pp. 125-131, 2001.
- [25] R. B. Polder and W. H. Peelen, "Characterisation of chloride transport and reinforcement corrosion in concrete under cyclic wetting and drying by electrical resistivity," *Cement and Concrete Composites*, vol. 24, pp. 427-435, 2002.
- [26] P. Basheer, P. Gilleece, A. Long, and W. Mc Carter, "Monitoring electrical resistance of concretes containing alternative cementitious materials to assess their resistance to chloride penetration," *Cement and Concrete Composites*, vol. 24, pp. 437-449, 2002.
- [27] R. Prakash, "Non-destructive testing of composites," *Composites*, vol. 11, pp. 217-224, 1980.
- [28] C. Fernández-Sánchez, C. J. McNeil, and K. Rawson, "Electrochemical impedance spectroscopy studies of polymer degradation: application to biosensor development," *TrAC Trends in Analytical Chemistry*, vol. 24, pp. 37-48, 2005.
- [29] M. Shi, Z. Chen, and J. Sun, "Determination of chloride diffusivity in concrete by AC impedance spectroscopy," *Cement and Concrete Research*, vol. 29, pp. 1111-1115, 1999.
- [30] B. Díaz, X. Nóvoa, and M. Pérez, "Study of the chloride diffusion in mortar: A new method of determining diffusion coefficients based on impedance measurements," *Cement and Concrete Composites*, vol. 28, pp. 237-245, 2006.
- [31] J. Deus, B. Díaz, L. Freire, and X. Nóvoa, "The electrochemical behaviour of steel rebars in concrete: an electrochemical impedance spectroscopy study of the effect of temperature," *Electrochimica Acta*, vol. 131, pp. 106-115, 2014.
- [32] R. Buck and E. Linder, "UPAC 46/89 Document "Recommendations for Nomenclature of Ion-Selective Electrodes"," *Analytical Chemistry Division, Commission on Analytical Nomenclature, Pure Appl. Chem*, vol. 66, pp. 2527-2536, 1994.
- [33] E. Bakker and M. Telting-Diaz, "Electrochemical sensors," *Analytical chemistry*, vol. 74, pp. 2781-2800, 2002.

- [34] R. Falciai, A. Mignani, and A. Vannini, "Long period gratings as solution concentration sensors," *Sensors and Actuators B: Chemical*, vol. 74, pp. 74-77, 2001.
- [35] K. Gowers and S. Millard, "Measurement of concrete resistivity for assessment of corrosion," *ACI Materials Journal*, vol. 96, 1999.
- [36] D. McPolin, P. Basheer, A. Long, K. Grattan, and T. Sun, "Obtaining progressive chloride profiles in cementitious materials," *Construction and Building Materials*, vol. 19, pp. 666-673, 2005.
- [37] R. L. Du Plooy, "The development and combination of electromagnetic non-destructive evaluation techniques for the assesment of cover concrete condition prior to corrosion," 2013.
- [38] R. Vedalakshmi, R. R. Devi, B. Emmanuel, and N. Palaniswamy, "Determination of diffusion coefficient of chloride in concrete: an electrochemical impedance spectroscopic approach," *Materials and Structures*, vol. 41, pp. 1315-1326, 2008.
- [39] R. Vedalakshmi, V. Saraswathy, H.-W. Song, and N. Palaniswamy, "Determination of diffusion coefficient of chloride in concrete using Warburg diffusion coefficient," *Corrosion Science*, vol. 51, pp. 1299-1307, 2009.
- [40] R. A. Robinson and R. H. Stokes, *Electrolyte solutions*: Courier Corporation, 2002.
- [41] J. Bisquert, V. Halpern, and F. Henn, "Simple model for ac ionic conduction in solids," ed: American Institute of Physics, 2005.
- [42] K. Funke and R. D. Banhatti, "Ionic motion in materials with disordered structures," *Solid State Ionics*, vol. 177, pp. 1551-1557, 2006.
- [43] J. Kawamura, S. Yoshikado, and T. Sakuma, *Superionic Conductor Physics: Proceedings of the 1st International Discussion Meeting on Superionic Conductor Physics (IDMSICP)*: World Scientific, 2007.
- [44] K. Funke, R. D. Banhatti, and M. D. Ingram, "Ion Transport in Glass-Forming Calcium Potassium Nitrate: From Complex Behaviours to Unexpected Simplicities," in *Diffusion Foundations*, 2019, pp. 140-159.
- [45] F. Rajabipour, J. Weiss, and D. M. Abraham, "Insitu electrical conductivity measurements to assess moisture and ionic transport in concrete (A discussion of critical features that influence the measurements)," in *Proceedings of the International RILEM Symposium on Concrete Science and Engineering: A Tribute to Arnon Bentur*, 2004.

# 7. PRELIMINARY INVESTIGATION OF GEOPOLYMER COATING SENSORS

## 7.1. Introduction

The work presented in this chapter brings together the work outlined in chapters 4-6 to demonstrate geopolymer skin sensors for detecting moisture and chloride levels in concrete structures. This chapter provides a preliminary laboratory feasibility test and characterizes the sensor response of geopolymer coatings applied onto small concrete samples.

The main objectives of the work described in this chapter were: (a) to test the feasibility of thin geopolymer coatings on concrete as moisture and chloride sensors; (b) to verify the validity of the calibration equations found for geopolymer cells in the case of coatings; (c) to find the difference of the sensor response between the case of a geopolymer cell and a geopolymer coating; and (d) to assess the sensor performance of coatings, in terms of sensor precision, and compare it to that of the geopolymer cells found in the previous chapters.

The remainder of this chapter starts with a brief theoretical section on the sensing principle of geopolymer coatings (section 7.2), then materials and methods used in the characterization experiment are described in section 7.3, while section 7.4 outlines the results of the experiment and provides a discussion on the findings. Finally, section 7.5 presents a summary and future work.

## 7.2. Theory: sensing principle of the geopolymer coating system

When looking at the geopolymer coating system, the presence of the concrete substrate will need to be taken into consideration, particularly if the geopolymer coating is thin. The sensing system will be comprised of the coating and a volume of concrete (and, potentially rebar) underneath the coating. In the work described here, small volumes of unreinforced concrete are used as substrates, and the geopolymer coatings are only 1 mm thick. The whole sample is thus considered to be a sensing cell.

Both geopolymer and concrete pore solutions are comprised of ionic electrolytes and the migration of ions and cations under an electrical potential gradient determines ionic conduction. In the previous two chapters, the ionic conduction of geopolymer materials, without the addition of other external ions, has been attributed to the migration of sodium ions ( $Na^+$ ), the main carriers of ionic current. When the geopolymer samples are soaked into sodium chloride (NaCl) solutions,  $Cl^-$  and more  $Na^+$  ions will be present inside the pore solution and this will result in an enhanced ionic conductivity of geopolymers at high moisture content. The factors affecting the ionic conductivity of geopolymers, such as water content, temperature and ion concentration, have already been investigated in detail in chapters 5 and 6.

On the other hand, in concrete, without the addition of other external ions, the major ionic species constituting the pore solution of conventional concretes consist of hydroxyl ( $OH^-$ ), potassium ( $K^+$ ), sodium ( $Na^+$ ), calcium ( $Ca^+$ ), sulfate ( $SO_4^{2-}$ ), and often chloride ( $Cl^-$ ) ions. Conductivity of the concrete pore solution depends on the valence, mobility, and concentration of each type of ion and therefore the total conductivity of concrete depends on the composition of its pore solution. In addition to its dependence on the pore solution composition, the conductivity of concrete also depends on some other factors including

temperature and moisture [1]. When concrete is soaked into sodium chloride (NaCl) solutions, more  $Cl^-$  and  $Na^+$  ions will be present inside the pore solution and this will result in an enhanced ionic conductivity of concretes at moisture contents not so low to allow connectivity between the pores, and not so high to provide a high dilution factor to the pore solution. At the same time, the combination of low water contents and high levels of NaCl in the pore solution may cause a saturation behaviour of the sensor response, due to an elevated density of ions in the solution.

As already mentioned in the previous two chapters, the bulk electrical conductivity in concrete and cementitious materials,  $\sigma$ , is a function of the conductivity of the pore solution,  $\sigma_0$ , the volume of the pore network filled with pore solution,  $\varphi_{con}$ , and the connectivity factor of the pore network,  $\beta$  [1], and this is described by means of the following equation:

$$\sigma = \sigma_0 \varphi_{con} \beta. \quad \text{Eq. 7.1}$$

This equation has been assumed to be valid also for geopolymers. Therefore, both concrete and geopolymer conductivities will depend on measurands which alter the three factors on the right hand side of equation 7.1: perhaps not to the same extent, but at least in the same manner. Also in concretes, as already seen for geopolymers, increasing temperature enhances ion mobility and encourages electrolytic dissociation, both of which increase  $\sigma_0$ . Therefore, provided there is no evaporation of water at high temperatures, the relationship between the geopolymer coating-concrete system's conductivity,  $\sigma$ , and temperature,  $T$ , is expected to follow the equation valid for cement systems [2], and demonstrated to be valid also for geopolymers in chapter 5:

$$\ln(\sigma) = \frac{D_8}{T} + D_9 T + D_{10}, \quad \text{Eq. 7.2}$$

where  $D_8$ ,  $D_9$  and  $D_{10}$  are constants.

Water content within the geopolymer coating-concrete system affects all three factors in equation 7.1: increasing water content reduces the conductivity of the pore solution,  $\sigma_0$ , by providing dilution of the pore solution, and at the same time it increases the pore filled volume,  $\varphi_{con}$ , and the connectivity between the pores,  $\beta$  [3]. On the other hand, very low water contents decrease dramatically conductivity, as the liquid electrolyte cannot cover the internal surfaces of the pores [3].

Previous studies of ordinary Portland cement systems report an exponential dependence of electrical conductivity on water content [4]. The admittance of a geopolymer sensor is defined as the inverse of impedance:

$$A = \frac{1}{Z} \tag{Eq. 7.3}$$

and, for a fixed cell geometry, the modulus of admittance,  $A_{mod} = |A|$ , is proportional to conductivity,  $\sigma$ . The results shown in chapter 5 agree on the exponential dependence of geopolymer impedance on moisture. The experimental results for the geopolymer coating-concrete system's impedance show that the dependence of impedance on water content can be described by the same equation found in the case of the geopolymer cell system, here recalled for completeness:

$$Z_{mod} = a_7 * e^{\frac{a_8}{W}} \tag{Eq. 7.4}$$

where  $Z_{mod}$  is the impedance modulus of concrete,  $W$  is the water content and  $a_7$  and  $a_8$  are constants.

Equation 7.4 can be re-expressed as:

$$\ln(Z) = \frac{D_{11}}{W} + D_{12}, \tag{Eq. 7.5}$$

By combining equations 7.2 and 7.5, the same characterization equation found for the geopolymer sensor cell is found in the case of the geopolymer coating-concrete system:

$$\ln\left(\frac{Z_{mod}}{Z_{mod,0}}\right) = \frac{G_6}{T} + G_7T + \frac{G_8}{W} + G_9T\frac{1}{W} + G_{10}, \tag{Eq. 7.6}$$

where  $G_{6,\dots,10}$  are constant. Also in this case, the surface equation 7.6 includes an additional cross-dependence term between moisture and temperature ( $G_9T/W$ ). The equation considers shifts in the modulus of the impedance only, and all  $Z_{mod}$  values were normalised by the impedance modulus value of the sensor at a moisture content of 78wt% and at a temperature of 20 °C,  $Z_{mod,0}$ , in order to make the equation less sensitive to variations in sensor geometry.

Finally, the NaCl concentration dependence of impedance of the geopolymer coating-concrete system has been found to be described by:

$$\frac{Z_{mod}}{Z_{mod,0}} = b_4 * e^{-b_5 \cdot c} + b_6 \quad \text{Eq. 7.7}$$

where  $Z_{mod}$  is the modulus of the impedance at different NaCl concentrations,  $Z_{mod,0}$  is the modulus of the geopolymer sample before the soaking into the NaCl solution,  $c$  is the concentration of NaCl inside the pore solution of the geopolymer coating-concrete sample, and  $b_{4, \dots, 6}$  are constants. Also here, equation 7.7 is normalised ( $\frac{Z_{mod}}{Z_{mod,0}}$ ) to eliminate the dependence on the geometry and the specific sample.

Equation 7.7 is the same found for the geopolymer cell characterised in chapter 6, and it is in accordance also with previous works on electrical resistivity measurements of concrete which have demonstrated an exponential dependence of resistivity on chloride content [5].

These equations have been used in the results section for the moisture, temperature and chloride concentration characterization of the sensor prototype.

## 7.3. Materials and methods

This section presents a detailed description of the materials and methods used for the manufacture, set-up, preliminary characterisation and testing of low calcium fly ash geopolymer coatings onto concrete samples as moisture, temperature and chloride sensor prototypes.

### 7.3.1. Sensor fabrication

The sensor prototype developed and tested in this work is an electrochemical cell comprised of a low calcium fly ash geopolymer patch applied on the top surface of a concrete rectangular sample. A photograph of the prototype is shown in Figure 7.1.

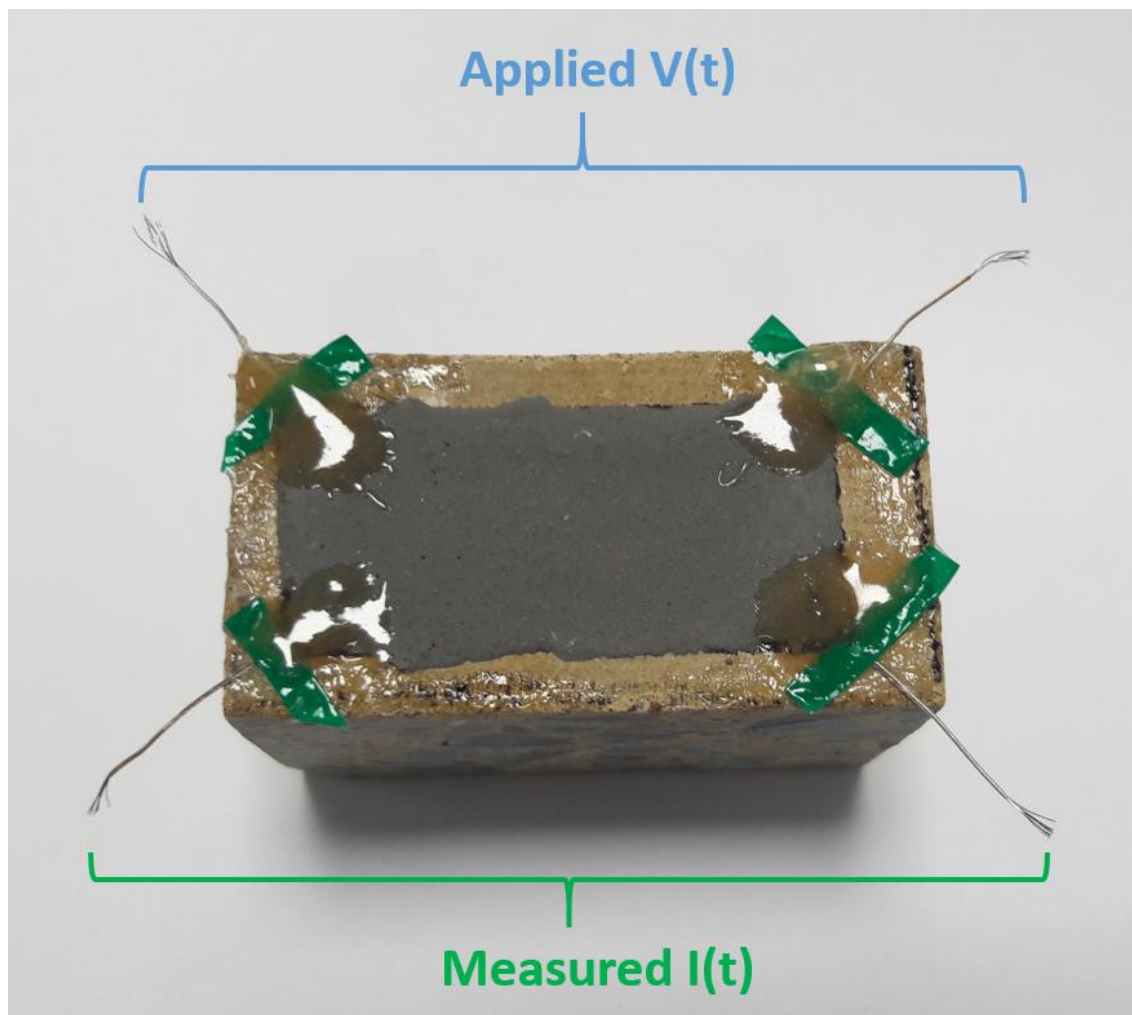


Figure 7.1 – Geopolymer coating on concrete cell sensor prototype

A geopolymer rectangular patch (dimensions 45mm × 20mm × 1mm), with 4 -wire braided stainless steel wire electrodes penetrating 2mm into the patch corners, in a Van Der Pauw configuration, is applied on the top surface of a concrete rectangular sample (dimensions 55mm × 30mm × 40mm). As demonstrated in chapter 4, the coating thickness of 1 mm guarantees the integrity of the coating.

The synthesis procedure of the geopolymer binder is the same as described in chapter 4: the binder was synthesized from low calcium fly ash and an alkaline solution made of sodium Hydroxide (SH) and sodium silicate (SS), with a liquid (L) to solid (S) ratio,  $L/S = 0.5$ , and the ratio between sodium hydroxide and sodium silicate is  $SH/SS = 0.4$ . The binder was mixed for 1 hour with an automatic mixer at  $500 \text{ min}^{-1}$  and then manually applied to the concrete substrate with a trowel. The samples were cured for 30 days at  $20^\circ\text{C}$  and 95% relative humidity in an environmental chamber prior to testing.

### 7.3.1. Interrogation system

As for the case of moisture/temperature and chloride/moisture sensing calibration of geopolymer samples described respectively in chapter 5 and in chapter 6, Electrochemical Impedance Spectroscopy (EIS) was applied to the geopolymer patch-concrete cells in the potentiostatic mode: a 10mV voltage was applied to the geopolymer patches, and the resulting pseudo-linear current response was measured, thus obtaining the impedance of the system. The frequency of the applied voltage was swept over the range  $10 - 10^5$  Hz during impedance characterization.

### 7.3.2. Calibration methods

This section is divided in two sub-sections, which describes the preliminary calibration procedure of the geopolymer coating-concrete system respectively for moisture and temperature sensing, and for NaCl concentration sensing at a fixed water content and temperature.

#### 7.3.2.1. Moisture and temperature calibration

The procedure for the moisture and temperature preliminary calibration for coatings is the same outlined in chapter 5 for geopolymer cells, summarised by the flowchart shown in Figure 5.6. Pictures of the geopolymer coating-concrete inside the sealed box for water homogenization and a scheme of the measurement experimental set up (where the environmental chamber was used) are shown respectively in Figure 7.2. in Figure 7.3.

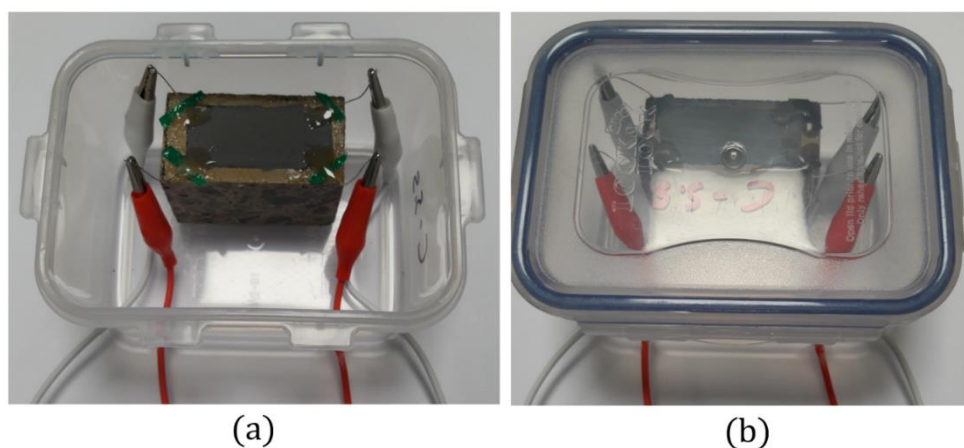


Figure 7.2 - (a) geopolymer coating-concrete cell inside the plastic box, connected to the electrodes of the interrogation system, before sealing; (b) geopolymer coating-concrete cell inside the sealed plastic box.

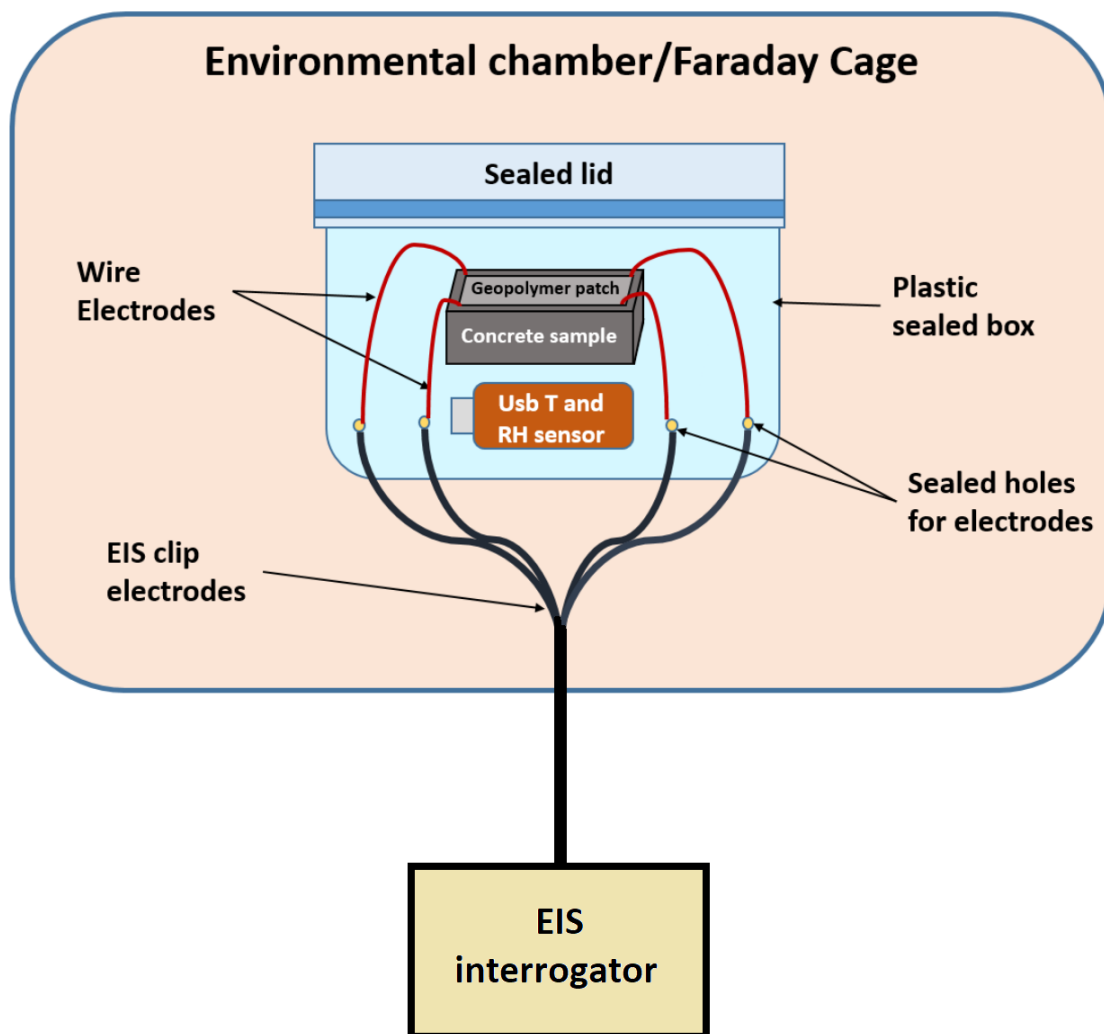


Figure 7.3 - Scheme of the geopolymer coating-concrete cell sample at each water content.

#### 7.3.2.2. NaCl calibration

The NaCl preliminary calibration of the coating sensor was conducted only at the saturation level (water content  $\sim 90$  wt%): no drying points were investigated. NaCl solutions with seven different concentrations were used. Nanopure water was used for the case of 0wt% concentration. The solutions were made by adding a certain amount of NaCl salt into nanopure water by using a volumetric flask of 1 liter. Also in this case, as in chapter 6, the concentrations of these solutions are called ‘applied concentrations’, but this time the coating cells were soaked in 1 liter of solution for 96 hours. Therefore, here it is made the assumption that applied concentration is quite close to the actual internal NaCl concentration of the geopolymer coating-concrete system.

The applied NaCl concentrations are listed in Table 7.1

Applied NaCl concentration [wt%]
$0.520 \pm 0.003$
$1.202 \pm 0.003$
$2.169 \pm 0.003$
$3.412 \pm 0.003$
$5.293 \pm 0.004$
$8.041 \pm 0.005$
$12.002 \pm 0.007$

Table 7.1 – NaCl applied concentrations

The NaCl calibration procedure used for the coating-concrete cells is the same conducted for the geopolymer cells, and summarised in the flowchart in Figure 6.3, with the only difference that this time the samples were soaked in 1 liter of solution for 96 hours, instead of 24 hours, and no drying points have been investigated, but only the saturation case. Also in this case, the normalized values  $\frac{Z_{mod}}{Z_{mod,0}}$  were used: the value of impedance modulus  $Z_{mod}$  for each cell was divided by the initial value of impedance of the same cell before being soaked in the solution,  $Z_{mod,0}$  (impedance value of the sample just after curing at 95% RH and 20°C, without any NaCl content). The experimental set up also in this case is shown in Figure 7.3 (where the Faraday cage was used).

## 7.4. Results and discussion

### 7.4.1. Coating-concrete cell impedance response

Figure 7.4 shows the typical Bode plots of phase  $\varphi$  and  $Z_{mod}$  for: (a) a geopolymer coating-concrete sensor cell at a temperature of  $20 \pm 1^\circ\text{C}$  and a water content of  $\sim 92 \pm 1 \text{ wt\%}$ ; (b) a geopolymer coating-concrete sensor cell at a temperature of  $20 \pm 1^\circ\text{C}$ , a water content of  $\sim 92 \pm 1 \text{ wt\%}$ , and an applied NaCl concentration  $\sim 5.3 \text{ wt\%}$ .

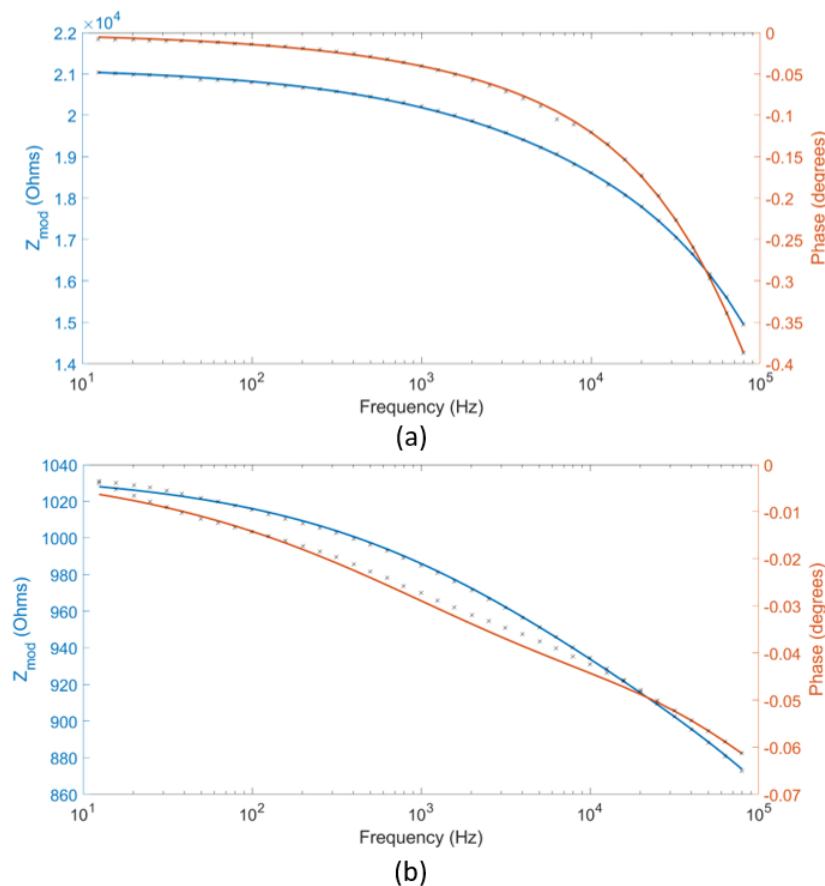


Figure 7.4 – (a) Bode plots for  $Z_{mod}$  and phase  $\phi$  obtained for a geopolymer coating-concrete at a temperature of  $20 \pm 1^\circ\text{C}$  and a water content of  $\sim 92 \pm 1\text{wt}\%$ . The fits use the equivalent circuit model given in Figure 7.5 (b). (b) Bode plots for  $Z_{mod}$  and phase  $\phi$  obtained for a geopolymer coating-concrete at a temperature of  $20 \pm 1^\circ\text{C}$ , a water content of  $\sim 92 \pm 1\text{wt}\%$  and an applied NaCl concentration  $\sim 5.3\text{wt}\%$ . The fits use the equivalent circuit model given in Figure 5.4 (b).

The fits in Figure 7.4 (a) made use of the equivalent circuit model given in Figure 7.5 (b). This is the same as the equivalent circuit used to describe concrete according to [6] (shown in Figure 7.5 (a)) with the difference that capacitors were replaced with Constant Phase Elements (CPE), since this better describes the net result of ion dynamics in electrochemical systems. The circuit elements in Figure 7.5 (a) are: the bulk capacitance of the concrete substrate,  $C_b$ ; the connected pore resistance,  $R_c$ , and unconnected pore resistance of the concrete substrate,  $R_{uc}$ ; and the pore wall capacitance of the concrete substrate,  $C_p$ . The values for each component of the circuit for all the water contents investigated are given in Table A 6 of Appendix 5.

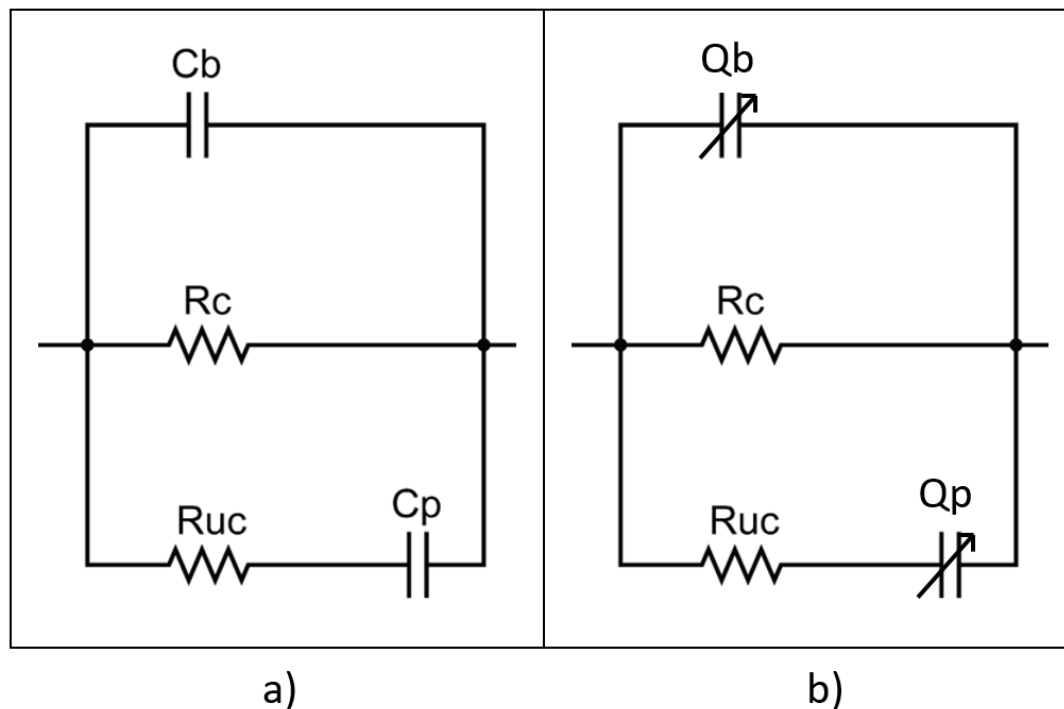


Figure 7.5 - a) Equivalent circuit used to describe concrete according to [6]. b) Equivalent circuit used to describe the geopolymer coating-concrete cells in this work, in case of no NaCl contamination presence inside the pores of the system.

The use of the equivalent circuit for concrete to fit the Bode plots of the sensing system and the high values of impedance modulus shown in Figure 7.4 (a) (of the order of 10 – 20 k $\Omega$ ) are an indication that, in absence of additional NaCl concentration, the impedance response of the geopolymer coating-concrete system is dominated by concrete. In this case it is possible to hypothesise that the geopolymer patch acts as a conducting layer to apply the ac signal directly onto concrete (i.e. acting analogous to a “solder material” rather than a conducting skin). This would explain why in this case the bulk capacitance can’t be approximated to be equal to 0 (as it was for pure geopolymer cells). The wire electrodes distance is similar, and the wire electrodes area is the same of the case of the geopolymer cell, but in this case all the geopolymer layer itself can perhaps be considered to be part of the electrode.

The fits in Figure 7.4 (b) made use of the equivalent circuit model in Figure 5.4 b), and the values for each component of the circuit are given in Table A 7 of Appendix 5 for the seven concentrations in Table 7.1. This result shows that the coating system in case of NaCl contamination behaves in a similar way to the geopolymer cell. Impedance modulus values are much lower than those in Figure 7.4 (a) (< 1 k $\Omega$ ) and comparable with the values of

impedance of the geopolymer cell. A possible explanation can be found in the fact that the higher ion concentration in the geopolymer patch makes its conductivity dominant respect to the conductivity of concrete, since concrete structure is more complex than geopolymer structures, with the presence of aggregates of different sizes, sand, and hardened cement paste.

Regardless of the mechanisms, this result constitutes a useful way to discriminate between water and chloride sensing responses: a different circuit model and a different magnitude of impedance describe the two cases. However, further investigations are needed to explain ion dynamics in this combined system.

### 7.4.2. Moisture, temperature, NaCl and frequency dependence

Figure 7.6 shows Bode plots for geopolymer coating-concrete sensors at temperatures ranging from 5 °C to 30 °C, and a water content of  $\sim 92 \pm 1 \text{ wt}\%$ . In this figure, isotherms have been plotted on the y-axis by taking the product of the modulus of admittance and temperature, or  $A_{mod} \cdot T$ .

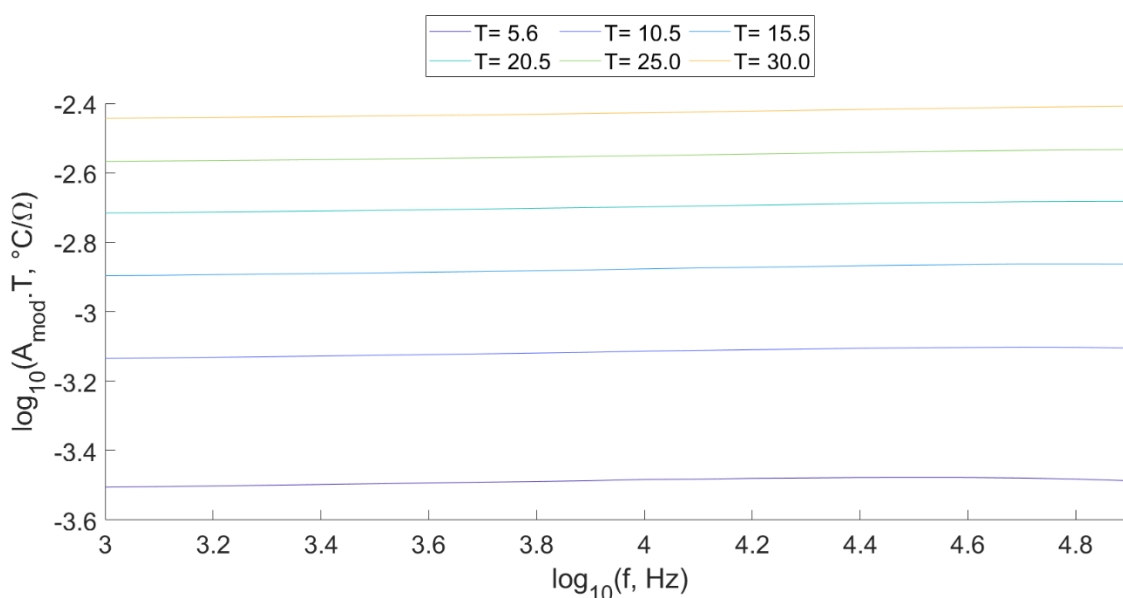


Figure 7.6 – Bode plots of isotherms of  $A_{mod} \cdot T$ . Data shown is for samples at a constant water content of  $W \sim 92 \text{ wt}\%$ .

Figure 7.6 seems to suggest that also the geopolymer coating-concrete sensors obey a scaling law typical of ionic conductors known as Summerfield scaling [7]: the shape of each Bode plot is independent of temperature (e.g. the  $T = 10\text{ }^{\circ}\text{C}$  line can be shifted up or down to superimpose onto any other temperature line). This means that it is possible to define a master curve, arbitrarily defining a baseline frequency of  $f_0 = 1000\text{ Hz}$ , and a baseline admittance at  $1000\text{ Hz}$  of  $A_{mod,0} = A_{mod}(1000\text{Hz})$  for each line. Here the scaling frequency has been chosen to be fixed at  $1000\text{ Hz}$ , because the impedance measurements during the thermal cycle for coatings have been found to not work for frequencies  $< 1000\text{ Hz}$ .

This allows us to plot all of the data shown in Figure 7.6 onto a single scaled Summerfield plot, which is shown in Figure 7.7 (a)Figure 5.11. In this case, the isotherms don't overlap very well and there is a large degree of scatter. This scattering can be quantified using a linear fit of the data and calculating the RMS parameter.  $RMS_{Tcoatings} = 0.0025$  is higher than that found for the geopolymer cell in chapter 6 ( $RMS_{Tgeopolymer} = 0.0019$ ). This may be because, without the presence of NaCl in the sample, the system impedance seems to be dominated by concrete impedance (as shown in section 7.4.1), and concrete, compared with the geopolymer system, has a variety of ions which may behave in different ways with temperature variation. Concrete also has a structure which is less disordered than that of geopolymer.

By repeating the scaled Summerfield plot process for water contents and NaCl concentrations, Figure 7.7 (b) and (c) are obtained respectively. The values of RMS for the three cases for coatings systems, and those found in chapter 6 for the same three parameters in the case of geopolymer cells are shown in Table 7.2.

	Parameter	T	W	c
RMS	Coatings	0.0025	0.0121	0.0063
	Geopolymers	0.0019	0.0058	0.0041

Table 7.2 – RMS parameters for coating and geopolymer cell systems in case of temperature (T), water content (W), and NaCl concentration (c) sensing.

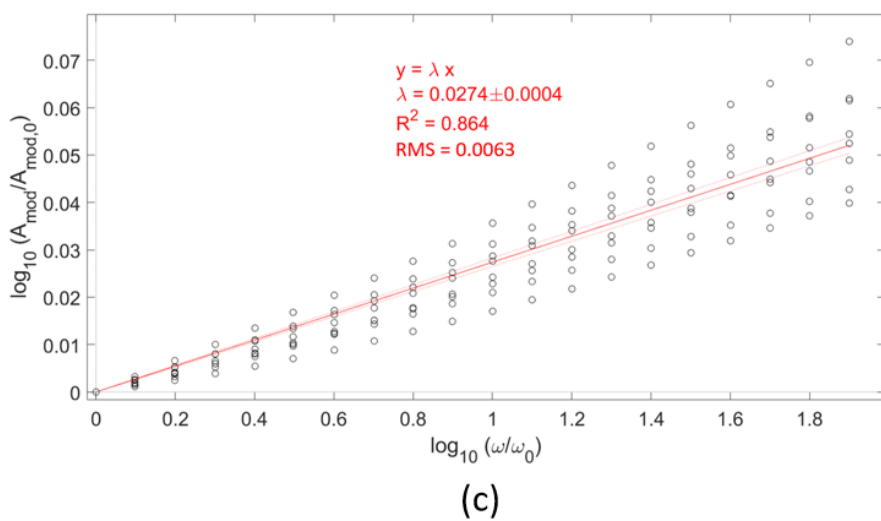
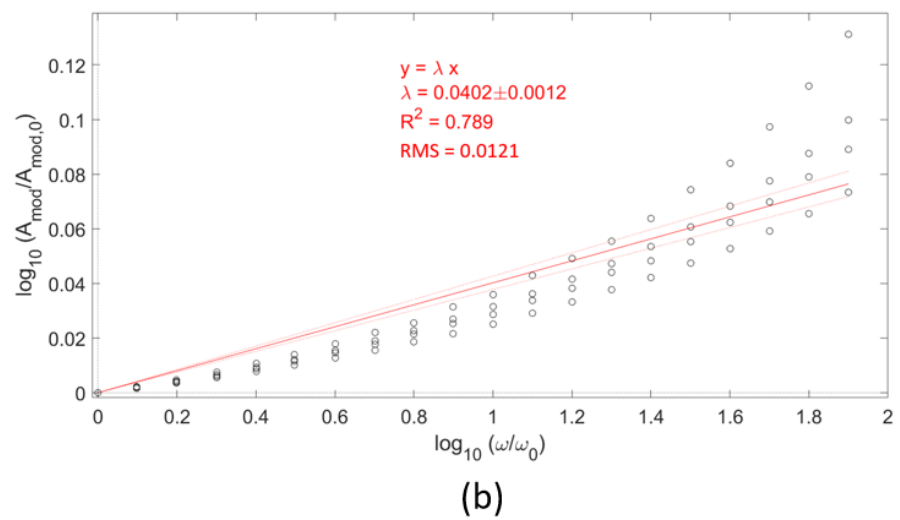
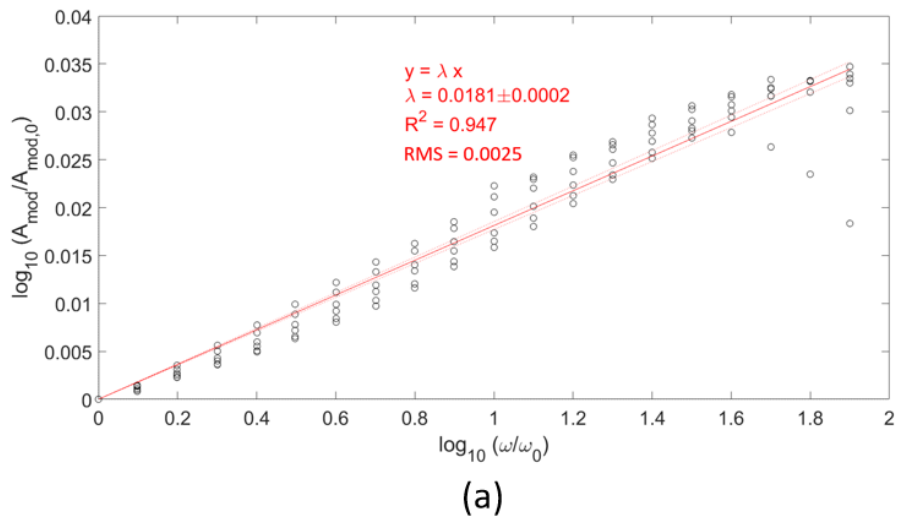


Figure 7.7 - Scalped Summerfield plots as a single data series for coatings in case of: (a) temperature variation; (b) moisture variation; and (c) NaCl concentration variation.

For all the three measurands, the RMS parameters are higher for coatings than for geopolymer cells.

However, by looking at the RMS parameters for coatings, compared to those for geopolymers, it is possible to see that in both cases temperature series shows the lowest scattering, water content series shows the highest non-linearity and NaCl concentration series shows an intermediate scattering. The reasons are broadly the same, but here are the key differences. The non-linearity in case of moisture is more evident here than in the case of geopolymer cells: this could be due to the presence of different ion species. Moreover, from the comparison between Figure 7.7 (b) and Figure 7.7 (c), it is possible to see that a difference between moisture and chloride series can be found in the fact that the second one presents a higher scattering, while the other one presents a higher non linearity of the curves, and a higher scattering only for frequencies near to 100 kHz. These differences may provide another method to distinguish sensor response between chloride and moisture sensing, also in coatings. For this reason, also in the case of coatings as for the geopolymer samples, the frequency chosen for moisture and temperature characterization is 10 kHz, while the frequency chosen for NaCl concentration characterization is 1 kHz.

### 7.4.3. Moisture and temperature preliminary characterisation

#### 7.4.3.1. Sensor response

Figure 7.8 shows plots of sensor response at 10 kHz to a) temperature and b) moisture content. Here the sensor response has been defined as  $\frac{Z_{mod}}{Z_{mod,0}}$ , where  $Z_{mod,0}$  is the modulus of impedance of the sensor at a water content of 78wt% and at a temperature of 20°C. As shown, equations 7.2 and 7.5 provide good non-linear fits to the data also for coatings, as in the case of geopolymer cells described in chapter 5.

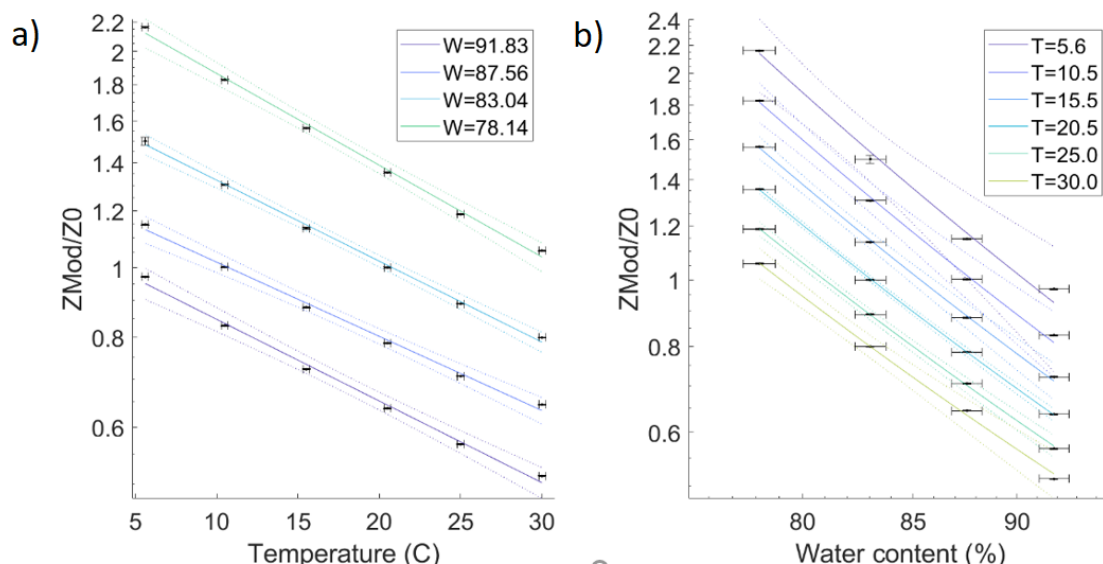


Figure 7.8 - a) Plots of  $Z_{mod}/Z_{mod,0}$  versus temperature for each water content. Non-linear fits use equation 7.2. b) Plots of  $Z_{mod}/Z_{mod,0}$  versus water content for each temperature. Non-linear fits use equation 7.5.

The overall response of the sensor for any general water/temperature combination is better characterized by fitting temperature and moisture simultaneously, using equation 7.6. Figure 7.9 shows the data from Figure 7.8 on a 3D scatterplot. Here the “dryness” of the sample has been defined as the inverse of its moisture content, or  $1/W$ . This allows to fit a surface described by equation 7.6, where the parameters of the fit and their standard errors are given in Table 7.3. This result constitutes the demonstration of the validity of the same calibration equations found for geopolymer cells, also in the case of coatings, despite the differences between the two systems.

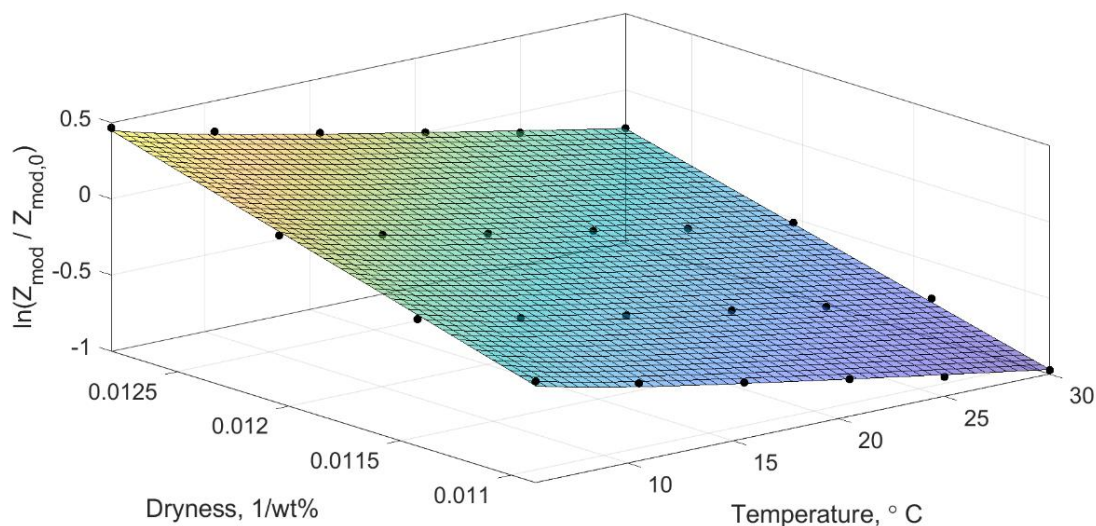


Figure 7.9 – 3D plot of calibration curve for sensor as a function of both moisture and temperature. The surface of best fit shown is described by equation 7.6.

Parameter	$G_6$	$G_7$	$G_8$	$G_9$	$G_{10}$	
Value	-5.081	436.1	0.0002	-2.02	0.511	
95% confidence bounds	Lower	-5.360	412.9	-0.0138	-3.20	0.200
	Upper	-4.802	459.3	0.0142	-0.84	0.822

Table 7.3 - Parameters and their 95% confidence bounds for the plane of best fit, equation 7.6, shown in Figure 7.9.

Using these parameterization constants, the water content of a sample can be ascertained if a second reference sensor (a nearby thermocouple) is used for temperature compensation as:

$$W = \frac{G_8 + G_9 T}{\ln\left(\frac{Z_{mod}}{Z_{mod,0}}\right) - \frac{G_6}{T} - G_7 T - G_{10}} \quad \text{Eq. 7.8}$$

### 7.4.3.2. Precision

Also for geopolymer coating-concrete cells, precision is higher when the conductivity of the sample is high, at high temperatures and moisture contents and is calculated by mapping the impedance fluctuations of the EIS interrogator onto the moisture and temperature axes, using the calibration surface in Figure 7.9 (the calculations are shown in detail in Appendix 1, sections A-1.1 and A-1.2).

The results for coating sensors precision, shown in Table 7.4, demonstrate that, even in worse case conditions, the precision of the sensor is acceptable, at  $\delta W = 0.2 \text{ wt}\%$  and  $\delta T = 0.2 \text{ }^\circ\text{C}$ , similar to the case of the geopolymer sensor. In typical conditions, precisions of  $\delta W = 0.05 \text{ wt}\%$  and  $\delta T = 0.02 \text{ }^\circ\text{C}$  are achievable, which are better than the case of geopolymer sensor. This could be due to the fact that the lower water content investigated for coating sensor calibration is 78wt%, while for geopolymer sensors was 25wt%. The choice of a different range of water contents in the case of coatings preliminary calibration is explained with the fact that in the coating cells the impedance is already high (of the order of 10 kHz) at water saturation ( $W \sim 92\text{wt}\%$ ), and the sensor could stop working at water contents lower than 78wt% and low temperatures.

	Moisture precision $\delta W, \text{ wt}\%$	Temperature precision $\delta T, \text{ }^\circ\text{C}$
<b>Worst case</b>	0.213	0.189
<b>Typical case</b>	0.046	0.019
<b>Best case</b>	0.031	0.002

Table 7.4 - Worst case, best case and typical precisions for moisture and temperature sensing of geopolymer coating-concrete

## 7.4.4. NaCl preliminary characterization

### 7.4.4.1. Sensor response

Figure 7.10 shows the plot of the sensor response at 1 kHz to the NaCl concentrations  $c$  listed in Table 7.1 (plus  $c = 0\text{wt}\%$ ), for saturation water content only ( $\sim 92 \pm 1\text{wt}\%$ ), and at a constant temperature of  $20 \pm 1\text{ }^\circ\text{C}$ . Here the sensor response has been defined as  $\frac{Z_{mod}}{Z_{mod,0}}$ , where  $Z_{mod,0}$  is the modulus of impedance of the sensor before soaking in NaCl solution. Also for coatings, as for geopolymer cells, equation 7.7 provides a good fit to the data, and the data points further from the curve can be attributed to experimental noise in temperature, water content values or chloride concentrations.

The parameters of the fit in Figure 7.10 and their standard errors are given in Table 7.5. By using the parameterization constants in Table 7.5, the NaCl concentration of a geopolymer coating-concrete cell at water content saturation can be ascertained as:

$$c = -\frac{1}{b_5} \cdot \ln\left(\frac{\frac{Z_{mod}}{Z_{mod,0}} - b_6}{b_4}\right) \quad \text{Eq. 7.9}$$

Also in the case of chloride sensing calibration this result confirms the validity of the same calibration equations found for geopolymer cells in chapter 6, and the same saturation of the sensor response is observed for concentrations  $> 5\text{wt}\%$ .

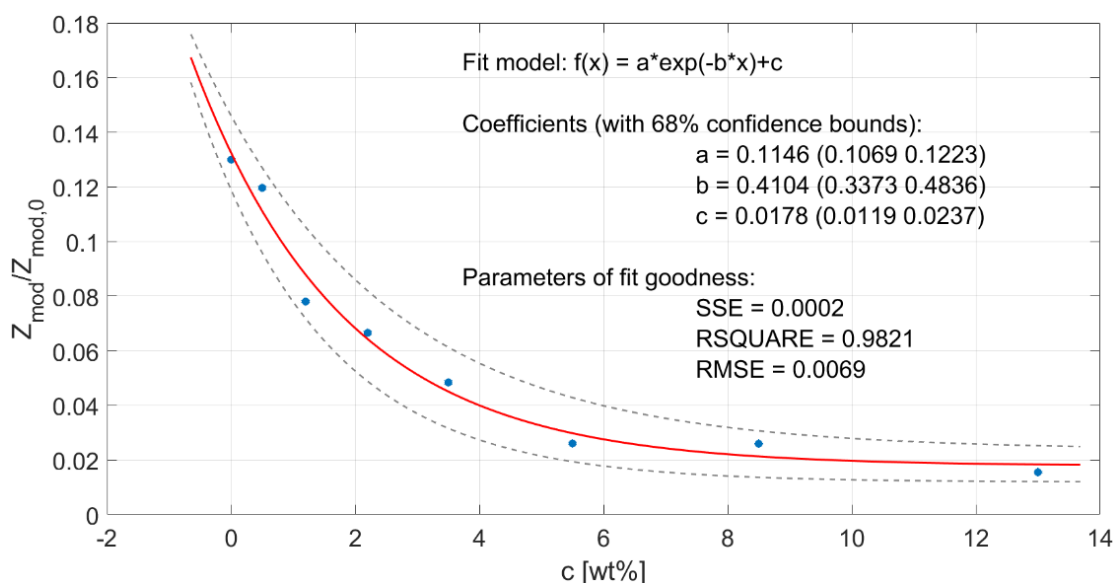


Figure 7.10 - Plot of  $\frac{Z_{mod}}{Z_{mod,0}}$  versus NaCl concentrations  $c$  (Table 7.1) plus  $c = 0\text{wt}\%$ . Non-linear fit uses equation 7.7.

	Parameter	$b_4$	$b_5$	$b_6$
	Value	0.1146	0.1069	0.1223
<b>68% confidence bounds</b>	Lower	0.4104	0.3373	0.4836
	Upper	0.0178	0.0119	0.0237

Table 7.5 - Parameters and their 68% confidence bounds for the line of best fit, equation 7.7, shown in Figure 7.10

#### 7.4.4.2. Precision

As for the case of geopolymer cells, for coatings precision is found by mapping the impedance fluctuations of the EIS interrogator onto the NaCl concentration axes, using the calibration fitting curve shown in Figure 7.10, equation 7.7 and equation 7.9 (by using the method schematically shown in Figure 6.17, and the calculations detailed in Appendix 1, section A-1.3). The precision values for NaCl coating sensors are listed in Table 7.6 The precision is not fixed for all NaCl concentrations: it is worse at high concentrations  $c > 5wt\%$  ( $\delta c = 0.14wt\%$ ) and better at low concentrations  $0wt\% \leq c \leq 1.2wt\%$  ( $\delta c = 0.01wt\%$ ). For intermediate concentration levels  $2.2wt\% \leq c \leq 3.4wt\%$  the typical sensor precision is  $\delta c = 0.05wt\%$ . These results are better than the case of geopolymer sensor cell, and the reason for this could be found in the fact that Figure 7.10 shows less fluctuations in the experimental data points than those observed in Figure 6.15, since all of them were measured at the same water content and at the same time (so the temperature fluctuations are much less than in the experiment where the drying points were investigated, thus implying that each drying point is measured in a different day). Besides, here the highest concentration investigated is  $\sim 12wt\%$ , not  $22wt\%$ .

	$\delta c, wt\%$
<b>Worst case</b>	0.14
<b>Typical case</b>	0.05
<b>Best case</b>	0.01

Table 7.6 - Worst case, best case and typical precisions for NaCl sensing in the range of NaCl concentrations between 0 and 12 wt%, for saturation water content only ( $\sim 92 \pm 1 wt\%$ ), and at a constant temperature of  $20 \pm 1 ^\circ C$ .

## 7.5. Summary and future work

This chapter has provided the first time demonstration of the feasibility of thin geopolymer coatings on concrete as *moisture sensors* at varying of temperature ( $5^\circ C < T < 30^\circ C$ ) and as *chloride sensors* at solution saturation (moisture content  $\sim 92wt\%$ ) and room

temperature (20°C). The validity of the calibration equations for temperature, moisture and NaCl concentration found for geopolymer cells has been demonstrated in the case of coatings, and the same saturation of the sensor response is observed for NaCl concentrations  $> 5\text{wt}\%$ . This constitutes an important scientific result on geopolymer/geopolymer coating sensing capability, and an optimistic result from the point of view of an industrial application of geopolymers as skin sensors for concrete.

Moreover, this chapter has also investigated and extended our knowledge of the electrical conduction mechanism of a system made by geopolymer thin coating on concrete: the proper circuit models which better describe the system with and without NaCl contamination were outlined and validated by experimental evidence. Although further investigations are needed to explain ion dynamics in this combined geopolymer-concrete system, the results of this investigation provide a useful way to discriminate between water and chloride sensing responses, since a different circuit model and different magnitude of impedance have been found to describe the two cases:

- in absence of additional NaCl concentration, the response of the geopolymer coating-concrete system appears to be dominated by concrete, and the geopolymer patch could be considered analogous to a “solder material” rather than a conducting skin: impedance values are of the order of  $\sim 10 - 20 \text{ k}\Omega$ , and the system has been found to be well modelled by a circuit analogous to that used to describe concrete;
- in case of NaCl contamination, on the other hand, the geopolymer coating-concrete system behaves in a similar way to a geopolymer cell: it has been found that it is well modelled by the same circuit model found for the geopolymer cells in chapters 5 and 6, and that the impedance modulus values are  $< 1 \text{ k}\Omega$  (comparable with the values of impedance of the geopolymer cell).

Finally, an estimation of sensor precision demonstrated that: in the worst case conditions investigated in this work (moisture content of 78wt%, temperature at 5-10°C and high NaCl concentrations  $5 \text{ wt}\% < c < 12 \text{ wt}\%$ ), the precision of the coating sensor is acceptable, at  $\delta W = 0.2 \text{ wt}\%$ ,  $\delta T = 0.2 \text{ }^\circ\text{C}$ , and  $\delta c = 0.14\text{wt}\%$ , and in typical conditions (moisture content of 83-87wt%, temperatures 15-25°C and NaCl concentrations  $2.2\text{wt}\% \leq c \leq 3.4\text{wt}\%$ ) precisions of  $\delta W = 0.05 \text{ wt}\%$ ,  $\delta T = 0.02 \text{ }^\circ\text{C}$  and  $\delta c = 0.05\text{wt}\%$  are achievable. However, it must be noted that, at difference of the case of geopolymer cell system calibration, for coatings the lowest moisture content and the highest NaCl concentration

investigated were  $W = 78\text{wt}\%$  and  $c = 12\text{wt}\%$ . Future work will need to demonstrate the feasibility of the coating sensor also for moisture contents below  $78\text{wt}\%$ . Besides, future work could consider also NaCl concentrations beyond  $12\text{wt}\%$ , in order to evaluate the formation of efflorescence on the system surface and the influence that this might have on its sensing function.

Moreover, future work will need also to conduct a more complete characterisation of the coating system: (a) characterise the coating system NaCl sensing response also at varying of moisture content and temperature; (b) evaluate the sensing performance of the system also in terms of repeatability and sensor drift/stability over 20 minutes or longer measurement times; (c) evaluate sensor precision also for concentrations  $>12\text{wt}\%$  and moisture contents below  $78\text{wt}\%$ .

## References

- [1] F. Rajabipour, J. Weiss, and D. M. Abraham, "Insitu electrical conductivity measurements to assess moisture and ionic transport in concrete (A discussion of critical features that influence the measurements)," in *Proceedings of the International RILEM Symposium on Concrete Science and Engineering: A Tribute to Arnon Bentur*, 2004.
- [2] N. Van Meurs, "Temperature dependence of the conductivity of electrolyte solutions," *Nature*, vol. 182, p. 1532, 1958.
- [3] K. Brantervik, A. Berg, G. Niklasson, B. Hedberg, and L.-O. Nilsson, "Percolation effects in the electrical conductivity of porous cement mortar," *EPL (Europhysics Letters)*, vol. 13, p. 549, 1990.
- [4] M. Saleem, M. Shameem, S. Hussain, and M. Maslehuddin, "Effect of moisture, chloride and sulphate contamination on the electrical resistivity of Portland cement concrete," *Construction and Building Materials*, vol. 10, pp. 209-214, 1996.
- [5] M. Fares, G. Villain, S. Bonnet, S. P. Lopes, B. Thauvin, and M. Thiery, "Determining chloride content profiles in concrete using an electrical resistivity tomography device," *Cement and Concrete Composites*, vol. 94, pp. 315-326, 2018.
- [6] G. Song, "Equivalent circuit model for AC electrochemical impedance spectroscopy of concrete," *Cement and concrete research*, vol. 30, pp. 1723-1730, 2000.
- [7] K. Funke and R. D. Banhatti, "Ionic motion in materials with disordered structures," *Solid State Ionics*, vol. 177, pp. 1551-1557, 2006.

## 8. CONCLUSIONS AND FUTURE WORK

This thesis has outlined the development of a self-sensing geopolymer repair technology based on low-calcium fly ash geopolymers, cured at 20°C and 95% Relative Humidity. The geopolymers developed can:

1. be cured in ambient conditions without additives, resulting in a non-structural repair for concrete;
2. act as stand-alone moisture, NaCl concentration, and temperature sensors;
3. act as coatings for concrete, monitoring the same measurands.

All three of these items are first-time demonstrations in their own right.

Calibration of the sensing system (points 2 and 3) was conducted in a steady-state configuration (stabilised and homogeneous temperature, water content and NaCl concentration for each calibration point). The investigation of the behaviour of the system in a dynamic regime is left to future investigation. This work has achieved its aim of demonstrating sensing feasibility.

The second aim was to develop ambient cured, additive-free geopolymer coatings with good integrity and suitable thermal and mechanical properties (point 1). This also required a novel approach. Contrary to previous studies, no additives were used (i.e. standard sand,

polypropylene (PP) fibers)[1-10] to improve properties or reduce the risk of cracking. Instead, changes to material composition and mixing time allowed for the demonstration of non-structural repairs, protective coatings, and an analogue “solder material” for connecting electrodes to concrete. Some additives could be incorporated in future to produce higher performance materials (e.g. structural repairs).

The industrial and scientific relevance of this thesis is outlined in Section 8.1. Section 8.2 outlines future scientific work required, and section 8.3 outlines other potential applications for the technology.

## 8.1. Industrial and scientific relevance

This work presented in this thesis provided important scientific contributions and demonstrated a promising technology for retrofitted concrete repairs, rehabilitation and sensing in a nuclear context. The following subsections present a summary of the industry relevance of the work carried out (subsection 8.1.1) and the main scientific findings and contributions (subsection 8.1.2).

### 8.1.1. Industry relevance of the work

Corrosion of steel rebars is the main cause of reinforced concrete degradation. In coastal zones, this is triggered by the interconnected role of moisture and chloride. Maintenance actions informed by monitoring are particularly needed for safety critical nuclear concrete structures such as nuclear stores. These are intended to last for 100 years, and some (like the SPRS store at Sellafield) make use of passive cooling systems which prevent the use of air filters. This leads to a lack of control over the ingress of sea water-spray which can condense onto concrete surfaces. In such a context, the need for moisture and chloride monitoring technologies is clear.

As outlined in chapter 2, environmental monitoring in UK nuclear store buildings makes use of relative humidity sensors and tokens for surface salt deposition measurements. There are no sensors employed for measuring moisture and chloride contents in concrete. The reason for this is found in the challenge of finding a suitable device to be applied in a nuclear context:

- Existing sensors need to be embedded into concrete. Drilling, and even embedding technologies into nuclear structures during construction, are viewed with scepticism in an industry which follows strict design requirements for safety.
- Radioactive packages inside the store are a source of heat and highly ionising radiation. Materials which produce  $\gamma$ -products under interactions with radiation are prohibited, and radiation resistant materials are preferred.

The sensor technology outlined in this thesis meets these requirements, as:

- (i) it offers measurements of self- or concrete-substrate- moisture and chloride levels;
- (ii) is non-invasive (electrodes are applied to another highly conductive medium, instead of directly onto concrete);
- (iii) the material itself has a good radiation resistance, and the lack of additives ensure this is maintained;
- (iv) it can be conveniently deployed in challenging conditions: which for this material means the relatively cool and humid ducts and air corridors of the stores.

There are several further advantages that make this an attractive technology across other applications, even in non-nuclear sectors:

- (v) the sensor patch also acts as a non-structural repair or protective layer;
- (vi) the material itself is cheap: the cost per sensor could be less than £100;
- (vii) there are minimal manufacturing and deployment steps required (no thermal curing, no fly ash grinding, no additives);
- (viii) patches and samples can be shaped when uncured and applied to structures of any shape and size;
- (ix) the patches could act as skin sensors to offer distributing sensing with the use of tomography over a patch

The solution could be mapped to applications in other sectors, and the technology could also be applied for the monitoring and protection of newly cast concrete structures.

### 8.1.2. Main scientific findings

The most important and novel findings of this thesis can be briefly summarised in the following points:

- Understanding the curing regime of geopolymers can be used to develop ambient-curable, thin (1 mm) geopolymer coatings for old/new-cast concrete. These coatings demonstrate British-European standard non-structural repair properties without additives or additional processes. This makes them more affordable and suitable to be applied within a nuclear context.
- Water-transport plays a critical role in coating integrity during curing, especially during geopolymerisation reaction processes. Curing geopolymer binders/coatings at high relative humidities (95%) can lead to efflorescence which can be partly tackled by adjusting mix designs.
- Even non-treated concrete substrate surfaces lead to good bond strength (>0.8 MPa) with the geopolymer coatings, thus making the technology even more affordable and easy to apply.
- Geopolymers can be used to monitor moisture and NaCl content via changes in their electrical impedance. Typical precisions for geopolymer cells were 0.1 wt% for moisture, and 0.8 wt% for NaCl concentration. Geopolymer sensors show particularly good sensor repeatability between 0.2 wt% and 1.5 wt% moisture, and a sensor drift of < 3% over a 20 min period.
- NaCl contamination could be measured for > 0.2wt% for patches on concrete: electrochemical impedance spectroscopy has demonstrated that the conduction response of thin (1 mm) geopolymer coating systems may be dominated by the concrete or by the geopolymer patch depending on the presence of NaCl contamination.

- Low temperatures, low moisture levels and NaCl concentrations > 5wt% lead to a worse precision for both geopolymer cells and coatings. The saturation of sensor response for NaCl concentrations was > 5wt%.
- The application of electrochemical impedance spectroscopy has demonstrated that the variation of temperature, moisture and NaCl concentration in both geopolymer and coating systems produce a different degree of linearity in the Summerfield scaled plot: this demonstrates that the three different parameters produce different changes in ionic conduction, conforming to currently understood theories of ionic conduction.

The following subsections summarise the main findings for each topic in more granular detail.

#### 8.1.2.1. Geopolymer coating integrity

This work, through a process of trial and error, demonstrated that ambient cured low calcium fly ash geopolymer coatings for concrete can be obtained by using:

- a ratio between the the liquid alkaline solution (L) and the solid fly ash (S)  $\frac{L}{S} = 0.5$ , and an alkaline solution comprised of sodium hydroxide (SH) and sodium silicate (SS) with ratio  $\frac{SH}{SS} = 0.4$ ;
- **low thickness** coatings (1 mm) to **reduce shrinkage** (in thin patches, water is more likely to evaporate during the first few hours while the geopolymer is still in a plastic state, and prior to any significant hardening);
- **no additives** (such as plastic fibers);
- **no additional grinding processes** (the fly ash used belongs to category S);
- **a mixing time of ~ 1 hour**, by using an automatic mixer at  $500 \text{ min}^{-1}$  (this has been found to allow geopolymer coatings to overcome water-loss induced cracking and to show an homogeneous surface without voids, bubbles and black dots formed by unreacted fly ash particles, by ensuring that only small extent of fly ash particles is unreacted);

- **a concrete substrate of any age** (it has been found that coating integrity doesn't depend on concrete maturity, thus allowing geopolymer coatings and linings to be applied to newly cast concrete structures, and not only to old structures which need repair);
- **curing them for 30 days at 20 °C and 95% Relative Humidity** (while they take almost one month to cure, they are touch-dry within one day).

It was also shown that for low-temperature, humid curing (above 70% RH) and prolonged storage conditions, geopolymer coatings on concrete showed, in most cases, evidence of efflorescence: white crystals on the surface 3-8 weeks after application and curing stemming from the crystallisation of excess alkaline solution. This presents another symptom of moisture transport within the sample, mainly due to the drying process. Indeed, one of the most important considerations coming from this study is the interaction between water-transport (a physical process) and the geopolymerisation reaction (a chemical process). This underpins coating integrity, efflorescence and strength gain.

#### 8.1.2.2. Geopolymer coatings as non-structural repairs for concrete

The evolution of strength is notably slower for ambient cured than for thermally cured geopolymers. Despite this, the mechanical properties tested for the sample specimens in this work could allow the material (vibrated and non-vibrated) to be classified as a **non-structural repair** (class R1 and R2 respectively) according to the standard BS EN 1504-3:2005 [11]. The following points summarise the main findings of this investigation.

- The **28 day compressive strength** for **non-vibrated** binders showed values which make them potential non-structural repairs of class R1 ( $\geq 10$  MPa), while **vibrated** binders demonstrated a 28 days compressive strength between class R1 ( $\geq 10$  MPa) and class R2 ( $\geq 15$  MPa) for non-structural repairs. These results showed that air bubbles are a limiting strength factor on a non-vibrated mix. It must be noted that there was a growing degree of strength variability in samples as they cure, and so these preliminary results need to be taken with caution, also because the measurement was not strictly complying with the standard BS EN 12190 for compressive strength testing methods for repair materials.
- The results for the **bond strength test**, conducted on vibrated geopolymer coatings applied onto **un-treated concrete** surfaces show a slightly higher bond strength

value ( $2.30 \pm 0.39$  MPa) than those applied onto **roughened concrete** surfaces ( $1.82 \pm 0.67$  MPa). This can be due to the process of roughening which contributes to smooth the depths of the holes in the surface, so that it is likely that less geopolymer binder can enter the holes lowering the bonding strength of a scoured concrete surface. However, looking at the errors, the two values are comparable. This implies that the patches can be likely applied directly onto concrete, without additional treatment.

- The **bond strength values for scoured and un-scoured concretes** were found to be both  $\geq 0.8$  MPa, which is the requirement to classify a material as a non-structural repair. This preliminary result constitutes a promising result for the geopolymer coatings, especially since they are ambient cured and very thin (1 mm). However, it must be said that the accuracy of the instrument used for the bond strength measurement (Elcometer) is  $\pm 15\%$ , much worse than that ( $\pm 2\%$ ) recommended by the standard BS EN 1542:1999 on the pull-out testing method for repair materials onto concrete. Despite this, the method chosen in this work is a manual, convenient and simple method, more suitable to test thin coatings and to provide a preliminary evaluation of the in-service performance of the coatings for the bond strength than the most of the other more accurate methods. This means that also in this case the results must be taken with caution and a further future work is needed.

Since the aim of this work was to demonstrate a non-structural repair, for the time being, measurements of elastic modulus were not required, according to BS EN 1504-3:2005 [11]. However, measurements were conducted to give an idea of the **coefficient of thermal expansion**,  $\alpha$ , between  $T = 20$  °C and  $T = 2$  °C, which is a representative range of the storage facility temperatures in ducts and air inlets (as internal reports for temperature and RH monthly measurements in the SPRS store in Sellafield show). The value found was  $\alpha = 10.6 \cdot 10^{-6}$ , which is in accordance with the range of variation of the coefficient of thermal expansion for geopolymer materials (from  $4 \cdot 10^{-6}$  to  $25 \cdot 10^{-6} K^{-1}$ , which comprises the value of the coefficient of thermal expansion for concrete:  $13 \cdot 10^{-6} - 14 \cdot 10^{-6} K^{-1}$ ).

### 8.1.2.3. Geopolymers as stand-alone moisture and temperature sensors

A major outcome of this work was the **first time demonstration and characterization of ambient cured fly ash geopolymers as moisture sensors**:

- it has been demonstrated that low calcium fly ash geopolymer materials **can be used to sense moisture** and temperature changes with typical precisions respectively  $\delta W = 0.1 \text{ wt\%}$  and  $\delta T = 0.1 \text{ }^\circ\text{C}$  in the water content range 80 – 25 wt% and in the temperature range 5 – 30 °C;
- a **calibration equation for temperature and moisture** has been found, from which moisture values can be ascertained when a second sensor for temperature compensation is present;
- **repeatability in moisture measurement** was 0.2 – 1.5 wt%, this can be linked to the fact that **ion leaching was minimal** during washing cycles;
- **sensor drift** is usually negative, and worst at high temperatures and low moisture contents, but is **always < 3%** over a 20 min period.

All of these results are encouraging for the long term performance of the sensor, and constitute both an important scientific finding and a promising result for industrial application.

#### 8.1.2.4. Geopolymers as stand-alone NaCl concentration sensors

The work also outlined a **first-time demonstration of geopolymer NaCl concentration sensors**:

- Changes in NaCl concentration inside the pore solution of the geopolymer cell demonstrated measurable changes in impedance with an **exponential dependence**;
- Sensor response **saturated for internal NaCl concentrations beyond 5wt%**;
- The **most sensitive region** for NaCl concentration sensing was found **in the range 0.2 – 5 wt%**, with **typical precisions of  $\delta c \sim 0.8 \text{ wt\%}$** , while the worst case precision  $\delta c \sim 5.8 \text{ wt\%}$  corresponds to high concentration values ( $c \geq 10 \text{ wt\%}$ ), and the best case precision corresponds to concentration values  $0.2 < c < 1 \text{ wt\%}$ .

Sensor calibration used actual internal NaCl concentrations covering the range 0 wt% – 22wt% which correspond to all the possible chloride contamination values and water contents in the range of those found in nuclear storage structures, such as SPRS. The results

for high concentrations led to the hypothesis that some change occurs in the physical mechanisms behind geopolymer ion conductivity when ion density in the solution is high, thus providing the saturation of sensor response for concentrations  $>5\text{wt}\%$ .

#### 8.1.2.5. Self-sensing coatings for moisture, NaCl

When used as coatings, geopolymers can still be used to detect moisture and chloride levels in concrete:

- thin (1 mm) **geopolymer coatings can act as moisture sensors** between 92wt% and 78wt% and at temperatures ( $5^{\circ}\text{C} \leq T \leq 30^{\circ}\text{C}$ );
- **they can also act as chloride sensors** (demonstrated for moisture contents of  $\sim 92\text{wt}\%$ , and at room temperature,  $20^{\circ}\text{C}$ ).
- **Calibration equations** for temperature, moisture and NaCl concentration **can be mapped from stand-alone cells to coatings** (although parameters do differ);
- the same **saturation of the sensor response** observed for geopolymer cells is observed **for coating cells at NaCl concentrations  $> 5\text{wt}\%$** .
- **typical precisions** of  $\delta W = 0.05 \text{ wt}\%$ ,  $\delta T = 0.02 \text{ }^{\circ}\text{C}$  and  $\delta c = 0.05\text{wt}\%$ , were found respectively for moisture content of 83-87wt%, temperatures 15-25°C and NaCl concentrations  $2.2\text{wt}\% \leq c \leq 3.4\text{wt}\%$  ;
- **electrochemical impedance spectroscopy** has provided a **useful way to discriminate between water and chloride sensing responses**: a different circuit model and different magnitude of impedance have been found to describe the two cases (higher impedance values were found in the case of geopolymer coatings with no NaCl contamination; NaCl contamination makes the 1mm thin geopolymer coating the dominating conducting medium, while absence of NaCl contamination shows conduction dominated by concrete).

These results constitute an important scientific result, and an optimistic result from the point of view of the industrial application of geopolymers as skin sensors for concrete.

## 8.2. Future work

Avenues for future work are outlined in the following tables: Table 8.1 (geopolymer coating integrity); Table 8.2 (geopolymer coatings as non-structural repairs for concrete); Table 8.3 (geopolymers as moisture and temperature sensors); Table 8.4 (geopolymers as NaCl concentration sensors); Table 8.5 (geopolymer coatings onto concrete as moisture, temperature and NaCl sensors).

Of these numerous items of future work, investigation of the following should be prioritised:

- The sensor response during dynamic changes in measurands should be investigated to establish the response time and its associated impact on errors.
- The behaviour of the geopolymer cells and coatings under gamma irradiation at the levels present in the radioactive storage area of concrete nuclear structures: impacts on the mechanical and sensing properties should be investigated.
- Characterization of the sensor response in terms of changes in impedance *phase* or overall *frequency dependence*. Indeed, these carry information about the capacitive behaviour of the sensor. If, for example, moisture and temperature have different impacts on the impedance at different frequencies, then this could be used to distinguish between the two without a second reference sensor.
- Development of lower cost interrogators that are compatible with wireless systems. The EIS device employed in this work is a piece of lab equipment: it provides highly accurate and detailed measurements of impedance spectra, but it is not suitable for deploying in field conditions (nor is it necessarily required – a simpler, low power device for measuring impedance may be adequate).
- Alternative geopolymer sources: fly ash geopolymers were chosen because they show: (i) a high workability (useful for coating applications); and (ii) a high durability and strength. Much of the work demonstrated could be mapped over to other geopolymer types (e.g. metakaolin). This would require further study, but could be useful in regions which have a faltering fly ash supply due to the shrinkage of the coal energy industry.

Geopolymer coating integrity
<ul style="list-style-type: none"><li>• Solutions to the issues of efflorescence in humid environments.</li><li>• Explore the influence of a concrete substrate water saturation.</li><li>• Test the durability under exposure to a variety of environmental conditions.</li><li>• Define methods for studying the relationship between coating thickness, shrinkage and integrity after prolonged geopolymer mixing.</li></ul>

Table 8.1 – Future work points in the reserce field of ‘Geopolymer coating integrity’.

Geopolymer coatings as non-structural repairs for concrete
<ul style="list-style-type: none"><li>• Assess compressive strength of the geopolymer binders strictly according to the relative standard.</li><li>• Test the bond strength and thermal expansion also for non-vibrated geopolymer binders.</li><li>• Test all the properties required by the standard BS EN 1504-3:2005 [11] not analysed in this work, for the assessment of non-structural repairs, for vibrated and not vibrated binders.</li></ul>

Table 8.2 - Future work points in the reserce field of ‘Geopolymer coatings as non-structural repairs for concrete’.

Geopolymers as moisture and temperature sensors
<ul style="list-style-type: none"><li>• Characterize the response time of the sensor.</li><li>• Further investigations to explore the behaviour of the sensing system in a dynamic state.</li><li>• Characterise the response of the sensor also for strain.</li><li>• Investigate field deployment methods.</li><li>• Explicitly demonstrate that moisture can be ascertained independently of temperature when a second reference sensor (a nearby thermocouple) is used for temperature compensation.</li></ul>

Table 8.3 - Future work points in the reserce field of ‘Geopolymers as moisture and temperature sensors’.

Geopolymers as NaCl concentration sensors
<ul style="list-style-type: none"><li>• A more complete calibration of the sensing system, which requires: (a) a temperature calibration for each NaCl concentration; (b) a strain characterization of the response of the sensor; (c) a higher measurement time for each impedance measurement (about 20 minutes) which would allow an</li></ul>

evaluation of sensor stability and drift; (d) a repeatability evaluation; and (e) a response time characterization of the sensor.

- Explore system dynamics: how the chloride concentration inside the sample changes as the sensor is exposed to chloride outside of the sample, and how this affects drift in the sensor response.
- An environmental chamber is preferred to the faraday cage for a future sensor cell characterization, in order to reduce fluctuations in temperature values.
- Explore the solutions to overcome sensor saturation for NaCl concentrations > 5wt%.
- Measure the degree of efflorescence of dry geopolymer cells after saturation at NaCl concentrations > 5wt%, and how this affects the sensing function and the sensor response saturation beyond 5wt%.
- Explicitly demonstrate that NaCl can be ascertained independently of water content when a second reference sensor is used for moisture compensation.

Table 8.4 - Future work points in the reserch field of 'Geopolymers as NaCl concentration sensors'.

#### Geopolymer coatings onto concrete as moisture, temperature and NaCl sensors

- Further investigations to explain ion dynamics in this combined geopolymer-concrete system.
- Further investigations to explore the behaviour of the sensing system in a dynamic state (water/NaCl solution diffusion and transport).
- Demonstrate the feasibility of the coating sensor also for moisture contents below 78wt%.
- Explore solutions to reduce the impedance values of the system at lower moisture contents.
- Investigate also NaCl concentrations beyond 13wt%, in order to evaluate the formation of efflorescence on the system (geopolymer + concrete) surface and the influence that this might have on its sensing function beyond 5wt%.
- A more complete characterisation of the coating system: (a) characterise the coating system NaCl sensing response also at variating of moisture content and temperature; (b) characterise the response of the sensor also for strain; (c) evaluate the sensing performance of the system also in terms of repeatability and sensor drift/stability over 20 minutes or longer measurement times; (d) evaluate sensor precision also for concentrations >13wt% and moisture contents below 78wt%.
- Investigate the sensor response for geopolymer coatings applied to reinforced concrete specimens.

- |   |
|---|
| <ul style="list-style-type: none"><li>• Investigate the sensor response, the conduction mechanisms and the circuit model for the system made by a geopolymer coating applied to a concrete surface belonging to a large concrete structure (i.e. reinforced concrete wall).</li></ul> |
|---|

Table 8.5 - Future work points in the reserce field of 'Geopolymer coatings onto concrete as moisture, temperature and NaCl sensors'.

### 8.3. Closing remarks on future direction of the technology

The self-sensing geopolymers described in this thesis could be deployed outside of the nuclear industry for monitoring all manner of utilised or decommissioned structures in corrosive environments, from bridges, to dams, to oil platforms and offshore wind turbine foundations. The technology supports increased knowledge of reinforced concrete degradation, and so could allow maintenance to become more proactive, and reduce the risk of tragic events such as the recent collapse of the Morandi bridge in Genoa (August 2018, due to the combined action of heavy traffic and an aggressive environment [12]).

To achieve this, the technology needs to be coupled with a suitable deployment method, and a means of acquiring the sensor data. In closing, the following two subsections very briefly propose some promising deployment and interrogation methods for the technology outlined in this thesis. These are considerations which will require more thought as the technology moves towards field deployment: they will underpin how and where the technology is used, and how it changes the risk landscape for the end user. This will affect the true costs of the technology, and its likelihood of being adopted.

#### 8.3.1. Deployment methods

Modern sensors and self-sensing materials themselves are becoming increasingly affordable, but their deployment poses significant labour costs, and risks to productivity and personnel. Sensor repeatability and robustness are also largely dependent on the quality of workmanship during installation.

Work carried out in this thesis has characterised a manually deployed technology. Recent work [13, 14] has focused on the development of remote deployment methods for geopolymers using robotically controlled 3D printing, and spray coating. This deployment

method could allow sensor-repairs to be more conveniently deployed in some of nuclear's harsh and remote environments, without risk to personnel.

Robotic deployment methods could offer the additional benefits of [14]: improving the repeatability of patch deposition (repeatability of repair and sensor performance), reducing labour costs, and providing fixed marginal costs per deployed sensor [15].

Stand-alone geopolymer cells could also be prefabricated and deployed in environments as tokens, acting as 'sentinel sensors'. Here, the small size and low weight (50 g) of the sensors come into play, as these allows the technology to be remotely deployed using drones or remotely piloted probes.

### 8.3.2. Interrogation and data transfer systems

For most applications outside of the nuclear industry, geopolymer moisture and chloride sensors could be interrogated using a wireless sensor network. In a nuclear environment, however, fully wireless systems are typically not permitted for security reasons.

A viable alternative in this case could be to use a computer station in a radiation free environment inside the structure, where the data can be sent through a wireless (Wi-Fi or Li-Fi) system transmitting inside the same structure, or simply by using short length shielded cables.

Another solution could be to deploy the technology and then only intermittently interrogate it using a remotely piloted robot, probe or drone: in this way, the geopolymer would provide a continuous repair, but not continuous monitoring, instead providing a means of non-destructively taking point measurements of chloride and moisture levels. Taking this route would eliminate some of the need to study the dynamic sensor response of the system. It would also reduce the exposure of sensitive electronics to radiation (the geopolymers themselves may be radiation hard, but the interrogating electronics is not).

## References

- [1] Z. Zhang, X. Yao, and H. Zhu, "Potential application of geopolymers as protection coatings for marine concrete I. Basic properties," *Applied Clay Science*, vol. 49, pp. 1-6, 2010.
- [2] Z. Zhang, X. Yao, and H. Wang, "Potential application of geopolymers as protection coatings for marine concrete III. Field experiment," *Applied Clay Science*, vol. 67, pp. 57-60, 2012.
- [3] Z. Zhang, X. Yao, and H. Zhu, "Potential application of geopolymers as protection coatings for marine concrete: II. Microstructure and anticorrosion mechanism," *Applied clay science*, vol. 49, pp. 7-12, 2010.
- [4] G. Fang, H. Bahrami, and M. Zhang, "Mechanisms of autogenous shrinkage of alkali-activated fly ash-slag pastes cured at ambient temperature within 24 h," *Construction and Building Materials*, vol. 171, pp. 377-387, 2018.
- [5] F. Puertas, S. Martínez-Ramírez, S. Alonso, and T. Vazquez, "Alkali-activated fly ash/slag cements: strength behaviour and hydration products," *Cement and Concrete Research*, vol. 30, pp. 1625-1632, 2000.
- [6] S. A. Bernal, J. L. Provis, B. Walkley, R. San Nicolas, J. D. Gehman, D. G. Brice, A. R. Kilcullen, P. Duxson, and J. S. van Deventer, "Gel nanostructure in alkali-activated binders based on slag and fly ash, and effects of accelerated carbonation," *Cement and Concrete Research*, vol. 53, pp. 127-144, 2013.
- [7] P. Nath and P. K. Sarker, "Effect of GGBFS on setting, workability and early strength properties of fly ash geopolymer concrete cured in ambient condition," *Construction and Building Materials*, vol. 66, pp. 163-171, 2014.
- [8] P. S. Deb, P. Nath, and P. K. Sarker, "The effects of ground granulated blast-furnace slag blending with fly ash and activator content on the workability and strength properties of geopolymer concrete cured at ambient temperature," *Materials & Design (1980-2015)*, vol. 62, pp. 32-39, 2014.
- [9] G. Fang, W. K. Ho, W. Tu, and M. Zhang, "Workability and mechanical properties of alkali-activated fly ash-slag concrete cured at ambient temperature," *Construction and Building Materials*, vol. 172, pp. 476-487, 2018.
- [10] P. S. Deb, P. Nath, and P. K. Sarker, "Drying shrinkage of slag blended fly ash geopolymer concrete cured at room temperature," *Procedia Engineering*, vol. 125, pp. 594-600, 2015.
- [11] B. EN, "1504-3 (2005) Products and systems for the protection and repair of concrete structures. Definitions, requirements, quality control and evaluation of conformity. Structural and non-structural repair," *British Standard Institute*.
- [12] R. Morandi, "The long-term behaviour of viaducts subjected to heavy traffic and situated in an aggressive environment: The viaduct on the Polcevera in Genoa," *IABSE reports of the working commissions*, vol. 32, pp. 170-180, 1979.
- [13] J. McAlorum, M. PERRY, C. VLACHAKIS, and L. BIONDI, "Autonomous Application of Smart Cement Sensor-repairs," *Structural Health Monitoring 2019*, 2019.
- [14] C. Vlachakis, M. Perry, L. Biondi, and J. McAlorum, "3D printed temperature-sensing repairs for concrete structures," *Additive Manufacturing*, p. 101238, 2020.
- [15] A. Durelli, "Experimental strain and stress analysis of solid propellant rocket motors," in *Mechanics and Chemistry of Solid propellants*, ed: Elsevier, 1967, pp. 381-442.

# APPENDICES

## Appendix 1 – Mathematical formulation of sensor precision

The precision characterises the noise in the sensor measurement [1]: it is the spread of the data (a set of constant measurements taken with a device) around the average value. This spread (the precision) can be characterised by the standard deviation, and it's due to noise during the measurement. Precision must always be larger or equal to the resolution (the smallest possible change in the measurand that the device can possibly measure). Most systems have noise, and this noise (i.e. data spread) > resolution. If it was possible to take away all the sources of noise in the system, then precision = resolution. In the sensor system characterised in this work there is some noise, and for this reason an evaluation of precision has been done for moisture, temperature and NaCl measurements. The following sub-sections outlines the method of calculating the precision of the geopolymer sensor cells in the case of the three measurands. Since geopolymer-coating sensor cells obey to the same calibration equations (although parameters do differ), the same methods apply also to coating sensors.

### A-1.1 Calculating sensor precision for moisture

The sensor response values were defined by means of a variable:

$$R = \ln\left(\frac{Z_{mod}}{Z_{mod,0}}\right) \quad \text{Eq. A1}$$

The error in  $R$  was found using the errors in  $Z_{mod}$ ,  $Error\_Z_{mod}$ , and  $Z_{mod,0}$ ,  $Error\_Z_{mod,0}$ , by means on the error propagation formula:

$$Error_R = R \cdot \sqrt{\left(\frac{Error_{Z_{mod}}}{Z_{mod}}\right)^2 + \left(\frac{Error_{Z_{mod,0}}}{Z_{mod,0}}\right)^2} \quad \text{Eq. A2}$$

Equation 5.17 was used to calculate:

1. the expected water content value,  $W$ , for each  $R$  and temperature value  $T$ ;
2. The upper bound for water content,  $W_{up}$ , for each  $R + Error_R$  value and temperature value  $T$ ;

3. The lower bound for water content,  $W_{down}$ , for each  $R - Error_R$  value and temperature value T.

Then the expected value of moisture was subtracted from the upper and lower bounds to get the  $+/-$  errors in water content:

$$(1) Upper_{Error_w} = W_{up} - W \quad \text{Eq. A3}$$

$$(2) Lower_{Error_w} = W_{down} - W$$

As typical of nonlinearity, the  $+/-$  errors are not exactly the same, but the difference between them is so small that it is possible to assume that:

$$Upper_{Error_w} \sim Lower_{Error_w} \quad \text{Eq. A4}$$

The moisture error can be stated as the mean value of (1) and (2):

$$Mean\_Error_w = \frac{Upper_{Error_w} + abs(Lower_{Error_w})}{2} \quad \text{Eq. A5}$$

For the moisture/temperature calibration case, because the sensor dependence is non-linear, moisture error is not constant, and  $Mean\_Error_w$  is a matrix. The worst case resolution is for (dry, cold samples), and the best resolutions are for (wet, warm samples). These values for the typical, best and worst case precision are showed in the first column of Table 5.5, in section 5.5.5 of chapter 5. They are obtained from the following calculations respectively:

$$Typical\_w\_precision = Mean(Mean(Mean\_Error_w)) \quad \text{Eq. A6}$$

$$Best\_w\_precision = Min(Min(Mean\_Error_w))$$

$$Worst\_w\_precision = Max(Max(Mean\_Error_w))$$

where the mean (typical case), min (best case) and max (worst case) of the matrix of moisture errors,  $Mean\_Error_w$ , is found by doing the mean, min and max respectively of the mean, min and max of each column of the matrix.

A-1.2 Calculating sensor precision for temperature

The calculations of precision in the case of temperature is a bit more complicated because of the form of equation 5.15.

The sensor response values and their errors were defined, also here, by means of equation A1 and equation A2 respectively.

If equation 5.15 is rearranged as:

$$\left(G_2 + G_4 \cdot \frac{1}{w}\right) \cdot T + \frac{G_1}{T} + \left(\frac{G_3}{w} + G_5 - \ln(R)\right) = 0 \quad \text{Eq. A7}$$

it can be re-written as:

$$A \cdot T + \frac{B}{T} + C = 0 \quad \text{Eq. A8}$$

where  $A = \left(G_2 + G_4 \cdot \frac{1}{w}\right)$ ,  $B = G_1$ ,  $C = \left(\frac{G_3}{w} + G_5 - \ln(R)\right)$ .

Equation A8 has two solutions:

$$1. \quad T = \frac{-\sqrt{C^2 - 4 \cdot A \cdot B} - C}{2A} \quad \text{Eq. A9}$$

$$2. \quad T = \frac{\sqrt{C^2 - 4 \cdot A \cdot B} - C}{2A}$$

which produce identical predictions for temperature.

As it was done for water content above, by using  $R$ ,  $R + Error_R$ ,  $R - Error_R$  and water content values  $W$  in equation A9, the following expected, upper and lower values respectively are obtained for temperature:  $T$ ,  $T_{up}$ ,  $T_{down}$ .

As for the previous case, the +/- errors in T are defined as:

$$(1) \quad Upper_{Error_T} = T_{up} - T \quad \text{Eq. A10}$$

$$(2) \quad Lower_{Error_T} = T_{down} - T$$

Also in this case, they are similar, and the temperature error can be stated as the mean of (1) and (2):

$$Mean\_Error_T = \frac{Upper\_Error_T + abs(Lower\_Error_T)}{2} \quad \text{Eq. A11}$$

Also in the case of temperature, because the sensor dependence is non-linear, temperature error is not constant, and  $Mean\_Error_T$  is a matrix. The worst case resolution is for (dry, cold samples), and the best resolutions are for (wet, warm samples). These values for the typical, best and worst case precision are showed in the second column of Table 5.5, in section 5.5.5 of chapter 5. As for moisture, for temperature they are obtained from the following calculations respectively:

$$Typical\_T\_precision = Mean(Mean(Mean\_Error_T)) \quad \text{Eq. A12}$$

$$Best\_T\_precision = Min(Min(Mean\_Error_T))$$

$$Worst\_T\_precision = Max(Max(Mean\_Error_T))$$

### A-1.3 Calculating sensor precision for chloride

The sensor response values were defined by means of a variable:

$$R = Z_{modNorm_w}(c) = \frac{\frac{Z_{mod}(W,c)}{Z_{mod,0}}}{\frac{Z_{mod}}{Z_{mod,0_{c=0,interpol}}}}(W) \quad \text{Eq. A13}$$

The error in  $R$  was found using the errors in:

$$Z_{norm} = \frac{Z_{mod}}{Z_{mod,0}}(W, c), \text{ and } Z_{norm\_w} = \frac{Z_{mod}}{Z_{mod,0_{c=0,interpol}}}(W),$$

by means of the error propagation formula:

$$Error_R = R \cdot \sqrt{\left(\frac{Error_{Z_{norm}}}{Z_{norm}}\right)^2 + \left(\frac{Error_{Z_{norm\_w}}}{Z_{norm\_w}}\right)^2} \quad \text{Eq. A14}$$

Equation 6.18 was used to calculate:

1. the expected NaCl internal actual concentration value,  $c$ , for each  $R$  value;

2. The upper bound for NaCl internal actual concentration value,  $c_{up}$ , for each  $R + Error_R$  value;
3. The lower bound for NaCl internal actual concentration value,  $c_{down}$ , for each  $R - Error_R$  value.

Then the expected value of NaCl concentration was subtracted from the upper and lower bounds to get the  $+/-$  errors in NaCl concentration:

$$(1) Upper_{Error_c} = c_{up} - c \quad \text{Eq. A15}$$

$$(2) Lower_{Error_c} = c_{down} - c$$

As typical of nonlinearity, the  $+/-$  errors are not exactly the same, but the difference between them is so small, that it is possible to assume that:

$$Upper_{Error_c} \sim Lower_{Error_c} \quad \text{Eq. A16}$$

The NaCl concentration error can be stated as the mean value of (1) and (2):

$$Mean_{Error_c} = \frac{(Upper_{Error_c} + abs(Lower_{Error_c}))}{2} \quad \text{Eq. A17}$$

The non-linear dependence of the sensor in response to NaCl concentration means that the precision is not fixed for all NaCl concentrations.  $Mean_{Error_c}$  is a matrix. The worst case precision occurs in the region where the sensor response shows saturation ( $c < 5$  wt%), and the best case precision corresponds to low concentrations ( $0.2$  wt%  $< c < 1$  wt%), where the sensor shows a better sensitivity to  $c$  changes. The precision results are shown in Table 6.10 of chapter 6. As for moisture and temperature, typical, best and worst case precision are obtained (in the useful range for precision definition  $0.2 < c < 15$  wt%) from the following calculations respectively:

$$Typical_c_{precision} = Mean(Mean(Mean_{Error_c})) \quad \text{Eq. A18}$$

$$Best_c_{precision} = Min(Min(Mean_{Error_c}))$$

$$Worst_c_{precision} = Max(Max(Mean_{Error_c}))$$

## Appendix 2 – Mathematical formulation of Pooled Repeatability

Each cycle for moisture in Figure 5.17 and each cycle for temperature in Figure 5.16 is made of a number  $P$  of points, which in this case are 6 for both moisture and temperature cycles. The impedance response of the sensor can be defined by mean of the variable  $R = \frac{Z_{mod}}{Z_{mod,0}}$ . To the response of each point in each curve it is possible to associate an index from 1 to  $P$ :  $R_1, \dots, R_P$ . Each curve shows a response  $R_i$  for each  $i$ -point. The repeatability between the cycles can be evaluated by means of the following equation for the Pooled Repeatability [2]:

$$R_{pooled} = \sqrt{\frac{(n_1-1) \cdot s_1^2 + (n_2-1) \cdot s_2^2 + \dots + (n_P-1) \cdot s_P^2}{n_1 + n_2 + \dots + n_P - P}} \quad \text{Eq. A19}$$

where the degree of freedom for each point,  $n_i$ , is equal to the number of cycles, and the standard deviation  $s$  for each point,  $s_i$ , is given by the following equation [2]:

$$s = \sqrt{\frac{\sum_{j=1}^n (R_j - R_{mean})^2}{n-1}} \quad \text{Eq. A20}$$

In equation A20,  $R_{mean}$  is the average of the  $R_j$  response for all the cycles, and  $n$  is their degree of freedom, which is equal to the number of cycles.

### Appendix 3 – Chloride geopolymer sensor characterization: Data Tables

#### A-3.1 Actual NaCl concentration values

Applied NaCl concentration [wt%]	Actual NaCl concentration [wt%]					
	Saturation	Point 1	Point 2	Point 3	Point 4	Point 5
0	$0.002 \pm 0.191 \cdot 10^{-4}$	$0.002 \pm 0.218 \cdot 10^{-4}$	$0.002 \pm 0.273 \cdot 10^{-4}$	$0.002 \pm 0.301 \cdot 10^{-4}$	$0.003 \pm 0.334 \cdot 10^{-4}$	$0.012 \pm 0.366 \cdot 10^{-4}$
0.52	$0.139 \pm 0.809 \cdot 10^{-2}$	$0.140 \pm 0.001$	$0.163 \pm 0.001$	$0.173 \pm 0.002$	$0.184 \pm 0.002$	$0.202 \pm 0.002$
1.202	$0.473 \pm 0.003$	$0.479 \pm 0.004$	$0.555 \pm 0.005$	$0.592 \pm 0.006$	$0.633 \pm 0.007$	$0.680 \pm 0.008$
2.169	$0.939 \pm 0.006$	$0.947 \pm 0.008$	$1.108 \pm 0.010$	$1.185 \pm 0.012$	$1.262 \pm 0.013$	$1.237 \pm 0.015$
3.412	$1.371 \pm 0.008$	$1.383 \pm 0.011$	$1.603 \pm 0.014$	$1.698 \pm 0.016$	$1.799 \pm 0.018$	$1.974 \pm 0.020$
5.293	$2.507 \pm 0.015$	$2.532 \pm 0.019$	$2.958 \pm 0.026$	$3.129 \pm 0.031$	$3.292 \pm 0.034$	$3.752 \pm 0.038$
8.041	$3.327 \pm 0.020$	$3.382 \pm 0.026$	$3.858 \pm 0.033$	$4.078 \pm 0.051$	$4.307 \pm 0.057$	$5.242 \pm 0.064$
12.002	$5.676 \pm 0.034$	$5.753 \pm 0.045$	$6.705 \pm 0.060$	$7.087 \pm 0.084$	$7.450 \pm 0.092$	$7.899 \pm 0.104$
16.175	$10.032 \pm 0.064$	$10.079 \pm 0.082$	$11.445 \pm 0.105$	$12.180 \pm 0.119$	$13.137 \pm 0.138$	$14.232 \pm 0.184$
28.568	$15.266 \pm 0.103$	$15.457 \pm 0.134$	$17.392 \pm 0.168$	$18.568 \pm 0.191$	$20.043 \pm 0.223$	$21.773 \pm 0.318$

Table A 1 - Actual internal NaCl concentration calculated values for each applied NaCl concentration, for chloride sensing characterization of the geopolymer cell, in chapter 6.

#### A-3.2 Water content values

Applied NaCl concentration [wt%]	Water content [wt%]					
	Saturation	Point 1	Point 2	Point 3	Point 4	Point 5
0	$87.29 \pm 0.91$	$85.90 \pm 0.90$	$74.27 \pm 0.80$	$69.79 \pm 0.77$	$65.42 \pm 0.74$	$61.94 \pm 0.71$
0.52	$87.29 \pm 0.90$	$86.64 \pm 0.89$	$74.18 \pm 0.79$	$69.72 \pm 0.76$	$65.82 \pm 0.73$	$61.36 \pm 0.76$
1.202	$84.89 \pm 0.92$	$83.96 \pm 0.91$	$72.44 \pm 0.82$	$67.81 \pm 0.78$	$63.38 \pm 0.74$	$60.40 \pm 0.78$
2.169	$85.20 \pm 0.92$	$84.40 \pm 0.91$	$72.05 \pm 0.81$	$67.34 \pm 0.77$	$63.22 \pm 0.74$	$60.31 \pm 0.77$
3.412	$86.45 \pm 0.93$	$85.67 \pm 0.93$	$73.82 \pm 0.83$	$69.65 \pm 0.79$	$65.66 \pm 0.76$	$62.65 \pm 0.79$
5.293	$86.32 \pm 0.94$	$85.45 \pm 0.94$	$72.91 \pm 0.83$	$68.82 \pm 0.79$	$65.33 \pm 0.76$	$62.12 \pm 0.79$
8.041	$87.47 \pm 0.96$	$86.01 \pm 0.94$	$75.15 \pm 0.85$	$70.98 \pm 0.81$	$67.10 \pm 0.78$	$63.03 \pm 0.81$
12.002	$87.10 \pm 1.06$	$85.89 \pm 1.04$	$73.17 \pm 0.92$	$69.03 \pm 0.88$	$65.50 \pm 0.84$	$61.57 \pm 0.88$
16.175	$86.92 \pm 1.10$	$86.09 \pm 1.09$	$75.67 \pm 0.98$	$70.30 \pm 0.93$	$65.76 \pm 0.88$	$60.70 \pm 0.83$
28.568	$87.20 \pm 1.31$	$85.69 \pm 1.29$	$75.26 \pm 1.16$	$69.81 \pm 1.09$	$64.47 \pm 1.02$	$59.02 \pm 0.96$

Table A 2 - Water content percentage values for each applied NaCl concentration, for each drying point of chloride sensing characterization of the geopolymer cell, in chapter 6. The error values were found as described in section 5.4.3 of chapter 5.

A-3.3 Volume values of NaCl solutions for sample soaking

Applied NaCl concentration [wt%]	Volume of NaCl solution for sample soaking [litre]		
0.002	0.907	±	0.006
0.520	0.902	±	0.002
1.202	0.613	±	0.003
2.169	0.391	±	0.003
3.412	0.181	±	0.002
5.293	0.253	±	0.002
8.041	0.251	±	0.001
12.002	0.251	±	0.001
16.175	0.247	±	0.004
28.568	0.247	±	0.004

Table A 3 - Volume of NaCl solution for sample soaking, for each applied concentration, for chloride sensing characterization of the geopolymer cell, in chapter 6.

## Appendix 4 - Circuit model parameters and fits for geopolymer cells with NaCl

### A-4.1 Circuit model parameters values

Applied NaCl concentration [wt%]	Actual internal NaCl concentration [wt%]	Re [ $\Omega$ ]	Rc [ $\Omega$ ]	Ruc [ $\Omega$ ]	Ri [ $\Omega$ ]	Yp [ $\mu$ F]	$\alpha_p$	Yi [ $\mu$ F]	$\alpha_i$	L [ $\mu$ H]	RL [ $\Omega$ ]
0.520	0.139	1.40E-05	9.69E+01	9.19E+02	5.15E+01	1.84E-07	6.82E-01	2.43E-04	5.27E-01	1.59E-13	5.70E+03
1.202	0.473	6.42E-06	1.40E+02	2.83E+02	2.10E+01	9.38E-06	7.16E-01	7.73E-06	7.43E-01	2.08E-03	5.31E+00
2.169	0.939	7.88E+01	7.64E+01	1.27E-02	9.55E+04	6.18E-04	3.62E-01	3.54E-01	7.06E-02	8.94E-02	6.32E+00
3.412	1.371	3.84E-04	1.20E+02	1.95E+02	1.17E+01	1.92E-04	6.23E-01	5.19E-06	7.82E-01	1.18E-03	5.37E+00
5.293	2.507	1.65E-06	1.04E+02	2.07E+02	1.37E+01	3.11E-04	5.74E-01	1.75E-05	6.78E-01	1.25E-01	2.59E+00
8.041	3.327	4.79E+01	3.95E+01	2.30E+01	1.36E+01	9.75E-04	6.21E-01	2.23E-05	6.63E-01	1.41E+01	9.81E-04
12.002	5.676	3.95E-03	8.29E+01	1.54E+01	1.12E+01	6.38E-06	8.81E-01	1.66E-06	8.50E-01	1.06E-02	4.60E+01
16.175	10.032	2.89E+01	4.85E+01	3.23E+01	6.99E+00	1.00E-04	5.61E-01	5.96E-06	8.01E-01	2.82E-01	2.15E+00
28.568	15.266	8.64E-04	5.10E+01	9.58E+01	1.31E+01	2.20E-05	6.83E-01	2.60E-05	6.55E-01	3.81E+00	1.34E+01

Table A 4 - Values of circuit element parameters used in the equivalent circuit model of Figure 5.4 b) for impedance data shown in Figure 6.5, for chloride sensing characterization of the geopolymer cell, in chapter 6.

### A-4.2 Bode plots for geopolymer cells contaminated with NaCl

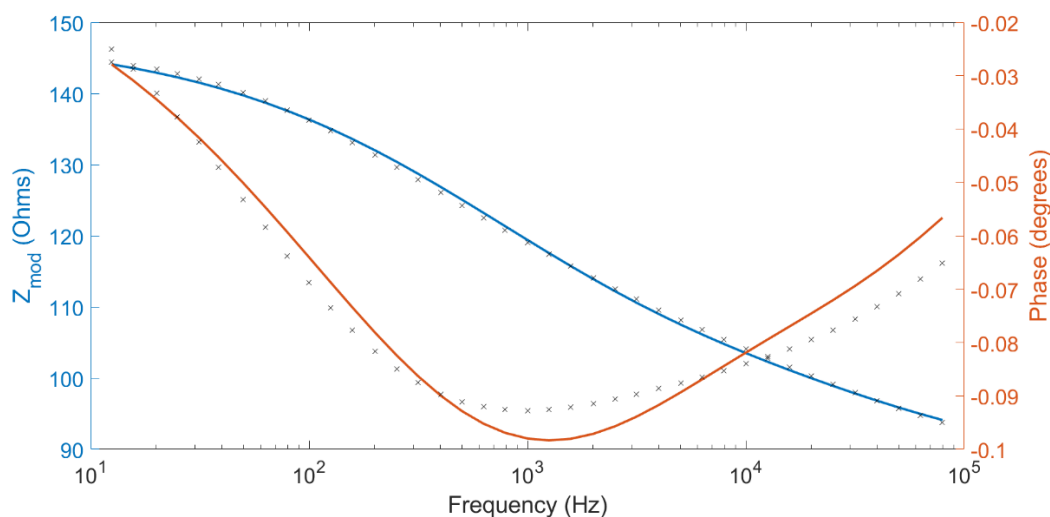


Figure A 1 - Bode plots for  $Z_{mod}$  and phase  $\phi$  obtained for a geopolymer sensor cell with 0.139 wt% actual internal NaCl concentration (applied NaCl concentration = 0.520 wt%), at water content  $W \sim 86 \pm 1$  wt% and temperature  $T = 20 \pm 1$  °C. The fits use the equivalent circuit model given in Figure 5.4 b).

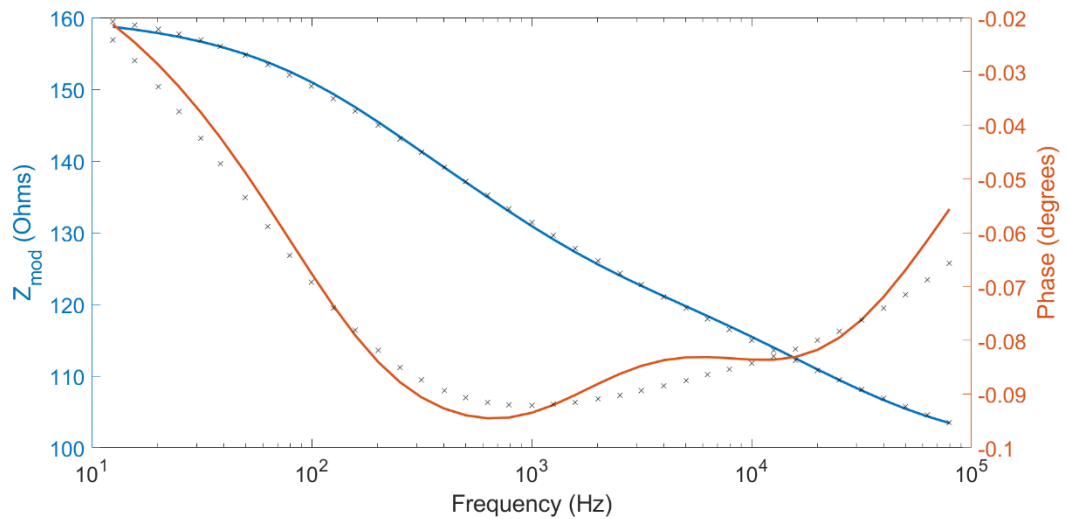


Figure A 2 - Bode plots for  $Z_{mod}$  and phase  $\varphi$  obtained for a geopolymer sensor cell with 0.473 wt% actual internal NaCl concentration (applied NaCl concentration = 1.202 wt%), at water content  $W \sim 86 \pm 1$  wt% and temperature  $T = 20 \pm 1$  °C. The fits use the equivalent circuit model given in Figure 5.4 b).

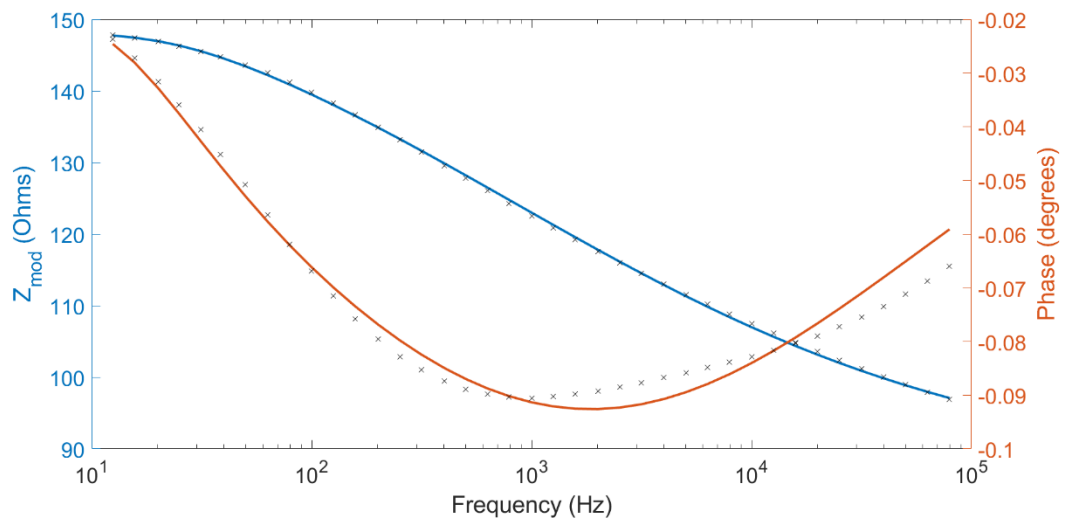


Figure A 3 - Bode plots for  $Z_{mod}$  and phase  $\varphi$  obtained for a geopolymer sensor cell with 0.939 wt% actual internal NaCl concentration (applied NaCl concentration = 2.169 wt%), at water content  $W \sim 86 \pm 1$  wt% and temperature  $T = 20 \pm 1$  °C. The fits use the equivalent circuit model given in Figure 5.4 b).

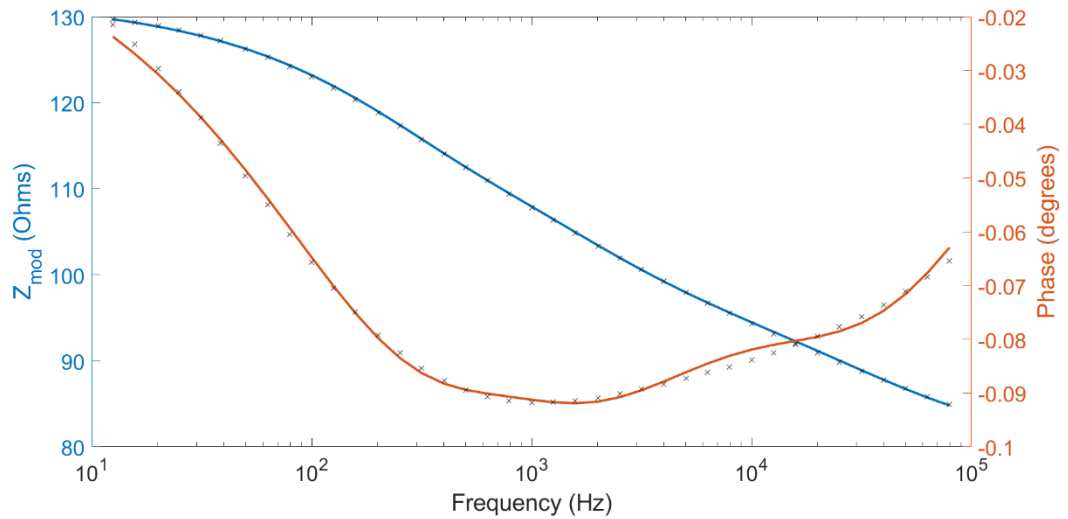


Figure A 4 - Bode plots for  $Z_{mod}$  and phase  $\phi$  obtained for a geopolymer sensor cell with 1.371 wt% actual internal NaCl concentration (applied NaCl concentration = 3.412 wt%), at water content  $W \sim 86 \pm 1$  wt% and temperature  $T = 20 \pm 1$  °C. The fits use the equivalent circuit model given in Figure 5.4 b).

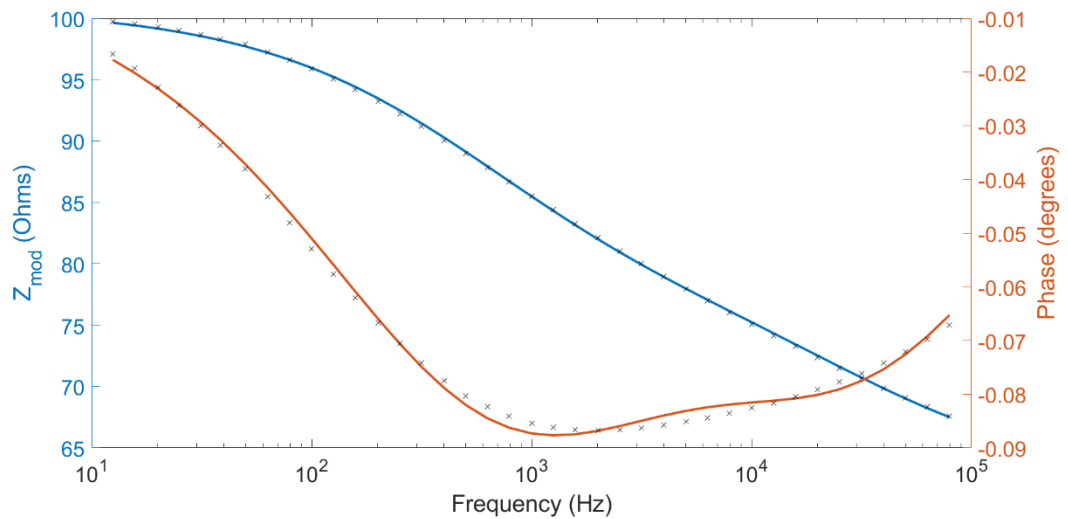


Figure A 5 - Bode plots for  $Z_{mod}$  and phase  $\phi$  obtained for a geopolymer sensor cell with 3.327 wt% actual internal NaCl concentration (applied NaCl concentration = 8.041 wt%), at water content  $W \sim 86 \pm 1$  wt% and temperature  $T = 20 \pm 1$  °C. The fits use the equivalent circuit model given in Figure 5.4 b).

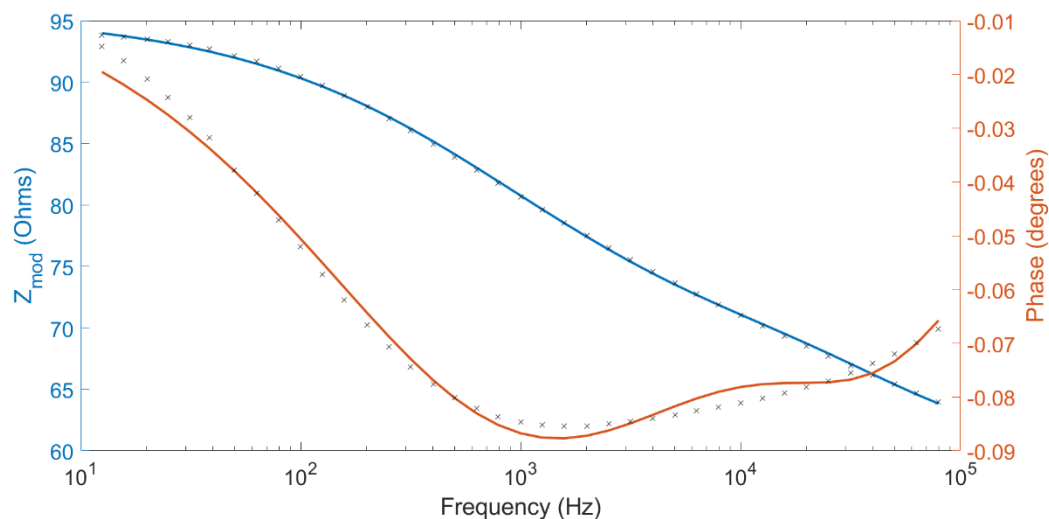


Figure A 6 - Bode plots for  $Z_{mod}$  and phase  $\varphi$  obtained for a geopolymer sensor cell with 5.676 wt% actual internal NaCl concentration (applied NaCl concentration = 12.002 wt%), at water content  $W \sim 86 \pm 1 \text{ wt\%}$  and temperature  $T = 20 \pm 1 \text{ }^\circ\text{C}$ . The fits use the equivalent circuit model given in Figure 5.4 b).

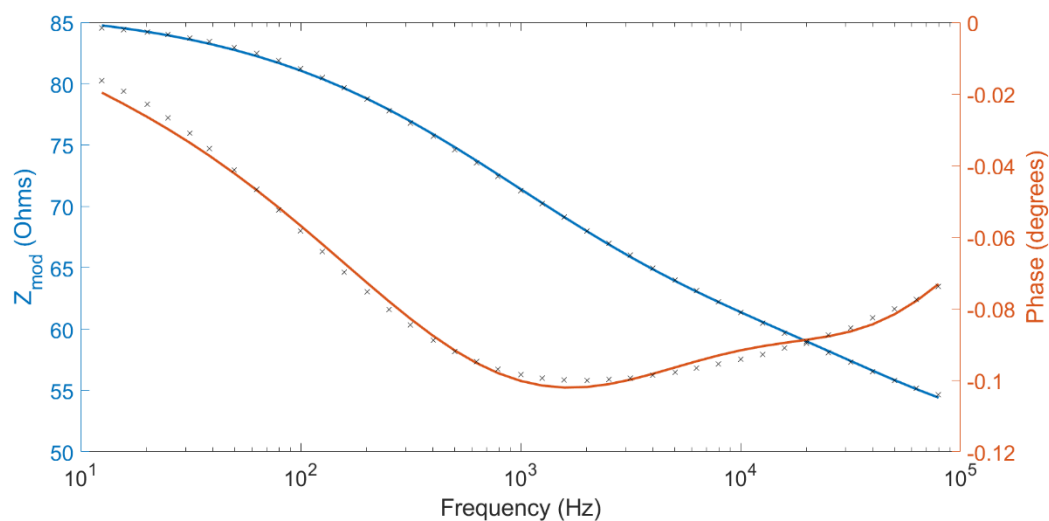


Figure A 7 - Bode plots for  $Z_{mod}$  and phase  $\varphi$  obtained for a geopolymer sensor cell with 10.032 wt% actual internal NaCl concentration (applied NaCl concentration = 16.175 wt%), at water content  $W \sim 86 \pm 1 \text{ wt\%}$  and temperature  $T = 20 \pm 1 \text{ }^\circ\text{C}$ . The fits use the equivalent circuit model given in Figure 5.4 b).

### Appendix 5 –Moisture calibration fit parameters for geopolymer cells with NaCl

<b>c, wt%</b>	<b>Parameter</b>		<b><math>a_5</math></b>	<b><math>a_6</math></b>
0.002	95% confidence bounds	Value	0.1355	164.2
		Lower	0.1122	152.7
		Upper	0.1587	175.7
0.139	95% confidence bounds	Value	0.1391	159.2
		Lower	0.1262	153.0
		Upper	0.1520	165.4
0.473	95% confidence bounds	Value	0.1184	163.4
		Lower	0.1012	153.9
		Upper	0.1355	172.8
0.939	95% confidence bounds	Value	0.1438	147.6
		Lower	0.1229	138.1
		Upper	0.1647	157.1
1.371	95% confidence bounds	Value	0.1023	167.8
		Lower	0.0779	151.7
		Upper	0.1268	183.9
2.507	95% confidence bounds	Value	0.1127	154.0
		Lower	0.1042	149.0
		Upper	0.1212	159.1
3.327	95% confidence bounds	Value	0.1012	155.2
		Lower	0.0620	128.7
		Upper	0.1404	181.8
5.676	95% confidence bounds	Value	0.0978	148.8
		Lower	0.0689	129.0
		Upper	0.1267	168.5
10.032	95% confidence bounds	Value	0.0829	140.4
		Lower	0.0503	114.1
		Upper	0.1155	166.7
15.266	95% confidence bounds	Value	0.0453	172.8
		Lower	0.0335	155.9
		Upper	0.0572	189.7

Table A 5 - Parameters and their 95% confidence bounds for the best fit curves, equation 6.6, shown in Figure 6.13, for chloride sensing characterization of the geopolymer cell, in chapter 6.

**Appendix 6 – Tables of circuit model parameters for coating cells**

Water content [wt%]	Rc [Ω]	Ruc [Ω]	Yp [μF]	αp	Yb [μF]	αb
<b>91.83</b>	6.87E+03	2.42E+05	1.90E-04	2.49E-02	6.24E-09	6.31E-01
<b>87.56</b>	1.32E+04	3.52E+04	7.39E-05	3.44E-02	4.41E-09	6.57E-01
<b>83.04</b>	4.16E+05	1.81E+04	3.04E-08	9.05E-01	1.47E-08	5.70E-01
<b>78.14</b>	6.89E+04	2.12E+04	5.62E-08	4.54E-01	3.87E-10	8.39E-01

Table A 6 - Circuit parameter elements for coating samples at four different water contents and at a temperature of 20 °C.

NaCl [%]	Re [Ω]	Rc [Ω]	Ruc [Ω]	Ri [Ω]	Yp [μF]	αp	Yi [μF]	αi	L [μH]	RL [Ω]
<b>0.5</b>	3.59E+03	2.51E+03	2.62E+03	1.51E+03	3.72E-09	8.74E-01	1.09E-05	4.99E-01	1.94E-03	9.12E+05
<b>1.2</b>	4.03E+03	5.49E+02	3.47E-01	2.94E+02	4.40E-07	8.08E-01	5.88E-06	9.32E-01	1.08E+02	5.19E-01
<b>2.2</b>	3.66E+02	6.41E+02	4.19E+03	2.75E+03	1.22E-06	9.15E-01	5.59E-08	9.26E-01	1.69E-01	2.19E+03
<b>3.5</b>	2.10E+03	4.47E+00	1.58E+05	3.89E+02	6.16E-06	1.26E-01	4.43E-06	6.15E-01	1.39E-01	1.05E+01
<b>5.5</b>	4.17E+02	6.27E-01	8.98E-05	8.52E+02	4.34E-01	3.12E-01	1.83E-07	9.44E-01	6.72E-02	7.16E+02
<b>8.5</b>	4.43E+02	2.46E+01	3.38E-02	1.33E+03	4.83E-03	5.66E-01	9.13E-08	9.64E-01	1.07E-01	1.19E+03
<b>13</b>	2.66E-09	5.93E+02	5.69E+02	7.35E+02	1.55E-02	1.00E+00	2.16E-07	9.41E-01	5.84E-02	6.18E+02

Table A 7 - Circuit parameter elements for coating samples at 8 different NaCl concentrations, at water content of ~92% and temperature of 20 °C.

## Appendices references

- [1] J. G. Webster and H. Eren, *Measurement, Instrumentation, and Sensors Handbook: Two-Volume Set*: CRC press, 2018.
- [2] A. Kallner and E. Theodorsson, "Repeatability imprecision from analysis of duplicates of patient samples and control materials," *Scandinavian Journal of Clinical and Laboratory Investigation*, pp. 1-5, 2020.